DTU Library

Advances in Piezoelectric Systems: An Application-Based Approach.

Zsurzsan, Tiberiu-Gabriel

Publication date:
2016

Document Version
Publisher's PDF, also known as Version of record

Technical University of Denmark

Gabriel T. Zsurzsan

Advances in Piezoelectric Systems: An Application-Based Approach

Ph.D. Dissertation, February 2016

DTU Electrical Engineering
Department of Electrical Engineering

Gabriel T. Zsurzsan

Advances in Piezoelectric Systems: An Application-Based Approach

Ph.D. Dissertation, February 2016

Advances in Piezoelectric Systems: An Application-Based Approach

Author:
Gabriel T. Zsurzsan

Supervisors:

Michael A. E. Andersen	—	DTU Elektro, Electronics Group
Zhe Zhang	—	DTU Elektro, Electronics Group
Nils A. Andersen	—	DTU Elektro, Automation and Control Group

Department of Electrical Engineering
Electronics Group
Technical University of Denmark
Elektrovej building 325
DK-2800 Kgs. Lyngby
Denmark

www.ele.elektro.dtu.dk
Tel: (+45) 45 25 38 00
Fax: (+45) 45 88 01 17
E-mail: hw@elektro.dtu.dk

Release date:	15^{th} February 2016
Category:	1 (public)
Edition:	First
Comments:	This thesis is submitted in partial fulfillment of the requirements for obtaining the PhD degree at the Technical University of Denmark.

To my beloved wife and longtime accomplice in all things silly,
Adriana

Preface and Acknowledgment

This thesis is submitted in partial fulfillment of the requirements for obtaining the PhD degree from the Technical University of Denmark. The research has been carried out at the Electronics group, Department of Electrical Engineering between the February 2013 and February 2016, under the supervision of prof. Michael A.E. Andersen, associate prof. Zhe Zhang and associate prof. Nils A. Andersen.

The PhD project titled *Control and sensor techniques for PAD servo motor control* was funded by the Danish National Advanced Technology Foundation (HTF) as part of the HTF project number 054-2011-1 titled *PAD Motor Piezoelectric Actuator Drive to Operate in High Magnetic Fields*. The research was conducted in close collaboration between DTU Electrical Engineering and the industrial partners:

- Noliac A/S
- IPU Technology Development
- Siemens AG, Healthcare Sector, Clinical Products Division

During the project, a 4-month external research stay was conducted at the Advanced Mechatronics Laboratory, led by prof. Akio Yamamoto at the Department of Precision Engineering, Graduate School of Engineering, University of Tokyo, Japan.

This hard, but wonderful three-year journey has now come to a end, but I would not have arrived at this point without the support of some amazing people along the way. I wish to hereby thank all who contributed in any way to this journey – be it moral support, kind words, technical knowledge or a good old kick in the rear to get me going again! My special thanks and deep appreciation goes to:

- My supervisors Michael A.E. Andersen, Zhe Zhang and Nils A. Andersen for inspiration, unending support, confidence in my skills and to allow my curiosity to be the main driver throughout the entire project.
- Yamamoto-Sensei and the whole Advanced Mechatronics Lab at the University of Tokyo: Nemoto-san, Takei-san, Nakamura-san, Kitazawa-san, Iguchi-san, Nabae-san, Wang-san, Xu-san and Hara-san for welcoming me with open arms, taking care of me, making my stay in Tokyo both fruitful and truly enjoyable and always receiving me warmly with each subsequent visit.
- Charles Mangeot, whose amazing humor and enlightening feedback I thoroughly enjoyed.
- Henriette, Hans-Christian, Allan, Dorte and Bertil for help, support, kind words and for always making me feel welcome. This group would not be able to function without you!

- Marzieh, whom I spent a great part of my PhD working with and whom I owe a great deal of my results and success to. I will fondly remember the long night Tokyo-Copenhagen remote software debugging sessions!
- All my colleagues at DTU Elektro for help, support, constructive discussions and jokes to keep spirits high during the long hours in the lab.
- A very special thanks to Maria, Juan, Paul, Marta, Riccardo, Maja, Milovan and Alexander. You've been there for me since day 1, sharing moments of joy and frustration, late-night lab and drinking sessions (sometimes both). You've also been there for me during one of the most important days of my life. You guys rock!
- Also a very special thanks to Marius, Emil, Bogdan, Daniel and Cristian for always being there to throw a beer my way when things got rough. Here's to hoping that never changes.
- My parents, who supported my choices and always understood that I need to see the world if I want to grow as a person – even though that meant being anywhere but home.
- Finally, a very very special thanks to my dear wife Adriana, who put up with me and all my shenanigans, frequent travels and extended leaves of absence and showed her unfaltering support for everything I did. I would not be here today if it weren't for you, and for that I am forever in your debt.

In short,

One big massive thank you!

Abstract

Piezoelectricity is a fascinating research topic with wide-branching applications due to the unique property of bidirectional energy transfer. Piezoceramics can be used as both actuators and sensors without imposing any constraints on their supporting circuitry. This property, coupled with their low manufacturing costs and high robustness has enabled wide-spread usage in applications ranging from simple spark lighters or pressure sensors to much more complicated energy harvesting systems and piezoelectric transformers.

One governing property of piezoelectric devices is the existence of a mechanical frequency of resonance, or the natural frequency of the device paired with an antiresonance, which are material and size-dependent. From an electrical standpoint, the equivalent behavior of a piezoelectric device depends on how close or far from its natural resonance the device is excited in terms of frequency. Based on this classification, three distinct, useful electrical behaviors can be identified: a capacitive behavior prominent at frequencies far from resonance, a resistive behavior encountered at resonance and antiresonance peaks and an inductive behavior, encountered at frequencies between the two.

These three distinct behaviors encountered in any piezoelectric device represents the basis of discussion in the thesis. Therefore the present PhD dissertation is an application-based approach to researching all three behaviors individually, while finding solutions to the challenges encountered along the way.

First, the capacitive behavior is studied, with the Piezoelectric Actuator Drive motor as a direct application. At low frequencies, piezoelectric devices are ideal as micro- and nanoscale positioning actuators but they are plagued by high levels of hysteretic nonlinearities. A model is developed to estimate this behavior, followed by a low-cost forward compensation method which achieves a positioning error reduction by a factor 20. Next, the characteristics of the PAD motor are researched and a method of extracting mechanical quality information and predict overload through feedback signal analysis is demonstrated.

The next behavior studied is the inductive behavior, specifically dealing with a bidirectional dc-dc power converter employing a piezoelectric transformer as major component. The main contribution here is achieving optimum tracking, hard-switching minimization and power flow control during bidirectional operation of a self-oscillating converter. Feasibility of using the converter in an MRI scanner is demonstrated.

The third and final behavior researched is the resistive behavior. This is widely encountered since most piezoelectric motors, ultrasonic baths and some energy harvesting systems operate at resonance. Friction control through squeeze-film application is achieved in an electrostatic surface actuator for the first time ever. This enables system functionality without glass gap material and concomitantly reduces minimum electrostatic operating voltage by 70%.

Resumé

Piezoelektricitet er et fascinerende forskningsemne med bredt forgrenede applikationer på grund af den unikke egenskab med tovejs energioverførsel. Piezokeramiske elementer kan bruges som både aktuatorer og sensorer uden at lægge nogen begrænsninger på deres elektronikkredsløb. Denne egenskab kombineret med deres lave produktionsomkostninger og høje robusthed har udbredt piezokeramisk brug i applikationer der spænder fra simple gnistlightere eller tryksensorer til meget mere komplicerede energihøst systemer og piezoelektriske transformatorer.

En styrende egenskab ved piezoelektriske enheder er eksistensen af en mekanisk resonansfrekvens, eller den naturlige frekvens af enheden, parret med en antiresonans, der er materiel- og størrelsesafhængig. Fra et elektrisk synspunkt afhænger den ækvivalente opførsel af en piezoelektrisk enhed af, hvor tæt på eller langt fra sin naturlige resonans enheden exciteres med hensyn til frekvens. Baseret på denne klassifikation, kan tre forskellige, nyttige elektriske virkemåder identificeres: En kapacitiv virkemåde der er fremtrædende ved frekvenser langt fra resonansspidsen, en resistiv virkemåde der findes ved det præcise resonanspunkt, og en induktiv virkemåde der er findes ved frekvenser mellem resonans- og antiresonansspidser.

Disse tre distinkte virkemåder, der findes hos alle piezoelektriske enheder, udgør grundlaget for diskussionen i afhandlingen. Den nuværende Ph.D.-afhandling bruger anvendelsesbaseret forskning indenfor alle tre virkemåder, samtidig med at der findes løsninger på de udfordringer, der er findes undervejs.

Først er den kapacitive adfærd undersøgt med en Piezoelectric Actuator Drive motor, som en direkte applikation. Ved lave frekvenser er piezoelektriske anordninger ideelle som mikro- og nanoskala positioneringsaktuatorer, men de er plaget af høje niveauer af hystereseulineariteter. En model er udviklet til at estimere denne adfærd, efterfulgt af en kompensationsmetode der kun kræver lav datakraft. Der opnår en positioneringsfejlreduktion med en faktor 20. Dernæst er PAD-motorens egenskaber udforsket og en fremgangsmåde til udtrække oplysninger om mekanisk kvalitet samt forudsige overbelastning gennem feedback-signal analyse er påvist.

Dernæst er den induktive funktionsmåde udforsket. Her arbejdes specifikt med en bidirektional DC-DC power konverter, som anvender en piezoelektrisk transformer som den centrale komponent. Det væsentligste bidrag her er at opnå optimal sporing, minimering af switchtab samt power flow kontrol under bidirektional drift af en selvoscillerende konverter. Muligheden for at benytte konverteren i en MR-scanner uden væsentligt billedeforringelse er påvist.

Den tredje og sidste funktionsmåde berørt i denne afhandling er den resistive adfærd. Dette er almindeligt kendt, da de fleste piezoelektriske motorer, ultralydsbade til rengøring og nogle energihøst-systemer fungerer ved resonans. Ved brug af en squeezefilm i en elektrostatisk overfladeaktuator er der for første gang nogensinde opnået en meget væsentlig reduktion af gnidningsmodstanden. Dette muliggør at systemet fungerer uden glasperler og samtidig kan den nødvendige elektrostatiske driftsspænding reduceres med 70%.

Contents

List of Abbreviations

CEZC	current estimation zero crossing
DDL	dynamic delay line
DOF	degrees of freedom
EMI	electromagnetic interference
FPGA	field-programmable gate array
HS	high-side
IDE	interleaved interdigitated electrode
LDM	laser displacement meter
LS	low-side
MRI	magnetic resonance imaging
ODT	optimum dead-time
PAD	piezoelectric actuator drive
PCI	peripheral component interconnect
PMA	piezoelectric multilayer actuator
PT	piezoelectric transformer
RF	radio frequency
RIO	reconfigurable input-output
RLC	resistor inductor capacitor
SNR	signal to noise ratio
SPI	serial peripheral interface
ZCS	zero-current switching
ZVS	zero-voltage switching

List of Figures

1

Introduction

If you want to find the secrets of the universe,
think in terms of energy, frequency and vibration.

– Nikola Tesla

The discovery of the capability of crystals such as quartz, topaz, cane sugar and Rochelle salt, among others, to produce an electric charge when subjected to mechanical stress is attributed to the Curie brothers who noticed this curiosity sometime in 1880. This effect was quickly dubbed *piezoelectricity*, to distinguish it from at the time already-established notions of static electricity and pyroelectricity. The converse effect, however, was not discovered but mathematically deduced through thermodynamic principles one year later, and then quickly proven experimentally.

This discovery at the time remained nothing more but a laboratory curiosity, as its subtle effects were gravely overshadowed by the more discernible benefits brought on by electromagnetism. Then came World War I and with it, the first truly impactful application for piezoelectricity in ultrasonic submarine detection. The success of this application spurred great interest from industrial nations, and the evolution never stopped since [1, 2].

Piezoelectricity is therefore the naturally occurring property encountered in specific crystalline materials whereby an electrical charge is accumulated in response to applied mechanical stress. Conversely, a structural deformation is observed under applied electrical charge. Thus, piezoelectricity is a bidirectional energy transformation phenomenon which converts energy between mechanical and electrical domains.

Just as the electrical and mechanical energy domains covered by piezoelectric devices are interchangeable, so too are the domains they can be modeled in. Therefore, an equivalent electrical representation of piezoelectric behavior is shown in Fig. 1.1(a) with its mechanical counterpart, represented in force-voltage analogy, illustrated in (b). In this representation, voltage sources in electrical domain become force sources in mechanical representation. Currents are represented by velocities, while resistors, inductors and capacitors become dampers, masses and springs, respectively.

Through their energy conversion capabilities, piezoelectric devices are ideal candidates for mixed-domain modeling. Thereby, in simplified terms, if the electrical domain is the system input, then they act as voltage-controlled force and displacement sources. Conversely, if the mechanical domain is considered the input, then they will act electrically

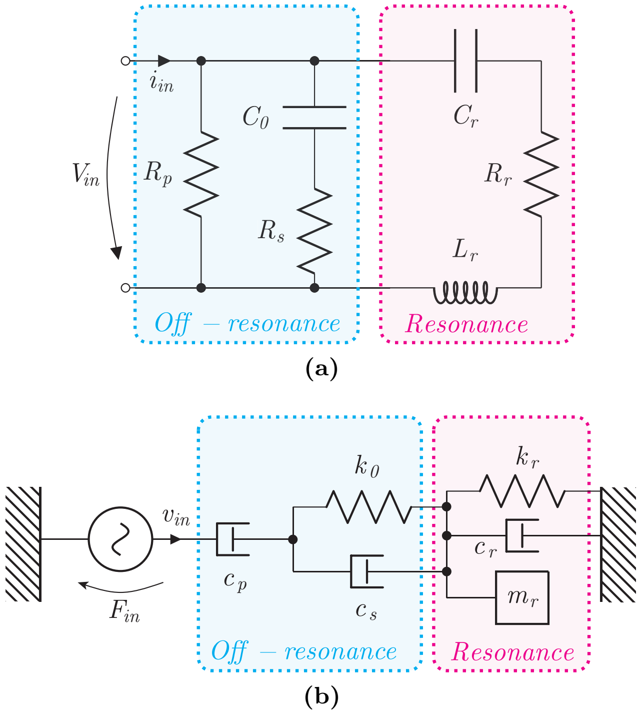

Figure 1.1: Guan model of unloaded piezoelectric ceramics (a) and its force-voltage mechanical equivalent (b).

Table 1.1: List of constitutive equation symbols and their units

Symbol	Name	SI Unit
S	Strain component	
D	Electric displacement component	C/m^2
E	Electric field component	V/m
T	Stress component	N/m^2
d	Piezoelectric constant	m/V or C/N
s	Elastic compliance constant	m^2/N
ϵ	Permittivity constant	F/m

as force-dependent voltage and charge sources.

The linear interdependence in between these four properties fully describes both the forward and reverse piezoelectric effects. This description is formalized through the introduction of the *piezoelectric constitutive equations*. These offer a good description of the *direct* and *converse* piezoelectric effects, or the mechanical-electrical and electrical-mechanical conversion directions, respectively. This defines a polarized piezoceramic as an energy transformation device. A multitude of forms describing different relationships can be encountered, and one such form which relates stress and electric displacement to strain and electric field is presented in (1.1).

$$\begin{aligned} S &= d \cdot E + s^E \cdot T \\ D &= d \cdot T + \epsilon^T \cdot E \end{aligned} \tag{1.1}$$

The superscripts in the equation represent constant condtions, i.e. $\square^T$ stands for constant stress conditions, whereby the piezoelectric device is unclamped and $\square^E$ repre-

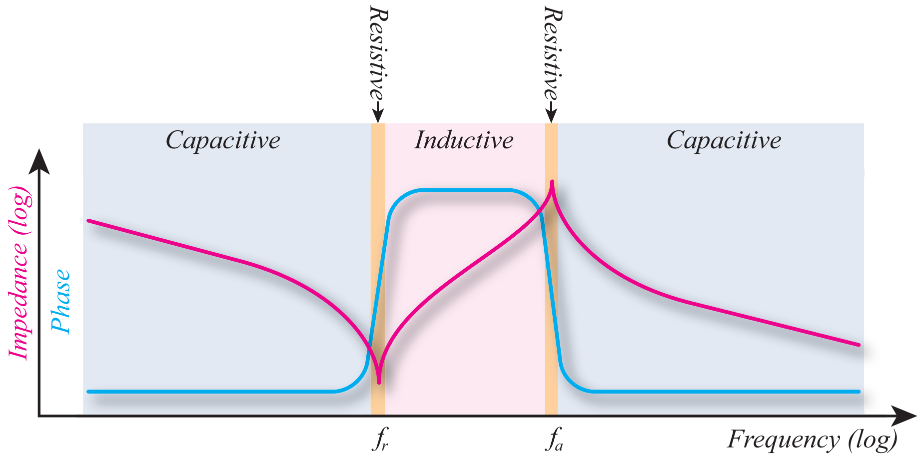

Figure 1.2: Typical impedance response of piezoelectric ceramics.

sents conditions of constant electric field, obtained usually by electrode short-circuiting. Table 1.1 describes all quantities involved in (1.1).

1.1 Thesis structure

The starting point for discussing the topics presented in the thesis focuses on the electrical-equivalent characteristic behavior of piezoelectric devices with respect to their excitation frequency. In light of this, relative to the resonance or natural frequency these devices exhibit, three distinct behaviors can be identified: *capacitive*, *inductive* and *resistive*. These definitions originate from the dependency of their electrical impedance on frequency of excitation, as illustrated in Fig. 1.2.

Thereby, piezoelectric devices operated at low frequencies are equivalent in behavior to capacitors, in that they store potential energy in an electric field. Mechanically, this is equivalent to potential energy stored in springs. As the excitation frequency increases, the impedance of the device reaches its minimum point. This point is called the resonance frequency, where the equivalent behavior becomes resistive. At this frequency, a maximum displacement enhancement is observed under a constant voltage drive condition, as current easily flows into the device. As the frequency increases further, the impedance starts to rise again until it reaches a maximum. The frequency corresponding to the point of maximum impedance represents the anti-resonance, which also exhibits high displacement but under a constant current drive condition. The region between the resonance and anti-resonance frequencies is where the piezoelectric device behaves inductively, as it stores kinetic energy similar to an inductor and its magnetic field. Mechanically, this is analogous to the kinetic energy stored in a moving mass.

These three distinct behaviors are encountered in any piezoelectric device, but they are usually tailored to operate normally in one of the three modes. Moreover, their field of application is most often behavior-specific. Therefore the present PhD dissertation is an application-based approach to researching all three behaviors individually, while presenting the challenges encountered along the way. The whole thesis is then structured around these distinct behaviors, divided into chapters that cover each individually.

A visual illustration of the thesis flow is given on the following page. The topics discussed in the key chapters are shown in the vertical flow and the connection between the discussed topics and overlapping publications is marked.

1.2 Scope and objectives

The scope of this thesis is to provide a non-exhaustive overview on different applications for piezoelectric devices through the prism of their equivalent electrical behavior. The results achieved are part of the research carried out between February 2013 and February 2016, as a PhD student at the Electronics Group, Technical University of Denmark. Most of the scientific results presented herein have been published or submitted for peer review as conference papers, journals or patent applications. These publications form a significant part of the thesis and are included in the appendices. Thereby, the thesis is to be viewed as a supplement to the publications, presenting a more cohesive overview of the research and topics involved.

The major project objectives are:

- Study piezoelectric stack actuator quasi-static behavior and the influence of hysteretic nonlinearities on positioning precision. The aim is to find methods to reduce the effects of these nonlinearities.
- Characterize the electrical and mechanical behavior of the Piezoelectric Actuator Drive motor and derive a method for closed-loop control. Test the feasibility of using this motor inside an MRI chamber.
- Design a control algorithm for maximizing the efficiency of piezoelectric transformer based switch mode power supplies while allowing bidirectional power transfer. Test the feasibility of using the converter inside an MRI chamber.
- Demonstrate the possibility of surface friction control through induced vibrations for use in an electrostatic surface actuator.

Advances in Piezoelectric Systems: An Application-Based Approach

1. Introduction

Structure, scope and technological background

2. Capacitive behavior

Piezoelectric Multilayer Actuators

Hysteresis modeling

IECON'15: Preisach model of hysteresis for the Piezoelectric Actuator Drive
Actuator'16: Temperature dependency of the hysteresis behaviour of PZT actuators using Preisach model

Hysteresis compensation

ECCE'14: Piezoelectric stack actuator parameter extraction with hysteresis compensation
TIE: Zero computational cost piezoelectric hysteresis compensation for quasi-dynamic applications

The Piezoelectric Actuator Drive

Characterization

UPEC'15: Control and sensor techniques for PAD servo motor drive
PEAC'14: Investigating the electromechanical coupling in Piezoelectric Actuator Drive motor under heavy load

Driving

ICIT'16: Class-D amplifier design and performance for driving a Piezo Actuator Drive servomotor

Sensorless operation

MRI behavior

3. Inductive behavior

Piezoelectric Transformers

Deadtime control

Patent 2015: Resonant power converter comprising adaptive dead-time control

Delay-based pulse shaping

TPEL: Optimum phase in the self-oscillating loop for piezoelectric transformer-based power converters

Bidirectional operation

Patent 2016: Resonant power converter with dead-time control of synchronous rectification circuit

MRI behavior

4. Resistive behavior

Ultrasonic lubrication

The Squeeze-film effect

ICAM'16: Using squeeze-film effect to reduce surface friction in electrostatic actuators

The Electrostatic Actuator

Combined system performance

ICAM'16: Evaluation of Breaking Performance in Vibration-Assisted Electron.ctrostatic Surface Induction Actuator

6. Other research interests

ICIT'16: Improved kayaking ergometer using a switch-mode converter-driven alternator

5. Conclusions

1.3 Technology background

Since the discovery of the effect, piezoelectricity and its numerous applications have grown exponentially and will continue to do so according to the trend of its total market value, which is estimated to reach $38 bn. by 2017 [3, 4] with the largest single market being the Asia-Pacific region. Although sparked by demonstrations of its benefits to military applications, the true growth of piezoelectricity started with the discovery of synthetic materials that can exhibit the effect after a process called poling [1, 5, 6].

The wide range of applications where piezotechnology is employed covers military, industrial, automotive and consumer markets. In military applications, piezoelectric devices see the most use as underwater acoustic detection and communications systems (sonar) [7, 8] or grenade fuses and detonation systems [9–11]. The use of sonars has expanded into civilian applications as well for naval depth measurements and fish finding [12].

In light of the topics discussed in the thesis, of more direct interest are the industrial, automotive, medical and consumer-oriented applications. Here, a year-by-year increase in industry automation coupled with the appearance of sophisticated consumer electronics and advancements in medicine are major drivers in both sales and research of piezoelectric devices. Notable applications with a mature market share segment include autofocus mechanisms in cameras, ultrasonic cleaners and welders, touch, impact, position and pressure sensors, seismic sensors, ultrasonic drilling, piezo-transformers, precision mechanics, ultrasonic imaging, flow meters, wheel balancers, motors, igniters, speakers, ultrasonic sewing, microphones, data storage components, print heads and the list goes on [4].

Individual applications in each market segment are too numerous to fully expand here, therefore emphasis will be placed on the applications discussed in the thesis, through the perspective of the three identifiable behaviors based on the piezoelectric impedance curve.

Capacitive

Capacitive behavior of piezoelectric devices is encountered at low-frequency operation, where their use in precise positioning applications is dominant [4]. The high stiffness of piezoelectric actuators allows for strong voltage-dependent actuation, and relatively linear behavior [13]. Coupled with their small strain of up to 1.7% the device size for single-crystal devices [14], piezoelectric actuators are ideal for micro- and nanoscale positioning and manipulation [15–19].

Piezoelectric actuators are nonetheless plagued by two major types of elastic nonlinearities: hysteresis and creep. Hysteresis affects actuator positioning accuracy in dynamic operation, while creep causes a drift in position during periods of static activity [20–22].

Modeling hysteresis in the piezoelectric motor is a necessary step in developing compensation methods to negate the effects [23]. The most encountered method of modeling hysteresis in literature remains the Preisach-Krasnoselskii scalar model [24], which provides a straightforward method of representing the hysteretic effect. Although initially developed for the purpose of modeling magnetic hysteresis, due to its phenomenological nature, the method can be used to model any type of hysteresis [25]. This fact, combined with the generally predictable performance has led the Preisach model to be the preferred method used when hysteresis is involved, as attested by the numerous publications dealing with the model and its inverse [26–30].

A less conventional application for piezoelectric actuators is in the Piezoelectric Actuator Drive motor, which, unlike most piezoelectric motors, runs at quasi-static frequencies. The PAD is a type of rotary, non-resonant motor that transforms the linear motion of piezoelectric stack actuators into a precise rotation [31, 32]. The operating principle is based on a wobble-style motor, where the motor ring is actuated into an off-center circular motion around an axially constrained shaft, thereby generating rotation. A micro-mechanical toothing interface is machined between the ring and shaft then enables both high positioning accuracy and output torque [33]. The actuation method, combined with the type of toothing and the inherent large stiffness of the piezoelectric stack actuators makes the PAD appropriate for open-loop control [34–36]. Manufactured completely out of non-magnetic materials, the PAD is safe for use in MRI scanners[37].

Inductive

Inductive behavior of piezoelectric devices is discussed in the thesis through the prism of piezoelectric transformers. These devices exhibit higher power density, higher efficiency, lower cost and lower electromagnetic interference compared to their conventional counterparts [38–40]. These advantages, together with their ceramic composition and resulting magnetic neutrality has increased their popularity in replacing conventional transformers [41].

Their high quality factor and high gain provided under matched load conditions [41, 42] make these devices ideal for driving cold cathode fluorescent lamps [43], electronic ballasts [44, 45], high voltage inverters [46] and other technology related displays [47] or LED lighting [48].

Although practically difficult, piezoelectric transformers are capable of achieving efficiencies of 98-99%, all while maintaining their magnetic neutrality. This allows them to operate in magnetically-sensitive environments such as MRI scanners [49]. Furthermore, design of switch-mode converter topologies based on piezoelectric transformers have proven to be capable of soft-switching while foregoing the use of any inductive components [50–54].

The capability of switch-mode power converters to achieve soft-switching is essential to increasing their efficiency, especially when coupled with high frequency resonant operation [55–57]. When using piezoelectric transformer-based resonant tanks, the capability of soft-switching relies entirely on transformer design and its ability to effectively operate in the inductive region [58–61]. By including this requirement in initial transformer design, an empirical ZVS factor can be used in order to ensure soft-switching capabilities [62]. This ensures the most favorable conditions for transformer inductive behavior while still avoiding the use of an added series inductor [63, 64].

Besides piezoelectric transformer applications, the inductive behavior of piezoelectric devices can also be used to replace inductors in power converters. These can then be used alongside existing piezoelectric transformers to lessen transformer requirements on soft-switching operation wile also maintaining magnetic neutrality [65, 66].

Resistive

Resistive behavior of piezoelectric devices focuses on operation at resonance, where the vibration response of the piezoelectric devices is amplified. This is useful for both actuation and sensing, as it arguably represents the optimal energy transfer method between domains [67–72] and is used extensively in piezoelectric motors, ultrasonic baths, structural damage detection and energy harvesting [72–78].

A less-used application in which resonant piezoelectric actuators play a key role is ultrasonic levitation through squeeze film induction, which is well-known in microfluidics and microacoustics [79–81]. A key role in this field is the high volumetric power density of piezoelectric devices and their feasibility in miniaturization. Nonetheless, piezo size reduction is limited by heat generation through losses [82].

By applying the same principle of induced squeeze film at a macroscopic level, levitation or ultrasonic lubrication can be achieved in large systems, resulting in a reduction of overall surface friction between contacting surfaces [83–89]. This provides a special benefit in haptic systems, where user feedback can be enhanced through friction modulation. Controlled vibration allows changing the relative feeling of smoothness in a touch-based interaction surface which creates a much more involved user experience compared to the smooth touch surfaces in use today [90–97].

Electrostatic film actuators are thin, lightweight and flexible actuators composed of fully transparent plastic films etched with fine-pitched electrodes [98, 99]. They have very wide areas of application such as particle transportation or flexible muscle actuation, but feature most prominently in haptcis and human-machine interfaces where their transparency allows them to be overlaid onto any traditional display surface or game board. This allows enhancing these interfaces with actuation, motion and feedback capabilities [100–103].

Despite their usefulness, a disadvantage of electrostatic actuators is the fact that they require a layer of very small glass beads between stator and slider films to act as both gap material and friction reducer. This reduces the feasibility of the actuators since the glass beads require periodic reapplication and also need cleaning up after use. By inducing a squeeze film between the contact surfaces through controlled piezoelectric vibration, the necessity for glass beads can be reduced or totally eliminated.

2

Capacitive behavior of piezoelectric actuators

This chapter touches on the first relative region of interest in terms of frequency for piezoelectric actuators – capacitive behavior, encountered at frequencies below resonance. This is also considered to be the quasi-static region of operation, ideal for positioning applications. Accuracy is highly limited by the hysteretic effect exhibited by the actuators between input voltage and output displacement. This effect is discussed in the first part of this chapter and covered more in-depth in appendices A, B and C , together with methods of compensating the behavior, detailed in appendix D. In the second part of the chapter, the Piezoelectric Actuator Drive is introduced, together with its characteristics, response and advantages. Details on this part can be found in appendices E, F and G.

In the capacitive region of operation piezoelectric devices behave electrically, as the name implies, like capacitors and mechanically like springs and active sources of force or displacement at the same time. It is this behavior that enables their use in a large variety of applications including structural vibration damping, micro- and nano-scale positioning or even more macroscopic applications such as linear or rotary motors.

2.1 Piezoelectric multilayer actuators

The range of elongation in piezoelectric ceramics is in the order of nano- to micrometers, and is therefore not inherently useful in macroscopic energy transfer applications. Stacking many layers of piezoceramics on top of each other creates a piezoelectric multilayer actuator (PMA). Fig. 2.1 illustrates the conceptual diagram (a) and actual image (b) of a multilayer actuator. The advantage of PMAs over their single layer counterparts is the ability to produce larger deflections and require a fraction of the voltage levels of its single layer counterparts. The cost comes in the form of larger exhibited capacitances and therefore higher currents for the same actuation speed.

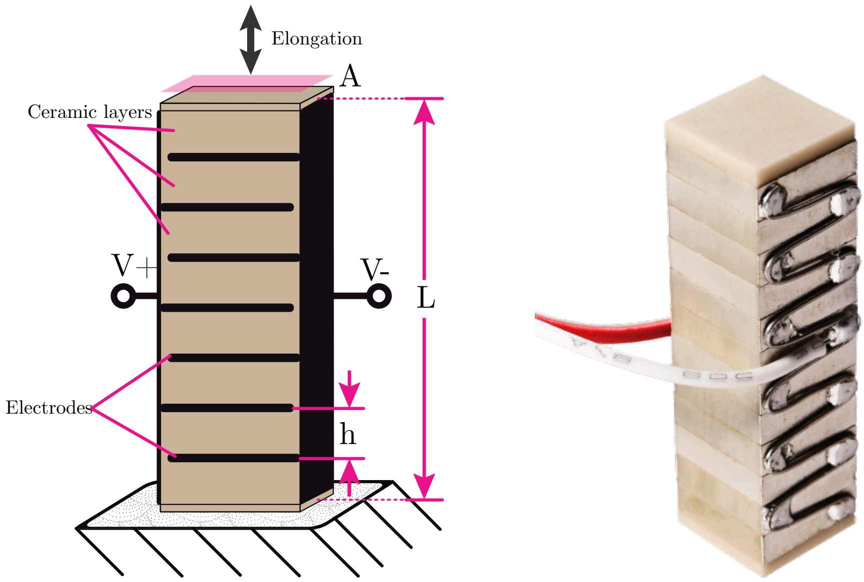

Figure 2.1: Piezoelectric multilayer actuator conceptual diagram (a) and photo (b).

A piezoelectric stack or multilayer actuator is made up of hundreds of individual piezoelectric layers separated by thin electrodes. These layers are in a parallel configuration electrically, enabling a reduced voltage level to produce the necessary electric field. Mechanically, they are in a series configuration and therefore the elongation of each layer adds up to produce a larger displacement than a single element would. The final stack capacitance is given by the sum of each individual layer capacitance, due to their parallel electrical configuration.

Besides their many desirable properties, piezoelectric devices in general exhibit two dominating forms of nonlinearity that are not accounted for through their linear constitutive equations: hysteresis and creep. Of the two effects, hysteresis has a much larger impact on the positioning accuracy of the devices, especially under dynamic operation while creep effects actuator position over long periods of static operation. Hysteresis represents a non-unique mapping between device input and output, whereby a specific input value can incur two different system output responses based on input signal slope polarity. In piezoelectric devices, hysteresis is encountered between applied voltage and obtained displacement and therefore output position cannot be correctly ascertained in systems where closed-loop operation is not feasible.

2.1.1 Hysteresis effects and modeling

Modeling hysteresis in piezoelectric actuators is a necessary step in developing compensation methods to negate the effects. The most encountered method of modeling hysteresis in literature remains the Preisach-Krasnoselskii scalar model [24], which provides a straightforward method of representing the hysteretic effect. Although initially developed for the purpose of modeling magnetic hysteresis, due to its phenomenological nature, the method can be used to model any type of hysteresis [25]. This fact, combined with the generally predictable performance has led the Preisach model to be the preferred method used when hysteresis is involved.

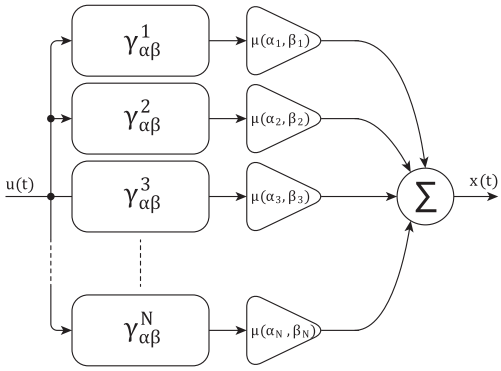

Figure 2.2: Parallel connection of elementary Preisach hysterons with weighting gains

The idea behind the classical scalar Preisach model consists of describing the hysteretic effect through the use of an infinite number of parallel-connected relay-type two-state discontinuous operators $\gamma_{\alpha\beta}[u(t)]$, called basic hysterons. These elements represent relay-like loops on the input-output plane with two values, α and β, acting as the 'on' and 'off' thresholds, with $\beta \leq \alpha$. When an input signal $u(t)$ becomes greater than α, the output of the operator becomes 'high' and goes to 'low' state only when the input becomes less than β. In between tresholds, the previous value is retained. More explicitly, in the case of piezoelectric devices this can be written mathematically as

$$\gamma_{\alpha\beta}[u(t)] = \begin{cases} -1 & u(t) \leq \beta; \\ \gamma_{\alpha\beta}[u(t)] & \beta \leq u(t) \leq \alpha; \\ 1 & u(t) \geq \alpha. \end{cases} \tag{2.1}$$

Hysteresis can therefore be described as a nonlinearity with a non-local memory effect, whereby the output of such a system depends on the current input as well as its past values.

The structural block diagram of infinite parallel hysteron connections is shown in Fig. 2.2. It illustrates the connection and weighting of individual elementary hysterons, whose sum produces the instantaneous output.

The proliferation of the Preisach hysteresis model is in no small part aided by its geometrical interpretation, which also facilitates a better understanding of the active and inactive surfaces that make up the hysteron plane or $\alpha{-}\beta$ plane. This interpretation is exemplified in Fig. 2.3.

In this plane, a so-called Preisach triangle T_0 is defined, which represents the region of operation of the actuator, bordered by $\alpha_{max}, \beta_{max}, \alpha_{min}$ and β_{min}. Only the surface above the diagonal given by $\alpha = \beta$ has any physical meaning and therefore T_0 is an upper triangular surface. The elementary hysterons $\gamma_{\alpha\beta}[u(t)]$ have a direct correlation to the $\alpha - \beta$ half-plane in such a way that at any point in time T_0 is divided into two surfaces S^+ and S^-, representing the (α, β) pairs for which $\gamma_{\alpha\beta}[u(t)] = 1$ or -1, respectively. Mathematically, this is expressed as

$$x(t) = \iint\limits_{S^+} \mu(\alpha,\beta)\gamma_{\alpha\beta}[u(t)]\,\mathrm{d}\alpha\,\mathrm{d}\beta + \iint\limits_{S^-} \mu(\alpha,\beta)\gamma_{\alpha\beta}[u(t)]\,\mathrm{d}\alpha\,\mathrm{d}\beta, \tag{2.2}$$

where $u(t)$ is the voltage input to the piezoelectric actuator, $x(t)$ represents the output

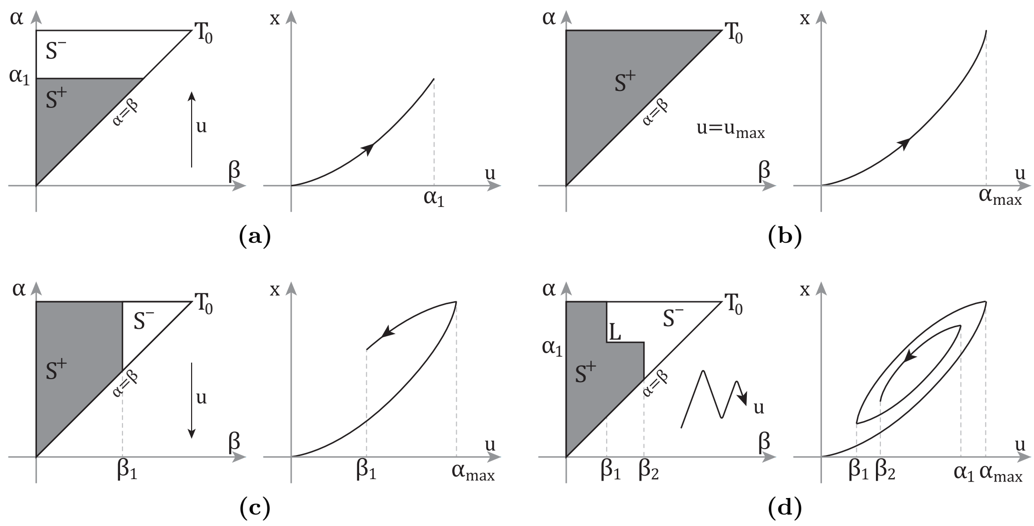

Figure 2.3: Representation of the Preisach triangle, with examples for increasing (a), maximum (b), decreasing (c) and progressively decreasing amplitude (d) triangular input and their respective surface divisions.

displacement, $\mu(\alpha, \beta)$ is the experimentally-obtained weighting function and $\gamma_{\alpha\beta}[u(t)]$ is the hysteron state.

Thereby, for a monotonic increase of the input $u(t)$, the input-output plane shows an ascending hysteresis branch, while the $\alpha - \beta$ half-plane 'fills up' from the bottom to the horizontal line defined by $\alpha = \{\alpha_1 | \alpha_1 \leq u(t)\}$. Similarly, a monotonic decrease in input will then determine the surface to 'empty', but this process is orthogonal to the one for increasing input. Therefore the 'filled' space T_0 will empty starting from the right towards the vertical line defined by $\beta = \{\beta_1 | \beta_1 \geq u(t)\}$. Thereby, a stochastic input signal with several extrema will be represented as a combination of 'filled' and 'emptied' areas on the triangle, delimited by a boundary staircase layer or memory curve denoted L. The coordinates of the corners on this curve will then fully describe the output value based on current and past inputs.

The next step in completing the Preisach hysteresis model is discretizing the half-plane and determining the $\mu(\alpha, \beta)$ weighting function. There are many ways in achieving this, both parametric and nonparametric, but a constrained least squares iterative minimization process is arguably the best suited nonparametric method for it [104] since no initial assumption is made on the distribution shape. Through this method, the square of the difference between actual and modeled outputs is iteratively minimized until the error is below a set threshold. The drawback is increased computational intensity for large amounts of data and high levels of discretization. This discretization is necessary for numeric implementation. Fig. 2.4 illustrates this process.

The weight distribution $\mu(\alpha, \beta)$ now retains one weight value for each discrete square in the discretized $\alpha - \beta$ half-plane. Therefore, the output of the model will have a limited number of discrete states it can attain and output changes are only determined when the input signal variation is larger than the discretization step. It is then immediately apparent that the model output approaches the real response as $N(\alpha, \beta) \to \infty$, where N is the number of levels in the plane.

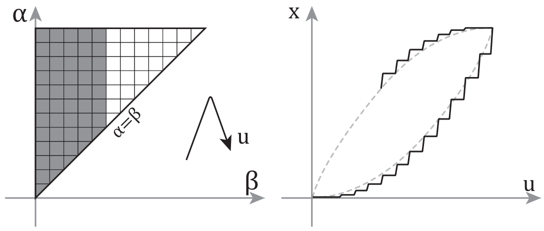

Figure 2.4: Division of the Preisach plane into $N = 12$ equally-distanced values for α and β, and the resulting 12 discrete levels obtained on the hysteresis curve.

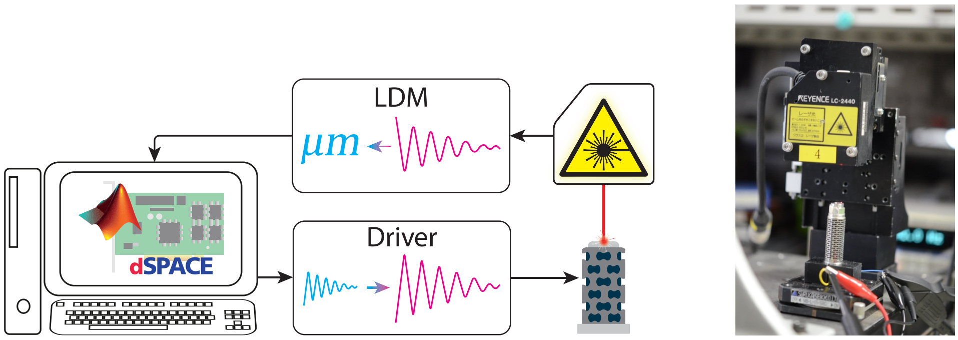

(a) **(b)**

Figure 2.5: Block diagram of the experimental set-up (a) with close-up detail image (b). A computer equipped with a PCI dSPACE board is used. The signal generated is amplified through a voltage amplifier. The unit under test is a Noliac custom piezoelectric stack actuator. Elongation is measured using a Keyence LC-2440 laser sensor connected to a Keyence LC-2400 laser displacement meter (LDM).

In order to use the minimization method for determining the weighting matrix, the full hysteretic effect needs to be mapped by applying a sufficiently rich identification signal to the device input and mapping its output response. In this respect, a laser displacement measurement system is used to measure piezoelectric elongation for a receding amplitude saw-tooth signal input. Fig. 2.5 illustrates the block diagram of the measurement set-up together with an image of the actual system.

The identification signal used together with its response are shown in Fig. 2.6(a) and (b), respectively, while (c) illustrates the hysteretic effect between the input and piezoelectric response. The input signal is a 1 Hz receding sawtooth that starts at maximum input amplitude and successively converges towards the bias point. There is a direct correlation between the number of input signal periods or inversions and the number of concentric hysteresis loops. For correct model identification, the number of reversals has to at least match the discretization level employed so that all hysterons are excited at least once.

The result of the identification procedure is then a weight matrix $\mu(\alpha, \beta)$, with each of its values assigned to a corresponding square in the Preisach plane. Fig. 2.7(a) illustrates the modeled versus measured responses while (b) presents the mapping of the weights onto the plane for a discretization level of $N = 30$. The main diagonal elements account for the bulk of the response and correspond to the quasi-linear diagonal shape of the hysteretic curve.

In order for the model to more faithfully represent the real system response, a higher

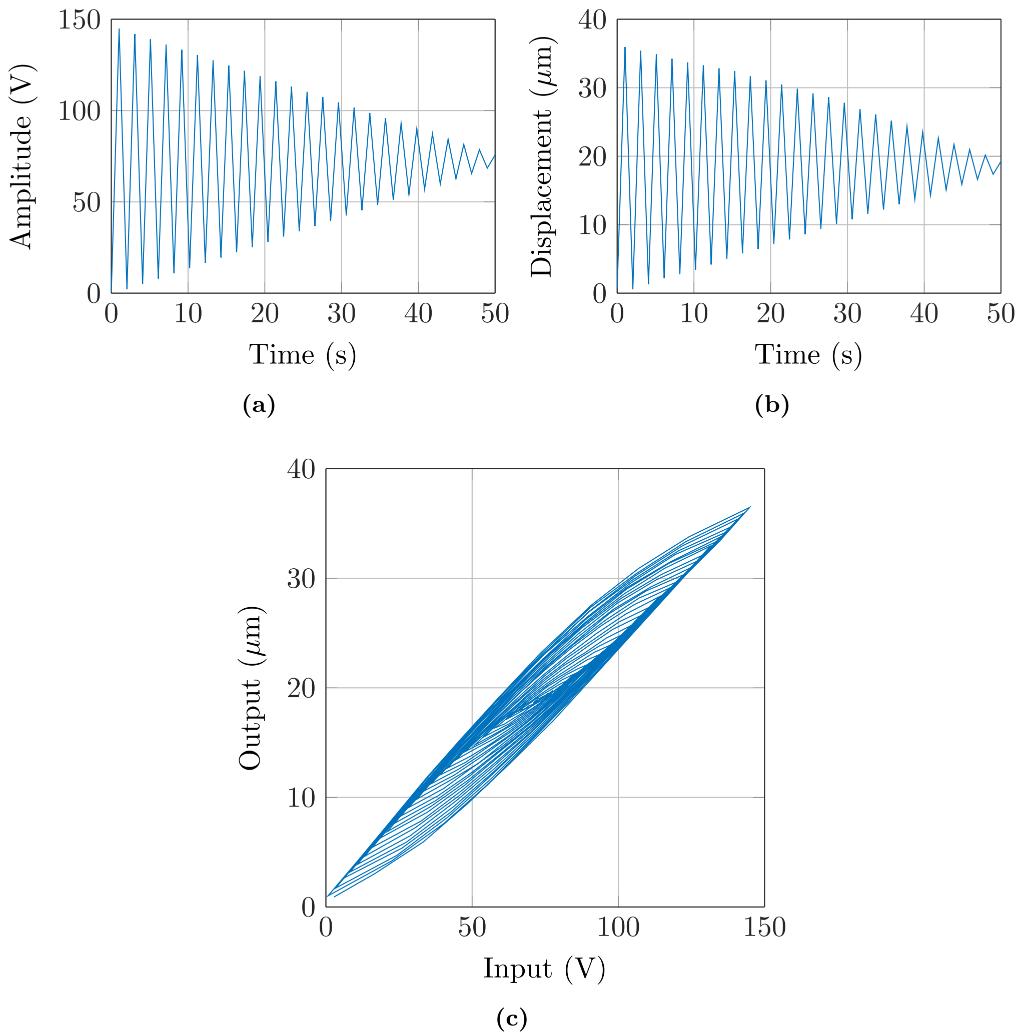

Figure 2.6: Receding amplitude sawtooth identification signal (a), obtained response (b) and resulting hysteresis (c).

discretization level is required. During the experimenting process, identification is performed with an input signal with 200 inversions and a corresponding discretization step is applied. Fig. 2.8 illustrates the weight distribution for this identification procedure. A simple visual comparison to Fig. 2.7(b) makes it obvious that the higher discretization level can capture details in the hysteretic behavior much more intricately. The cost comes in the form of time taken for the identification process. While the simpler model with $N = 30$ steps takes 22 s to complete, for the much larger model with $N = 200$ steps this time increases to approximately 2 h. Nonetheless, this one-time penalty is the only disadvantage, since after the identification process the modeling time itself does not substantially increase with discretization, while its accuracy does.

The Preisach hysteresis model presented so far is a powerful method in *black box*-type phenomenological hysteresis modeling. It is capable of representing any hysteresis shape with complete disregard for the underlying physical phenomena involved. Nonetheless, one major disadvantage of the method is its incapability, in its standard form, of modeling either rate or temperature dependence – two effects that piezoelectric actuators

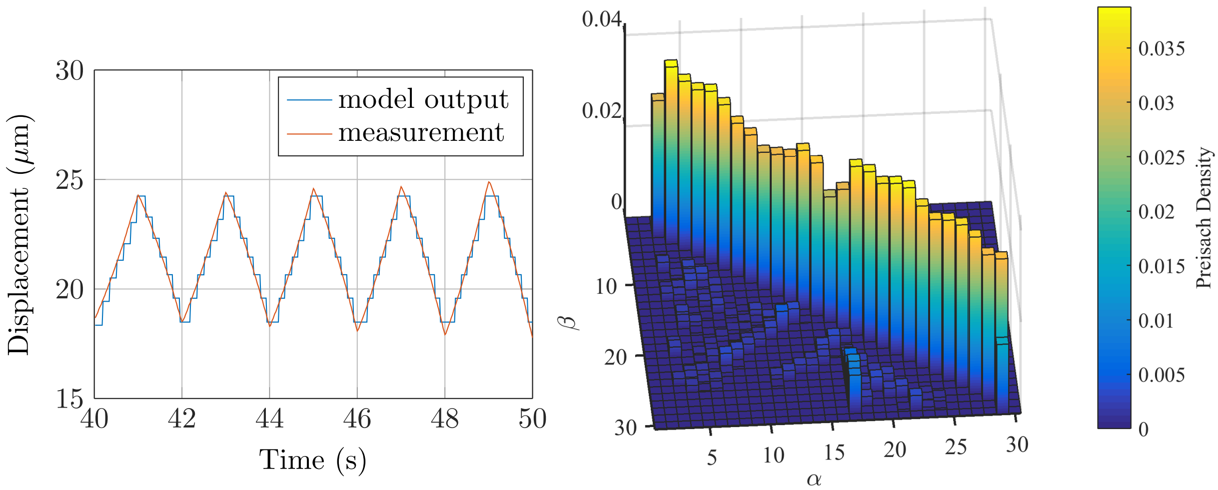

(a) **(b)**

Figure 2.7: Detail view of modeled versus measured responses (a) and corresponding weight matrix (b) for a discretization level of $N = 30$.

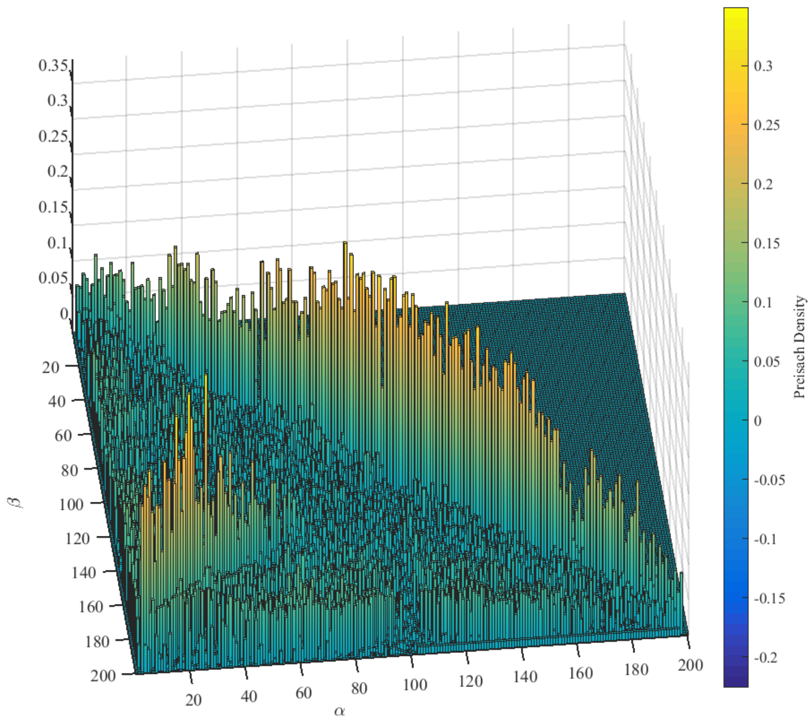

Figure 2.8: A weight distribution plot for a discretization level of $N = 200$.

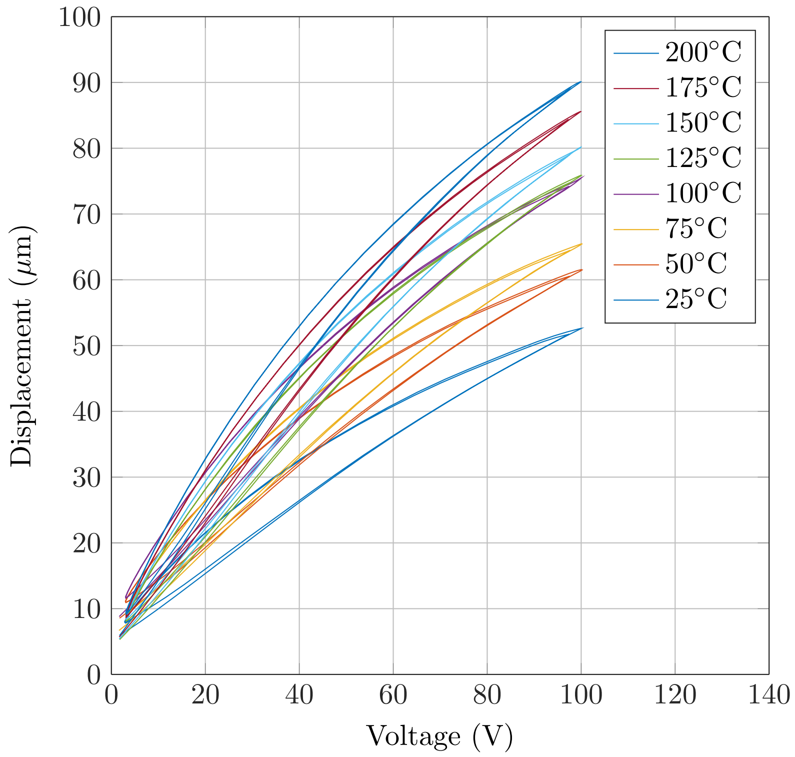

Figure 2.9: Hysteresis versus voltage.

suffer from.

In order to analyze the effect of temperature on stack actuator operation and consequently on the modeling process, a set of measurements was performed wherein the same identification function from Fig. 2.6(a) is applied to a piezoelectric actuator input. Its response is then measured for 8 different temperature levels, ranging from 25 °C to 200 °C. The previously presented Preisach identification procedure is then applied with a low discretization step of $N = 20$, in order to enable quicker interpretation of the results. Thereby, 8 separate weighting matrices are obtained that correspond to the 8 different temperature levels.

Fig. 2.9 shows one loop of the hysteresis behavior of the studied device for each temperature level. Herein, the maximum obtainable stroke of the piezoelectric actuator increases with temperature, with the free displacement obtained at 200 °C showing a 70 % increase over room temperature values.

The Preisach model is then used to obtain 8 sets of different distribution matrices. From the previous figure it can be observed that temperature only changes the maximum stroke, but does not significantly distort the hysteresis shape. This is also reflected in the obtained distributions, as the effects of temperature are only prominent on the components situated on the main diagonal. Therefore, in order to visually illustrate the effects of temperature on the Preisach plane, only the main diagonals of the obtained matrices are analyzed. Fig. 2.10 shows the elements on these diagonals plotted in increasing temperature order. The figure exhibits the same type of quasi-linear increase in diagonal coefficients between temperature levels.

The results obtained in this experiment support previous claims [105, 106] that the

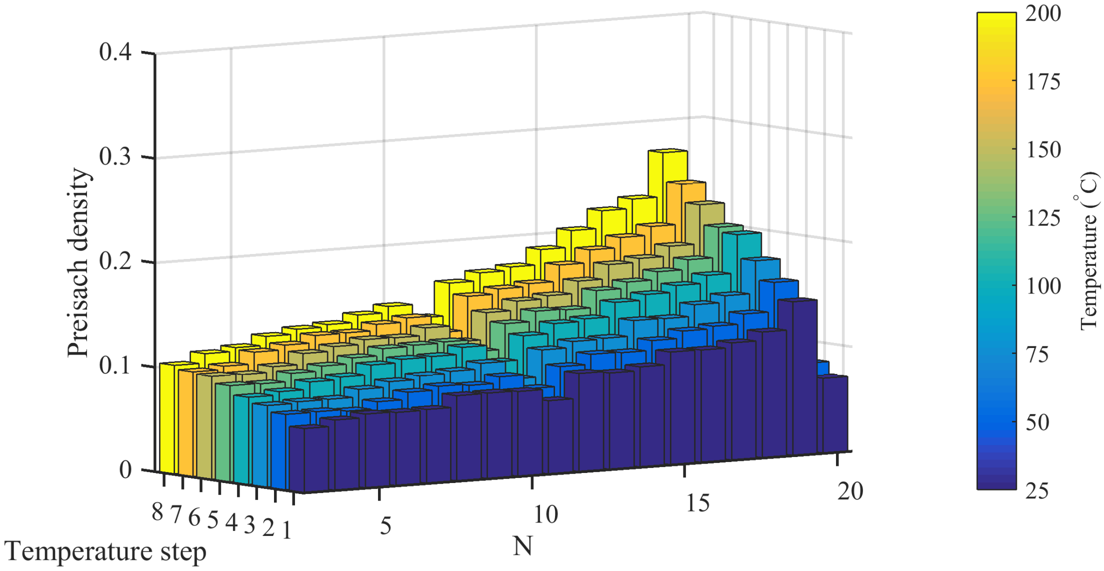

Figure 2.10: Value of Preisach distribution diagonal elements versus temperature.

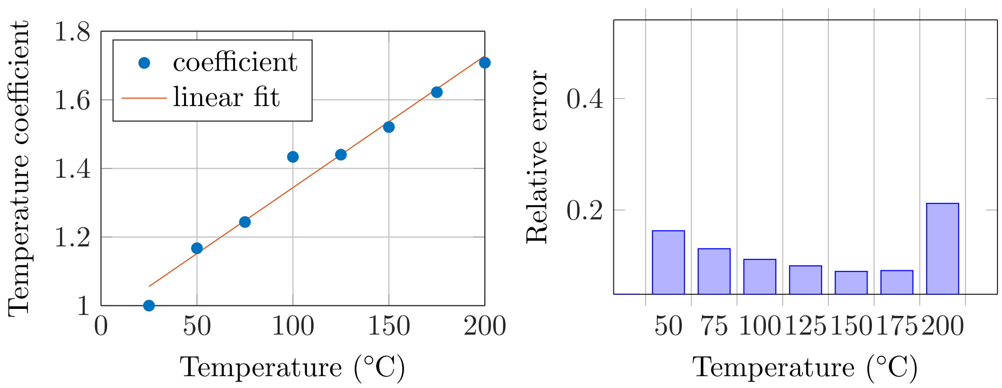

(a) **(b)**

Figure 2.11: Linear fit of the temperature trend (a) and obtained maximum relative error for each temperature value (b).

piezoelectric stroke increases with temperature. Moreover, in the range of measurement, a quasi-linear dependency between the two is observed. This previous research then explains this trend by introducing a set of temperature-dependent constitutive equations wherein the charge constant is directly proportional to temperature. Since the Preisach model is phenomenological in nature, this physically-attributed temperature trend is not inherently useful. Therefore, a better approach is to augment the obtained weight function to include the temperature dependence as an added overall linear weighting factor.

Fig. 2.11(a) shows the mean relative trend of the weights on the main diagonal of the Preisach distribution matrix with respect to temperature. This linear fit can now be used to extrapolate model weights for different temperatures. Plot (b) in the same figure then shows the evaluation of this approach by illustrating the maximum relative error obtained at each temperature level versus the real weights directly modeled. Although a deviation from the real weight by 22 % seems significant, this is the worst-case scenario for one single value in the entire diagonal. The actual average error is approximately 3 %.

Therefore, the method proposed is considered suitable for extending the Preisach hysteresis model to cover temperature dependencies, when at least two sets of temperature data are available and assuming a linear temperature relationship in the desired operation area. In the case studied here, this area of operation stays linear over a large temperature range.

2.1.2 Hysteresis compensation

Compensation of the effects of hysteresis is necessary in order to improve the positioning accuracy of piezoelectric devices in applications where open-loop control is desirable. Even in closed-loop applications, precompensation of hysteresis can help reduce requirements on control law dynamics and improve overall system behavior. In this respect, an inverse Preisach model is built from the one presented in the previous section. One of the disadvantages of the discrete Preisach method now becomes apparent, in that it does not have an analytical inverse. Therefore, an approximate inverse is calculated, based on a closest-match algorithm [107]. In short, the algorithm compares a desired output to the output of the Preisach model and then successively increases or decreases the input to the model until the two outputs are within specified tolerances.

This approximate inverse model can now be used in order to shape the input signal such that the desired output displacement trajectory is obtained. The results of this procedure will now be presented graphically, together with a verification process by which a signal other than the one used for identification is set as trajectory and the piezo output is measured to see the extent of the compensation. Fig. 2.12(a) shows the measured and desired responses of a piezoelectric device. The desired trajectory is used as an input to the Preisach inversion algorithm. The resulting input voltage is presented in (b), and the measured response in (a) is the result obtained for this input signal. The hysteresis plot in (c) shows a much more linear input-output response of the device compared to Fig. 2.6(c). This proves that hysteresis precompensation greatly reduces the nonlinear effects.

In order to further evaluate the performance of this compensation method, a pure sinusoidal displacement profile is set as the desired trajectory. The voltage signal obtained from the Preisach inversion is then fed to the piezo device again, with the results being shown in Fig. 2.13. Plot (a) shows a good match between desired and measured responses, with the nonlinearities almost completely eliminated. This is then reinforced by the x-y plot showing hysteresis between desired and measured responses in (b). In order to prove that the nonlinear effects have been transfered to the input voltage signal, plot (c) shows its hysteretic response with respect to the measured output. From these results it can be concluded that the hysteresis inversion method used is effective in obtaining a more linear response in piezoelectric devices with respect to their output displacement. Through the closest-match inversion algorithm, an inverse hysteretic relationship is embedded into the piezo voltage input. As a result, the direct and inverse effects cancel each other out.

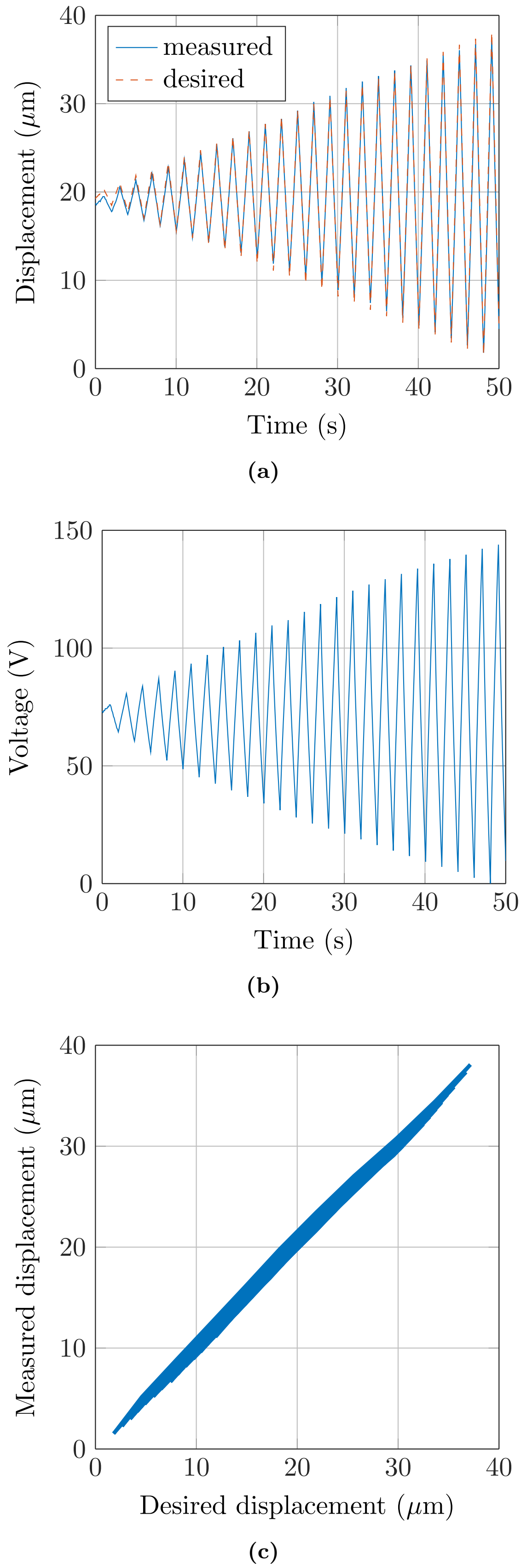

Figure 2.12: Response of the system to an inverted identification input signal. The desired and measured trajectory (a), obtained inverse input voltage (b) and hysteresis between desired and measured trajectory (c).

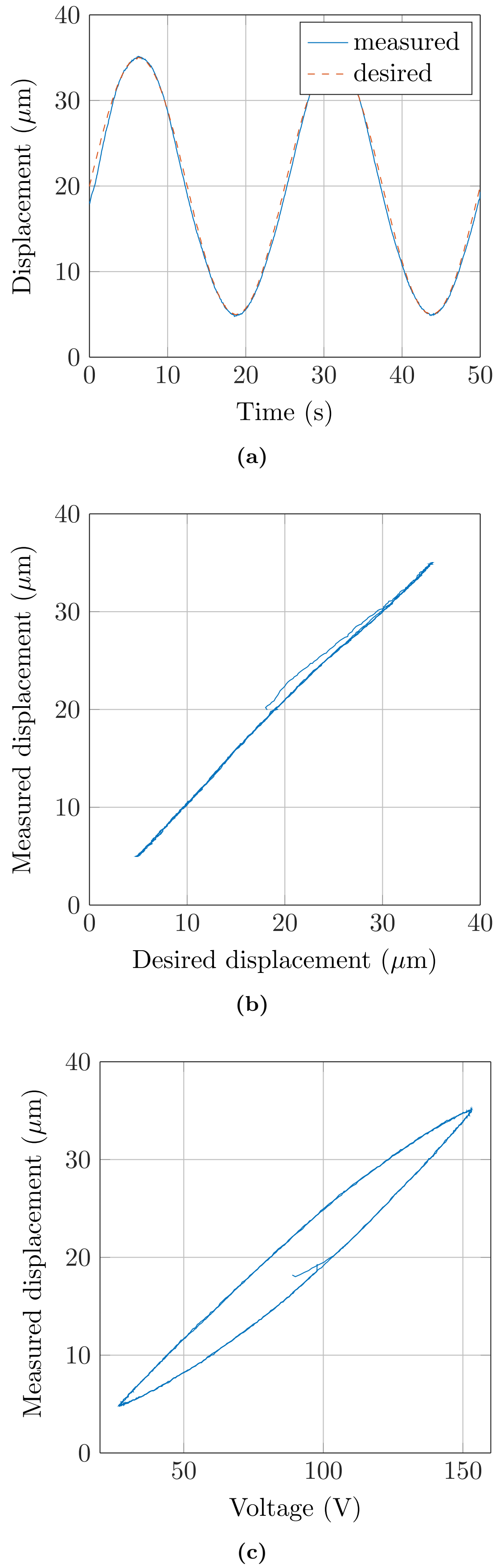

Figure 2.13: Response of the system to a sinusoidal excitation. The desired and measured trajectory (a), hysteresis between the two (b) and hysteresis between inverted system input and measured output (c). The hysteresis shape is inverted in this case.

Figure 2.14: Piezoelectric Actuator Drive motor. Production unit.

2.2 The Piezoelectric Actuator Drive (PAD)

The Piezoelectric Actuator Drive (PAD) is a new type of electrical rotary motor that employs piezoelectric multilayer actuators to impart motion. A micro-mechanical gearing is used to transform the linear motion of these actuators into a precise rotation. These micrometer-sized teeth enable the PAD to achieve high positioning accuracy, similar to stepper motors. The motor has a positioning accuracy of less than 2 arc-seconds without the use of any positioning sensors. At the same time, the PAD achieves high typical output torques of 4 N m without extra gearing. Unlike steppers, the motor is not back-drivable and holds its position even when not powered due to its mechanical gearing. Furthermore, its actuation principle places no lower limit on motor speed.

Another great advantage of using the PAD as a replacement for conventional servo drives is the fact that, by machining all parts and housing out of titanium, the PAD preserves the non-magnetic properties of the piezoelectric actuators used. This extends the range of applications in which the PAD can be used beyond the possibilities of more conventional drives, such as operation in high radiation or strong magnetic fields. One such case is operation close to the bore of a magnetic resonance imaging (MRI) scanner, as a patient table positioning motor to enable patient positioning without disturbing the image produced by the scanner itself. This specific application is also a base performance metric in the project.

Fig. 2.14 shows one version of a final production-unit motor, while Fig. 2.15 offers an exploded view of the motor components.

Despite the advantages of the PAD, there are some challenges associated with its operation. The piezoelectric devices used in its construction are stack actuators that exhibit 3.3 µF to 3.5 µF capacitance each. Purely capacitive loads, also called reactive loads, do not dissipate power, but store it as energy within a half-cycle and pump it back into the power supply in the other half-cycle. Thus, the power delivered to the motor is highly reactive. Since only the real part of the power is effectively transformed into

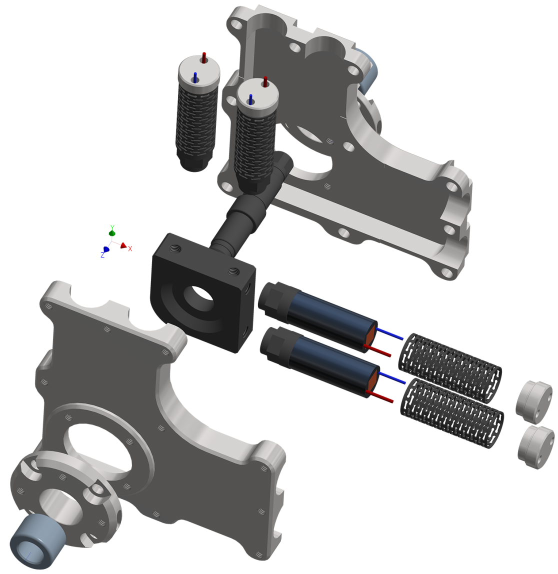

Figure 2.15: Exploded view of PAD components (image courtesy of Noliac A/S).

mechanical work and loss, the converter used to drive the motor needs to be able to cope with large amounts of reactive power in order to be efficient.

Furthermore, sensorless operation of the PAD is desired in order to reduce fabrication cost, improve reliability and maintain magnetic neutrality. This requires extracting information about rotor position, speed and motor torque from the motor signals without the use of expensive external sensors. Due to the stiff nature of the ceramic actuators, the load has very little influence on the motor signals and is therefore difficult to correctly estimate. Adding to this difficulty is the highly hysteretic behavior of piezoelectric ceramics in general. This hysteresis needs to be compensated for in order to correctly estimate rotor position.

2.2.1 Characterization

The internal conceptual structure of the motor is shown in Fig 2.16(a). Four piezoelectric multilayer actuators are placed inside the motor housing – two sets of parallel actuators, with the pairs having a 90° geometrical displacement between them. These are fixed to the motor housing on one side and to the motor ring on the other. This ring has a square exterior profile with a circular cutout in its center which houses the motor shaft. Both the surface on the inside of the motor ring and the circumference of the shaft are machined into fine teeth with a pitch of 100 µm. Fig. 2.16(b) shows a microscope image of the motor shaft and teeth. The ring and shaft have 313 and 312 teeth, respectively, with the shaft having one tooth less than the ring. This forms a robust contact point between surfaces, suited for power transfer while also gives the PAD the ability to output high levels of torque.

The multilayer actuators expand and contract linearly along their length, pushing and pulling against the motor ring. This creates two axes of actuation within the plane of the motor ring and shaft in which the ring exhibits a non-concentric movement around the shaft. The contact point between the two then brings the ring into rotation through friction.

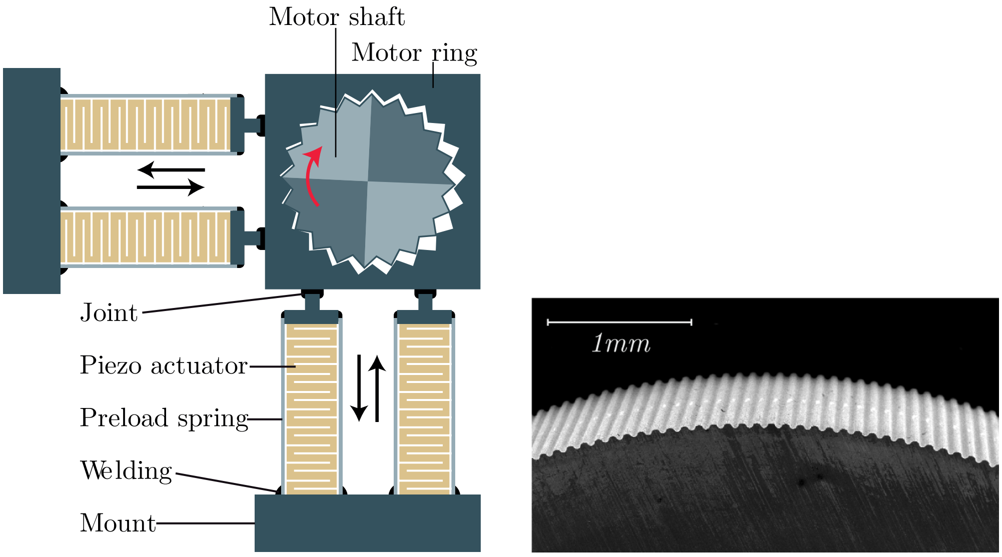

(a) (b)

Figure 2.16: PAD principle (a) with a microscope image of the fine gearing on the motor shaft (b) (image courtesy of Noliac A/S).

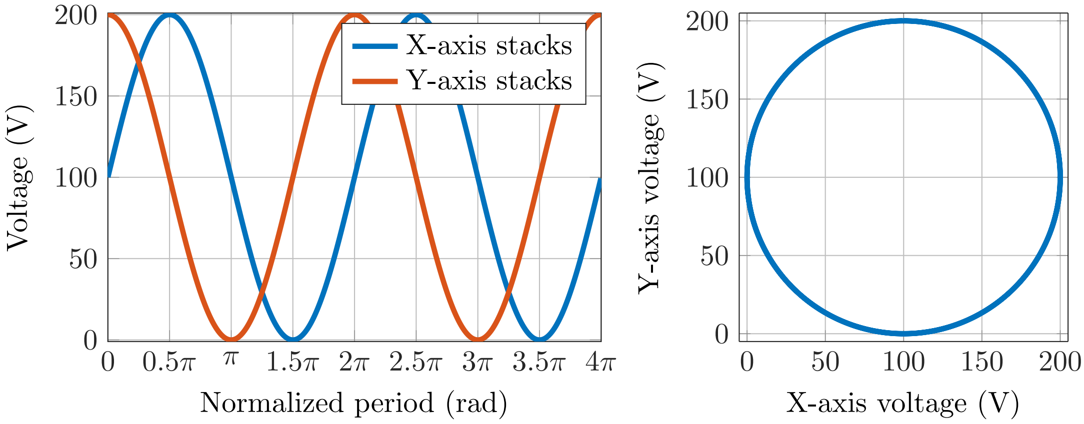

(a) (b)

Figure 2.17: Sine and cosine voltage signals applied to the actuators, normalized to their period (a) and ideal spatial trajectory obtained (b)

By applying a dc-biased sinusoidal voltage to the actuators on one axis and a phase shifted version of the same signal with a 90° phase shift to the other actuation axis, the resulting spatial trajectory will be circular. Fig. 2.17(a) shows the voltages applied to the actuators normalized to their sinusoidal periods, while Fig. 2.17(b) illustrates the resulting trajectory. Thereby, the motor ring exhibits an off-center circular motion around the shaft which is rotated in the opposite direction through the contact point between them.

Each full period of the applied sinusoidal voltages determines the motor ring to do a full revolution around the shaft and this, in turn, makes the shaft rotate a distance equivalent to one tooth step. This is due to the inherent gearing ratio present through the micromechanical toothing. Therefore, a 360° rotation of the contact point between

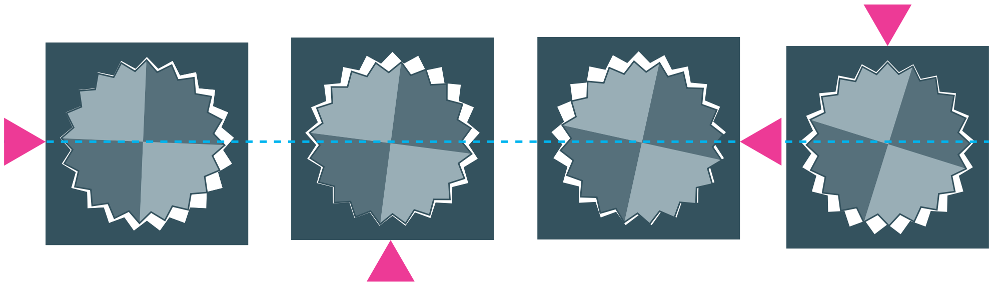

Figure 2.18: The principle of rotation in the PAD motor. The magenta arrows represents the direction of actuation, which is the same as the position of the contact point. The shaft is fixed by a bearing, shown here by the dotted line, while the ring is free to rotate around it.

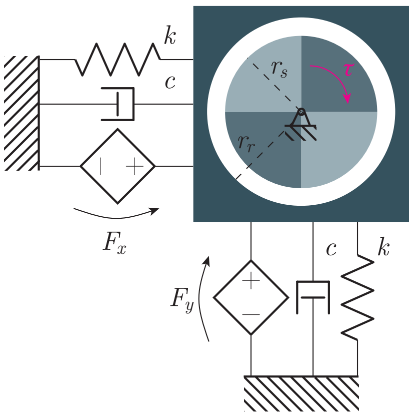

Figure 2.19: Simplified mechanical representation of the PAD motor with voltage-driven force sources.

the motor ring and shaft produces a 1.15° rotation in the output shaft of the motor through the gear coupling with a ratio of 1/312. This style of actuation, illustrated in Fig. 2.18, makes the PAD similar to other wobble motors that employ the same principle. Moreover, the motor shaft angular position and speed with respect to electrical angle and driving frequency can be expressed as

$$\theta_{mech} = \frac{N_{ring} - N_{shaft}}{N_{ring}} \cdot \theta_{el} \tag{2.3}$$

$$\nu = \frac{N_{ring} - N_{shaft}}{N_{ring}} \cdot \frac{f}{60}, \tag{2.4}$$

where θ_{mech} is the shaft angle, θ_{el} the electrical angle, ν is the shaft rotation speed in RPM, N_{ring} and N_{shaft} represent the number of teeth on the motor ring and shaft, respectively, while f is the frequency in Hz of the applied input voltage. The electrical angle is a time-varying quantity that can be linked to the same signal frequency f through the relationship $\theta_{el}(t) = 2\pi f t$.

In order to expand on the principle of rotation, a simple model for the PAD motor that shows the power transfer between electrical and mechanical domains is derived. Hereby, Fig. 2.16 can be extended to show a simplified mechanical representation of the motor, as illustrated in Fig 2.19.

Particularizing the piezoelectric constitutive equations for expressing one-dimensional motion of stacked piezoelectric actuators, the displacement of the motor ring on each individual axis can now be expressed in terms of piezoelectric coefficient d_{33}, spring constant k_p, generated force $F_{x,y}$ and axis voltage $V_{x,y}$ as

$$\begin{aligned} x(t) &= -\frac{1}{k_p}F_x(t) + d_{33}v_x(t) \\ y(t) &= -\frac{1}{k_p}F_y(t) + d_{33}v_y(t). \end{aligned} \tag{2.5}$$

The quantities expressed here are the equivalent combination of the parallel stack formation. Considering ideal driving voltages

$$\begin{aligned} v_x(t) &= V_0 + V cos(\theta_{el}(t)) \\ v_y(t) &= V_0 + V sin(\theta_{el}(t)), \end{aligned} \tag{2.6}$$

then (2.5) can be rewritten to solve for the axis forces as

$$\begin{aligned} F_x(t) &= k_p d_{33} V cos(\theta_{el}(t)) - k_p x(t) \\ F_y(t) &= k_p d_{33} V sin(\theta_{el}(t)) - k_p y(t). \end{aligned} \tag{2.7}$$

In the previous equations, bias voltage V_0 has been omitted since its effect can be encompassed into correct consideration of displacement starting point. Now, the motion of the ring around the shaft can also be expressed geometrically as

$$\begin{aligned} x(t) &= (r_r - r_s)cos(\theta_{ring}(t)) \\ y(t) &= (r_r - r_s)sin(\theta_{ring}(t)), \end{aligned} \tag{2.8}$$

where r_r and r_s are the ring and shaft radii, respectively. The position of the ring center with respect to the shaft center is variable and will in practice not overlap during operation, unlike illustrated in 2.19. Therefore, θ_{ring} is defined as the complementary of the angle formed by the contact point between ring and shaft and the x-axis. Motor torque can now be expressed as the work done by the resultant force developed by the two axes of actuation, coupled through the gearing ratio N_{gear}

$$\tau = \frac{1}{N_{gear}} F_{res} r_s, \tag{2.9}$$

with $N_{gear} = (N_{ring} - N_{shaft})/N_{ring}$. Time dependency is dropped for clarity. The resultant tangential force is the scalar product of the individual axis forces [34], therefore

$$F_{res} = -F_x(t) sin(\theta_{ring}) + F_y cos(\theta_{ring}). \tag{2.10}$$

The previous relationship results from the distance between ring and shaft centers during operation. Now, by combining (2.7) and (2.8) and taking (2.10) into consideration, an expression for the torque developed by the PAD motor can be given:

$$\tau = \frac{k_p r_s}{N_{gear}} d_{33} V sin(\theta_{el} - \theta_{ring}). \tag{2.11}$$

Hereby, an externally-applied torque to the motor ring will incur a phase shift between electrical and mechanical angles. This is equivalent in practice to a lag with respect to electrical angle of the contact point between ring and shaft and is proportional with the applied torque. The maximum torque developed by the motor is therefore dependent on the coefficient of friction between the ring and shaft.

2.2.2 Driving

The model presented in the previous section uses ideal phase-shifted sinusoidal voltages to drive the two sets of stacks. Unlike resonant-type piezoelectric motors, the power capabilities of the PAD are significant. The stacks inside the motor are rated at 200 V. With their capacitive behavior and a rated small-signal capacitance of 3 µF per stack, operation at higher frequencies places a significant burden on the power driver, as the current draw is proportional to frequency in capacitors.

The peak power required to operate one actuator in the PAD at its maximum rated frequency of 200 Hz can be estimated [108] through

$$P = \pi f C_p tan(\delta) V^2, \tag{2.12}$$

where f is the excitation frequency, C_p is the small-signal capacitance, $tan(\delta)$ is the piezoelectric loss factor and V is the applied voltage amplitude. By using a typical loss factor of 10 %, a peak power estimation of 20 W is obtained. Therefore, in order to drive all four stacks in the motor, the power stage needs to be able to deliver 80 W. In reality, under dynamic operation these values are much higher.

Peak power, or apparent power in off-resonance piezoelectric actuators is high because they behave like highly reactive loads. Apparent power, denoted S and measured in VA, is a measure of total power in systems with reactive loads present. It represents the vector sum of the total active and reactive power components. The phase angle between voltage and current determines the amount of reactance, and consequently how large each power component is. Apparent power can be expressed as

$$S = \sqrt{P^2 + Q^2}, \tag{2.13}$$

where P is the active power while Q is the reactive power. A set of measurements are performed with the help of a power analyzer, in order to assess the real levels of all power components in the motor. The measurements, shown in Fig. 2.20 represent total motor power and are done with varying levels of load torque in order to map load influence on power requirements. These measured values are much higher than the ones initially estimated, with apparent power peaking at almost 250 VA. This proves that the standard piezoelectric power estimation formulas do not hold for the PAD motor. Since applied voltage amplitude is constant, power increases almost linearly with frequency. Moreover, it is interesting to see that the highest reactive power is encountered when no load on the motor is applied. Conversely, real power increases linearly with load. This is explained through the fact that only the real part of the power gets delivered to the load, while the energy in the reactive part gets sent back to the driver. Adding a load torque to the motor therefore only increases the real part of the motor power, therefore reducing the phase angle between applied voltage and current. The system becomes more *resistive*. This concept is illustrated with the help of power phasors in Fig. 2.21. This behavior is also in agreement with the motor torque model expressed in the previous section, and therefore a correlation between measurement and model is acknowledged.

In order to drive the PAD motor, a power stage capable of satisfying the studied power requirements is built. Fig. 2.22 shows a first version of motor driver, which employs linear amplification to achieve desired driving signals. This is a 4-channel linear amplifier based on high power op-amp modules capable of outputting 400 W of

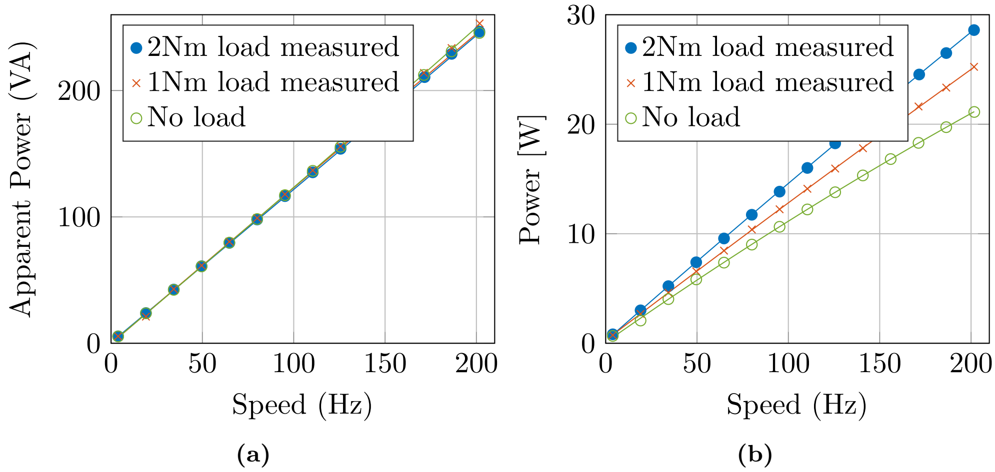

Figure 2.20: Comparison between apparent (a) and real (b) powers versus frequency for different load levels

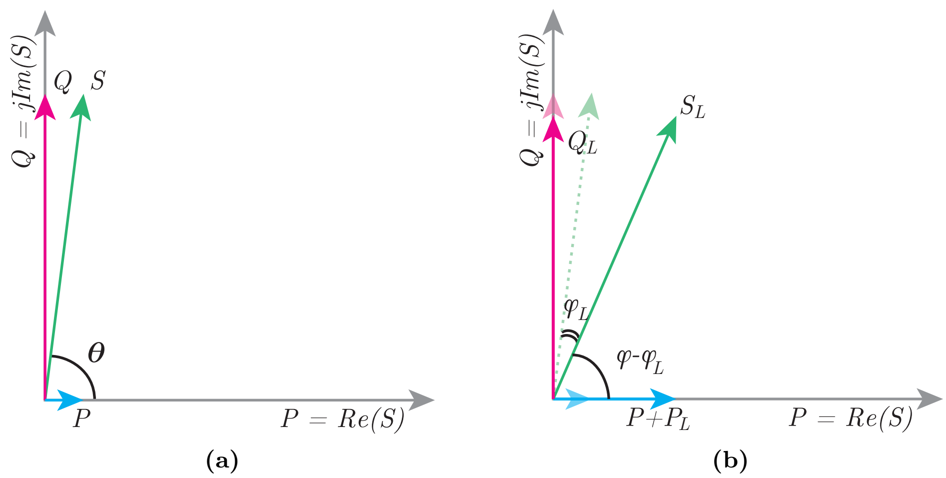

Figure 2.21: The relationship between active, reactive and apparent power in the unloaded (a) and loaded motor (b).

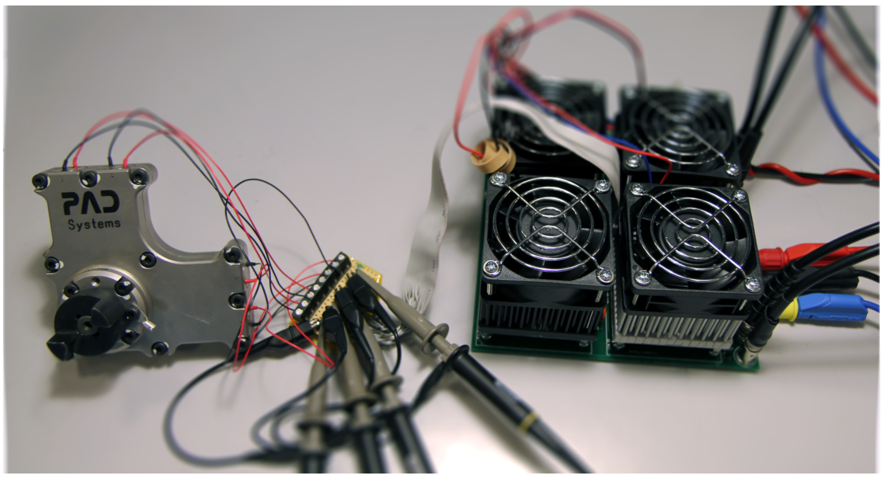

Figure 2.22: 4-channel linear amplifier for driving the PAD motor.

(a) (b)

Figure 2.23: Switch-mode driver for the PAD motor (a) with thermal characteristics under full load (b).

power per module. Designed with a gain factor of 40, a provided 2.5 V biased input signal is amplified to required voltage levels. The reason for choosing an initial linear design is due to their very low distortion levels, as the PAD is sensitive to the presence of high-frequency noise in its drive signals. Furthermore, a 4-channel approach was chosen to both reduce the per-channel load and offer the flexibility of individually driving each stack inside the motor.

The major disadvantage of driving the PAD with a linear stage is the fact that this type of amplifier is incapable of bidirectional operation. Therefore, the large amounts of reactive energy cannot be transferred back to the supply and is thus burned off as heat on the amplifier. Even though the active cooling present in the amplifier is capable of sustaining 165 W of dissipation, this is severely limiting overall system efficiency and also puts unnecessary thermal stress on the power stage.

Therefore, switch-mode half bridge-based amplifier was designed in parallel to the linear one, as part of a student thesis project. This design, although having only 2 channels, is much more efficient in operation since it can feed energy back to the power supply. It therefore runs much cooler, even under full load. The amplifier itself is shown in Fig. 2.23(a), while (b) presents its loaded thermal performance.

2.2.3 Sensorless operation

Sensorless operation refers to the ability of a system, usually a motor drive, to operate in closed-loop without feedback from explicit external sensors such as position or torque sensors. The benefit lies mainly in reduced cost and increased reliability, but the PAD has the added benefit of retaining its magnetic neutrality.

While the drivers covered in the previous section are capable of providing the necessary power to run the PAD motor, a correct reference trajectory needs to also be provided, in the form of the two sinusoidal driving signals as amplification reference. Furthermore, to obtain sensorless closed-loop operation of the PAD, a feedback network is necessary. One property that can be exploited in this respect is the capability of piezoelectric devices to simultaneously act as both actuators and sensors.

In order to model the sensing capabilities of the actuators used in the motor, it is useful to look at the constitutive equation that maps the dependence of charge on both force

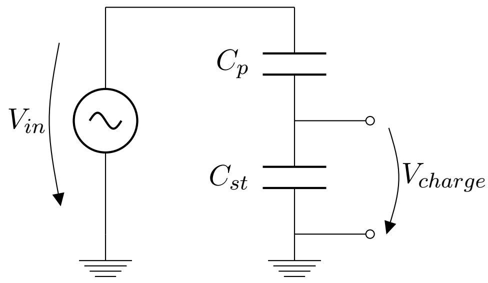

Figure 2.24: Sawyer-Tower measurement circuit.

and voltage. A particularization of the equation to the current application yields the following charge-force-voltage relationship:

$$\begin{aligned} q_x(t) &= -d_{33}F_x(t) + C_p v_x(t) \\ q_y(t) &= -d_{33}F_y(t) + C_p v_y(t), \end{aligned} \tag{2.14}$$

where the charges on each axis, q_x and q_y are related to their respective axis forces $F_{x,y}$ and voltages $v_{x,y}$. By replacing the forces with (2.7) and using the ring trajectory from (2.8), the charge can be expressed as

$$\begin{aligned} q_x(t) &= (C_p - d_{33}^2)V cos(\theta_{el}) + k_p d_{33}(r_r - r_s)cos(\theta_{ring}) \\ q_y(t) &= (C_p - d_{33}^2)V sin(\theta_{el}) + k_p d_{33}(r_r - r_s)sin(\theta_{ring}). \end{aligned} \tag{2.15}$$

Since charge is here dependent on the angle of the contact point between ring and shaft with respect to shaft center, an externally-applied load torque will then be sensed through the piezoelectric charge. One way of sensing charge is by using a Sawyer-Tower measurement circuit, shown in Fig. 2.24, whereby a large capacitor is added in series with the piezoelectric actuator. The voltage across this capacitor is now a proportional representation of the charge through the circuit branch. This method is prominent throughout literature and is extensively used for ferroelectric device characterization.

The disadvantage of the Sawyer-Tower method, despite its simplicity, is the dependence of measurement accuracy on the reliability and linearity of the measuring capacitor. Moreover, since the circuit acts as a capacitive divider, the extra added capacitance needs to be much larger than the measured sample, in order to maximize the voltage drop on the device itself. In the case of the PAD, this means adding in a capacitor of at least 300 µF, which is very bulky in size.

In order to circumvent these limitations, a more modern approach is sensing the current through the branch by means of an added sense resistor in the ground path of the capacitor. Then, through either an integrating op-amp or digital integration using a signal processor, the value of charge can be obtained from this current.

The need for a signal processor in the project for driving purposes has guided the choice towards the digital integration method, which offers additional flexibility compared to an analog integrator. Therefore, in order to provide driving signals to the motor and sense the charge on each actuator, both a 4-channel signal generator and 4-channel current measurement circuit were developed.

Fig. 2.25(a) shows the signal generator, which employs two 16-bit 2-channel D/A converters that can generate arbitrary signals up to 1 MHz. This is significantly more than the needed 200 Hz bandwidth for the motor. The two converters are digitally-fed from

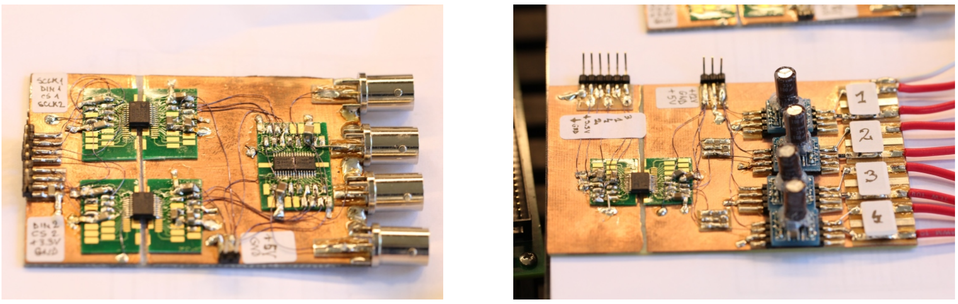

(a) (b)

Figure 2.25: D/A-based 4-channel signal generator (a) and afferent 4-channel current sensing circuit (b).

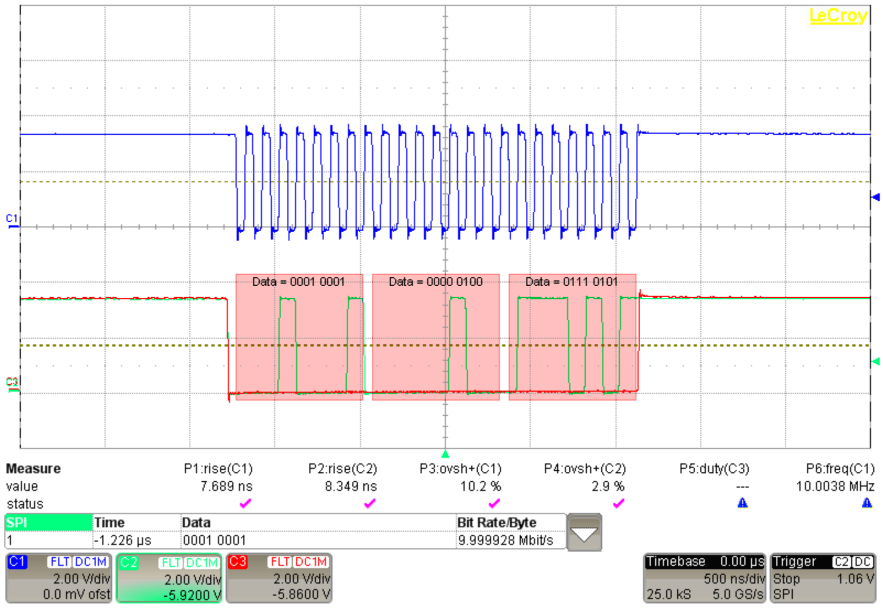

Figure 2.26: Custom SPI-like unidirectional protocol running at a data clock rate of 10 MHz.

the circuit input through an isolation barrier, in order to fully isolate the digital and analog parts of the motor system and driver, thereby protecting the digital processor from mishaps and improving overall noise performance.

The D/A converters used for signal generation require a custom serial peripheral interface (SPI) communication protocol with a payload of 24 bits, out of which 16 bits are data and the other 8 are configuration and overhead. Each D/A converter is independently fed and provides two output channels which are time-multiplexed on the data lines. Use of a field-programmable gate array (FPGA) enabled the development of a high-throughput custom protocol by minimizing payload overhead and foregoing standard SPI bidirectionality, since this is not required here. Fig. 2.26 shows one data packet to the D/A converter. The operating communications clock frequency is 10 MHz, which, by taking into account minimum set-up times between packets and multiplexing of two channels on one line, yields a final theoretical signal sampling rate of 550 kHz.

Fig. 2.27 then shows the four outputs from the signal generator. These are individually controllable in amplitude, frequency and phase and therefore offer a high flexibility in

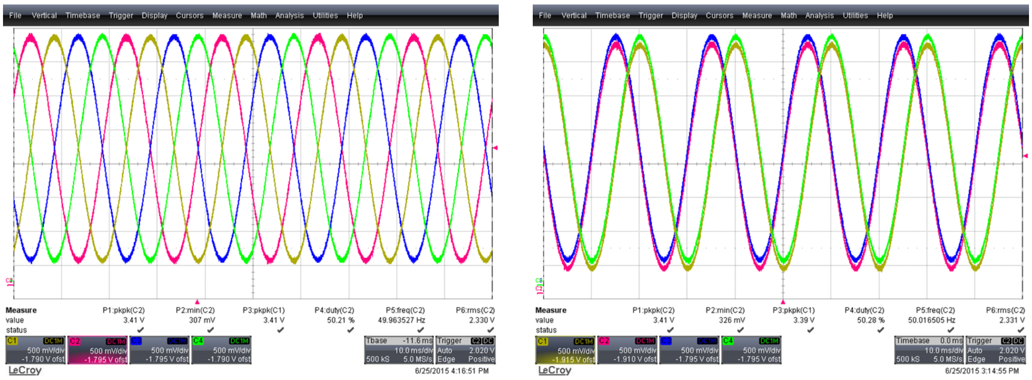

(a) (b)

Figure 2.27: Signal generator board output showing full quadrature (a) or two-by-two in-phase operation (b).

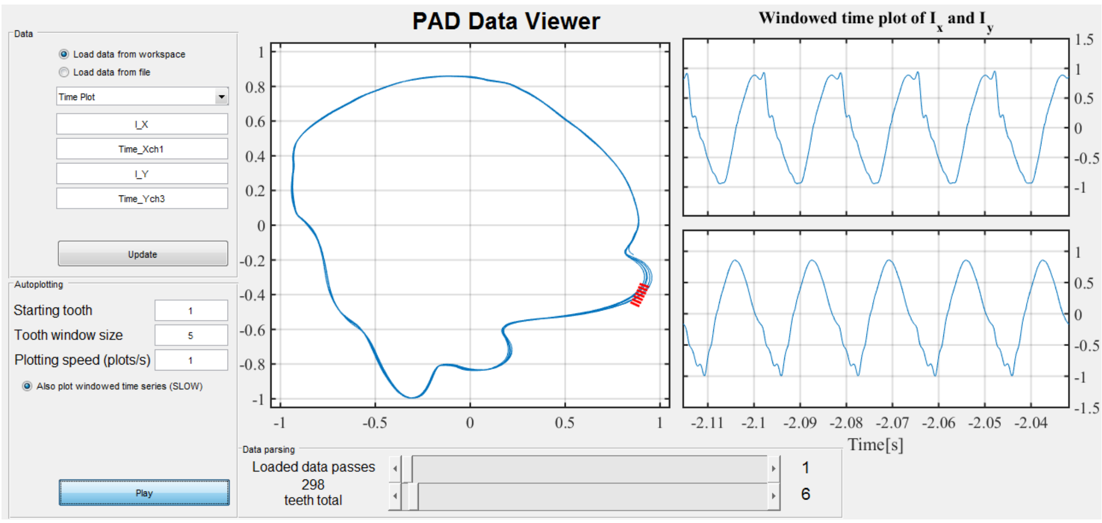

Figure 2.28: Graphical interface for qualitative trajectory assessment.

researching different PAD driving modes and geometrical configurations.

One weakness of the PAD motor not yet discussed until now is its sensitivity to manufacturing tolerances, mechanical irregularities and assembly process. Ring and shaft alignment, roundness and tooth quality all affect the driving performance and torque output of the motor. When too high torque is applied to the shaft, the motor ring will slip and tooth skipping will occur. The geometrical point at which this occurs is repeatable and represents the weakest connection point between ring and shaft. This is determined by the afore-mentioned manufacturing process, as well as the final mechanical assembly and centering.

In order to be able to qualify this tooth skipping phenomenon, a toolbox is developed that allows a visual inspection of the trajectory of the ring around the shaft by analyzing the different motor signals it couples into. Fig. 2.28 illustrates the designed user interface used to perform this analysis.

Offline, previously-acquired data from the two driving axes can be imported and is then displayed in the central spatial plot in the figure. The number of teeth the motor passes

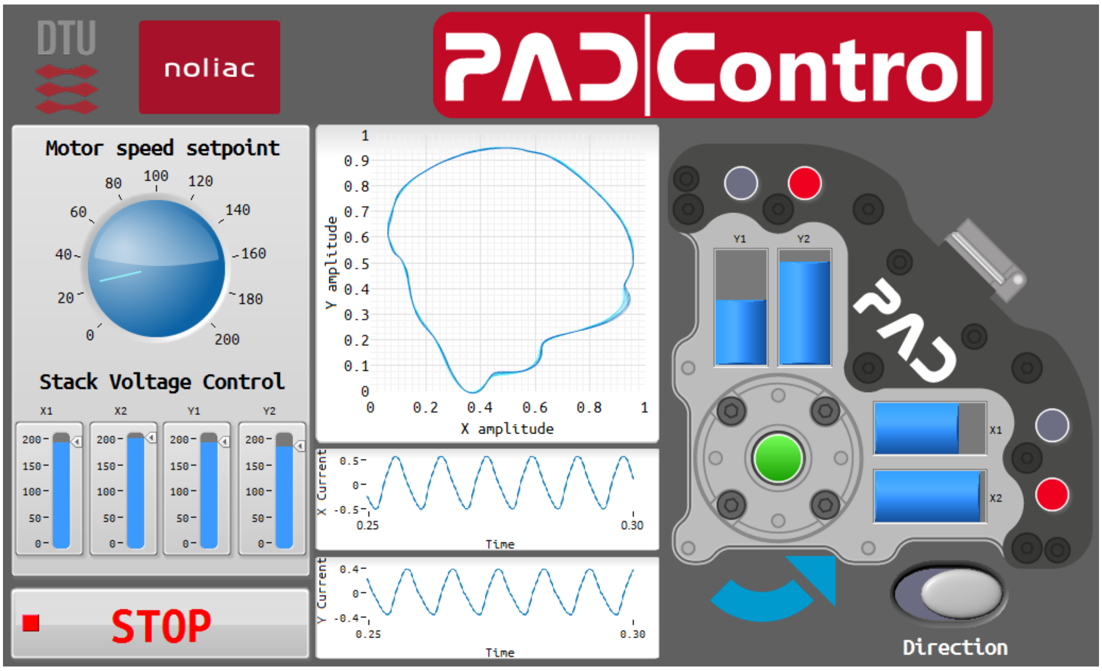

Figure 2.29: PAD graphical user interface.

through is then calculated, and the interface allows the user to display any desired tooth *window* that is of interest. Concomitantly, either a windowed time plot or spectrum can be viewed on the right-hand side.

The roundness of the spatial plot of the axes currents gives an indication of the overall motor contact point quality. Whenever the motor is nearing its overload point, ringing can be observed on the circular trajectory. The amplitude of the oscillation then steadily increases until tooth skipping occurs. This allows not only preempting when the motor nears its limit, but also pinpointing the location and exact tooth at which skipping will occur.

Finally, as part of the development process, an overall system user interface is designed, which combines all the capabilities presented thus far. This enables quick driving and experimentation with the motor system itself without in-depth knowledge of the system hardware or software intricacies. This interface is shown in Fig. 2.29. Hereby, all necessary hardware and software steps and precautions are taken and the system is ready for intricate control algorithm development, live motor parameter estimation or even adding features such as back-drivability through torque sensing.

2.2.4 MRI behavior

Magnetic resonance imaging is a medical principle that uses a magnetic field and pulses of radio wave energy to perform imaging of organs and structures inside the body. Therefore, it is important that all equipment used inside the scanner room complies with medical standards. The goal of this part of the project is to test the feasibility of using the presented PAD motor inside such a scanner room, in order to drive the patient positioning table. Thus, a basic requirement is fabricating all motor parts and housing out of non-magnetic materials. For the final design, the choice was narrowed down to titanium.

The performance of the motor inside an MRI scanner is then evaluated, by placing the motor close to the scanner bore and analyzing the resulting influence on images of standard oil and water test phantoms. The test was performed in collaboration with Siemens Healthcare and one of their Magnetom Spectra 3 T scanners was used.

Fig. 2.30 shows the test set-up, wherein the motor is placed approximately 150 mm from the center of the measurement, which in turn lies in the center of the oil phantom shown. Fig. 2.31 illustrates a perspective view of the three different imaging planes that are presented in the upcoming results. Motor placement here is indicated by the magenta arrows.

In order to be able to qualify the results, a first image is taken with the motor absent from the set-up. This is shown in Fig. 2.32. The top row of images represent the water phantom, and are used to assess radio-frequency (RF) interference coupled into the image. These will exhibit the presence of white areas within the ball, corresponding to interfering frequencies. Even when no harmonic components are present, the overall graininess of the images will increase with general RF noise present.

The bottom row of images show the oil phantom. Any magnetic materials present around the scanner bore will incur a shift in its nominal resonance frequency. This is visible in the oil phantom as black/white transitions, where every such transition corresponds to a 0.25 ppm shift. In order for a device to be deemed suitable for operation in MRI conditions, its presence must not provoke more than one 0.25 ppm shift in resonance frequency measured directly in the center of the phantom.

Fig. 2.33 shows the influence of the unpowered motor on the images. Naturally, no RF components are present in the water phantom, while the oil phantom shows one transition in the center of the image, which is deemed acceptable. Fig. 2.34 shows the case where the motor is running at 10 Hz. There is no significant influence on the phantoms, compared to the unpowered case.

Conversely, there is no interference on the motor itself from the scanner as it is able to operate normally. Torque output is also tested by coupling the motor to a load spring. Its performance is identical both inside and outside the MRI room.

Finally, in order to justify the choice of titanium as a construction material for the motor, Fig. 2.35 shows a measurement of the oil phantom with an older version of the PAD motor which used stainless steel as its housing material. Even though stainless steel is also deemed a non-magnetic metal, it is clear that its influence on the scanner image is unacceptable.

The measurements performed here attest the usability of the PAD motor inside MRI scanners, thereby proving its potential for medical or other highly-magnetic applications.

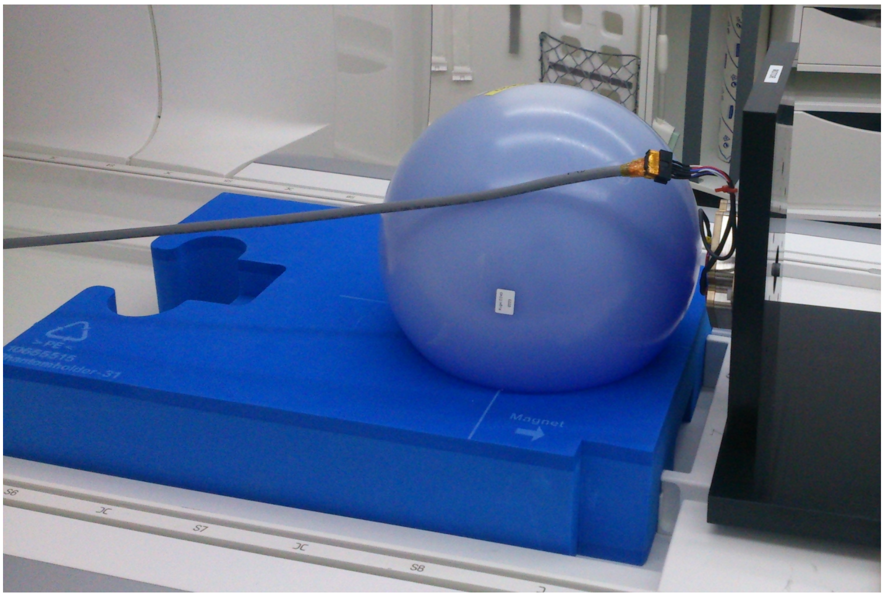

Figure 2.30: Placement of motor at 150 mm versus oil phantom ball center.

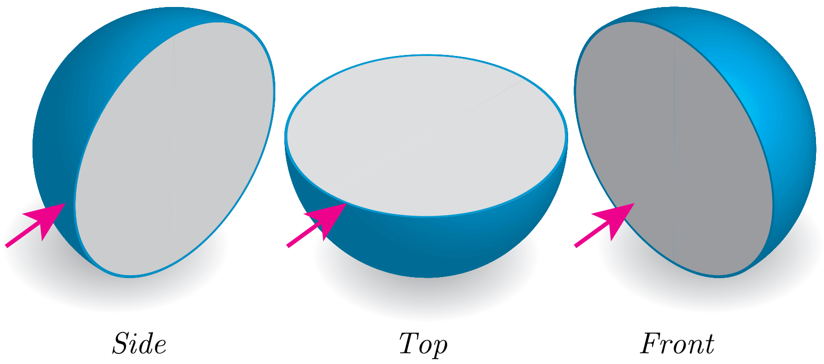

Figure 2.31: Placement of motor at 150 mm versus oil phantom ball center.

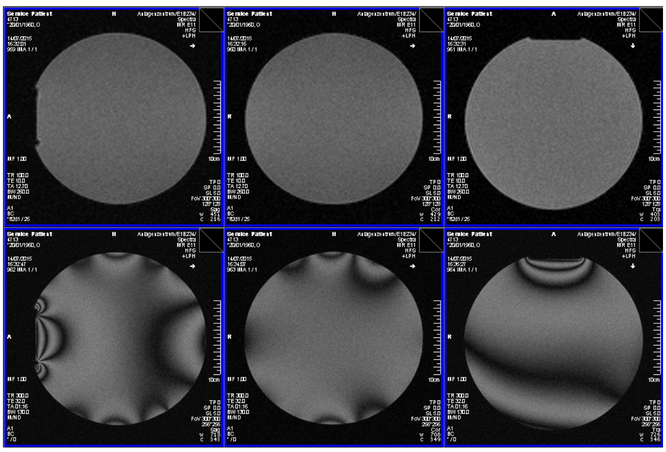

Figure 2.32: Reference image with PAD motor absent.

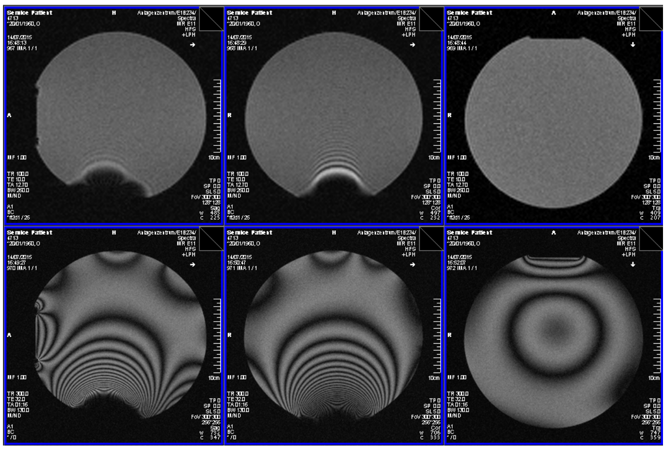

Figure 2.33: MRI signal degradation in the presence of the PAD motor. Motor is not powered.

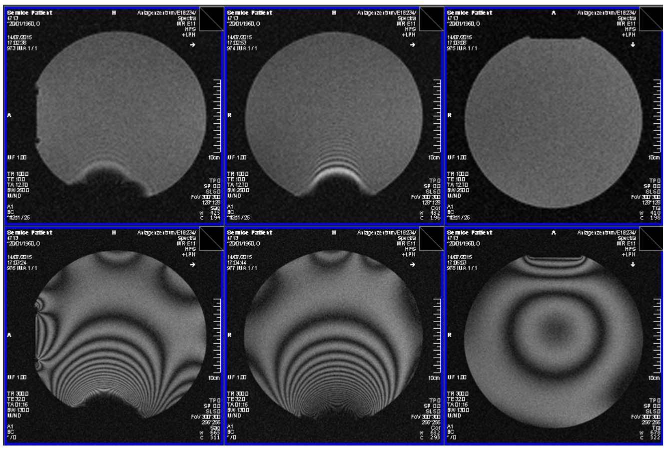

Figure 2.34: MRI signal degradation in the presence of the PAD motor. The motor is running at 10 Hz

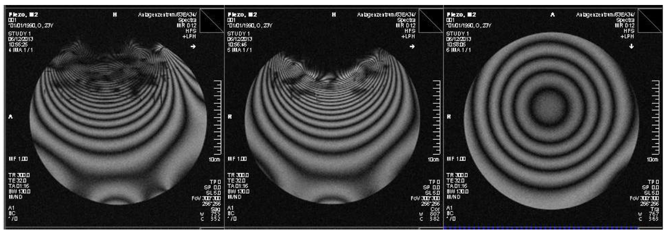

Figure 2.35: Old version of PAD using stainless steel as housing material.

2.3 Chapter summary

This chapter focuses on the low-frequency operation of piezoelectric devices, where they exhibit a capacitive behavior from an electrical point of view. This enables their use in quasi-static applications, where the focus lies on either sensing, as a direct effect, or positioning and actuation, as a converse effect.

The research focuses specifically on piezoelectric stack actuators, which couple several active piezoelectric layers together in order to obtain a larger net stroke at a reduced input voltage, compared to their single-layer counterparts. Used in positioning applications, the hysteretic nonlinearities between applied input and resulting output stroke are highly detrimental with respect to positioning accuracy.

Therefore, the extents of the effect are studied in detail and the concept of Preisach model of hysteresis is introduced. This enables a phenomenological characterization of hysteresis and, following an identification process and approximate inversion, allows both estimation and compensation of the undesired hysteresis. Furthermore, the influence of temperature on piezoelectric stacks is studied and a method of inclusion in the model is presented.

This leads to the introduction of the Piezoelectric Actuator Drive, a type of motor drive that employs stack actuators to impart motion. Motor structure and characteristics are presented in detail and a simplified model is introduced that links the forces generated by the actuators to torque output. Next, power requirements are presented and two separate power stages that can drive the motor are introduced. A discussion about the concepts of sensorless operation and its benefits follows, together with a presentation of the analog and digital interfaces developed to support it.

Finally, the motor is intended for operation inside a magnetic resonance chamber, as a driving stage for the patient positioning table. In this respect, the magnetic neutrality of the PAD is exploited and measurements inside an MRI scanner follow in order to demonstrate the feasibility of this type of application.

Further details about the concepts discussed in this chapter, covering both hysteresis modeling and motor characteristics and driving can be found in appendices A, B, C, D, E, F and G.

3

Inductive behavior of piezoelectric actuators

This chapter touches on the second relative region of interest in terms of frequency for piezoelectric actuators – inductive behavior, encountered between the resonance and anti-resonance frequency peaks. The voltage across the piezoelectric device leads the current through it at these frequencies. Therefore, the device electrically behaves like an inductor. This behavior is almost exclusively encountered in piezoelectric transformers. Besides their other benefits, piezoelectric transformers are also magnetically neutral. This property is of exceptional interest since they can be used in non-magnetic power converters and therefore be placed inside MRI scanners with little impact on imaging quality. Focus is placed on a mixed analog and digital control method based on dead-time control, detailed in-depth in appendices H, I and J. The final behavior is evaluated inside an MRI room.

Operation in the inductive region is almost exclusively encountered in piezoelectric transformer (PT)-based applications, since in this frequency region the piezoelectric ceramic behaves like an equivalent inductor. Unlike the capacitive and resistive behaviors, the benefit of this type of operation is only apparent when energy from the piezo is transfered through a mechanical interface back into electrical domain. Therefore, as a transformer, the device is actually composed of two mechanically-coupled actuators that act as a two-port energy conversion circuit. An ac excitation signal on one side is converted into a proportional mechanical vibration. This is then coupled to the other side, which converts the mechanical vibration back into an electrical signal.

The high desirability of piezoelectric transformers stems in no small part from their ability to single-handedly act as resonant tank circuits, thereby enabling the design of high-frequency soft-switching power converters without the use of discrete inductor components. This is imperative in order to develop an MRI-compliant power converter. Furthermore, a strong mechanical coupling between the two devices comprising a transformer is desired for efficient energy transfer. A resulting drawback is that the

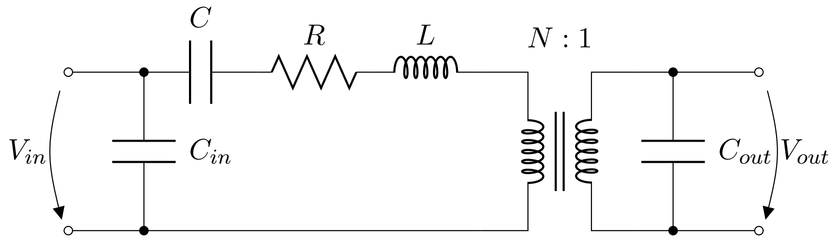

Figure 3.1: Mason model of single-resonance piezoelectric transformer.

quality factor Q of the structure will be high and therefore the bandwidth for inductive operation is greatly reduced. Moreover, the frequency behavior of these transformers changes with both load and thermal characteristics and is affected by aging.

All of these factors lead to a greatly increased difficulty in maintaining circuit stability with respect to frequency. A control circuit needs to therefore track the resonance and keep the input signal frequency within the desired operating region for maximum efficiency.

3.1 Piezoelectric transformers

Presenting an equivalent electrical or mechanical circuit model is useful for expressing the frequency behavior of the transformer with respect to its complex impedance. Fig. 3.1 shows the Mason-equivalent electrical representation of a piezoelectric transformer. This is the idealized case in which only one resonance is modeled. Any additional resonances can be represented by adding an equivalent number of series RLC structures in parallel with the original one. This combination of both inductive and capacitive elements enables transformer use in resonant-type switching power converters. While a move to high frequency conversion brings many benefits, switching losses also start to dominate. Therefore, soft-switching becomes an imperative design metric in order to achieve high overall efficiencies [55–57].

Soft-switching in a switch-mode power converter represents the phenomenon by which state changes in the switching nodes happen only when either voltage across or current through them is zero. These methods are called zero-voltage or zero-current switching, or ZVS and ZCS, respectively. In the idealized case, this completely eliminates losses during switching events. Therefore, focus throughout the whole design procedure is placed on achieving ZVS capabilities, which in the case of piezoelectric transformers is a property of the transformer itself [109]. Conversely, hard-switching represents switching with no regards to loss minimization.

Although the macroscopic behavior of different piezoelectric transformers is the same, the actual mechanical construction can greatly vary based on shape and vibration coupling direction. Throughout the present research, different models of transformers are used, which were designed by Noliac A/S in close collaboration with DTU Electronics. Fig. 3.2 shows two different designs of radial mode transformers. Of the two, the round design was the major focus for experiments and analysis, since it presents both stable operation and good ZVS capabilities. Fig. 3.3 shows a few designs of interleaved electrode transformers with more exotic electrode configurations, where the main focus was an improvement in power throughput while also adding additional features such as

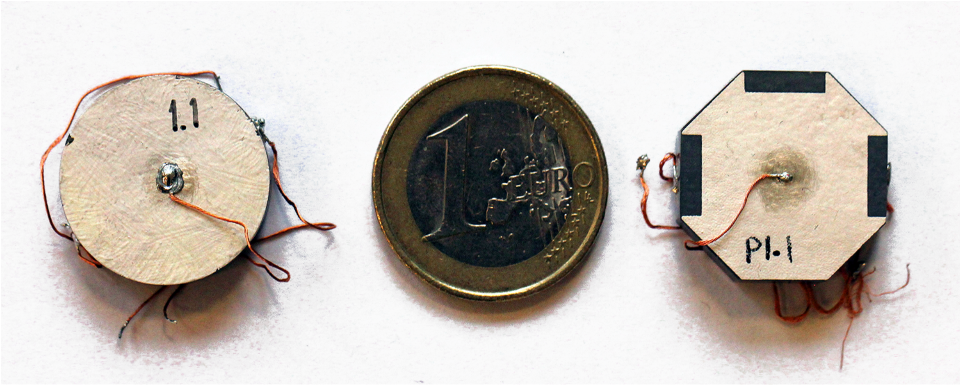

Figure 3.2: Radial mode piezoelectric transformers.

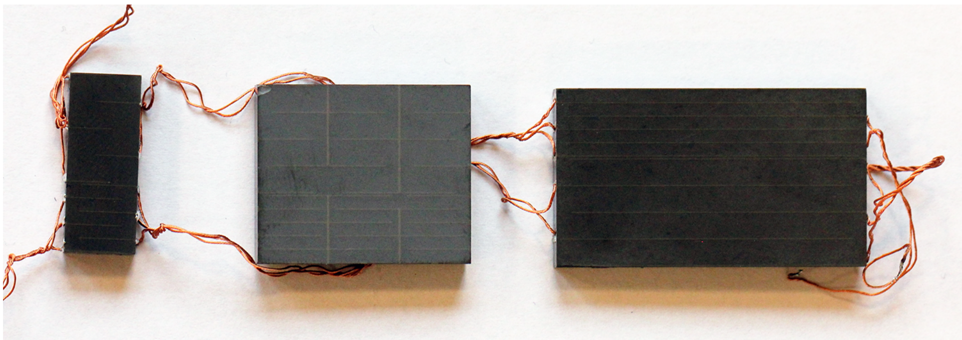

Figure 3.3: Interleaved interdigitated electrode (IDE) piezoelectric transformers.

current sensing elements [49, 110].

3.1.1 Dead-time control

If a piezoelectric transformer-based switch-mode power converter is capable of ZVS operation, then one way of ensuring this is by controlling the time when both high and low side switches are off. This implies variable-frequency control, since the period of the switching signals varies with their off time.

Fig. 3.4 shows the block diagram of the a half-bridge switch-mode power converter used for developing the control algorithm that ensures ZVS operation. Fig. 3.5 illustrates the concept of on and off time between the pulses driving the half-bridge. Dead-time is represented by the magenta areas in the figure, and is generally expressed in % of one switching period. This time needs to be sufficient for the current into the transformer to carry enough energy in order to to charge and discharge its input capacitance. At the same time, it needs to ensure that the switches are never on simultaneously, in order to avoid shoot-through. An optimal dead-time ensures that the switching events happen only when the voltage difference is null between the switched node and V_{cc} for high-side activation or ground for low-side activation. This represents the basis for ZVS operation and sets the stage for *delay-based pulse-shaping*.

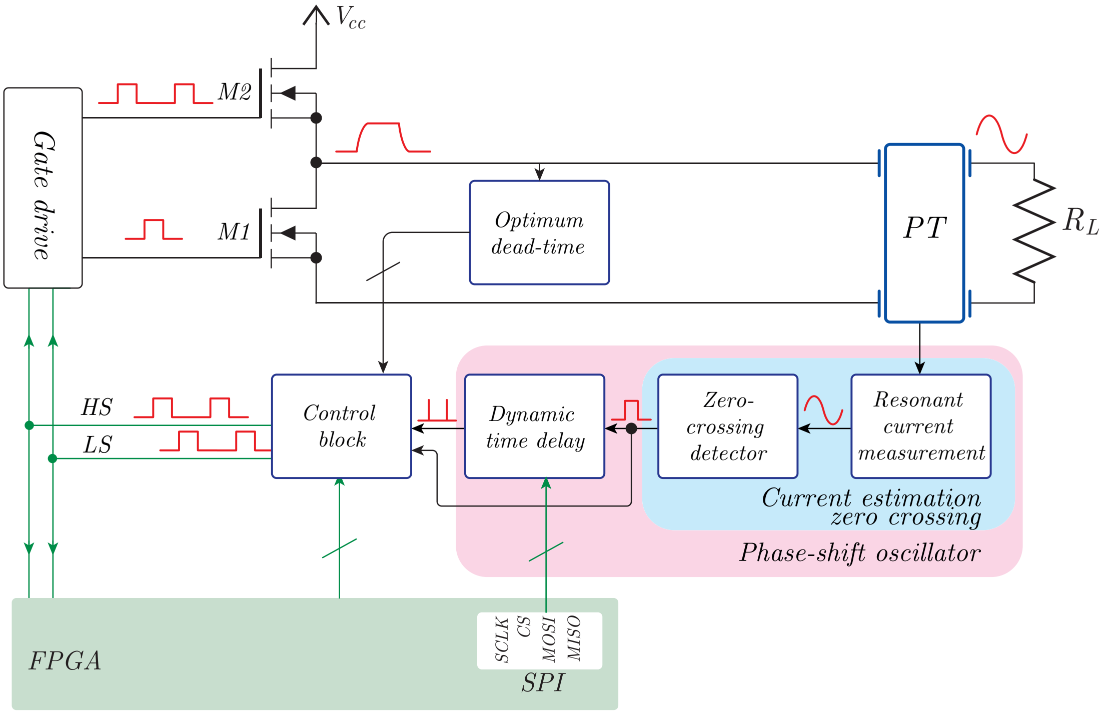

Figure 3.4: Operational block diagram of the PT-based power converter with closed-loop control.

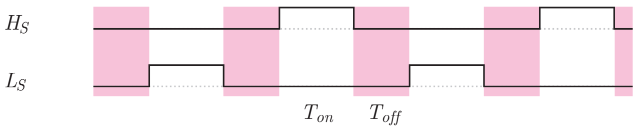

Figure 3.5: Illustration of on versus off time in a half-bridge switch-mode converter.

Optimum dead-time

In order to ensure the most favorable amount of dead-time necessary, a so-called *optimum dead-time* circuit is developed. This is an analog detection algorithm whose operation principle is illustrated by Fig. 3.6. Basically, the switching node voltage is tracked and four conditions are tested for:

- if the node voltage equals or exceeds the voltage rail, then activate high-side;
- if the node voltage equals or is below reference, then activate low-side;
- if the node voltage has reached its local maximum, then activate high-side;
- if the node voltage has reached its local minimum, then activate low-side;

In normal operation, the transformer has enough energy in its oscillation so its capacitance will be charged and discharged all the way to rail and ground. Two comparators ensure that, when either level is reached, the voltage is clamped to the corresponding side, since the transformer's voltage swings outside of the rails. Thereby, minimum energy loss and maximum power transfer is ensured. This is represented by the two comparison blocks in the figure.

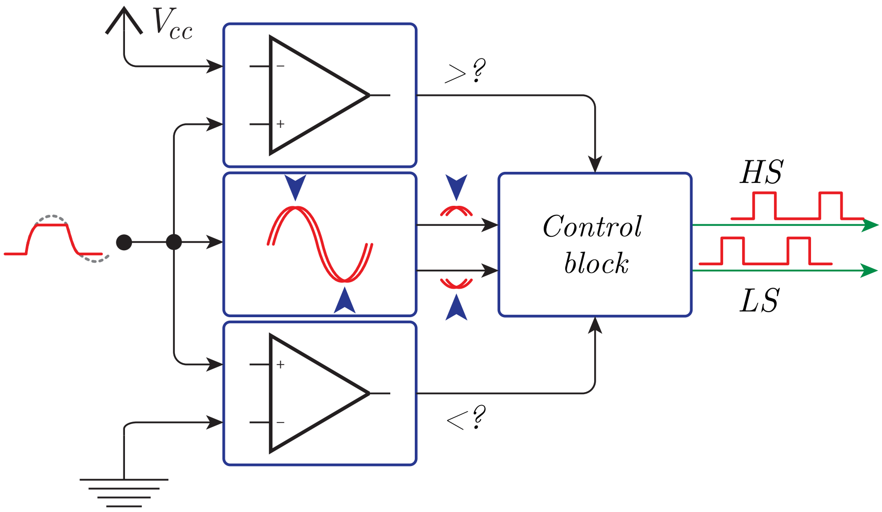

Figure 3.6: Principle of operation of the optimum dead-time block (ODT).

There are cases, such as the start-up sequence or sub-optimal operation for example, where the resonant current does not have the necessary energy to charge the input capacitor. In these cases, while soft-switching cannot occur, there is still an optimum point of oscillation corresponding to the least amount of energy wasted through hard-switching. This is the point where the distance between the oscillating voltage and either one of the rails is minimal. Therefore, it is the representation of the signal extrema before it starts to fall, respectively rise again. These points are detected through an analog *extrema detector* circuit, whereby the input signal is compared to a minimally delayed version of itself. The crossing points between the original and delayed signals will represent a fairly good approximation of the minimum or maximum reached in the current oscillation cycle. The approximation becomes more accurate as the amount of delay tends towards zero. In practice, if too little delay is used, noise will cause spurious fake detections. The detector is represented by the block between the two comparators in the figure.

All of these four distinct events generate triggers which, through logic processing in the control block, will mark the rising edges of either high- or low-side pulses, thereby concluding the respective dead-time periods in the cycle. Therefore, the optimum dead-time block ensures either continued ZVS operation or at least minimum hard-switching, if full soft-switching is not possible.

3.1.2 Delay-based pulse shaping

Due to the high mechanical coupling between stages in piezoelectric transformers, the frequency band where these behave inductively is quite narrow. Therefore, piezoelectric impedance in this region has a very steep slope with regards to frequency. Thus even minor changes in the operation point of transformers due to load or temperature changes will cause a relatively large shift in its frequency. Since, as previously mentioned, tracking this frequency is essential in maximizing performance, the resolution at which this needs to occur presents a non-trivial challenge.

In order to maintain converter agility, fast response times and cycle-by-cycle control,

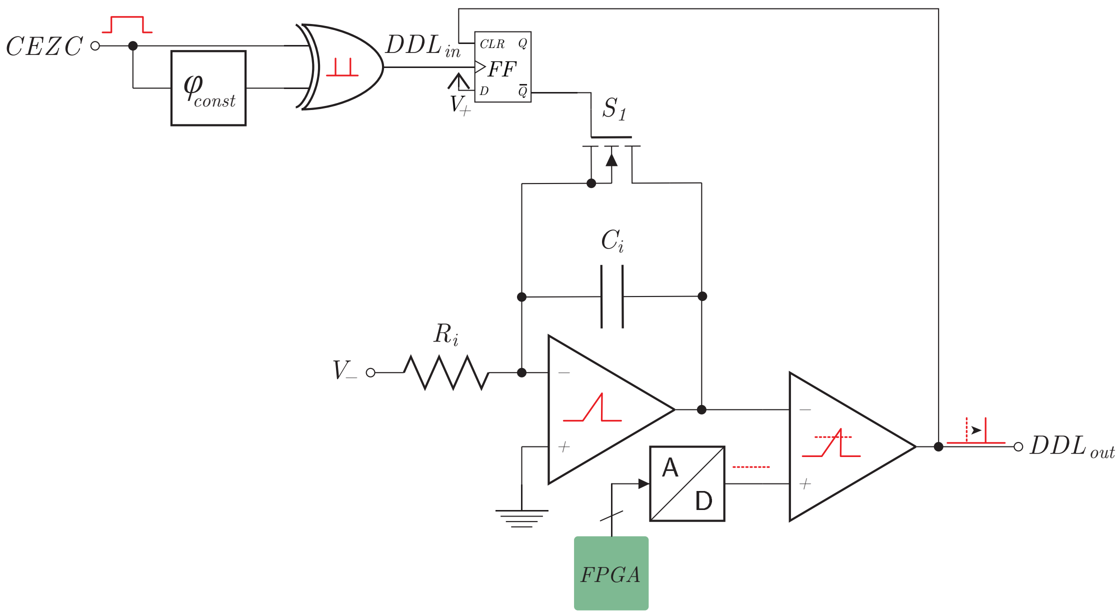

Figure 3.7: Simplified circuit of the dynamic delay line.

frequency tracking through integrative means such as phase-locked loops are not considered. Since the converter is controlled by means of dead-time and the operation is periodic, the desired frequency tracking performance can be translated to a minimum time resolution necessary to detect changes and adjust its operation from one cycle to the next.

With regards to ensuring this, the current feedback path using transformer resonant current to generate switching pulses is employed, as shown in Fig. 3.4. This is called a self-oscillating loop, whereby the switching frequency and transformer oscillation frequency are locked together. Next, in order to be able to correctly track changes in transformer operation, the phase shift within the loop needs to be kept at zero. There will always be some phase shift added by the different components in the loop, but due to the periodicity of the converter operation, zero shift is equal to 2π shift in phase. The role of the controller is therefore to detect this and apply the correct amount of time delay to ensure a 2π shift.

Dynamic time delay

Initial investigation of the time step resolution required to finely adjust the total loop delay is performed by mapping relative changes in transformer frequency to output voltage changes. The result of this investigation shows that there is an outstanding change in the amplitude of the PTs output voltage for every 10 Hz change in switching frequency. Due to high mechanical coupling, the quality factor of transformers is also very high. This implies that the slope of the impedance curve for inductive behavior is very steep, which explains the large operating point changes observed with only small frequency variations. For example, if the operating frequency of 100 kHz increases by 10 Hz, the output voltage shows a considerable change in amplitude. Therefore, a precision of minimum 10 Hz in frequency is required for an ideal operation, which is equivalent to 1 ns time delay resolution, as

$$\Delta t_{res} = \left| \frac{1}{f_2} - \frac{1}{f_1} \right| \quad \Rightarrow \quad \left| \frac{1}{100000} - \frac{1}{100010} \right| \approx 1\,\text{ns}. \tag{3.1}$$

Implemented in digital alone, this would equate to having to use a digital controller with a clock frequency of at least 10 GHz and even then, only 10 discrete time steps are possible within a period.

Therefore, a mixed analog and digital control method through *delay-based pulse shaping* is developed. This is implemented as the dynamic time delay block in Fig. 3.4. A simplified version of the circuit diagram that shows its operation is presented in Fig. 3.7. The output signal of the current estimation zero crossing block (CEZC) is roughly a 50% duty cycle square wave signal, whose flanks represent the points where the resonant current crosses zero. This signal has therefore the same frequency as the transformer. The output of the CEZC block is then tied to the dynamic time delay block (DDL).

The edges of this CEZC signal are considered as start triggers to the hardware integrator in the dynamic time delay. Namely, when any input signal edge is encountered, the feedback capacitor in the op-amp negative feedback starts charging, thereby creating a fixed voltage slope. This is then compared to the variable reference voltage provided by the FPGA through a D/A converter. Upon crossing the reference, the integrator is reset through the switch by discharging the feedback capacitor. Since the input pulse triggers the start of the integration, the variable reference provided to the comparator by the D/A converter coupled with the voltage slope work together to create a time-delayed version of the input pulse which is proportional to the D/A converter value. The comparator output is then latched for a short time to provide one-shot pulses to the output of the DDL.

Hereby, the maximum delay is selected through adjusting the value of the integrating capacitor. Since the D/A converter used has 16 bits of resolution, this allows a very fine time delay adjustment with a minimum theoretical step of $1/(2^{16} - 1)$. The generated delay pulses will then be used as trigger for the beginning of the dead-time period.

Next, Fig. 3.8 shows a detailed drawing of the main signal waveforms in the circuit. The influence of the previously-presented optimum dead-time circuit as well as any propagation delays are ignored for clarity. V_f is the transformer's primary-side voltage while exhibiting soft-switching and stable operation. I_{res} shows its ideal resonance current. This current is dependent on the characteristic parameters of the PT and it changes its polarity when either switch turns on. Therefore, depending on the operating frequency and temperature of the PT, there is a phase shift between the resonance current and switching voltage. Consequently, it is important that the circuit is capable of compensating for this phase shift as well. DDL_{in} represents the input signal to the delay block after edge detection. This signal is then arbitrarily delayed in order to provide DDL_{out}, which in turn deactivates the switches, thereby determining the start of the dead-time period.

The performance of the implemented time delay is evaluated through an automated test set-up which measures the instantaneous delay obtained compared to the input pulse as well as the stability of the output signal by means of its mean jitter averaged over 5 seconds in every possible point. The measurement was performed using a 2 GHz bandwidth LeCroy oscilloscope and took four days to complete.

The maximum obtainable delay was arbitrarily set to 3 µs, thereby obtaining a theo-

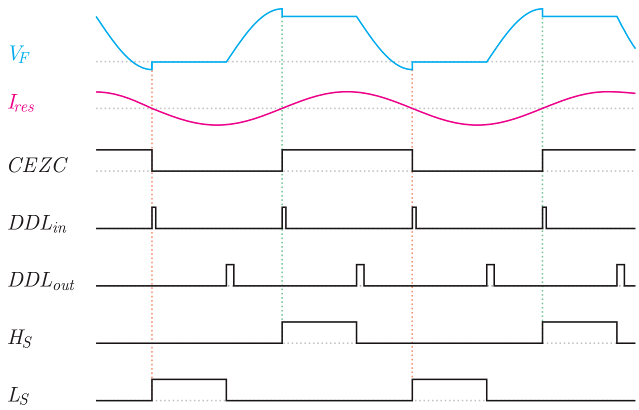

Figure 3.8: Timing diagram.

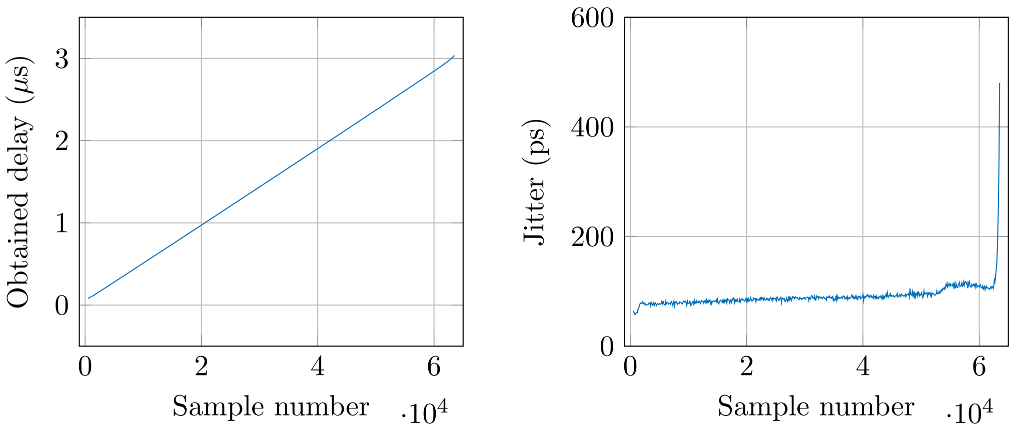

(a) **(b)**

Figure 3.9: Timing diagram. The left figure (a) shows the obtained delay at every sample and proves that linearity is not an issue. The right figure (b) shows a plot of the jitter at every corresponding delay point.

retical minimum step size of 46 ps. The results in Fig. 3.9 show that the delay obtained is very linear with respect to given reference. On the other hand, the jitter plot on the right shows an average overall jitter of 85 ps, which is larger than the minimum time step, but nonetheless well within initial design parameters of the desired 1 ns resolution.

Control block

The contributions of both the *optimum dead-time* and *dynamic time delay* finally come together in the aptly-named *control block*. The block diagram of this is shown in Fig.3.10. This is the part of the circuit that is responsible for generating the final gate drive signals used to drive the half-bridge switches. It is constructed fully of logic gates and two flip-flops. The flip-flops are configured to act as set-reset latches, whereby their data input D is permanently wired to logic high and their clock and clear inputs are used to set and reset their respective outputs.

During normal operation, the signals that turn on the half-bridge switches are provided by the ODT block and pass through unhindered to the clock inputs of the two flip-

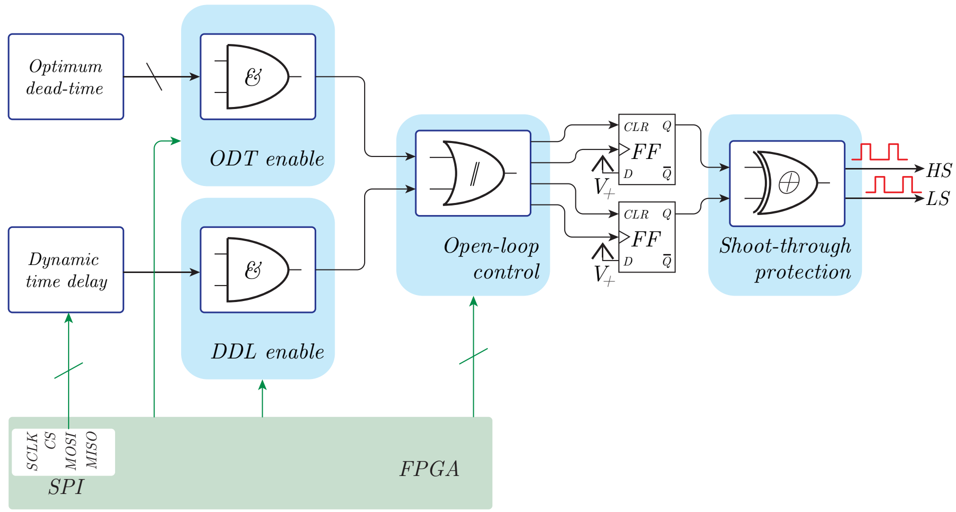

Figure 3.10: Conceptual diagram of the control block.

flops. Thereby, either the high or low side switch is activated. Next, the delayed signal provided by the dynamic time delay is wired to both clear inputs of the flip-flops, driving the switches low. In this state, the role of the FPGA is only to adjust the provided delay in order to drive the loop phase to an integer 360°.

For flexibility during research and for debugging purposes, the FPGA is able to override the functionality of either the ODT, DDL or both at the same time. By breaking the self-oscillating loop and providing the drive signals directly, it is able to control the converter in open-loop. This is useful whenever the transformer is replaced with a different one, as a frequency sweep here can help quickly identify new operating conditions.

The last block in the diagram is added for protection, in order to deactivate the half-bridge entirely in case the pulses to the switches overlap.

The functionality of this control block was essential during the development stage, as it allowed isolating the effects of the different collaborating parts in the circuit, thereby speeding up the debugging stage.

3.1.3 Bidirectional operation

One of the major advantages of piezoelectric ceramics in general, and piezoelectric transformers in particular is their capability of bidirectional energy transfer. The concepts previously-introduced in this chapter can be fully duplicated and applied to the secondary side of the transformer, thereby blurring the line between *primary* and *secondary* sides and allowing for power to be effectively transfered both ways. This is especially desirable in systems with complex, reactive loads or applications where the direction of power flow depends on the desired system state, such as off-grid systems with local storage.

Therefore, Fig. 3.11 expands the diagram introduced in Fig. 3.4 by adding a second half-bridge coupled to a capacitive load, with full accompanying circuitry to allow self-oscillation and control. In this implementation, the system symmetry enables a load connection on either side of the transformer. Moreover, since the implemented

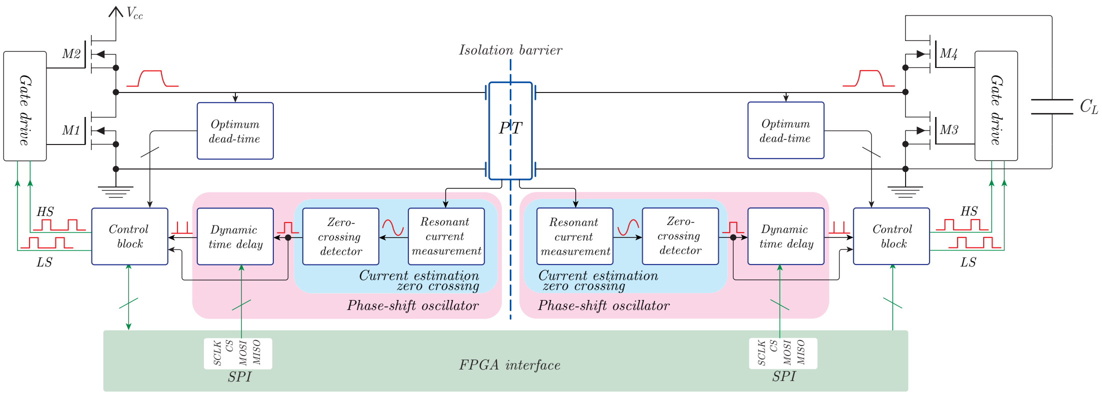

Figure 3.11: Operational block diagram of the bidirectional piezoelectric transformer-based power converter with closed-loop control.

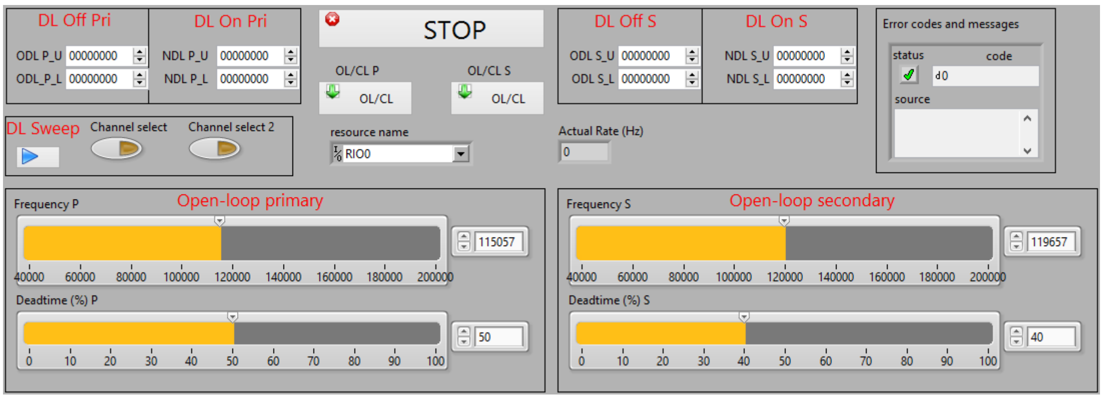

Figure 3.12: Graphical user interface for converter interaction.

control method does not require an electrical connection between the two sides of the transformer, the added benefit of galvanic isolation between sides is also obtained.

The advantage of using an FPGA board as controller also becomes more obvious at this stage, since a field-programmable gate array is capable of true parallel operation. Thereby, two of the D/A converter custom communication protocols detailed in the previous chapter are implemented and operate independently from each other. Nevertheless, it is still possible to pass data between regions of the FPGA through direct memory access. This is a main requirement in developing a future master control algorithm, as well as expanding converter capabilities.

An FPGA development board from National Instruments was chosen, in order to speed up the design process. Specifically, a power electronics-oriented single board RIO equipped with both an FPGA, a powerful signal processor accompanied by an attached mezzanine card containing a large amount of peripherals enabled a quick start on the design and a fast development process on the software side. The final iteration of the control system has a graphical user interface, allowing quick demonstrations and ease of use. This interface is shown in Fig. 3.12. All previous capabilities are maintained, with the added possibility of running both converter sides in open-loop, both in closed-loop or a mix of open and closed operation.

The block-based design approach to the whole system started to be prevalent during the debugging process. This is when the flexibility of the mix and match possibilities provided by the digital block truly started to become apparent in speeding up development. Therefore, the whole system – both hardware and software – were designed with this in mind. Software-wise, different modes of operation are implemented and the user can quickly switch between these at whim. On the hardware side of things, a motherboard was built that fits onto the FPGA mezzanine extension. This motherboard is a base that holds and interconnects the different circuit modules used.

Everything is kept fully modular, and this brings with it many benefits from a research point of view. Firstly, the circuit complexity and component count are both high so this design approach allows a quick replacement of just a part of the circuit in case of catastrophic failure. Furthermore, the whole converter can quickly be reconfigured from unidirectional to bidirectional operation on either side of the transformer by swapping out modules. Adding to this is the ease through which different implementations of the same module can be tested out. Finally, a complete reconfiguration of signal paths is also possible on the fly in order to try out different system iterations. All of these features were used extensively during the whole research period.

The fully-assembled final system illustrating this modular design principle is shown in Fig. 3.13(a), with the piezoelectric transformer itself featured prominently. Fig. 3.13(b) shows the same set-up from the front, whereby the amount of circuit board stratification can be seen.

Finally, a snapshot showing bidirectional converter operation is presented in Fig. 3.14. All important signals are shown, with the contribution from the optimum dead-time block being concentrated into the four signals ending with DL_{on}. The dynamic delays are represented by signals ending with DL_{off}, while also showing all gate drive signals as well. Lastly, analog channels $C1$ and $C2$ are the measured voltages on both sides of the transformer. The delays on the two sides of the transformer are fine-tuned in order to obtain ZVS operation. The converter is hereby self-oscillating at 115 kHz.

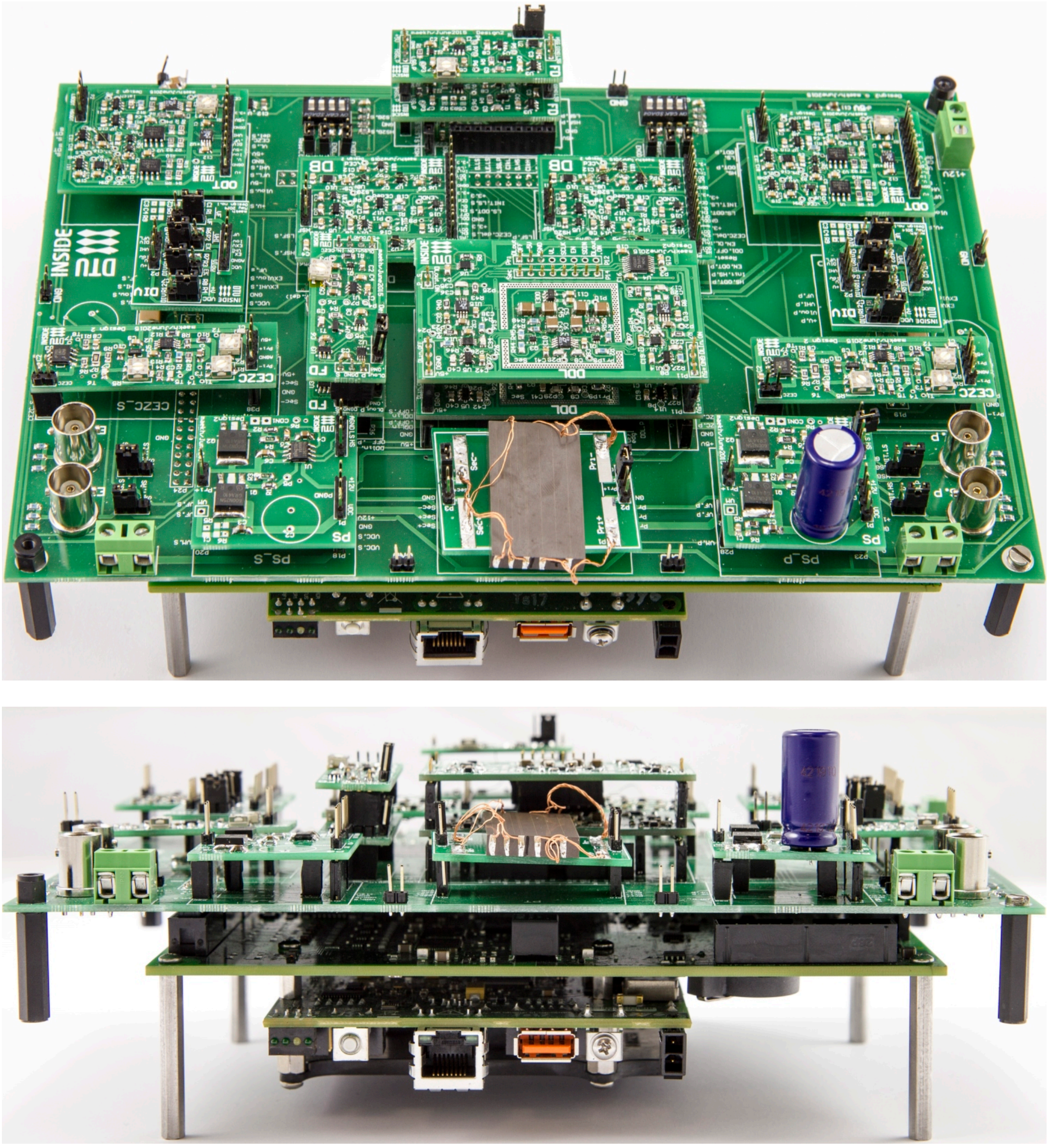

Figure 3.13: Image of the final system used for bidirectional control of piezoelectric transformers. Top view (a) and side view (b).

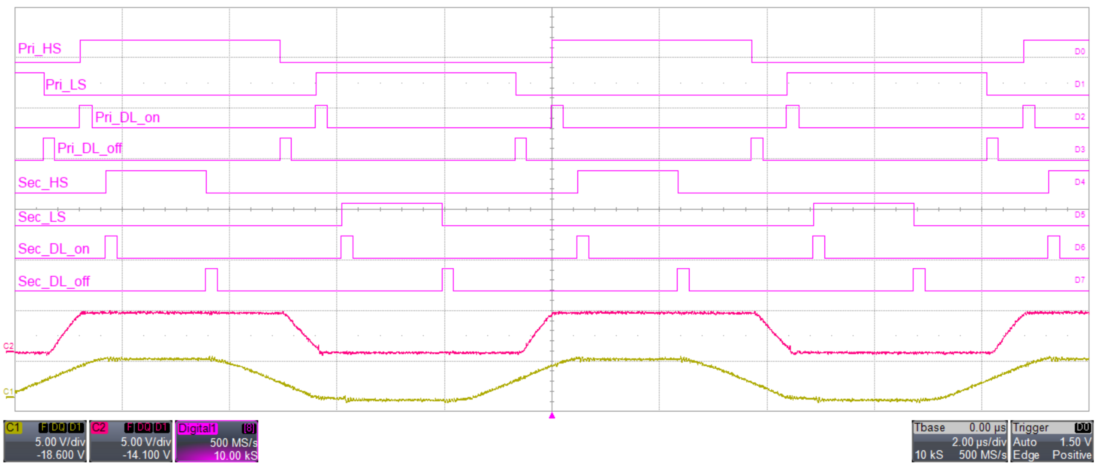

Figure 3.14: Oscilloscope snapshot showing bidirectional converter operation.

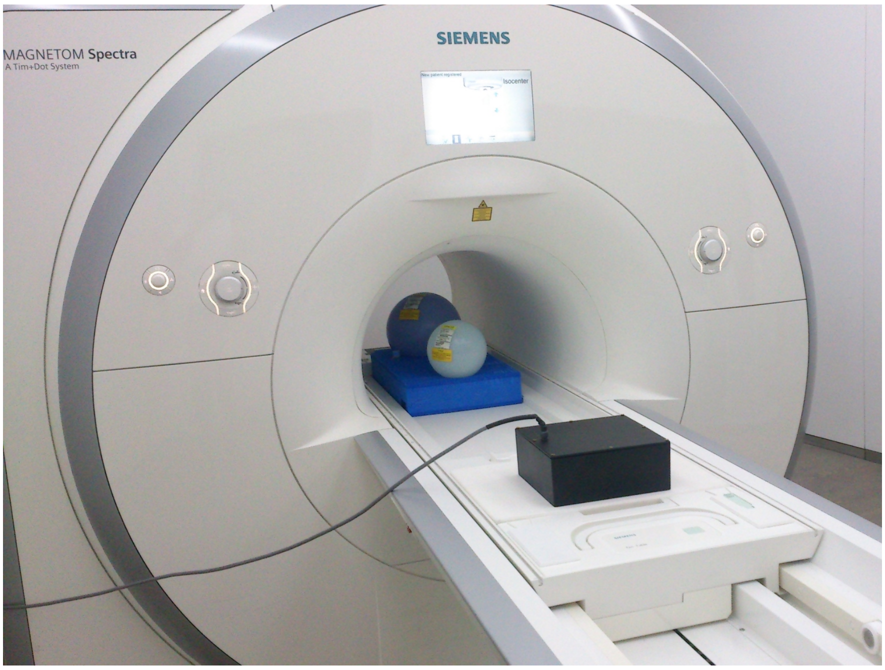

Figure 3.15: Placement of enclosure containing converter at 400 mm versus MRI bore center.

3.1.4 MRI behavior

Part of the MRI testing phase introduced in Chapter 2 included evaluating the feasibility of operating the piezoelectric transformer-based converter inside a large magnetic field. Evaluation is performed, as before, based on the quality of imaging obtained from both an oil and a water phantom.

The oil phantom rests in the center of the scanner bore, while the water phantom is placed right next to it, as shown in Fig. 3.15. The converter is encased in an EMI shielding enclosure, placed 400 mm from the center of the bore.

During this test, the whole relevant frequency spectrum for MRI was scanned with the antennas inside the magnet bore in order to detect any disturbing stray radiation at fixed frequencies. The nominal resonance frequency in the volume of the oil phantom is 125.25 MHz, while the measurement span is approximately 9 minutes.

From an RF perspective, neither the self-oscillating switching frequency of 116.2 kHz or the FPGA clock frequency of 80 MHz have any higher-order harmonic components that directly interfere with the measurement. Even so, the overall signal to noise ratio of the imaging system is reduced by approximately 10 dB. Conversely, the large magnetic field has absolutely no influence on converter operation.

Since the distance of the circuit from the bore is significant, no influence is seen on the oil phantom. Therefore, only the image from the water phantom is shown in Fig. 3.16. The right hand side image shows the measurement with the converter in place but not powered, while the left hand side image represents the same measurement with the converter on. Any direct interfering frequency component would be visible as a lighter area withing the phantom. The visibly higher granularity in the image with the converter running represents an overall SNR degradation of 10 dB. This degradation is attributed to the large physical size of the boards used and a sub-optimal choice of enclosure, since the one used here is lacking a conductive lid seal.

Despite the SNR reduction, the experiment proves that the piezoelectric transformer-based power converter is a suitable candidate for use in very large magnetic fields. Careful circuit design will prevent any switching harmonics from appearing in the resonance image of the scanner, while a good EMI shielding enclosure will reduce RF noise emanation and MRI SNR degradation.

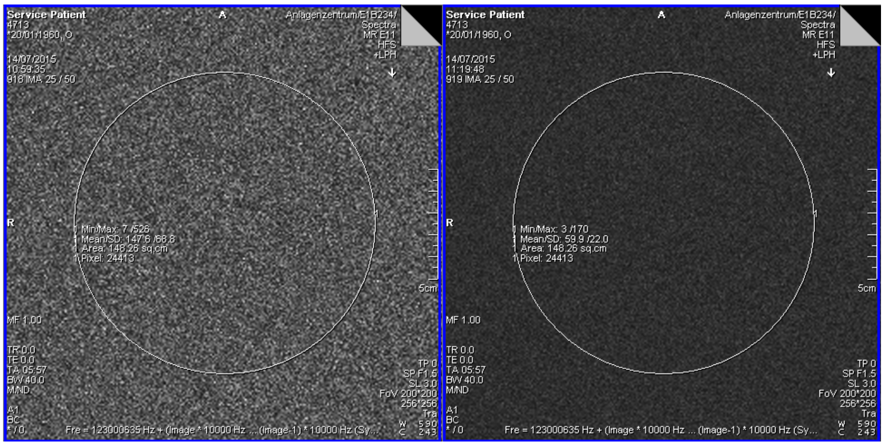

Figure 3.16: RF noise generated by the converter circuit inside the MRI scanner, as measured by the water phantom.

3.2 Chapter summary

Operation above mechanical resonance enables piezoelectric ceramics to behave inductively, allowing them to act as transformers capable of highly efficient soft-switching when coupled with resonant switch-mode power converter designs. Even more so, they still retain their other benefits such as bidirectional operation and high power density, while sidestepping the issue of magnetic radiation that plagues traditional transformer-based designs.

This last property allows them to be used in power supplies designed for applications where magnetic neutrality is imperative. This was the basis for the bidirectional converter presented in this chapter, which is intended to be used inside MRI chambers to power the PAD motor presented in the previous chapter.

Designing an inductorless power converter is in and of itself a nontrivial challenge. This is furthermore enhanced by the accuracy and sensitivity required in precisely controlling the piezoelectric transformer to maintain its ideal operating point where its efficiency is maximized. Power considerations throughout the chapter were not touched upon since, at this stage, power throughput is still severely limited by transformer manufacturing processes. Therefore, the focus of this part of the project was on innovation through newly-developed mixed-signal control methods.

This innovation is considered to be achieved through the development of dead-time optimality tracking and delay-based pulse shaping, both of which provide a good starting point for new avenues of research. Also, the overall system design allows for great flexibility in further experiments through the combination of modular hardware and software design. All of these concepts are tested and proven to work both in the lab and in a real-world test inside an MRI scanner, and are therefore the subject of two individual patent applications and publications.

Further details on the design principles presented here as well as more measurements and performance metrics are found in appendices H, I and J.

4

Resistive behavior of piezoelectric actuators

This chapter touches on the third relative region of interest in terms of frequency for piezoelectric actuators – resistive behavior, encountered at the resonance peak. The natural mechanical vibration amplification encountered at this specific frequency is coupled into a large surface fitted with an electrostatic actuator. By matching the resonant frequency of the actuators with a higher-order resonance in the actuated surface, a squeeze-film is created on the electrostatic actuator surface. The effect is that of a large reduction in friction while the vibration is active. System details and performance are presented in appendices K and L

Operation at mechanical resonance is probably the most desirable application for piezoelectric actuators, since at this precise frequency any interference on the actuator input is constructive and additive in nature. Therefore, any input signal at this frequency will naturally yield an amplified response from the excited actuator.

From an electrical standpoint, this corresponds with the point of least impedance and is therefore also the most energy-efficient frequency of operation for voltage-based excitation, as minimum input energy is required to keep the vibration going. Moreover, at this point, the voltage across and current through the piezoelectric device are in phase and therefore the device behaves like a resistive load.

This mode of operation is employed by all forms of ultrasonic cleaning devices as well as industrial ultrasonic baths, crystal oscillators, frequency-tuned transducers, vibration energy harvesters and ultrasonic lubrication.

4.1 Ultrasonic lubrication

This rather unusual terminology of *ultrasonic lubrication* is not something commonly encountered in literature, but nonetheless, it is the author's belief that it perfectly sums

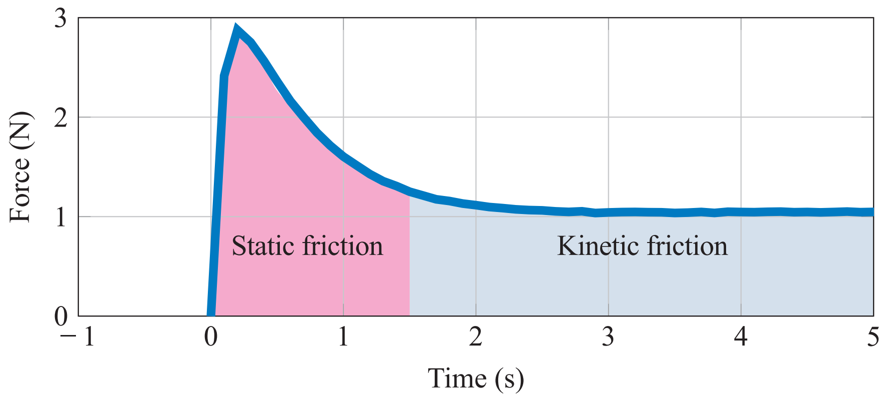

Figure 4.1: Concepts of static and kinetic friction.

up the effect of friction reduction through application of vibration energy. Humans have an innate understanding of the principle and effect produced, as even children learn early on that a heavy object which is stuck in place is easier to move by slowly rocking and twisting it, rather than just pulling on it. Formally, what needs to be overcome in this case is the phenomenon of static friction (stiction), which is one of the components of dry friction. Thereby, if two surfaces are in continuous relative motion with respect to each other, stiction can never settle in. Thus, by inducing vibration into one of the contacting surfaces, the effects of stiction can be eliminated.

Unfortunately, kinetic friction, the second component of dry friction, is proportional to the relative velocity between two contacting surfaces and is therefore normally increased through vibration. Fig. 4.1 illustrates the principle of dry friction, being composed of static and kinetic parts. The graph shows the variation of an external force acting horizontally on a rigid mass resting on a flat surface while it is set into motion.

Nonetheless, ultrasonic lubrication can actually be used to both eliminate static friction and reduce kinetic friction as well, if it is correctly tuned to the system such that it creates a so-called squeeze-film effect between surfaces.

4.1.1 The electrostatic actuator

Electrostatic film actuators are thin, lightweight and flexible, composed of plastic films etched with fine-pitched electrodes. Because their only components are either conductors or insulators, these actuators can be made fully transparent. Their principle of actuation is presented in Fig. 4.2. A three-phase voltage is applied to electrodes in both the stator surface and the slider, which are facing each other through a small gap maintained traditionally by glass beads. This then generates an electrostatic attraction force between the two. By phase-shifting these signals with respect to each other, a spatial displacement of electrostatic potential is created which allows controlling the horizontal component of this electrostatic force in both magnitude and orientation.

This type of actuator has wide areas of application such as nanoparticle transportation, flexible muscle actuation, paper feeding system, and features most prominently in haptics and human-machine interfaces where their transparency allows them to be overlaid onto traditional display surfaces or game boards. This allows enhancing these interfaces with actuation, motion and feedback capabilities, essentially allowing a coex-

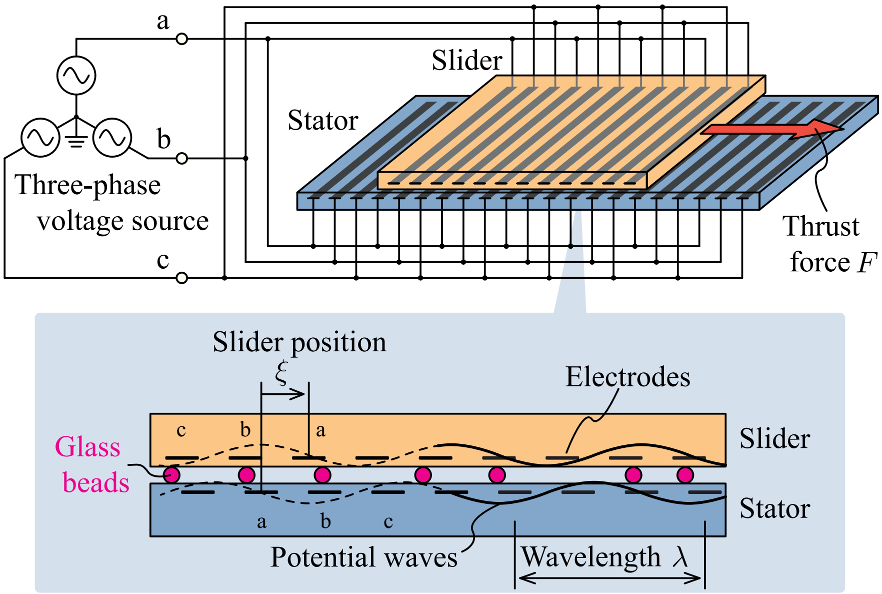

Figure 4.2: The principle of operation for electrostatic actuators [101].

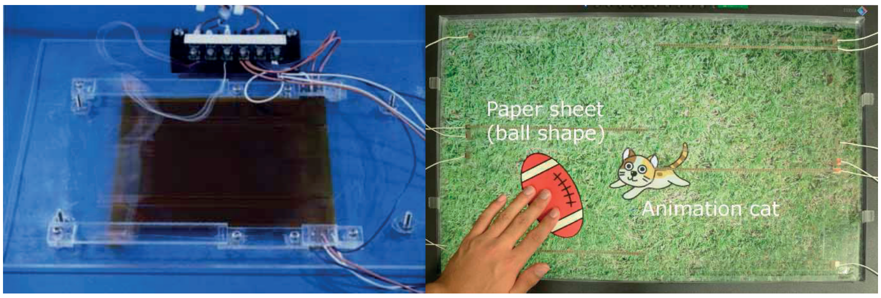

Figure 4.3: Example applications for electrostatic actuators [100, 101]. High-force linear actuator (left) and interactive haptic surface (right).

istence of tangible objects with digital information, thereby enriching human-computer interaction. Two examples of applications involving electrostatic actuators are shown in Fig. 4.3. The image on the left shows a unidirectional high-force flexible actuator that can be used as muscle, while the image on the right shows a human-machine interaction system where the user can play catch with the animated cat using a paper football.

Despite their usefulness, a disadvantage of electrostatic actuators is the fact that they require a layer of small, 100 µm glass beads between stator and slider films to act as both gap material and friction reducer. This reduces the feasibility of actuators since the glass beads require periodic reapplication and also require clean-up after operation. The necessity for glass beads can be reduced or totally eliminated by introducing a squeeze-film between the contact surfaces through controlled piezoelectric vibration. This vibration traps a very thin layer of air (or any other gas) between parallel plate surfaces, thereby creating the squeeze-film effect. This thin air layer can successfully substitute the use of glass beads in electrostatic film actuators.

Figure 4.4: Perceived effect of squeeze-film on human tactile senses.

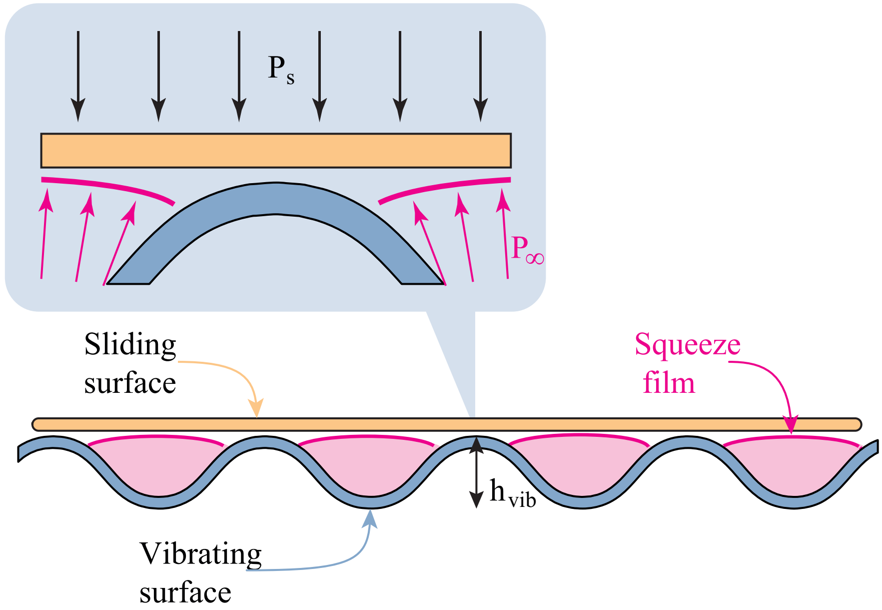

Figure 4.5: Exaggerated effect shown for greater detail.

4.1.2 Squeeze-film effect

The squeeze-film effect is the effect whereby a very thin layer of gas gets trapped between parallel surfaces if these are kept in relative motion versus one another. This effect is the result of an overpressure phenomenon present between these surfaces when the correct structural wavelength is excited [111]. The effects are most prominent in hydrodynamic fluid bearings, a low-maintenance high-performance bearing type which relies on compression of some form of fluid – mostly air – instead of bearing balls to reduce friction.

Another research area that has noticed the benefits of this effect is human tactile stimulation, where squeeze-film is used to create stronger haptic immersion through friction modulation [96, 97]. Thereby, the sense of friction a human hand feels on a surface with vibration applied to it can be changed by correctly adjusting the vibration frequency, as illustrated in Fig. 4.4. The result is that the same surface can feel either rough or smooth to the touch, enabling the creation of more engaging human-machine interfaces.

The analytical model for the overpressure generated by squeeze-film effect was derived by Biet et al. in [97], while taking into account the width of the epidermal ridges in fingers. Because in the current application the two surfaces in contact are relatively large compared to their surface roughness, the equation for the air film thickness, denoted as (1) in the cited publication, can be simplified to:

$$h(t) = h_r + h_{vib}(1 + cos(\omega_0 t)), \tag{4.1}$$

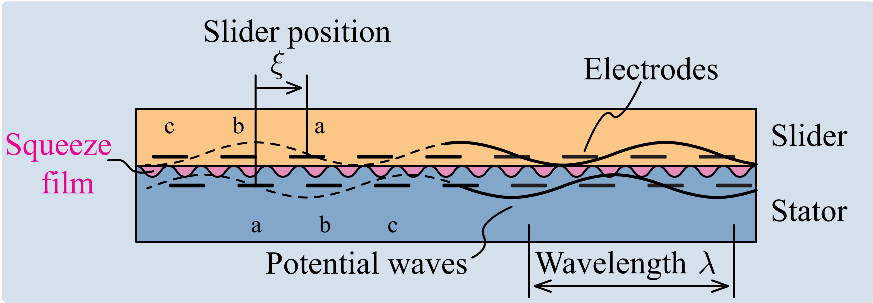

Figure 4.6: Electrostatic actuator principle without the need for glass bead separation gap.

where h_r denotes the total surface roughness of both stator and slider, h_{vib} is the vibration amplitude and ω_0 is the frequency. After obtaining the one-dimensional Navier-Stokes equation and finding the non-dimensional governing Reynolds equation [97], the expression for mean normalized pressure inside the air gap for infinite contacting surface areas becomes:

$$P_\infty = \sqrt{\frac{3}{2}} p_0 \cdot \frac{\epsilon}{\sqrt{1-\epsilon^2}}, \tag{4.2}$$

where p_0 is the surrounding air pressure and ϵ represents the normalized vibration amplitude. The reduction in relative friction coefficient on the electrostatic surface actuator is now expressed as:

$$\frac{\mu'}{\mu} = 1 - \frac{(P_\infty - 1)}{P_s}, \tag{4.3}$$

with P_s representing the pressure exerted by the slider on the vibrating surface. This is illustrated in exaggerated fashion in Fig. 4.5.

Thus, when correctly applied, the squeeze-film effect reduces the friction coefficient in electrostatic actuators, eliminating the continued need for glass beads as gap material. Thereby, the principle previously illustrated in 4.2 becomes the one shown in 4.6.

4.1.3 Effects of squeeze-film on the electrostatic surface actuator

In order to effectively apply the squeeze-film effect to an electrostatic actuator, design must start at a structural level while taking into consideration system constraints. The goal of the design is to match resonant frequencies of both exciter and excited surface in order to maximize coupling. Specifically, an enhancement of already-existing actuators is desired and therefore the starting point is a large glass plate base with electrodes printed on top, which the Advanced Mechatronics Lab at the University of Tokyo already had in stock. After determining the constraints, analyzing the system and selecting desired excitation frequencies, piezoelectric actuators can be sized accordingly.

A good starting point for the design is the modal analysis of the existing glass plate. This plate measures 345mm in length, 250mm in width with a thickness of 1.8 mm. In order to obtain a strong squeeze-film effect, the plate needs to be excited at one of its mechanical resonances. Moreover, the excitation frequency needs to be beyond human hearing range, in order to maximize usability and comfort. Therefore a full modal, frequency and time-analysis is performed using Comsol Multiphysics. The existence of the printed electrodes is ignored at this point, since the added mass through screen

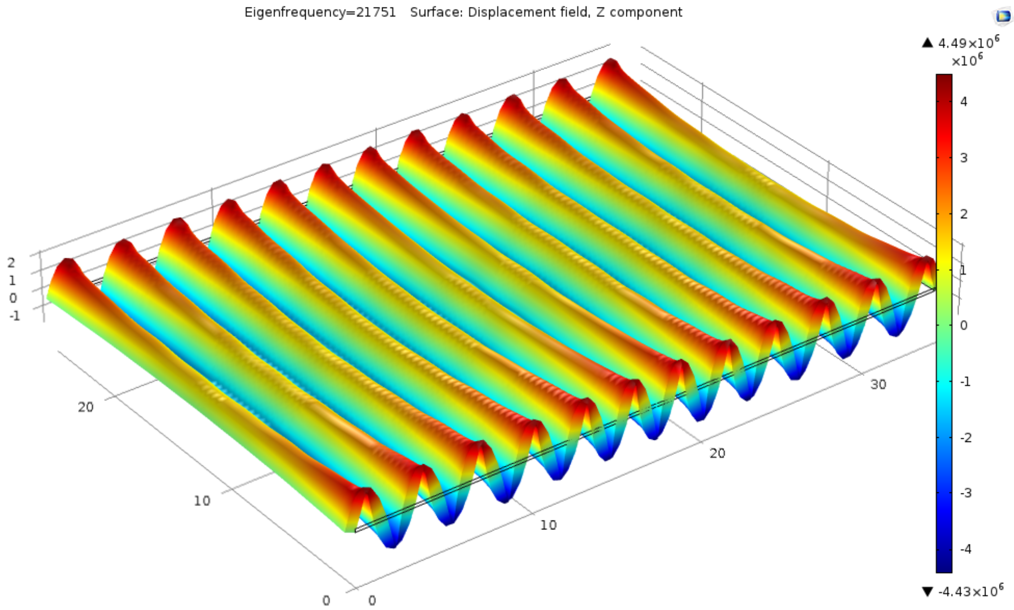

Figure 4.7: Modal analysis of a 345mm x 250mm x 1.8mm glass plate.

printing is deemed insignificant compared to the glass itself. Fig. 4.7 shows the result of the analysis, with a good resonance found at 21.7 kHz, giving a surface vibration half-wavelength of 12.5 mm.

In order to correctly excite the glass at the obtained frequency, two copper-berylium resonators with attached piezoelectric actuators were sized and glued to the glass plate through epoxy resin, based on a design introduced by Giraud et al. [96]. The difference between and challenge compared to the cited design lies with the significantly larger surface that needs actuation.

Therefore, the resonators underwent the same analysis as the glass plate. In the final design, they measure 250mm x 50mm x 2 mm, where the long edge is constrained by the width of the glass while their width is determined through modal analysis in order to obtain the same half-wave as the glass surface. The width of the CuBe resonators permits forming of two full wavelengths in transversal direction and the actuators are therefore placed on the peak of the first wave looking into the center of the glass plate, as shown in Fig. 4.8

The initial design used six 11mm x 50mm x 1mm piezos on each resonator, designed to operate in $d31$ mode. Unfortunately, due to manufacturer delivery times on fully custom-sized actuators, these were substituted with two 120mm x 10mm x 5mm actuators which were readily available. Also, their final placement shifted into the center of the resonators.

The final system sketch is shown in Fig. 4.9. The substantial difference in size with respect to the original design resulted in a resonance frequency shift of the entire system into the audible range. Fortunately, this specific size also hits a resonance in the glass-CuBe assembly, albeit at around 18 kHz, as illustrated in Fig. 4.10.

An image of the final system, with the large replacement piezos, etched glass plate and resonators is then shown in Fig. 4.11. The final system shows a very strong resonant

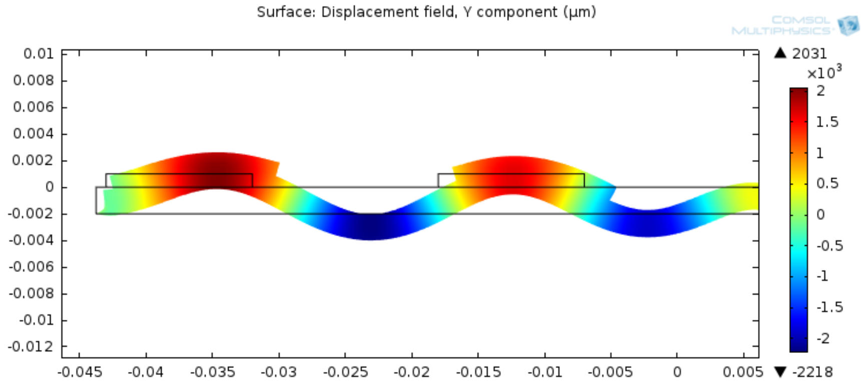

Figure 4.8: 2D modal analysis of CuBe resonators with attached piezoelectric actuators.

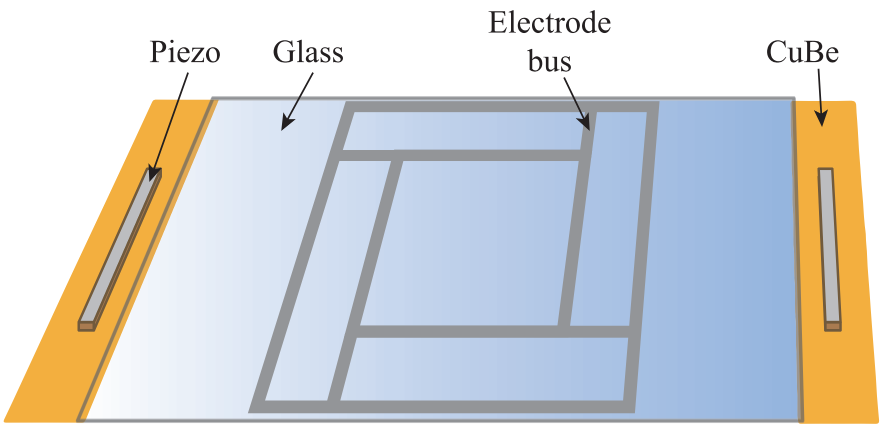

Figure 4.9: Sketch of the electrostatic actuator glass surface with attached resonators and piezoelectric actuators.

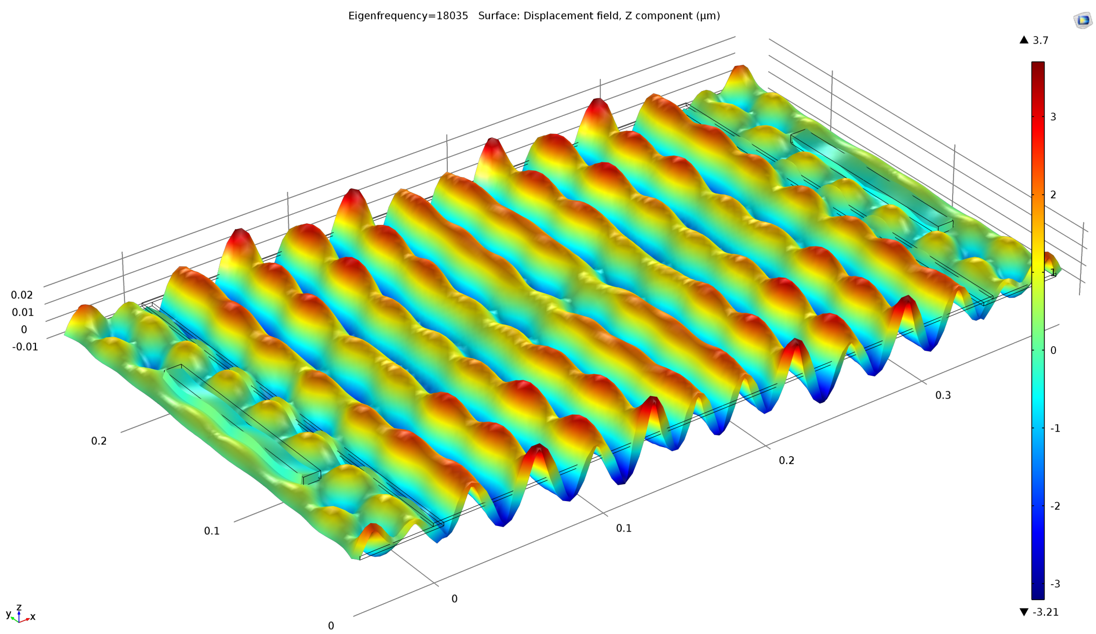

Figure 4.10: Squeeze-film effect on electrostatic actuators.

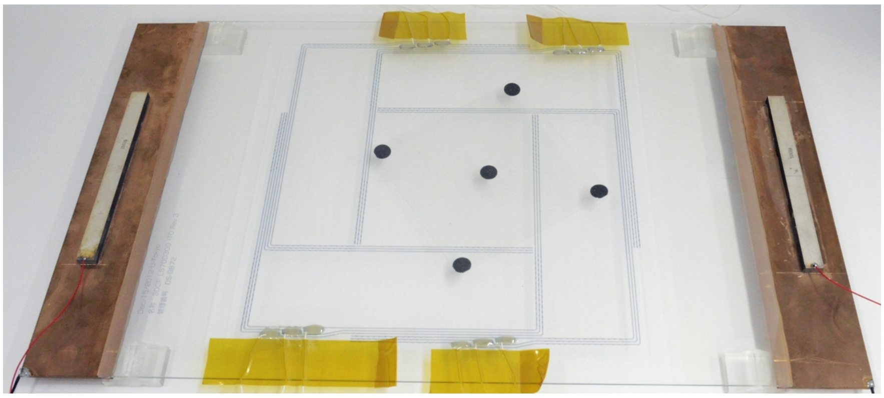

Figure 4.11: Squeeze-film effect on electrostatic actuators.

coupling at 18.6 kHz, which is very close to the simulated 18 kHz.

Differences in resonance between the real and modeled systems can be attributed to material parameter differences, since the exact glass composition is unknown and therefore standard silicon dioxide glass parameters were used. Another source of discrepancy is bonding and coupling between structures, since ideal rigid couplings are used in the model instead of the epoxy resin used in the real system.

While the obtained resonance frequency is high enough to be inaudible for some people, the high coupling factor between the resonators and glass produced some unbearable screeching, so much so that the experiments had to be limited to evenings when the laboratory was empty and they had to be carried out while wearing serious ear protection. Therefore, fitting the system with the originally-sized piezoelectric actuators is highly recommended for continued ease of operation and auditory safety.

Nevertheless, the system shows promising performance enhancements since it meets the goal of eliminating the need for glass beads in the electrostatic actuator system used. Moreover, an initial measured minimum voltage of 500 V on the electrostatic system is necessary in order to create enough force to overcome static friction. This value becomes 150 V with the vibration active. This equates to a 70% reduction in electrostatic voltage requirements, which could allow for smaller pitches on the electrodes and therefore larger generated forces overall.

As a second performance metric of the coupling strength of the vibration into the glass, a round, rigid glass plate with a diameter of 100 mm was placed on the surface. When the vibration is activated, the glass sheet levitates erratically across the surface, with no electrostatic force present. This proves that a significant reduction in relative friction is achieved.

With the vibration-enhanced electrostatic surface actuation system, a new, previously-inexistent capability is also added – friction modulation. By activating and deactivating the piezoelectric vibrator, the surface friction coefficient can be changed. Thereby, friction can be reduced for enhanced slider acceleration, whereas friction can be increased for sudden stop of the slider. This feature increases the dynamic response of the whole actuator system, and is particularly beneficial in interactive systems such as the one presented in [100], where an object needs to stop instantly when an obstacle is detected.

In order to test the performance of the system with and without squeeze-film, an exper-

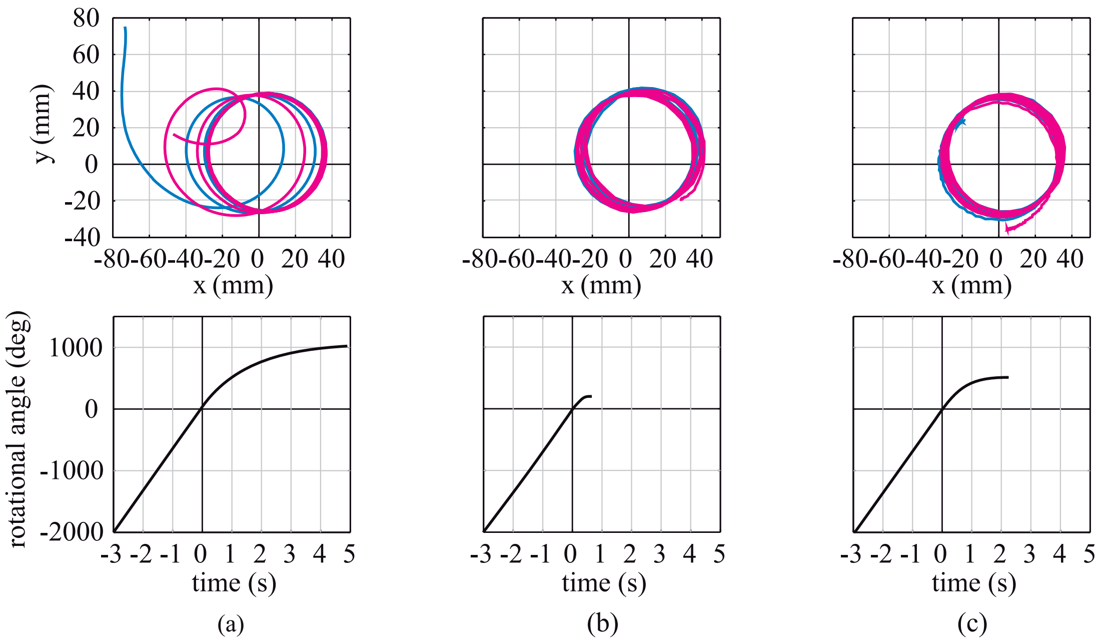

Figure 4.12: Stopping performance of the system under different conditions. In (a), the electrostatic actuation force is removed. In (b), the vibration is eliminated while (c) shows both effects being disengaged.

iment is carried out where a round 80 mm transparent slider cut from a sheet of OHP is accelerated to a constant rotational velocity through the use of electrostatic actuation and under the influence of squeeze-film. Three cases are then tested: removing the electrostatic actuation, removing the vibration and cutting both at the same time.

The slider is equipped with two fiducial marks and the motion is captured by a Keyence VW-6000 high-speed camera. The result of the experiment is presented in Fig. 4.12. The top set of graphs show the spatial trajectory of the two fiducial marks as captured by the camera, while the lower set corresponds to the time it takes for the slider to come to a full stop in each case.

In Fig. 4.12(a), removal of the electrostatic force causes the slider to drift out of control, due to reduced surface friction. It comes to a full stop in approximately 5 s, after hitting the electrical connections and piezoelectric elements. Case (b) shows that when vibration is removed but electrostatic force is kept active, the slider comes to a stop in just 0.5 s and with no positional instability. This is significantly faster than case (c), where both effects are removed. The reason is that due to the sudden increased friction, the vertical attractive component of the electrostatic force dominates, increasing friction even more.

This simple test case proves that the enhancements to the electrostatic surface actuator through squeeze-film application are significant. Hereby, the basis has been set for even more improvements, such as continuous friction modulation through piezo burst-mode operation which can be combined with different electrostatic voltage sequences for added effect.

4.2 Chapter summary

Friction reduction through application of vibration energy, coined here as *ultrasonic lubrication*, is definitely an area of research with great potential for innovation. Even more so, it is a quite thrilling topic due to the visible and tangible benefits it provides.

Squeeze-film theory has a well-documented industrial presence in fluid bearing operation, but, as shown in this chapter, other areas can also benefit from the effect. Specifically, the electrostatic surface actuator, a 2-DOF planar actuation system particularly plagued by high friction forces, has shown a significant improvement in its dynamic response through the use of vibration. Not only that, but the small, messy glass beads used previously to provide an air gap and less friction can now be completely eliminated.

Nothing comes without a cost though, as system complexity and financial cost is increased. Applying the squeeze effect properly to any system requires an arduous analysis process, coupled with a good final design. The whole procedure is very error-prone, because the whole concept of mechanical resonance greatly depends on material properties, total mass and surface area. Materials can contain impurities, or the required parameters for modeling could be missing. Moreover, modeling every system detail is not usually feasible. Therefore, the final result may drift from the original design in significant ways. In terms of energy cost, a conclusion cannot be stated at this time since no measurements were made that take into account total system energy with and without vibration active. It is estimated though that with proper design, the system total energy can be kept at least at the same levels as or lower than before vibration application.

Nevertheless, all the added benefits and extra capabilities brought on by the application of squeeze-film to the electrostatic surface actuator are deemed to outweigh the presented difficulties. Ultrasonic lubrication is therefore a research topic of great future interest.

More details on the squeeze-film system design, its application to the electrostatic surface actuator as well as the performance measurements can be found in appendices K and L.

5 Conclusion

This chapter summarizes the results of the research in all three piezoelectric behaviors. Furthermore, perspectives on future work are given.

Although the fascination for piezoelectricity began with encountering the very unique Piezoelectric Actuator Drive at the start of this PhD project, the vast area of existing applications covered by piezoceramics and their large potential for providing innovation in numerous areas more, due to their as of yet untapped potential, have led the author to both figuratively and literally broaden the spectrum of his research to cover their different behaviors and usage scenarios.

By considering the equivalent electrical impedance behavior of piezoelectric devices with respect to frequency as a unifying characteristic, the approach to the research presented herein is defined through the prism of three distinguishable behaviors: capacitive, inductive and resistive.

The capacitive section focuses on static and quasi-dynamic behavior of piezoelectric stack actuators, while considering their inherent nonlinear behavior. Focus is then shifted to the implications of their use in the PAD motor. The contributions in this section are:

- A hysteresis model based on the classical discrete Preisach method is successfully demonstrated to capture incrementally finer details of piezoelectric stack hysteresis by increasing the discretization factor. A pseudo-inverse model is implemented through the closest-match algorithm. Thereby, hysteresis precompensation is achieved and the relative hysteretic positioning error is reduced by a factor of 20.
- An investigation of the thermal effects on stack hysteresis shows a quasi-linear dependency between its temperature and free displacement. This dependency directly translates into the Preisach hysteresis weighting matrix, and a method is proposed for its inclusion in the model. Results show an average deviation of 3 % between real hysteresis model at 200 °C and its extrapolated counterpart from 25 °C.
- A simplified model for the Piezoelectric Actuator Drive corroborates empirical observations of the relationship between motor torque and electrical phase lag. This is further enforced through a thorough motor power analysis that illustrates a slight lowering in the total reactance with added mechanical load.

- The effects on motor assembly and manufacturing tolerances on the quality of feedback signals is studied. A graphical user interface is designed that allows a qualitative evaluation of the motor and detection of weak points on the ring and shaft. Concomitantly, tooth skipping through mechanical overload can be predicted.

- An MRI test proves the usability of the PAD motor inside a scanner bore. The motor causes an acceptable frequency shift in MRI resonance of 0.25 ppm when placed 150 mm from the imaging area center.

The inductive section focuses on control design for non-magnetic piezoelectric transformer-based power converters to allow efficient, bidirectional energy transfer. The contributions in this section are:

- A new method for ensuring ZVS operation or minimizing hard-switching in a PT-based power converter is developed through the concept of dead-time optimization. The implementation is based on detecting the peaks and valleys in transformer resonant voltage and turning on the converter switches when the maximum amplitude is reached.

- Implementation of dynamic delay is performed through a mixed digital-analog solution based on analog integration and digital referencing. It offers a selectable delay range, 16-bit delay step control and exhibits high linearity and low jitter. Demonstration done on a 3 µs delay range shows a 46 ps time step with an average jitter of 85 ps.

- By combining the optimized dead-time with the dynamic delay, full digital control of converter self-oscillation is implemented and demonstrated. Control is performed through a graphical user interface and the methods developed are the subject of a patent application.

- These concepts are extended to the converter secondary side. Thereby, full bidirectional power transfer with power flow control is demonstrated with ZVS operation. The implementation is the subject of a second patent application.

- The feasibility of using the converter in an MRI scanner is demonstrated. The circuit causes no artifacts in the imaging process and RF noise is acceptable.

The resistive section focuses on analysis of resonant vibrations and its effects on the surface friction coefficient. The contributions in this section are:

- Resonance coupling in the glass base of an electrostatic surface actuator is analyzed and vibration is applied through the use of piezoelectric actuators. The existence of a squeeze film between the electrostatic surface and overlaying slider is proven experimentally, for the first time ever.

- The achieved reduction in friction prevents the need for using glass beads as gap material in the actuator. Moreover, the minimum electrostatic driving voltage required for actuator operation is reduced by 70 %.

5.1 Perspectives on Future Work

The ambitious scope of the research has resulted in advancements and improvements in all three behaviors covered and has at the same time opened the door for further innovation. Some key points for future research are:

- The frequency dependency of piezoelectric hysteresis has not been considered. Inclusion of rate-dependency in the Preisach model would therefore allow it to offer a more complete solution in hysteresis compensation. Furthermore, use of a less demanding identification process could enable real-time modeling and control.
- The effects of hysteresis compensation in improving PAD positioning accuracy have been theorized, but experimental results are needed to demonstrate a definite improvement.
- The control method introduced for PT-based power converters has only been proven conceptually. Scaling it to high power is essential in order to prove its practical use, but piezoelectric transformer production limitations prevented a move to higher power. Moreover, the method is applicable to any resonant-type power converter but further investigation is required to prove its feasibility with other topologies.
- The benefits of adding ultrasonic lubrication to electrostatic surface actuators has been proven, but the capabilities thereby acquired actually extend beyond the initial scope. More research needs to be performed in order to fully benefit from the concept. Moreover, investigations into other applications that can benefit from this form of friction reduction are certain to yield interesting results.

Much research area has been covered but many more possibilities lie beyond the horizon for all forms of piezoelectric applications. It will be interesting to see what innovations the future will bring. The author would therefore like to conclude with the same quote the thesis began with, and after three years of research this quote rings true now more than ever:

If you want to find the secrets of the universe,
think in terms of energy, frequency and vibration.

– Nikola Tesla

6

Other Research Topics

This chapter briefly presents other research interests, that were co-authored during the PhD studies.

Besides the topic of piezoelectricity, during the course of the PhD other ideas were also pursued. Born out of either necessity or chance, but nonetheless tackled with a healthy dose of curiosity, these ideas covered challenges such as designing an automated employee door sign generator based on an active database look-up, programming an FPGA-based pulse test sequence for an in-house designed IC or supervising the design of an enhanced kayaking ergometer. Of particular interest is this last topic, which is covered in detail in appendix M, but will be presented here in brief.

6.1 Improved Kayaking Ergometer Using a Switch-mode Converter Driven Alternator

The work concerns an improvement on existing professional indoor rowing machines by replacing its mechanical resistance with a controlled alternator to offer variable

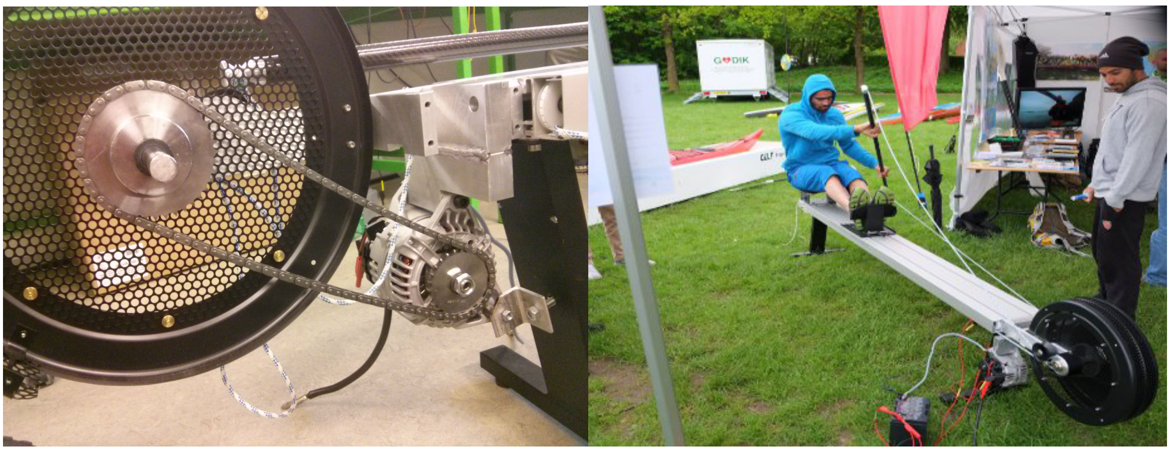

(a) **(b)**

Figure 6.1: Close-up of the system (a) and its use at the 2015 Canoe World Cup (b).

resistance. With mechanical systems, the stroke through water cannot be emulated correctly, as the resistance exhibited by commercial ergometers is constant throughout the stroke. By adding a controllable resistance in the form of a converter-powered alternator, water drag can be emulated by sensing the paddle position with respect to a defined water level and applying resistance only when the paddle is under this level.

Furthermore, the system can be expanded through dynamically changing the resistance based on a computer model of the athlete-kayak-paddle system. This offers marked improvements compared to any commercially-available ergometer today. This was confirmed by the system's warm reception, in its non-final state, by professional athletes at the 2015 Canoe Sprint World Cup. Some rowers stated that it is superior to other professional ergometers, even without advanced dynamics-based resistance modeling.

Bibliography

[1] "Piezoelectric materials," *Solid Mechanics and Its Applications, Solid Mech. Appl*, vol. 212, pp. 7–32, 2014.

[2] I. PIEZO SYSTEMS. (2010) Hystory of piezoelectricity. [Online]. Available: http://www.piezo.com/tech4history.html

[3] C. Industry. (2013) Expanding markets for piezoelectrics. [Online]. Available: http://www.ceramicindustry.com/articles/93845-expanding-markets-for-piezoelectrics

[4] T. Abraham, "Et-117 piezoelectric ceramic, polymer and ceramic/polymer composite devices - types, materials, apllications, new developments, industry structure and global markets," Innovative research and products, INC., Tech. Rep., 01 2014.

[5] T. Maillarda, F. Claeyssena, R. LeLettya, O. Sosnikia, A. Pagesa, and A. V. Carazo, "Piezo mechatronic based systems in aircraft, space and defense applications," *Proc. SPIE Int. Soc. Opt. Eng., X-ray and Gamma-ray Instrumentation for Astronomy*, vol. 7331, no. 1, p. 73310K, 2009.

[6] M. R. Ridlo, T. Lestari, and Mardiyanto, "Poling process optimization of piezo nano composite pzt/polimer." *AIP Conference Proceedings*, vol. 1555, no. 1, p. 17, 2013.

[7] A. Safari and E. K. Akdogan, *Piezoelectric and acoustic materials for transducer applications*. Springer Science+Business Media, LLC, 2008.

[8] B. Aronov and D. A. Brown, "Historical review of underwater acoustic cylindrical transducer development in russia for sonar arrays," *Journal of the Acoustical Society of America*, vol. 136, no. 4, p. 2131, 2014.

[9] S. M. Calvert, "Piezoelectric pebble explosive," Aug. 11 2015, uS Patent 9,103,635.

[10] H. Gawlick and U. Brede, "Piezoelectric fuze, especially for projectiles," Jul. 6 1976, uS Patent 3,967,555.

[11] and others, "Piezoelectric fuse," Sep. 25 1956, uS Patent 2,764,091.

[12] A. Sánchez, S. Blanc, P. Yuste, A. Perles, J. J. Serrano *et al.*, "An acoustic modem featuring a multi-receiver and ultra-low power," *Circuits and Systems*, vol. 6, no. 01, p. 1, 2015.

[13] A. D. B. Ferreira, P. R. Nóvoa, and A. T. Marques, "Multifunctional material systems: A state-of-the-art review," *Composite Structures*, 2016.

[14] K. Uchino, "Glory of piezoelectric perovskites," *Science and Technology of Advanced Materials*, 2016.

[15] D. Ruiz, A. Donoso, J. C. Bellido, M. Kucera, U. Schmid, and J. L. Sánchez-Rojas, "Design of piezoelectric microtransducers based on the topology optimization method," *Microsystem Technologies*, pp. 1–8, 2016.

[16] G.-Y. Gu, L.-M. Zhu, C.-Y. Su, and H. Ding, "Modeling of piezoelectric-actuated nanopositioning stages involving with the hysteresis," in *Nanopositioning Technologies*. Springer, 2016, pp. 183–212.

[17] Q. Xu and K. K. Tan, "Adaptive impedance control of piezoelectric microgripper," in *Advanced Control of Piezoelectric Micro-/Nano-Positioning Systems*. Springer, 2016, pp. 209–232.

[18] R. Dong, Y. Tan, and Y. Xie, "Identification of micropositioning stage with piezoelectric actuators," *Mechanical Systems and Signal Processing*, 2016.

[19] S.-T. Ho and S.-J. Jan, "A piezoelectric motor for precision positioning applications," *Precision Engineering*, vol. 43, pp. 285–293, 2016.

[20] K. K. Leang and A. J. Fleming, "Tracking control for nanopositioning systems," in *Nanopositioning Technologies.* Springer, 2016, pp. 213–244.

[21] J. Shan, Y. Liu, U. Gabbert, and N. Cui, "Control system design for nano-positioning using piezoelectric actuators," *Smart Materials and Structures*, vol. 25, no. 2, p. 025024, 2016.

[22] Q. Xu and K. K. Tan, "Adaptive impedance control of piezoelectric microgripper," in *Advanced Control of Piezoelectric Micro-/Nano-Positioning Systems.* Springer, 2016, pp. 209–232.

[23] M. Lallart, G. Sebald, J.-F. Capsal, B. Ducharne, and D. Guyomar, "Modeling of hysteretic behavior in ferroelectric polymers," *Journal of Polymer Science, Part B: Polymer Physics*, vol. 54, no. 4, pp. 499–508, 2016.

[24] T. Doong and I. D. Mayergoyz, "On numerical implementation of hysteresis models," *IEEE Trans. Magn.*, vol. MAG-21, no. 5, pp. 1853–1855, 1985.

[25] I. Mayergoyz and G. Friedman, "Generalized preisach model of hysteresis," *Magn., IEEE Trans.*, vol. 24, no. 1, pp. 212–217, Jan 1988.

[26] R. Ganguli, D. Thakkar, and S. R. Viswamurthy, "Piezoceramic actuator hysteresis," in *Smart Helicopter Rotors.* Springer, 2016, pp. 129–164.

[27] X. Gao, X. Ren, C. Zhang, and C. Zhu, "Online identification and robust adaptive control for discrete hysteresis preisach model," in *Proceedings of the 2015 Chinese Intelligent Systems Conference.* Springer, 2016, pp. 41–49.

[28] G.-Y. Gu, L.-M. Zhu, C.-Y. Su, and H. Ding, "Modeling of piezoelectric-actuated nanopositioning stages involving with the hysteresis," in *Nanopositioning Technologies.* Springer, 2016, pp. 183–212.

[29] R. Iyer, X. Tan, and P. Krishnaprasad, "Approximate inversion of the preisach hysteresis operator with application to control of smart actuators," *IEEE Trans. Autom. Control, Joint Automatic Control Conference*, vol. 50, no. 6, pp. 798–810, 2005.

[30] R. Iyer and R. Paige, "On the representation of hysteresis operators of preisach type," *Physica B-Condensed Matter*, vol. 372, no. 1-2, pp. 40–44, 2006.

[31] A. Kappel, B. Gottlieb, and C. Wallenhauer, "Piezoelectric actuator drive (PAD)," *At - Automatisierungstechnik*, vol. 56, no. 3, pp. 128–135, 2008.

[32] A. Kappel, B. Gottlieb, C. Wallenhauer, R. Zeichfuessl, M. Vogl, T. Kraus, and T. C. Lueth, "PAD - a scalable drive technology," *Actuator*, pp. 558–561, 2008.

[33] J. Rucha, H. Liess, J. Heinzl, A. Kappel, T. Schwebel, and B. Gottlieb, "Applicability of a piezo actuator drive as a sensorless high precision drive," *10th Int. Conf. on New Actuators*, 2006.

[34] R. Zeichfussl, B. Gottlieb, C. Wallenhauer, S. Herzig, A. Kappel, and T. Luth, "A method for auto-adjustment of a new piezoelectric drive," in *Mechatronics, 2009. ICM 2009. IEEE Int. Conf. on*, April 2009, pp. 1–6.

[35] R. Zeichfuessl, B. Gottlieb, C. Wallenhauer, A. Kappel, M. Vogl, T. Kraus, and T. C. Lueth, "Synchronously controlled piezoelectric actuator drives (PAD) as motors of a delta-3 robot," *Actuator*, pp. 125–128, 2008.

[36] M. Vogl, T. Kraus, R. ZeichfüSSl, C. Wallenhauer, B. Gottlieb, A. Kappel, and T. C. Luth, "Konstruktion und messung der steifigkeiten des hoch präzisen PAD-delta3-roboters mit piezorotationsantrieben, construction and measurement of the stiffnesses of the highly precise PAD-delta3-robot with piezo-rotary drives," *Vdi Berichte, Vdi-berichte, Vdi Ber*, no. 2012, pp. 63–66, 2008.

[37] M. Vogl, T. Kraus, R. Zeichfuessl, C. Wallenhauer, B. Gottlieb, A. Kappel, and T. C. Lueth, "Development of a MRI-safe piezo actuator drive (PAD)," *Actuator*, pp. 576–579, 2008.

[38] E. L. Horsley, M. P. Foster, and D. A. Stone, "State-of-the-art piezoelectric transformer technology," *Eur. Conf. Power Electron. Appl., EPE*, p. 4417637, 2007.

[39] G. Ivensky, I. Zafrany, and S. Ben-Yaakov, "Generic operational characteristics of piezoelectric transformers," *Power Electronics, IEEE Transactions on*, vol. 17, no. 6, pp. 1049–1057, 2002.

[40] V. Loyau, Y.-P. Liu, and F. Costa, "Analyses of the heat dissipated by losses in a piezoelectric transformer," *Ultrasonics, Ferroelectrics, and Frequency Control, IEEE Transactions on*, vol. 56, no. 8, pp. 1745–1752, 2009.

[41] M. Ekhtiari, Z. Zhang, and M. A. Andersen, "State-of-the-art piezoelectric transformer-based switch mode power supplies," in *Industrial Electronics Society, IECON 2014-40th Annual Conference of the IEEE*. IEEE, 2014, pp. 5072–5078.

[42] A. V. Mezheritsky, "Quality factor concept in piezoceramic transformer performance description," *Ultrasonics, Ferroelectrics, and Frequency Control, IEEE Transactions on*, vol. 53, no. 2, pp. 429–442, 2006.

[43] Y. Fuda, K. Kumasaka, M. Katsuno, H. Sato, and Y. Ino, "Piezoelectric transformer for cold cathode fluorescent lamp inverter," *Japanese journal of applied physics*, vol. 36, no. 5S, p. 3050, 1997.

[44] C. Moo, W. Chen, and H. Hsieh, "Electronic ballast with piezoelectric transformer for cold cathode fluorescent lamps," in *Electric Power Applications, IEE Proceedings-*, vol. 150, no. 3. IET, 2003, pp. 278–282.

[45] R. L. Lin, F. C. Lee, E. M. Baker, and D. Y. Chen, "Inductor-less piezoelectric transformer electronic ballast for linear fluorescent lamp," in *Applied Power Electronics Conference and Exposition, 2001. APEC 2001. Sixteenth Annual IEEE*, vol. 2. IEEE, 2001, pp. 664–669.

[46] S. Kawashima, O. Ohnishi, H. Hakamata, S. Tagami, A. Fukuoka, T. Inoue, and S. Hirose, "Third order longitudinal mode piezoelectric ceramic transformer and its application to high-voltage power inverter," in *Ultrasonics Symposium, 1994. Proceedings., 1994 IEEE*, vol. 1. IEEE, 1994, pp. 525–530.

[47] F. Wang, Y. Jia, J. Wu, X. Zhao, and H. Luo, "Piezoelectric/electroluminescent composites for low voltage input flat-panel display devices," *Applied Physics A*, vol. 90, no. 4, pp. 729–731, 2008.

[48] L. Le, Y. Yang, and M. Radecker, "Low profile led off-line phase-cut dimming ballast with piezoelectric transformer," pp. 1–4, 2015.

[49] M. Ekhtiari, T. Andersen, M. A. Andersen, and Z. Zhang, "Dynamic optimum dead time in piezoelectric transformer-based switch-mode power supplies," *Trans. Power Electron.*, 2016, accepted for publication.

[50] M. S. Rødgaard, "Piezoelectric transformer based power converters; design and control," 2012.

[51] S. Bronstein and S. Ben-Yaakov, "Design considerations for achieving zvs in a half bridge inverter that drives a piezoelectric transformer with no series inductor," in *Power Electronics Specialists Conference, 2002. pesc 02. 2002 IEEE 33rd Annual*, vol. 2. IEEE, 2002, pp. 585–590.

[52] M. Sanz, P. Alou, A. Soto, R. Prieto, J. Cobos, and J. Uceda, "Magnetic-less converter based on piezoelectric transformers for step-down dc/dc and low power application," in *Applied Power Electronics Conference and Exposition, 2003. APEC'03. Eighteenth Annual IEEE*, vol. 2. IEEE, 2003, pp. 615–621.

[53] E. Horsley, N. Nguyen-Quang, M. Foster, and D. Stone, "Achieving zvs in inductor-less half-bridge piezoelectric transformer based resonant converters," in *PEDS*, 2009, pp. 446–451.

[54] M. Ekhtiari, "Nonmagnetic driver for piezoelectric actuators," *Proceedings of Icecs 2014*, 2014.

[55] J. A. Pedersen, M. P. Madsen, A. Knott, and M. A. E. Andersen, "Self-oscillating galvanic isolated bidirectional very high frequency dc-dc converter," *Proceedings of APEC 2015*, 2015.

[56] M. Kovacevic, "Advances in very high frequency power conversion," Ph.D. dissertation, Technical University of Denmark, Department of Electrical Engineering, 2015.

[57] B. Andreycak, “Zero voltage switching resonant power conversion,” in *UNITRODE Power Supply Design Seminar SEM-700*, 1990.

[58] J. Díaz, F. Nuño, J. M. Lopera, and J. A. Martín-Ramos, “A new control strategy for an ac/dc converter based on a piezoelectric transformer,” *Industrial Electronics, IEEE Transactions on*, vol. 51, no. 4, pp. 850–856, 2004.

[59] T. Andersen, M. S. Rødgaard, O. C. Thomsen, and M. A. Andersen, “Low voltage driven dielectric electro active polymer actuator with integrated piezoelectric transformer based driver,” in *SPIE Smart Structures and Materials+ Nondestructive Evaluation and Health Monitoring*. International Society for Optics and Photonics, 2011, pp. 79 762N–79 762N.

[60] T. Andersen, “Piezoelectric transformer based power supply for dielectric electro active polymers,” Ph.D. dissertation, Technical University of Denmark, Department of Electrical Engineering, 2012.

[61] M. S. Rodgaard, “Bi-directional piezoelectric transformer based converter for high-voltage capacitive applications,” *Conf. Proc. IEEE Appl. Power Electron. Conf. Expo. (APEC))*, pp. 1993–1998, 2015.

[62] K. S. Meyer, M. A. E. Andersen, and F. Jensen, “Parameterized analysis of zero voltage switching in resonant converters for optimal electrode layout of piezoelectric transformers,” *IEEE Annu. Power Electron. Spec. Conf. (PESC)*, pp. 2543–2548, 2008.

[63] M. P. Foster, E. Horsley, and D. A. Stone, “Predicting the zero-voltage switching profiles of half-bridge driven inductor-less piezoelectric transformer-based inverters,” *Power Electronics, IET*, vol. 5, no. 7, pp. 1068–1073, 2012.

[64] E. L. Horsley, A. V. Carazo, N. Nguyen-Quang, M. P. Foster, and D. A. Stone, “Analysis of inductorless zero-voltage-switching piezoelectric transformer-based converters,” *Power Electronics, IEEE Transactions on*, vol. 27, no. 5, pp. 2471–2483, 2012.

[65] B. Ju, W. Shao, L. Zhang, H. Wang, and Z. Feng, “Piezoelectric ceramic acting as inductor for capacitive compensation in piezoelectric transformer,” *IET Power Electronics*, vol. 8, no. 10, pp. 2009–2015, 2015.

[66] R. Saito, T. Hosobata, A. Yamamoto, and T. Higuchi, “Linear resonant electrostatic induction motor using electrical resonance with piezoelectric transducers,” *Mechatronics, Mechatronics, Mechatronic, Mechatronics Mechanics Electronics Control*, vol. 24, no. 3, pp. 222–230, 2014.

[67] V. Todorova and D. Kolev, “Piezoelectric resonance sensor array,” *27th International Spring Seminar on Electronics Technology*, 2005.

[68] A. Reinhardt and C. Billard, “Piezoelectric resonators and filters,” *Integr. of Ferroelectric and Piezoelectric Thin Films: Concepts and Appl. for Microsystems*, pp. 249–295, 2013.

[69] Y. Yu, J. Xu, J. Ma, and H. Y. Chen, “Piezoelectric resonant temperature sensor,” *Advanced Materials Research*, vol. 3265, no. 981, pp. 632–635, 2014.

[70] Y. Jin, B. Bonello, and Y. Pan, “Acoustic metamaterials with piezoelectric resonant structures,” *Journal of Physics D: Applied Physics*, vol. 47, no. 24, p. 245301, 2014.

[71] Y. K. Fetisov, “Piezoelectric resonance sensors of dc magnetic field,” *IEEE Sensors Journal*, vol. 14, no. 6, pp. 1817–1821, 2014.

[72] H. Gulec, A. G. Akyurekli, M. Gul, M. Gurbuz, B. Koc, and A. Dogan, “Wide-band piezoelectric resonance frequency energy harvester,” *2014 Joint IEEE International Symposium on the Applications of Ferroelectrics, International Workshop on Acoustic Transduction Materials and Devices and Workshop on Piezoresponse Force Microscopy (ISAF/IWATMD/PFM)*, pp. 71–74, 2014.

[73] X. Li, Z. Yao, and R. Wu, “Modeling and analysis of stick-slip motion in a linear piezoelectric ultrasonic motor considering ultrasonic oscillation effect,” *International Journal of Mechanical Sciences*, 2016.

[74] S.-T. Ho and S.-J. Jan, “A piezoelectric motor for precision positioning applications,” *Precision Engineering*, vol. 43, pp. 285–293, 2016.

[75] X. Chen, Z. Chen, X. Li, L. Shan, W. Sun, X. Wang, T. Xie, and S. Dong, “A spiral motion piezoelectric micromotor for autofocus and auto zoom in a medical endoscope,” *Applied Physics Letters*, vol. 108, no. 5, p. 052902, 2016.

[76] K. Dziedziech, L. Pieczonka, P. Kijanka, and W. J. Staszewski, “Enhanced nonlinear crack-wave interactions for structural damage detection based on guided ultrasonic waves,” *Structural Control and Health Monitoring*, 2016.

[77] L. Pahlavan and G. Blacquière, “Fatigue crack sizing in steel bridge decks using ultrasonic guided waves,” *NDT & E International*, vol. 77, pp. 49–62, 2016.

[78] N. Li, J. Sun, J. Jiao, B. Wu, and C. He, “Quantitative evaluation of micro-cracks using nonlinear ultrasonic modulation method,” *NDT & E International*, vol. 79, pp. 63–72, 2016.

[79] D. MacIsaac *et al.*, “Acoustic levitation and ultrasonic tweezers: liquid droplets (clemson), polystyrene (argonne, sao paulo), etc.” *The Physics Teacher*, vol. 54, no. 1, pp. 62–62, 2016.

[80] K. Jia, K.-j. Yang, and B.-f. Ju, “Performance and robustness improvements in ultrasonic transportation against large-scale streaming,” *Journal of Vibration and Acoustics*.

[81] D. Baresch, J.-L. Thomas, and R. Marchiano, “Observation of a single-beam gradient force acoustical trap for elastic particles: acoustical tweezers,” *Physical Review Letters*, vol. 116, no. 2, p. 024301, 2016.

[82] W. Shi, H. Zhao, J. Ma, Y. Yao, and K. Uchino, “Investigating the frequency spectrum of mechanical quality factor for piezoelectric materials based on phenomenological model,” *Japanese Journal of Applied Physics*, vol. 54, no. 10, p. 101501, 2015. [Online]. Available: http://stacks.iop.org/1347-4065/54/i=10/a=101501

[83] D. Koyama and K. Nakamura, “Self-running non-contact ultrasonically levitated stage,” *Next-generation Actuators Leading Breakthroughs, Next-gener. Actuators Lead. Breakthroughs*, pp. 401–412, 2010.

[84] A. Torii, S. Sone, K. Doki, and S. Mototani, “Levitation caused by vertical vibration of a piezoelectric actuator,” *Proceedings of the 15th International Conference of the European Society for Precision Engineering and Nanotechnology, Euspen 2015, Proc. Int. Conf. Eur. Soc. Precis. Eng. Nanotechnol., Euspen*, pp. 273–274, 2015.

[85] S. Mojrzisch and J. Wallaschek, “Amplitude modulation of nonlinear piezoelectric transducers for ultrasonic levitation,” *ASME 2011 Conference on Smart Materials, Adaptive Structures and Intelligent Systems, SMASIS 2011*, vol. 2, pp. 289–293, 2011.

[86] R. Pratap, S. Mohite, and A. K. Pandey, “Squeeze film effects in mems devices,” *J. the Indian Institute of Science*, vol. 87, no. 1, pp. 75–94, 2007.

[87] W. Littmann, H. Storck, and J. Wallaschek, “Reduction of friction using piezoelectrically excited ultrasonic vibrations,” *Proc. of SPIE - the Int. Society for Optical Engineering, Smart Structures and Materials 2001: Damping and Isolation*, vol. 4331, pp. 302–311, 2001.

[88] S. Bharadwaj and M. J. Dapino, “Effect of load on active friction control using ultrasonic vibrations,” *Proc. of SPIE - the Int. Soc. for Optical Eng., Ind. and Commercial Applicat. of Smart Structures Technologies 2009*, vol. 7290, no. 1, p. 72900G, 2009.

[89] V. Kumar and I. Hutchings, “Reduction of the sliding friction of metals by the application of longitudinal or transverse ultrasonic vibration,” *Tribology Int.*, vol. 37, no. 10, pp. 833–840, 2004.

[90] Y. Kim and M. Harders, “Haptic displays,” in *Scholarpedia of Touch.* Springer, 2016, pp. 817–827.

[91] P. Sergeant, F. Giraud, and B. Lemaire-Semail, “Geometrical optimization of an ultrasonic tactile plate,” *Sensors and Actuators A-physical*, vol. 161, no. 1-2, pp. 91–100, 2010.

[92] L. Winfield, J. Glassmire, J. E. Colgate, and M. Peshkin, "T-pad: Tactile pattern display through variable friction reduction," *Proceedings - Second Joint EuroHaptics Conference and Symposium on Haptic Interfaces for Virtual Environment and Teleoperator Systems, World Haptics 2007*, pp. 421–426, 2007.

[93] V. Levesque, L. Oram, K. MacLean, A. Cockburn, N. D. Marchuk, D. Johnson, J. E. Colgate, and M. A. Peshkin, "Enhancing physicality in touch interaction with programmable friction," *Conf. on Human Factors in Computing Systems - Proc.*, pp. 2481–2490, 2011.

[94] M. Guizzetti, V. Ferrari, D. Marioli, and T. Zawada, "Thickness optimization of a piezoelectric converter for energy harvesting," in *Proc. of the COMSOL Conf. 2009*, ser. COMSOL '09, 2009.

[95] C. Hudin, J. Lozada, and V. Hayward, "Localized tactile stimulation by time-reversal of flexural waves: case study with a thin sheet of glass," *2013 World Haptics Conf.*, pp. 67–72, 2013.

[96] F. Giraud, M. Amberg, B. Lemaire-Semail, and G. Casiez, "Design of a transparent tactile stimulator," *Haptics Symposium 2012 - Proc.*, pp. 6 183 835, 485–489, 2012.

[97] M. Biet, F. Giraud, and B. Lemaire-Semail, "Squeeze film effect for the design of an ultrasonic tactile plate," *IEEE-ACM Trans. Networking*, vol. 15, no. 6, pp. 2678–2688, 2007.

[98] A. Yamamoto, T. Higuchi, and T. Nishijima, "Deformable electrostatic linear motor," *2004 1st IEEE Technical Exhibition Based Conf. on Robotics and Automation - Proc., TExCRA 2004*, pp. 27–28, 2004.

[99] A. Yamamoto, "Applications of electrostatic actuators within special environments," *Next-generation Actuators Leading Breakthroughs*, pp. 363–373, 2010.

[100] K. Amano and A. Yamamoto, "Tangible interactions on a flat panel display using actuated paper sheets," *ITS 2012 - Proceedings of the ACM Conference on Interactive Tabletops and Surfaces*, pp. 351–354, 2012.

[101] T. Hosobata, A. Yamamoto, and T. Higuchi, "2-dof synchronous electrostatic actuator with transparent electrodes arranged in checkerboard patterns," *IEEE Int. Conf. on Intelligent Robots and Systems*, pp. 6 697 066, 4919–4924, 2013.

[102] R. Iguchi, T. Hosobata, and A. Yamamoto, "Transparent electron.ctrostatic actuator with mesh-structured electron.ctrodes for driving tangible icon in tabletop interface," in *Proc. of the 2014 ACHI Int. Conf. on Advances in Computer-Human Interactions.* IARIA, 2014, pp. 288–293.

[103] N. Yamashita, K. Amano, and A. Yamamoto, "Interaction with real objects and visual images on a flat panel display using three-dof transparent electron.ctrostatic induction actuators," in *Proc. of the 2014 ACHI Int. Conf. on Advances in Computer-Human Interactions.* IARIA, 2014, pp. 294–299.

[104] R. Iyer and X. Tan, "Control of hysteretic systems through inverse compensation," *Control Systems, IEEE*, vol. 29, no. 1, pp. 83–99, Feb 2009.

[105] M. W. Hooker, "Properties of pzt-based piezoelectric ceramics between -150 and 250 c," 1998.

[106] D. Wang, Y. Fotinich, and G. Carman, "Influence of temperature on the electromechanical and fatigue behavior of piezoelectric ceramics," *Journal of Applied Physics, J. Appl. Phys, J Appl Phys, Jap*, vol. 83, no. 10, pp. 5342–5350, 1998.

[107] R. Iyer, X. Tan, and P. Krishnaprasad, "Approximate inversion of the preisach hysteresis operator with application to control of smart actuators," *Automatic Control, IEEE Transactions on*, vol. 50, no. 6, pp. 798–810, June 2005.

[108] T. Jordan, Z. Ounaies, J. Tripp, and P. Tcheng, "Electrical properties and power considerations of a piezoelectric actuator," in *MRS Proceedings*, vol. 604. Cambridge Univ Press, 1999, p. 203.

[109] K. S. Meyer, M. A. E. Andersen, and F. Jensen, "Parameterized analysis of zero voltage switching in resonant converters for optimal electrode layout of piezoelectric transformers," *PESC Rec. IEEE Annu. Power Electron. Spec. Conf.*, pp. 4 592 323, 2543–2548, 2008.

[110] M. Ekhtiari, E. Bruun, M. A. E. Andersen, and Z. Zhang, "Bi-directional high-side current sense circuit for switch mode power supplies," *Proceedings of 29th Ann. IEEE Appl. Power Electron. Conf. and Expo.*, pp. 630–633, 2014.

[111] E. Salbu, "Compressible squeeze films and squeeze bearings," *Journal of Basic Engineering*, vol. 86, no. 2, pp. 355–364, 1964.

A

Piezoelectric stack actuator parameter extraction with hysteresis compensation

2014 IEEE 16th European Conference on Power Electronics and Applications (EPE'14-ECCE Europe)

Piezoelectric stack actuator parameter extraction with hysteresis compensation

Tiberiu-Gabriel Zsurzsan[1],Charles Mangeot[2],
Michael A.E. Andersen[1],Zhe Zhang[1],Nils A. Andersen[1]

[1]Technical University of Denmark
Oersteds Plads, building 349
Kgs. Lyngby, Denmark
Phone: +45 45 25 34 81
Email: tgzsur@elektro.dtu.dk
URL: http://www.ele.elektro.dtu.dk

[2]Noliac A/S
Hejreskovvej 18
Kvistgaard, Denmark
Phone: +45 49 12 50 34
Email: cm@noliac.com
URL: http://www.noliac.com

Keywords

<<Piezo actuators>>, <<Non-standard electrical machine>>, <<Servo-drive>>, <<Regulation>>, <<Measurement>>.

Abstract

The Piezoelectric Actuator Drive (PAD) is a type of rotary motor that transforms the linear motion of piezoelectric stack actuators into a precise rotational motion. The very high stiffness of the actuators employed make this type of motor suited for open-loop control, but the inherent hysteresis exhibited by piezoelectric ceramics causes losses.

Therefore, this paper presents a straightforward method to measure piezoelectric stack actuator equivalent parameters that includes nonlinearities. By folding the nonlinearities into a newly-defined coupling coefficient, the inherent hysteretic behavior of piezoelectric stack actuators can be greatly reduced through precompensation. Experimental results show a fitting accuracy of 98.8 % between the model and measurements and a peak absolute error reduction by a factor of 10 compared to the manufacturer-provided parameter. This method improves both the static and dynamic performance of the Piezoelectric Actuator Drive (PAD) while still permitting open-loop control.

Introduction

Piezoelectric stack actuators are widely used in applications ranging from rotary motors [1] and micropumps [2] to structural vibration damping [3]. Their advantage lies in very high stiffness and larger deflections (100 μm range), while reducing applied voltage levels compared to their bulk ceramic counterparts.

Often, the stack datasheets only provide information limited to free displacement and blocking force, maximum applied voltage range, travel range and piezoelectric material constants such as d coefficients,

s coefficients and coupling (k) coefficient. This gives no indication about the highly hysteretic behavior present between the mechanical and electrical parameters that the stacks exhibit [4]. This behavior limits usage of piezoelectric stacks in applications where precise dynamic operation is required without positional feedback possibilities.

A type of rotary motor that converts periodic elongation of piezoelectric stack actuators into precise rotational motion of a rotor is the Piezoelectric Actuator Drive (PAD). The operating principle is illustrated in Figure 1. The micro-mechanical toothing present in the ring and shaft enables high positioning accuracy and output torque. This type of toothing combined with the inherent large stiffness of the piezoelectric stack actuators makes the PAD appropriate for voltage-driven open-loop control [5]. Nonetheless, the hysteresis effects inherently present in the stack actuators are detrimental to efficient open-loop operation.

Therefore the paper presents a simple method for measurement and identification of the nonlinear piezoelectric one-dimensional bulk equivalent parameters in a piezoelectric stack actuator along its actuation dimension. The piezoelectric parameters' extraction is based on the quasi-static measurement method, due to its simplicity and comparable accuracy to other methods [6]. The accuracy of the achieved nonlinearity compensation is verified against measurements.

Piezoelectric stack actuator and model

Figure 2 shows the typical structure of a piezoelectric stack actuator. The stack can be considered to comprise hundreds of individual piezoelectric layers separated by thin electrodes. These layers are in a parallel configuration electrically, enabling a reduced voltage level to produce the necessary electric field. Mechanically, they are in a series configuration and therefore the elongation of each layer adds up to produce larger displacement than a single element would.

A widely-used model for piezoelectric structures is described in the IEEE Standard on Piezoelectricity [7], but this model does not inherently take nonlinear behavior into consideration. Other models exist that take nonlinearities into consideration [8], [9], but these separate the linear piezoelectric and hysteretic components. Moreover, these models require intimate knowledge of all the physical properties of the stacked actuator such as number and thickness of the layers, active area and number of inactive layers. This information is usually not provided by manufacturers.

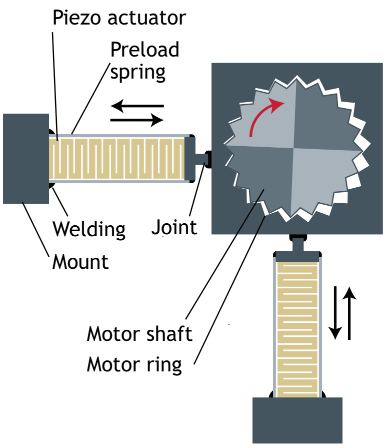

Fig. 1: Piezo Actuator Drive (PAD) principle [1]

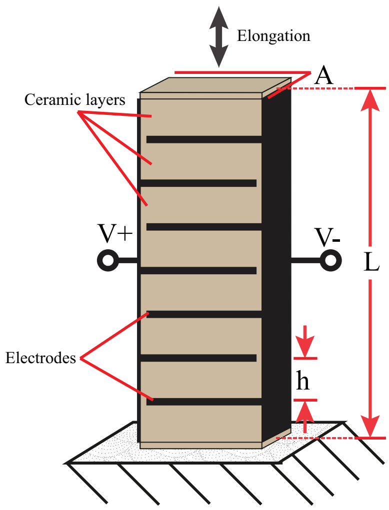

Fig. 2: Diagram of a piezoelectric stack actuator. A, L and h represent the stack's surface area, length and layer height, respectively

Equations (1) and (2) represent the second alternative form of the constitutive equations given by the IEEE Standard [7], particularized for direction 3, which is the dimension of actuation for a stack actuator, assuming no stress in other directions. Table I shows the quantities, their names and their units of measurement.

$$S_3 = d_{33} \cdot E_3 + s_{33}^E \cdot T_3 \tag{1}$$

$$D_3 = d_{33} \cdot T_3 + \epsilon_{33}^T \cdot E_3 \tag{2}$$

Although the constitutive equations presented in (1) and (2) are widely recognized [7], they can be rewritten to couple easily measurable quantities by substituting S, D, E and T with their definition in (3) – (6).

$$S = \frac{\Delta x}{L} \tag{3}$$

$$D = \frac{q}{A} \tag{4}$$

$$E = \frac{V}{h} \tag{5}$$

$$T = \frac{F}{A} \tag{6}$$

Table II presents the redefinition of the quantities presented in the constitutive equations. Based on these and (3) – (6) and considering that strain is measured in conditions of no stress and that dielectric displacement (charge) is measured with no applied electrical field, the constitutive piezoelectric equations can be simplified to (7) – (8).

$$\Delta x = n \cdot d_{33} \cdot V \quad |_{T_3=0} \tag{7}$$

$$Q = n \cdot d_{33} \cdot F \quad |_{E_3=0} \tag{8}$$

Where $n = L/h$ is the number of piezoelectric layers inside the stack and $Q = n \cdot q$ denotes the total stack charge. While the physical quantities of surface area and stack length can be easily measured, the number

Table I: List of constitutive equation symbols and their units

Symbol	Name	SI Unit
S_3	Strain component	
D_3	Electric displacement component	C/m^2
E_3	Electric field component	V/m
T_3	Stress component	N/m^2
d_{33}	Piezoelectric constant	m/V or C/N
s_{33}	Elastic comliance constant	m^2/N
ϵ_{33}	Permittivity constant	F/m

Table II: Redefined constitutive equation symbols and their units

Symbol	Name	SI Unit
Δx	Displacement	m
q	Layer charge	C
V	Applied voltage	V
F	Applied force	N
A	Stack active surface area	m^2
L	Stack active height	m
h	Stack layer height	m

of active piezoelectric layers inside the stacks is not usually disclosed. The only way to find the internal layer structure is by destructive dissection, which renders the stack useless. The method proposed in this paper circumvents this problem by folding the actuator physical properties into the coupling factor d_{33}. Therefore, a new piezoelectric coefficient is defined in (9).

$$D_{33} = n \cdot d_{33} \tag{9}$$

This coefficient is now directly measurable and better represents the electrical-mechanical or mechanical-electrical coupling inside a given piezoelectric stack. The disadvantage of this redefinition is that unlike d_{33}, which is material-specific, D_{33} is now specific to material and structural composition. Moreover, access to the stack is required before it is embedded in an application. In a small-scale usage scenario, this drawback is negligible when only a few stacks need to be characterized.

Measurement setup

In order to measure the piezoelectric equivalent parameters, the piezoelectric stack under test is connected to a power amplifier with a reference signal input. The amplifier is fed by a signal generator with a 0.1 Hz sine wave reference. The output of the amplifier is a sinusoidal voltage with a 110 V_{DC} bias and 90 V amplitude. This produces a quasi-sinusoidal displacement ranging between 3 μm and 35 μm, measured by an LVDT probe connected to a gage amplifier. All data is acquired through data acquisition card to a PC and post-processed using MATLAB. The mock-up of the measurement setup can be seen

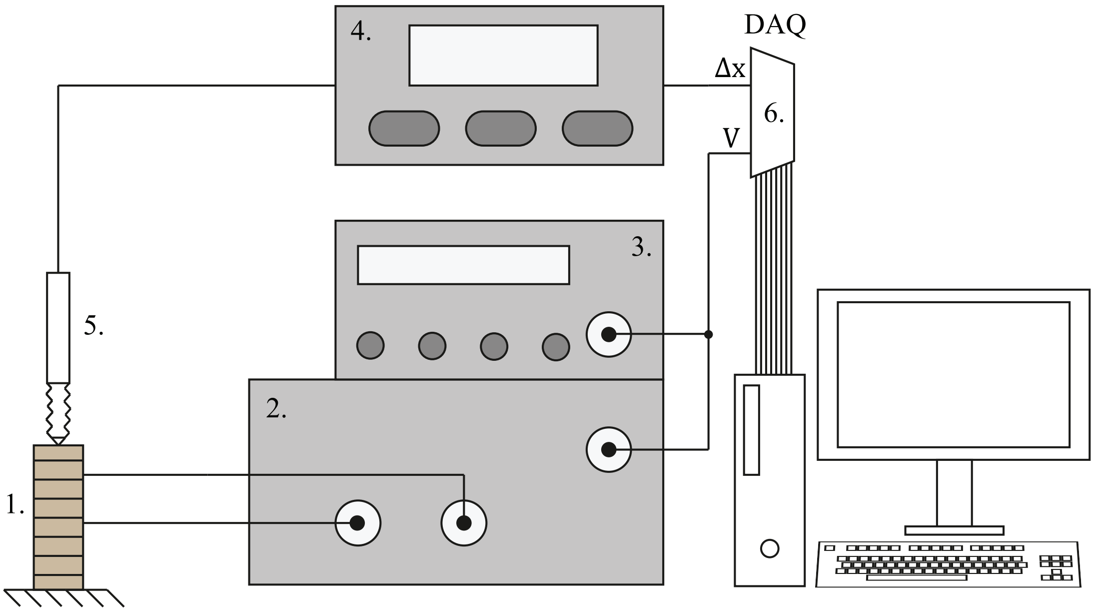

Fig. 3: Mock-up of the measurement setup

Table III: Devices in the measurement setup

Item	Name	Model
1	Piezoelectric stack under test	-
2	Power amplifier	Noliac NDR6880
3	Signal generator	Agilent 33250A
4	Gauge amplifier	TESA Tesatronic TT60
5	LVDT probe	TESA S32080861
6	Data acquisition board	Measurement Computing PCI-DAS6014

in Figure 3, while Table III provides the names and manufacturer models of the devices used.

Hysteresis compensation and experimental results

Figure 4 illustrates a typical piezoelectric stack hysteretic behavior between applied voltage and measured free displacement. This means that the $\Delta x - V$ characteristic is nonlinear and open loop positioning repeatability cannot be guaranteed without nonlinearity compensation.

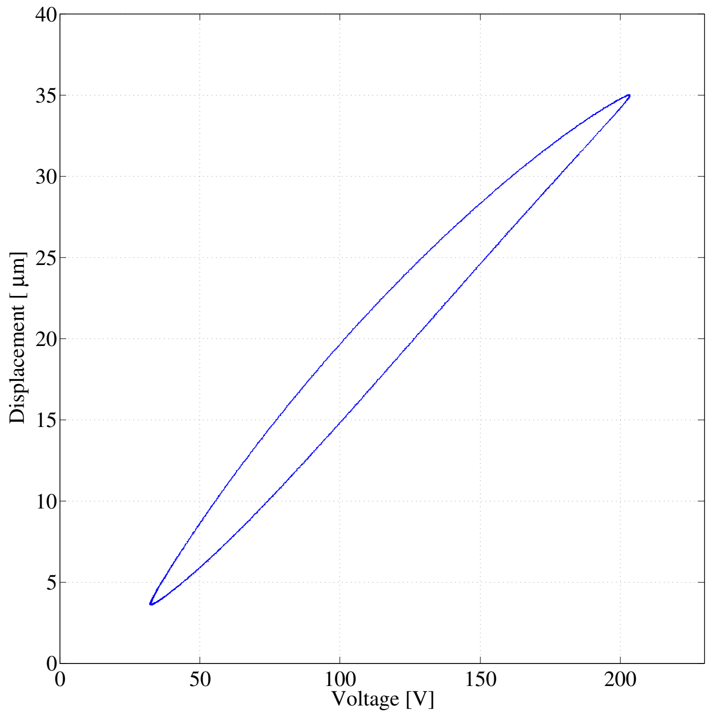

Fig. 4: Stack hysteretic behavior between applied voltage and measured displacement

The proposed solution for this compensation consists in encapsulation of the nonlinearities into the defined D_{33} coefficient. The quasi-static measurement method is used by applying a sinusoidal voltage input and measuring the output displacement. Piecewise discretization and differentiation of the obtained hysteresis curve yields a vector of slopes representing D_{33} in a nonlinear form, as shown in (10). Linear interpolation of the obtained vector gives a piecewise linear approximation of the hysteretic behavior.

$$D_{33} = \frac{\mathrm{d}(\Delta x)}{\mathrm{d}V} \tag{10}$$

Figure 5 shows good matching between the measured and compensated displacement values, as opposed to the uncompensated response which shows large deviation from measured values. The detail view shows slight mismatching at the waveform minima, attributed to presence of a small friction in the displacement measurement probe. The effect of the compensation on the hysteresis loop can be seen in Figure 6. The compensated behavior is approximately linear compared to the uncompensated one.

The relative error graph, calculated as the ratio between the absolute error and instantaneous measured value, is shown in Figure 7. While the uncompensated response shows a peak relative error of 21.3 %, this peak is reduced through compensation to 9.1 %. Moreover, the nonlinear model fits the measurements in proportion of 98.9% on average. As shown in Figure 8, the maximum absolute error sees a reduction by a factor of 10, from 3.6 μm to 0.36 μm.

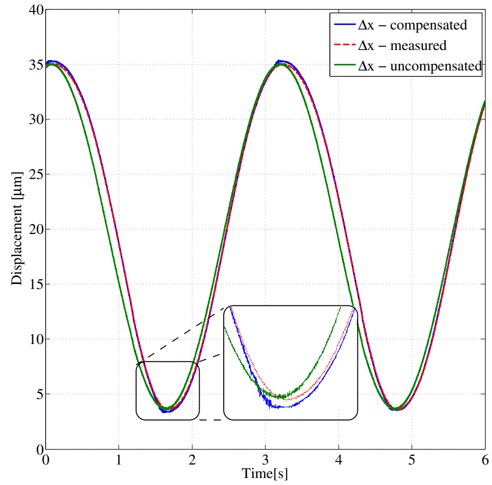

Fig. 5: Dynamic behavior of compensated, uncompensated and measured displacements

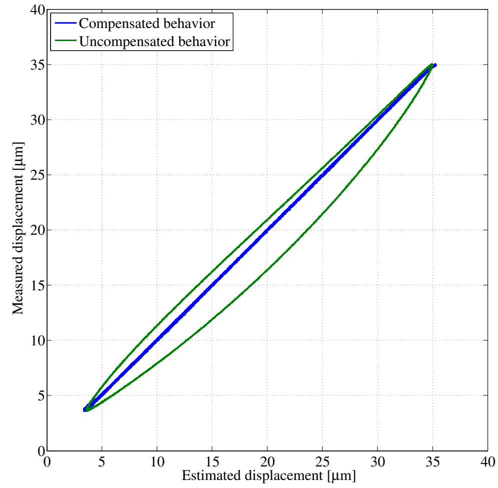

Fig. 6: Hysteresis compensation

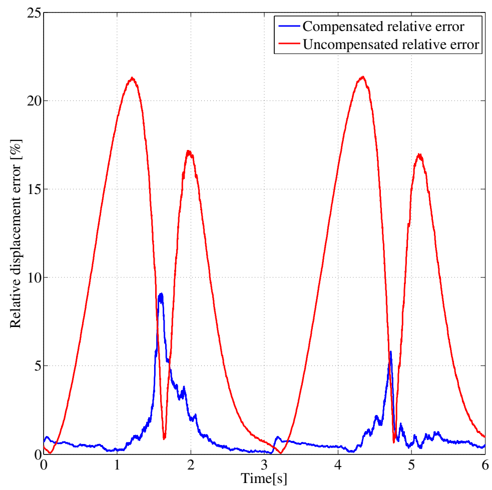

Fig. 7: Relative error comparison

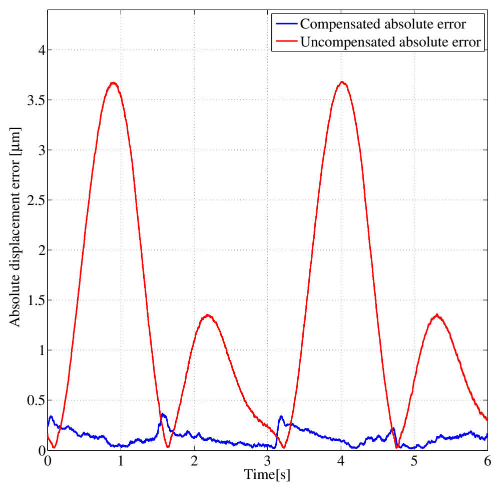

Fig. 8: Absolute error comparison

Conclusion

This paper presents a straightforward method for piezoelectric equivalent parameters measurement for a multilayer piezoelectric stack. The effective piezoelectric constant is redefined to include both nonlinearities and stack structural information. The nature of this result enables real-time hysteresis compensation after initial characterization. By inherently acting as a look-up table, this approach is both fast and requires little to no processing power and is therefore embedded processor friendly. Therefore, the proposed method is ideal for use in conjunction with the PAD, yielding an improved static and dynamic behavior of the motor during open-loop operation.

The results obtained show a good fit with experimental measurements and a large improvement over the parameters provided on the datasheet. The maximum absolute error is reduced through nonlinear compensation by a factor of 10 compared to the uncompensated case. Therefore, the dynamic performance of the piezoelectric stack is greatly increased and performance in piezoelectric applications where feedback is not available is improved.

References

[1] C. Wallenhauer, B. Gottlieb, A. Kappel, T. Schwebel, J. Rucha, and T. Lueth, “Accurate load detection based on a new piezoelectric drive principle employing phase-shift measurement,” *Journal of Microelectromechanical Systems*, vol. 16, no. 2, pp. 344–350, 2007.

[2] X. Li, Y. Liu, G. Liu, J. Liu, and X. Sun, “Experiment on dual-chamber parallel piezoelectric stack pump for electrorheological fluids,” *2011 IEEE International Conference on Mechatronics and Automation, ICMA 2011*, pp. 842–846, 2011.

[3] J. M. Rodriguez-Fortun, J. Orus, J. Alfonso, F. Buil Gimeno, and J. A. Castellanos, “Flatness-based active vibration control for piezoelectric actuators,” *IEEE-ASME Transactions on Mechatronics*, vol. 18, no. 1, pp. 221–229, 2013.

[4] L. Juhasz, J. Maas, and B. Borovac, “Parameter identification and hysteresis compensation of embedded piezoelectric stack actuators,” *Mechatronics*, vol. 21, no. 1, pp. 329–338, 2011.

[5] R. Zeichfussl, B. Gottlieb, C. Wallenhauer, S. Herzig, A. Kappel, and T. Luth, “A method for auto-adjustment of a new piezoelectric drive,” in *Mechatronics, 2009. ICM 2009. IEEE International Conference on*, April 2009, pp. 1–6.

[6] J. Fialka and P. Benes, “Comparison of methods for the measurement of piezoelectric coefficients,” *IEEE Transactions on Instrumentation and Measurement*, vol. 62, no. 5, pp. 1047–1057, 2013.

[7] “Standard on piezoelectricity,” *IEEE*, 1988.

[8] H. Adriaens, W. de Koning, and R. Banning, “Modeling piezoelectric actuators,” *IEEE-ASME Transactions on Mechatronics*, vol. 5, no. 4, pp. 331–341, 2000.

[9] Y. Chen, Y. Wen, and P. Li, “Characterization of dissipation factors in terms of piezoelectric equivalent circuit parameters,” *IEEE Transactions on Ultrasonics, Ferroelectrics and Frequency Control*, vol. 53, no. 12, pp. 2367–2375, 2006.

B

Preisach model of hysteresis for the Piezoelectric Actuator Drive

2015 41st Annual Conference of the IEEE Industrial Electronics Society (IECON 2015)

IECON2015-Yokohama
November 9-12, 2015

Preisach model of hysteresis for the Piezoelectric Actuator Drive

Tiberiu-Gabriel Zsurzsan, Michael A.E. Andersen, Zhe Zhang, Nils A. Andersen
DTU Electrical Engineering
Technical University of Denmark
Oersteds Plads, bld. 349
Kgs. Lyngby, Denmark
Email: tgzsur@elektro.dtu.dk

***Abstract* — The Piezoelectric Actuator Drive (PAD) is a precise piezoelectric motor generating high-torque rotary motion, which employs piezoelectric stack actuators in a wobble-style actuation to generate rotation. The piezoelectric stacked ceramics used as the basis for motion in the motor suffer from hysteretic nonlinearities. In order to model these nonlinearities, the first-order hysteresis reversal curves of the actuators are measured and a discrete Preisach model is derived. This forms a basis that enables the study of different compensation methods. The results show matching between measured and estimated responses within 95.8%**

Keywords* — *motor, actuator, piezoelectric, stack, multilayer, hysteresis, model, Preisach

I. INTRODUCTION

The Piezoelectric Actuator Drive (PAD) shown in Fig. 1 is a type of rotary motor that transforms the linear motion of piezoelectric stack actuators into a precise rotation [1]. The operating principle, illustrated in Fig. 2, is based on a wobble-style motor, where the motor ring is actuated into an off-center circular motion around an axially constrained shaft, thereby generating rotational motion. A micro-mechanical toothing interface is machined between the ring and shaft, as shown in Fig. 3. This enables both high positioning accuracy and output torque [2]. The actuation method, combined with the type of toothing and the inherent large stiffness of the piezoelectric stack actuators makes the PAD appropriate for open-loop control [3].

By construction, the PAD motor behaves like a fully capacitive rotary machine, due to the piezoelectric stack actuators it employs. These actuators exhibit desirable properties such as large stiffness and a reversibility of the piezoelectric effect, enabling them to act as both actuators and sensors [4]. Nevertheless, two dominating nonlinearities persist in the control of piezoelectric-based actuation, namely hysteresis and creep [5]. Of the two effects, hysteresis has a much larger impact on the positioning precision of the motor, especially under dynamic operation. The purpose of this paper is to model this effect in order to correctly predict the response of the PAD.

Modeling hysteresis in the piezoelectric motor is a necessary step in developing compensation methods to negate the effects. The most encountered method of modeling hysteresis in literature remains the Preisach-Krasnoselskii scalar model [6], which provides a straightforward method of representing the hysteretic effect. Although initially developed for the purpose of modeling magnetic hysteresis, due to its fenomenological nature, the method can be used to model any type of hysteresis [7]. This fact, combined with the generally predictable performance has led the Preisach model to be the preferred method used when hysteresis is involved.

Fig. 1: The Piezoelectric Actuator Drive (PAD)

Many modifications and improvements to the original model have been proposed, such as accounting for dynamic input changes [8], [9] or reducing the computational complexity by simplifying the parameter identification process [10]. For this paper, simplicity and real-time execution are the most important factors in determining the method used. Therefore, the classical model enhanced with Mayergoyz's observations on determining the Everett function from the first-order inverting loops [6], [11] is chosen. The paper starts by presenting the underlying principle of the classical Preisach model in section II, followed by a short description of the experimental set-up and tests performed in section III. The model response is then compared to experimental measurements in Section IV, after which the conclusion is presented in section V.

II. THE CLASSICAL PREISACH MODEL

The idea behind the classical scalar Preisach model consists of describing the hysteretic effect through the use of an

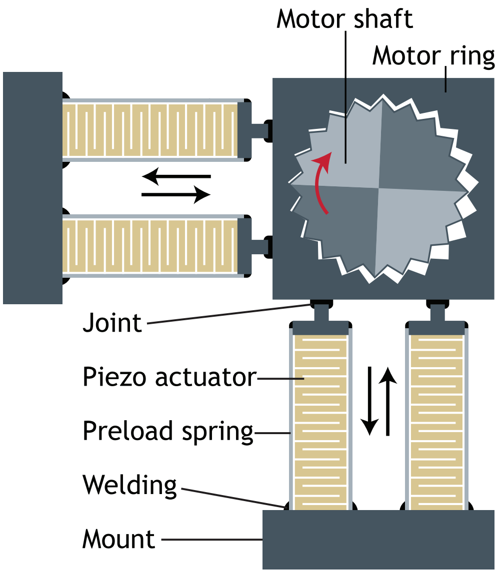

Fig. 2: PAD operating principle

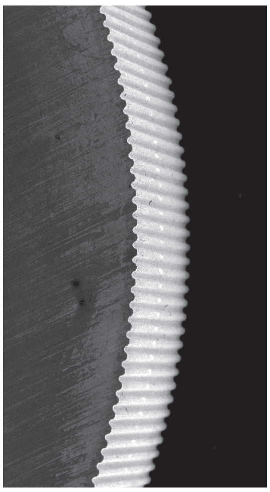

Fig. 3: Microtoothing on the motor shaft. Tooth distance is 120 µm and depth is 38 µm

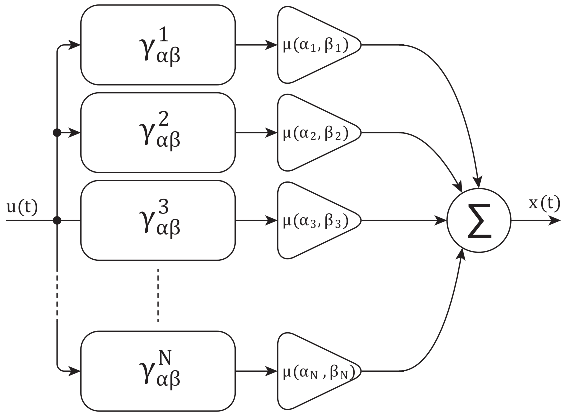

Fig. 4: Parallel connection of elementary Preisach hysterons with weighting gains

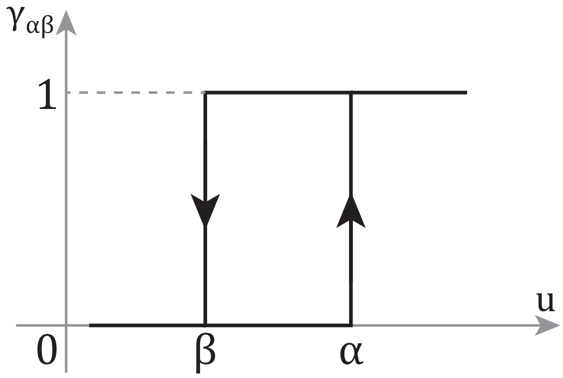

Fig. 5: The elementary Preisach hysteron with thresholds α and β. The arrows represent one-way state transitions

infinite number of parallel-connected relay-type two-state discontinuous operators $\gamma_{\alpha\beta}[u(t)]$, called basic hysterons. These elements represent relay-like loops on the input-output plane with two values, α and β, acting as the 'on' and 'off' thresholds, with $\beta \leq \alpha$. When the input signal $u(t)$ becomes greater than α, the output of the operator becomes 'high' and goes to 'low' state only when the input becomes less than β. In between tresholds, the previous value is retained. More explicitly, in the case of piezoelectric devices this can be written mathematically as

$$\gamma_{\alpha\beta}[u(t)] = \begin{cases} 0 & u(t) \leq \beta; \\ \gamma_{\alpha\beta}[u(t)] & \beta \leq u(t) \leq \alpha; \\ 1 & u(t) \geq \alpha. \end{cases} \tag{1}$$

This representation of the basic hysteretic operator, represented graphically in Fig. 5, is in agreement with the property of a hsyteretic system where the output depends not only on the input, but past values of the input as well. In other words, hysteresis is a nonlinearity with a non-local memory effect.

In order to be able to reproduce a wide range of hysteresis curves, the outputs of the basic hysterons are then weighted with an experimentally-determined weighting function $\mu(\alpha,\beta)$. Determining this function represents the major challenge in deriving and using the Preisach hysteresis model.

The structural block diagram of the Preisach model is shown in Fig. 4. It illustrates the parallel connection and weighting of individual elementary hysterons, whose sum produces the instantaneous output. Mathematically, this is expressed as

$$x(t) = \iint\limits_{\alpha \geq \beta} \mu(\alpha,\beta)\gamma_{\alpha\beta}[u(t)]\,\mathrm{d}\alpha\,\mathrm{d}\beta \tag{2}$$

where $u(t)$ is the voltage input to the piezoelectric actuator, $x(t)$ represents the output displacement, $\mu(\alpha,\beta)$ is the experimentally-obtained weighting function and $\gamma_{\alpha\beta}[u(t)]$ is the hysteron state.

A geometrical interpretation of the hysteron plane (also called the $\alpha-\beta$ plane) greatly facilitates the understanding of (2) and the Preisach model in general. In this plane, a so-called

Preisach triangle T_0 is defined, which represents the region of operation of the actuator, bordered by $\alpha_{max}, \beta_{max}, \alpha_{min}$ and β_{min}. Only the surface above the diagonal given by $\alpha = \beta$ has any physical meaning and therefore T_0 is an upper triangular surface. The elementary hysterons $\gamma_{\alpha\beta}[u(t)]$ have a direct correlation to the $\alpha - \beta$ half-plane in such a way that at any point in time T_0 is divided into two surfaces S^+ and S^-, representing the (α, β) pairs for which $\gamma_{\alpha\beta}[u(t)] = 1$ or 0, respectively. This is in stark contrast to the method being applied to describe magnetic hysteresis, where in order to wipe out the magnetization, a negative input has to be applied. In other words, in piezoelectric phenomena a lack of excitation field results in a zero net output.

Thereby, for a monotonic increase of the input $u(t)$, the input-output plane shows an ascending hysteresis branch, while the $\alpha - \beta$ half-plane 'fills up' from the bottom to the horizontal line defined by $\alpha = \{\alpha_1 | \alpha_1 \leq u(t)\}$. Similarly, a monotonic decrease in input will then determine the surface to 'empty', but this process is orthogonal to the one for increasing input. Therefore the 'filled' space T_0 will empty starting from the right towards the vertical line defined by $\beta = \{\beta_1 | \beta_1 \geq u(t)\}$. Thereby a stochastic input signal with several extrema will be represented as a combination of 'filled' and 'emptied' areas on the triangle, delimited by a boundary staircase layer, denoted L. The problem then boils down to finding the area under the obtained staircase curve. This process is visually exemplified in Fig. 6.

An important property of the Preisach model is the wipe-out feature, whereby the input history is erased when the input increases above (or decreases below) the previous points of extrema. Specifically, in Fig. 6d if the input were to increase beyond α_1, then the pair (α_1, β_2) would be removed from the history. Visually, the corner represented by (α_1, β_2) on the half-plane would be 'engulfed' by the vertically increasing S^+ surface. In time domain, this coincides with $u(t)$ increasing in amplitude beyond its previous extremum. This feature is important in order to prevent excessive history growth.

Using the presented geometric interpretation, the Preisach model (2) can be rewritten as

$$x(t) = \iint\limits_{S^+} \mu(\alpha, \beta) \gamma_{\alpha\beta}[u(t)] \, \mathrm{d}\alpha \, \mathrm{d}\beta + \iint\limits_{S^-} \mu(\alpha, \beta) \gamma_{\alpha\beta}[u(t)] \, \mathrm{d}\alpha \, \mathrm{d}\beta \tag{3}$$

Considering that in the case of piezoelectric actuators $\gamma_{\alpha\beta}[u(t)] = 0|_{u(t) \leq \beta}$ and $\gamma_{\alpha\beta}[u(t)] = 1|_{u(t) \geq \alpha}$, (3) can be reduced to

$$x(t) = \iint\limits_{S^+} \mu(\alpha, \beta) \, \mathrm{d}\alpha \, \mathrm{d}\beta \tag{4}$$

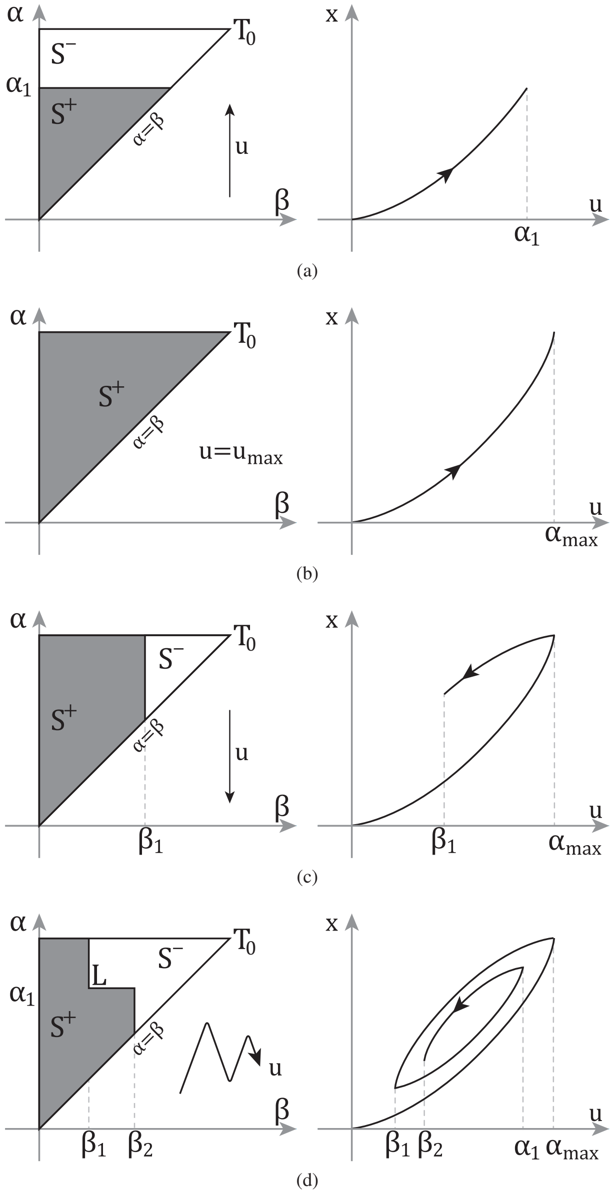

Fig. 6: Representation of the Preisach triangle, with examples for increasing (a), maximum (b), decreasing (c) and progressively decreasing amplitude (d) triangular input and their respective surface divisions.

The next step in completing the Preisach hysteresis model is determining the $\mu(\alpha, \beta)$ weighting function. This is done more easily by using the system's first-order reversal curves, shown in Fig. 7a, to construct the describing Everett function [12], thereby eliminating the computationally-intensive double integration. A term denoted with x_α is defined as the piezoelectric expansion on the limiting ascending branch of the hysteresis curve corresponding to an input value of α and, similarly, $x_{\alpha\beta}$ is defined as the expansion on the descending branch that starts at the previous x_α. Hereby, the Everett function is defined as

$$X(\alpha, \beta) = \frac{1}{2}(x_\alpha - x_{\alpha\beta}) \tag{5}$$

By choosing two arbitrary points x_α and $x_{\alpha\beta}$ as shown in Fig. 7b and expressing them in terms of Preisach equation, the geometric interpretation of the Everett function shows that:

$$x_\alpha = \iint\limits_{S^+ + T_1} \mu(\alpha, \beta) \, \mathrm{d}\alpha \, \mathrm{d}\beta \tag{6}$$

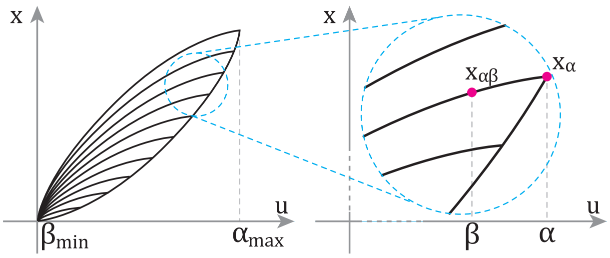

(a)

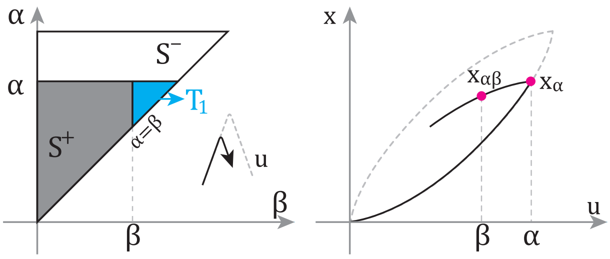

(b)

Fig. 7: First-order reversal curves used to construct the Everett function (a) and an example of obtaining the function together with the graphical interpretation (b). The surface T_1 represents the difference in S^+ when the input decreases from α to β.

$$x_{\alpha\beta} = \iint\limits_{S+} \mu(\alpha,\beta)\,\mathrm{d}\alpha\,\mathrm{d}\beta \tag{7}$$

(8)

Now by rewriting (5) and taking (7) and (6) into account while considering that the double integral over the total surface $S^+ + T_1$ is equal to the sum of the integrals over each surface, $X(\alpha,\beta)$ becomes:

$$X(\alpha,\beta) = \frac{1}{2}\iint\limits_{T_1} \mu(\alpha,\beta)\,\mathrm{d}\alpha\,\mathrm{d}\beta \tag{9}$$

This shows that the Everett function represents the double integral of the weighting function over a component surface. Finding the actual weighting function $\mu(\alpha,\beta)$ requires a double differentiation of the measured sum of Everett functions, but doing that with noisy, experimental data introduces even more noise and might render the result unusable. Therefore, it is more convenient to now introduce the discrete Preisach model and re-express the initial formulation shown in (2) to include the Everett terms [8]. By considering an N number of memorized extrema, the piezoelectric expansion becomes:

$$x(t) = \begin{cases} X(u(t),\beta_N)+ \\ +\sum\limits_{i=1}^{N}(X(\alpha_i,\beta_{i-1})-X(\alpha_i,\beta_i)) & \dot{u}(t) > 0; \\ X(\alpha_N,\beta_{N-1})-X(\alpha_N,u(t))+ \\ +\sum\limits_{i=1}^{N}(X(\alpha_i,\beta_{i-1})-X(\alpha_i,\beta_i)) & \dot{u}(t) < 0. \end{cases} \tag{10}$$

In order to obtain the values needed for each Everett function,

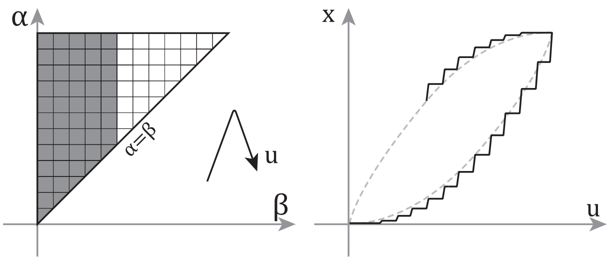

Fig. 8: Division of the Preisach plane into $N = 12$ equally-distanced values for α and β, and the resulting 12 discrete levels obtained on the hysteresis curve.

and consequently the discrete Preisach model, the previously-defined limiting triangle T_0 is now split up into a mesh containing values for the point pairs $\{(\alpha_i,\beta_j)|i = 1..N, j = i..N\}$. Fig. 8 shows the geometrical interpretation of the discrete Preisach plane on the left hand side, together with the obtained input-output representation on the right-hand side, for an arbitrary value of $N = 12$. The number of α and β values equals the number of discrete steps on the hysteresis curve. Naturally, the higher N is chosen, the finer the mesh becomes and consequently, the finer the hysteresis representation will become. This is at the expense of exponentially increasing memory requirements to store all the values.

III. Experimental Set-up

Through (10), a theoretical basis for modeling hysteresis in piezoelectric actuators is set. The PAD motor employs four piezoelectric stack actuators in order to generate rotational motion, as presented in Fig. 2. In order to be able to model the effects of hysteresis in the motor, the first-order reversal curves of these actuators have to be measured and the corresponding Preisach plane needs to be created. To accomplish this, an experimental set-up that can measure these parameters was built.

The experimental setup is presented in Fig. 9 and consists of a computer with a dSPACE single-board PCI system, a linear voltage amplifier and a laser displacement sensor. The laser sensor is a Keyence LC-2440 sensor head connected to a Keyence LC-2400 controller. The measurement system has measuring range of ±3 mm, maximum resolution of 0.2 µm and a bandwidth of 20 kHz. The unit under test is a Noliac custom piezoelectric stack actuator laser-welded into a spring-load casing with 750 N preloading. The actuator is rated for 200 V input voltage, producing a maximum elongation of 60 µm.

A Matlab script is used to produce a positively biased receding sawtooth waveform which is then amplified and drives the actuator. The waveform is adjustable in time, envelope slope and number of teeth. This type of waveform is chosen in order to eliminate the effects of creep while keeping all hysteresis information intact. Data acquisition of the position value is then performed and all data is stored into Matlab for processing.

IV. Measurements and Results

In order to identify the Preisach model and build the $\alpha - \beta$ plane, the first-order reversal curves are measured for a

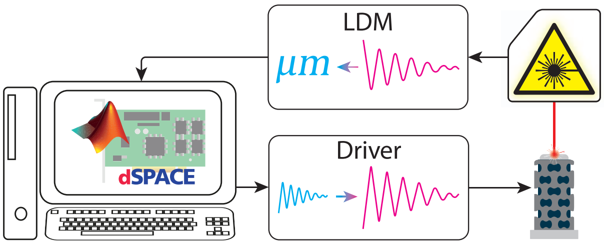

Fig. 9: Block diagram of the experimental set-up. A computer equipped with a PCI dSPACE board is used. The signal generated is amplified through a voltage amplifier. The unit under test is a Noliac custom piezoelectric stack actuator. Elongation is measured using a Keyence LC-2440 laser sensor connected to a Keyence LC-2400 laser displacement meter (LDM).

single piezoelectric actuator from the four. The other actuators are assumed to be identical with the measured one. This assumption is reasonable, within the fabrication tolerances of the actuators themselves but it will of course impact the model accuracy.

Fig. 10a shows the receding sawtooth voltage signal applied to the stack actuator, as measured from the output of the voltage amplifier. The frequency of the signal is 0.5 Hz, it has a length of 50 periods and a linear recession slope of −2 V per period. The low frequency is chosen so that the dynamic properties of the actuator do not affect its response.

The measured displacement of the actuator corresponding to the input voltage is shown in Fig. 10b. It has the same frequency and length as the input signal, but the envelope of the recession shows an exponential response with a sub-unitary exponent, instead of the linear recession seen in the voltage signal. The glitches present in the signals at around the 45 second mark are the result of the measurement system buffer overflowing and missing some samples. A new set of measurements needs to be carried out with special attention to acquisition buffer size and amount of data.

Nevertheless, the response estimated by the developed model is in good agreement with the measured response. Fig. 11 shows a comparison between the real and modeled displacements for an applied voltage signal swinging between 31 V-173 V-33 V-171 V. This specific input voltage swing was chosen at random out of the ranges for which measurements exist, so as to be able to evaluate the model response. The relative error plot in Fig. 11c illustrates that the model response matches the measurements within 95.8%. Therefore the model correctly estimates the actuator's exponential displacement response as a direct result of the triangular input excitation.

V. Conclusions

This paper models the effects of hysteresis in the piezoelectric stack actuators that make up the Piezoelectric Actuator Drive motor. A discrete Preisach model was chosen due to its popularity as a hysteresis modeling tool, relative simplicity and ease of implementation. The model was built based on the measurement of 50 hysteresis reversal curves, from which the corresponding Everett functions were extracted. Validation against a randomly-chosen input variation was done. Finally, the developed and implemented discrete Preisach model allows estimating the displacement of the stacks within the motor with a relative accuracy of 95.8% and serves as a good starting point for studying and developing different compensation algorithms that are able to eliminate hysteresis.

Future work will focus both on deriving an inverse model for compensation, as well as studying improvements to the developed model. Increasing the number of reversal curves measured to obtain higher accuracy, as well as investigating the effects of higher frequency dynamics on the model are being considered.

Acknowledgements

The authors would like to thank Noliac A/S for providing a PAD motor to be dissected and investigated, as well as the Danish National Advanced Technology Foundation for financial support.

References

[1] A. Kappel, B. Gottlieb, and C. Wallenhauer, "Piezoelectric actuator drive (pad)," *AT-AUTOMATISIERUNGSTECHNIK*, vol. 56, no. 3, pp. 128–135, 2008.

[2] J. Rucha, H. Liess, J. Heinzl, A. Kappel, T. Schwebel, and B. Gottlieb, "Applicability of a piezo actuator drive as a sensorless high precision drive," *10th International Conference on New Actuators*, 2006.

[3] R. Zeichfussl, B. Gottlieb, C. Wallenhauer, S. Herzig, A. Kappel, and T. Luth, "A method for auto-adjustment of a new piezoelectric drive," in *Mechatronics, 2009. ICM 2009. IEEE International Conference on*, April 2009, pp. 1–6.

[4] C. Wallenhauer, B. Gottlieb, A. Kappel, T. Schwebel, J. Rucha, and T. Lueth, "Accurate load detection based on a new piezoelectric drive principle employing phase-shift measurement," *Journal of Microelectromechanical Systems*, vol. 16, no. 2, pp. 344–350, 2007.

[5] T.-G. Zsurzsan, C. Mangeot, M. Andersen, Z. Zhang, and N. Andersen, "Piezoelectric stack actuator parameter extraction with hysteresis compensation," in *Power Electronics and Applications (EPE'14-ECCE Europe), 2014 16th European Conference on*, Aug 2014, pp. 1–7.

[6] T. Doong and I. D. Mayergoyz, "On numerical implementation of hysteresis models," *IEEE Transactions on Magnetics*, vol. MAG-21, no. 5, pp. 1853–1855, 1985.

[7] I. Mayergoyz and G. Friedman, "Generalized preisach model of hysteresis," *Magnetics, IEEE Transactions on*, vol. 24, no. 1, pp. 212–217, Jan 1988.

[8] R. B. Mrad and H. Hu, "Dynamic modeling of hysteresis in piezoceramics," vol. 1, pp. 510–515 vol.1, 2001.

[9] X. Wang, V. Pommier-Budinger, Y. Gourinat, and A. Reysset, "A modified preisach model for hysteresis in piezoelectric actuators," *Informal Proceedings of the 11th International Workshop of Electronics, Control, Measurement, Signals and Their Application To Mechatronics, Ecmsm 2013, Informal Proc. Int. Workshop Electron., Control, Meas., Signals Their Appl. Mechatronics, Ecmsm*, p. 6648956, 2013.

[10] F. Weibel, Y. Michellod, P. Mullhaupt, and D. Gillet, "Real-time compensation of hysteresis in a piezoelectric-stack actuator tracking a stochastic reference," *2008 AMERICAN CONTROL CONFERENCE, VOLS 1-12*, pp. 2939–2944, 2008.

[11] I. D. Mayergoyz and G. Friedman, "On the integral equation of the vector preisach hysteresis model," *IEEE Transactions on Magnetics*, vol. MAG-23, no. 5, pp. 2638–2640, 1987.

[12] I. Mayergoyz, "Mathematical-models of hysteresis," *IEEE TRANSACTIONS ON MAGNETICS*, vol. 22, no. 5, pp. 603–608, 1986.

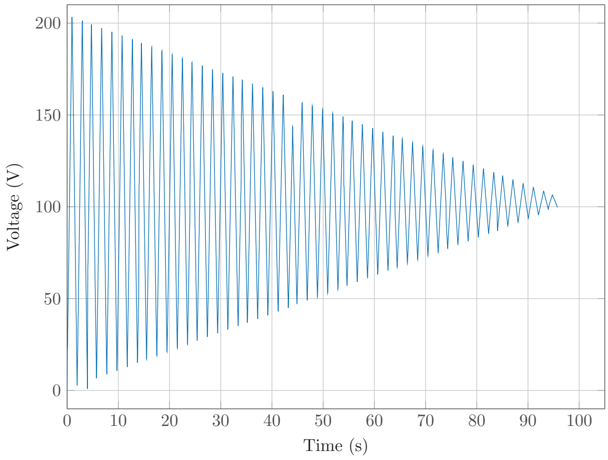

(a)

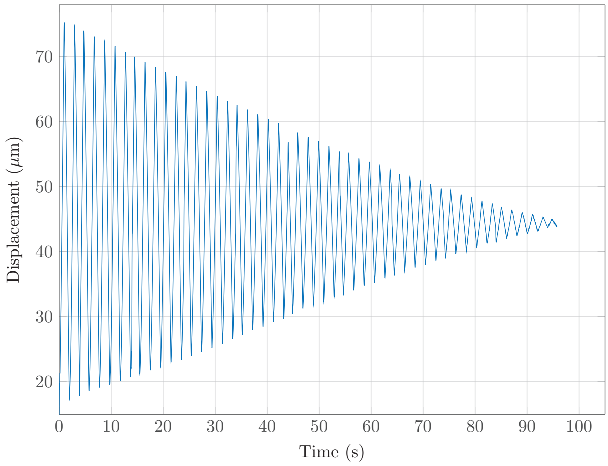

(b)

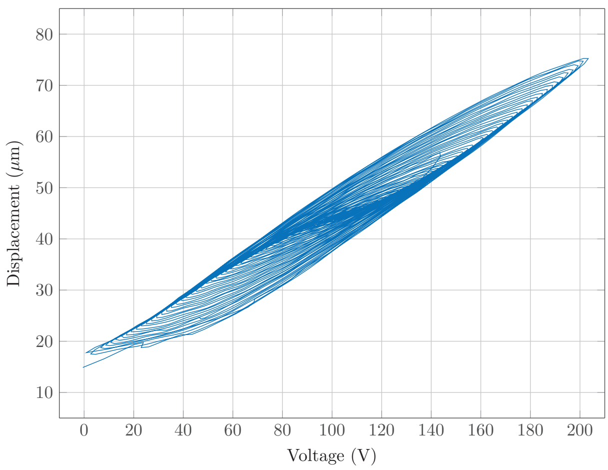

(c)

Fig. 10: Measurement of the first order reversal curves used to extract the model parameters. (a) shows the receding sawtooth signal applied to the piezoelectric stack actuator, measured from the output of the amplifier. (b) is the measured displacement of the piezoelectric actuator. (c) shows the actual reversal curves obtained.

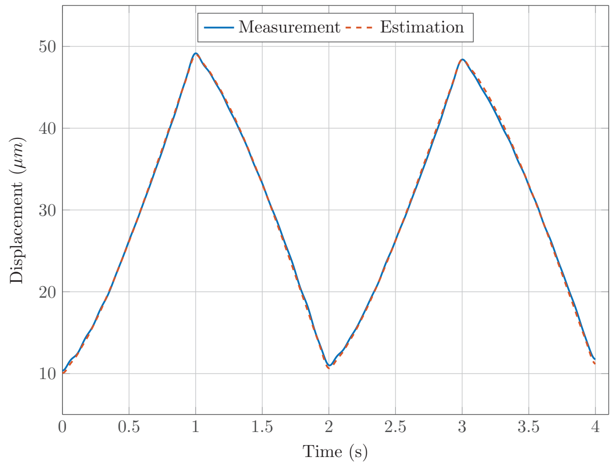

(a)

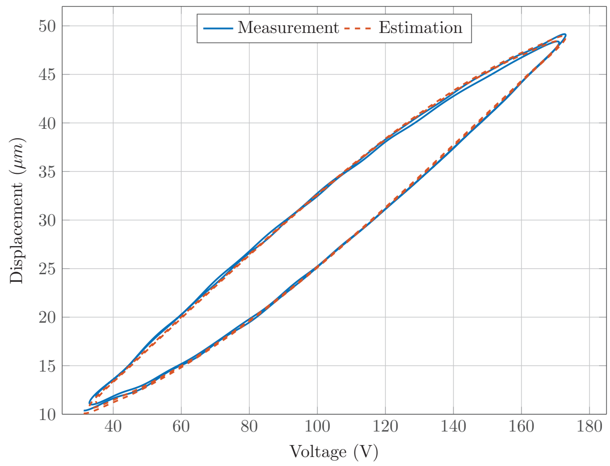

(b)

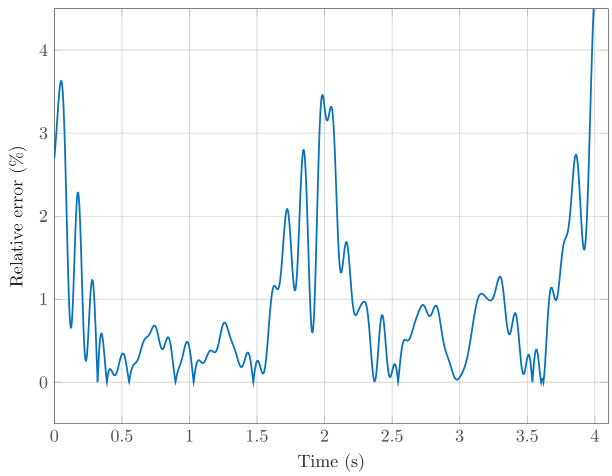

(c)

Fig. 11: Result of the model compared with the actual measured output for an input voltage pattern swinging between 31 V-173 V-33 V-171 V. (a) shows the comparison in time, (b) shows the matching hysteresis curves and (c) contains the relative error plot.

C

Temperature dependency of the hysteresis behaviour of PZT actuators using Preisach model

2016 15th International Conference on New Actuators & 9th Exhibition on Smart Actuators and Drive Systems

Temperature dependency of the hysteresis behaviour of PZT actuators using Preisach model

C. Mangeot[1]*, T.-G. Zsurzsan[2]
[1]Noliac A/S, Kvistgaard, Denmark
[2]Technical University of Denmark, Kgs. Lyngby, Denmark
*Corresponding author, email cm@noliac.com

Abstract:
The Preisach model is a powerful tool for modelling the hysteresis phenomenon on multilayer piezo actuators under large signal excitation. In this paper, measurements at different temperatures are presented, showing the effect on the density of the Preisach matrix. An interpretation is presented, aiming at defining a temperature-dependent phenomenological model of hysteresis for a better understanding of the non-linear effects in piezo actuators.

Keywords: Piezoelectric; multilayer; actuator; Preisach; model; temperature

Introduction

Quasi-static multilayer piezoelectric actuators are generally used in quasi-static applications under large signal excitation. In these conditions, the hysteresis effect is pronounced and can become a limitation, in particular for positioning applications.
To address this, two main approaches are possible: sensor-based or model-based. In the sensor-based approach, a sensor (displacement, force…) is used to close the loop and effectively linearize the piezoelectric effect. Although it provides excellent results, this approach is not always preferred or even possible, because of cost, size or performance. In the model-based approach, the behaviour of the actuator is characterised and this model is inverted to provide open-loop control of the actuator. This approach has become very popular with the availability of powerful real-time controllers. Several models have been proposed [1, 2], among others Ishlinskii hysteresis model [3], Maxwell resistive capacitor-based lumped-parameter model [4], variable time relay hysteresis model [5] and Preisach model [6].
The Preisach model [7, 8] is a phenomenological approach that can accurately describe any hysteresis behaviour. It is often the preferred approach for piezoelectric actuators and its large number of degrees of freedom makes it possible to adjust very precisely to experimental data.

The Preisach model

In a simple Preisach model, the hysteresis effect is decomposed into an infinity of individual elements called hysterons. These elements act as relays with an activation threshold α and a de-activation threshold β.
A geometrical interpretation of the hysteron plane greatly facilitates the understanding of the Preisach model in general. In this plane, a so-called Preisach triangle T_0 is defined, which represents the region of operation of the actuator, bordered by $\alpha_{max}, \alpha_{min}, \beta_{max}$ and β_{min}. Only the surface above the diagonal given by $\alpha = \beta$ has any physical meaning and therefore T_0 is an upper triangular surface. The elementary hysterons have a direct correlation to the half-plane in such a way that at any point in time T_0 is divided into two surfaces S^+ and S^- representing the (α, β) pairs for which the relay elements are active or inactive, respectively.
Thereby, for a monotonic increase of an input $u(t)$, the input-output plane shows an ascending hysteresis branch, while the T_0 half-plane 'fills up' from the bottom to the horizontal line defined by $\alpha = \{\alpha_1 \mid \alpha_1 \leq u(t)\}$. Similarly, a monotonic decrease in input will then determine the surface to 'empty', but this process is orthogonal to the one for increasing input. Therefore the 'filled' space T_0 will empty starting from the right towards the vertical line defined by $\beta = \{\beta_1 \mid \beta_1 \geq u(t)\}$. Thereby, a stochastic input signal with several extrema will be represented as a combination of 'filled' and 'emptied' areas on the triangle, delimited by a boundary staircase layer, denoted L. The problem then boils down to finding the area under the obtained staircase curve. This is illustrated in Fig. 1.

The standard equation for this type of model is:

$$x(t) = \iint_{\alpha \geq \beta} \mu(\alpha, \beta) \gamma_{\alpha\beta}[u, \gamma_0](t)\, d\beta\, d\alpha$$

Where x is the model output, μ represents a weighting matrix that mathematically particularizes the model to fit different hysteresis shapes and $\gamma_{\alpha\beta}$ represents the hysteron elements that can take values from the set $\{-1, 1\}$.
Terms on the diagonal ($\alpha = \beta$) dictate the general trend of the curve without hysteresis while the density

within the triangle ($\alpha > \beta$) corresponds to hysteresis effects.

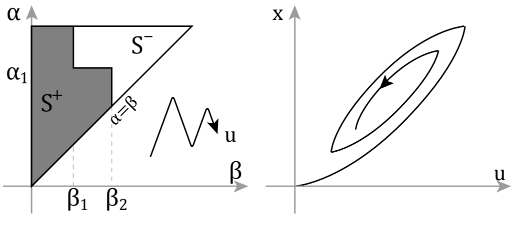

***Fig. 1:** Illustration of Preisach model*

In many applications, the actuator will be required to operate over a wide temperature range, which will affect the Preisach triangle. In such case, working with a constant Preisach model will induce errors in the open-loop control of the actuator.
In the present paper, a Preisach model is applied to the hysteresis relationship between dielectric charge and voltage (electric field). This set of parameters was chosen because it can be further processed in an electrostrictive behaviour model [9, 10]. However other parameter sets such as displacement versus voltage can be considered directly.

Experiment design

In our experiments, a multilayer piezoelectric element was submitted to a variable voltage while its dielectric charge was measured using a Sawyer-Tower circuit [11]. The element was placed in an oven (Fig. 2), allowing measurement between 25 and 200°C by steps of 25°C.

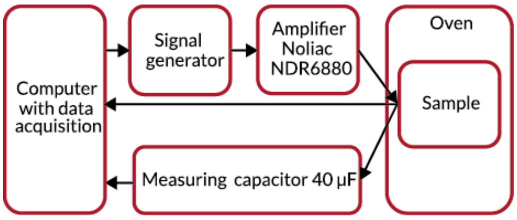

***Fig. 2:** Experiment setup*

Experimentation was performed using different input signals. In the end we selected a sinusoidal signal at 100Hz with a DC offset of 50V (corresponding to 1,5kV/mm, half the maximum peak-peak amplitude) and an amplitude decreasing by steps. Each wave is repeated to provide a statistical basis. The input signal is illustrated on Fig. 3. The first activation cycle at maximum voltage effectively “resets” the initial state of the Preisach matrix.

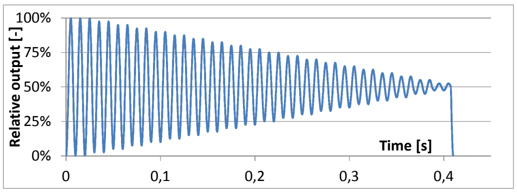

***Fig. 3:** Voltage input signal*

From these measurements we used two different methods to evaluate the Preisach matrices: analytical and recursive.
The analytical method is based on the following process:

- Identification of voltage reversal points. These define separation lines within the α - β plane, creating subdivisions of the plane. The selected input signal presents 40 reversal points, therefore a 39*39 discrete Preisach matrix can be built.
- Interpolation of charge values when the input signal crosses the separation lines.
- Starting from the smallest loop, charge differences can be calculated. The charge value in the Preisach matrix corresponds to the measured charge increase minus the charge increase measured over the same range in smaller loops (in other words the sum of the terms already identified in the same line for increasing voltage or in the same column for decreasing voltage).
- Charge density values (in C/V^2) are calculated by dividing each charge value by the area of the subdivision.

The recursive method relies on setting up a constrained least-squares minimization problem of the form:

$$\mu(\alpha,\beta) = \min_{\mu(\alpha,\beta)} || \Gamma[u,\gamma_0](t) - x(t) ||^2,$$

Where μ represents the weight matrix, Γ is the Preisach operator, u is the current input, γ_0 represents the initial relay state vector while x is the measured system output.
Thereby, the square of the difference between modelled and measured outputs is iteratively minimized until the error lies below a set threshold. A weight matrix $\mu(\alpha,\beta)$ is obtained, which contains the hysteretic nonlinearities specific to the modelled system. This method is implemented in MATLAB.
The two methods give comparable results.

Results

The graphs on Figs. 4 to 6 are 3D representations of the identified Preisach matrix at respectively 25, 100 and 200°C (using the analytical method). The scaling is identical for comparison and the colour scale is deliberately finer in the lower values.

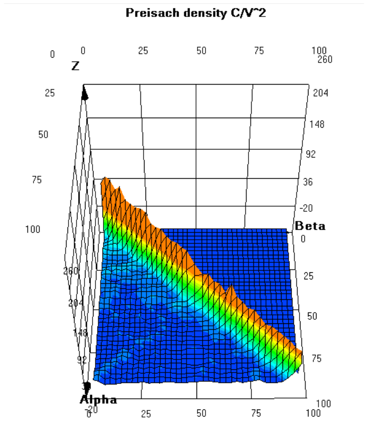

Fig. 4: *Hysteresis matrix at 25°C*

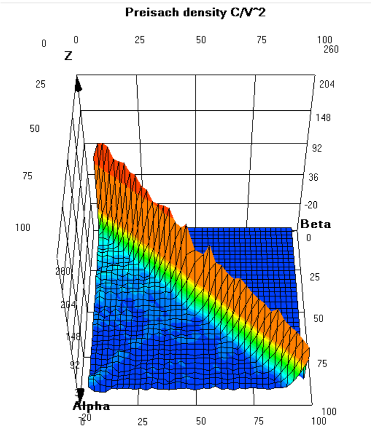

Fig. 5: *Hysteresis matrix at 100°C*

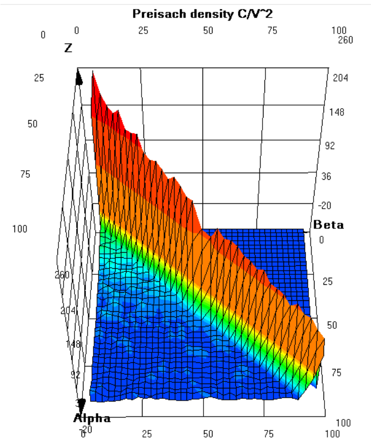

Fig. 6: *Hysteresis matrix at 200°C*

The density is characteristic of soft-doped PZT actuators, with most of the hysteresis present at low α values. These correspond to the "belly" of the hysteresis curve. In other words the P-E curves tend to get more elongated at high field as previously observed in [12].
Considering how the density evolves with temperature, two observations can be made:

- The density along the diagonal increases rapidly with temperature. This corresponds to the well-known increase of capacitance with temperature and is analysed in more details in [13].
- The density within the triangle increases only marginally with temperature. This indicates that, in proportion, hysteresis decreases at high temperature.

Analysis

The Preisach model can also be interpreted in terms of energy, where a given hysterion needs an activation energy corresponding to a voltage α to change state and returns to its original state if energy falls below a level corresponding to a voltage β. In a physical approach, the "switching" can correspond to domain re-orientation or domain wall movement; however the Preisach approach being phenomenological, the cause of the hysteresis is not relevant. Still, the effect of high temperature will be to facilitate the activation and de-activation of these "switches". In other words, hysterons shift towards the origin in the Preisach matrix.
This phenomenon has been studied for electromagnetics, for which it was proposed to use temperature-dependent scale factors for α and β [14]. However in the case of piezoelectric actuators, the relationship still needs to be formalised.
Nevertheless, it can be considered that both the Preisach density and the state line are affected by temperature. Using the same example as in Fig 1, if the element is subsequently submitted to a temperature change from θ_0 to θ_1, the state line will shift (Fig 7). Therefore the poling state of the element will change since a certain area (a) will switch to S^-.

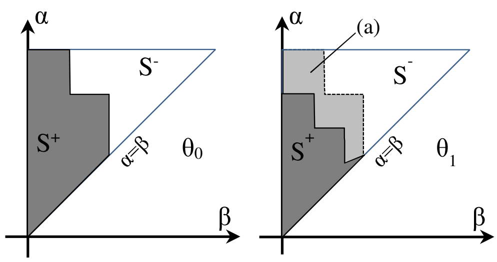

Fig. 7: *Illustration of the impact of temperature on the state line*

Also, it would make sense to extend the Preisach plane in the $\beta < 0$ range. This range would correspond to remanent poling. Obviously, the behaviour at θ_1 will be different from θ_0. But in addition, after return to θ_0 the initial state of the element will not be the same. Some remanent poling may be "lost" (S^-). However it can be easily recovered at the first activation. This phenomenon is often observed on soft-doped PZT, often in the fact that an actuator will provide a large free displacement at the first activation.

Extension of the model

Due to the adoption of a simple Preisach model, the proposed approach cannot include time-dependent phenomena such as frequency dependency and creep. This is contrary to observations. More advanced variants of the Preisach model have been proposed that include frequency dependency by adding $\frac{dx}{dt}$ as a parameter for the weighing function μ. Also the model can be extended to describe "viscous" effects such as creep by adding a random noise on the input signal [6].
However these implementations are complex and do not catch the full extent of poling dynamics as described for example by [15]. It is proposed to apply such behaviour models to individual hysterons, leading to time-dependency both in terms of creep and frequency dependency.

Control aspects

A temperature-dependent Preisach model is a very useful element of a reliable control circuit for a piezoelectric actuator. Several configurations can be considered:
In a sensor-less configuration (temperature unknown), this model is however of little interest. The controller will have to assume a certain temperature in order to estimate the state of the actuator.
If the temperature information is available, the controller would be capable of constantly adapting the Preisach matrix, thereby keeping an image of the state of the actuator, for example its free displacement.
It is also possible to sense the charge absorbed by the actuator. In such a case, the controller can compare the actual charge to the model and deduct the temperature of the actuator.
Finally, a combination (temperature + charge measurement) would allow the controller to deduct two variables such as position and external force. Combinations with displacement or force sensors are of course also possible, each additional parameter allowing the estimation of a variable or a consolidation of the estimates.

Conclusions

The target of this paper is to propose a temperature-dependent phenomenological model of hysteresis. Depending on the adopted sensor configuration, this model can be used within a control loop in order to determine the state of an actuator (free displacement), its temperature or the generated force.
Essentially, the target is to reach a better characterisation of the non-linearity of piezoelectric actuators and a better understanding of non-linear effects, leading to improved control capabilities.
Measurements give an indication of how the Preisach density evolves with temperature, with a general scaling as well as a shift of the hysterons towards the origin.
The adoption of a simple Preisach model implies rate-independent behaviour, however it would be possible to extend it to a rate-dependent model.

References

[1] S. H. Lee, M.B. Ozer, T.J. Royston, Journal of Materials Processing and Manufacturing Science, 9.1 (2001), 33–52.
[2] G. Kadar, G. Szabo, Journal of Magnetism and Magnetic Materials 215-216 (2000), 592–596.
[3] M. Al Janaideh, P. Krejci, Physica. B, Condensed Matter, 407.9 (2012), 1365–1367.
[4] Y. Liu et al., Smart Materials and Structures, 22.11 (2013), 115020.
[5] Z. Guo, Y. Tian, H. Qi, "Modified Rate-Dependent Hysteresis Modeling of Piezoelectric Actuator." (2014): 206–210.
[6] I.D. Mayergoyz, The Science of Hysteresis I, (2006), 293–446.
[7] F.Z. Preisach, Zeitschrift für Physik 94 (1935), 277-302
[8] D.H. Everett, W.I. Whitton, Transactions of the Faraday Society 48 (1952), 749-757
[9] C.L. Hom, N. Shankar, Proceedings of the second international conference on intelligent materials (1994), 623-634
[10] P. Weaver et al, IEEE Transactions on Ultrasonics, Ferroelectrics, and Frequency Control 58, 9 (2011), 1730 – 1736
[11] C. B. Sawyer, C. H. Tower, Physical Review vol. 35, 3 (1930), 269
[12] C. Mangeot, B. Andersen, Advances in Applied Ceramics (2016)
[13] G. T. Zsurzsan, IEEE Transactions on Industrial Electronics (2016)
[14] Berlotti G. et al, The Science of Hysteresis II (2005), 57
[15] A. Belov, W. S. Kreher, Ferroelectrics, 391 (2010), 12-21

D

Zero computational cost piezoelectric hysteresis compensation for quasi-dynamic applications

IEEE Transactions on Industrial Electronics

Zero computational cost piezoelectric hysteresis compensation for quasi-dynamic applications

***Abstract* — The Piezoelectric Actuator Drive (PAD) is a precise piezoelectric motor generating high-torque rotary motion, which employs piezoelectric stack actuators in a wobble-style actuation to generate rotation. The piezoelectric stacked ceramics used as the basis for motion in the motor suffer from hysteretic nonlinearities. In order to model these nonlinearities, a least squares constraint algorithm is used to extract a weighting function and a discrete Preisach model is derived. Hysteresis temperature dependence is discussed and a linear influence of temperature on the Preisach weights is proposed, with an average error of 3 % between extrapolated and measured responses at 200 °*C*. Compensation is achieved through an improved closest-match algorithm. The results show a relative error of less than 3 % between measured and reference responses, validated with two separate trajectory signals.**

Keywords* — *motor, actuator, piezoelectric, stack, multilayer, hysteresis, model, Preisach

I. Introduction

The Piezoelectric Actuator Drive (PAD) shown in Fig. 1 is a type of rotary motor that transforms the linear motion of piezoelectric stack actuators into a precise rotation [1]. The operating principle, illustrated in Fig. 2, is based on a wobble-style motor, where the motor ring is actuated into an off-center circular motion around an axially constrained shaft, thereby generating rotational motion. A micro-mechanical toothing interface is machined between the ring and shaft, as shown in Fig. 3. This enables both high positioning accuracy and output torque [2]. The actuation method, combined with the type of toothing and the inherent large stiffness of the piezoelectric stack actuators makes the PAD appropriate for open-loop control [3].

By construction, the PAD motor behaves like a fully capacitive rotary machine, due to the piezoelectric stack actuators it employs. These actuators exhibit desirable properties such as large stiffness and a reversibility of the piezoelectric effect, enabling them to act as both actuators and sensors [4]. Nevertheless, two dominating nonlinearities persist in the control of piezoelectric-based actuation, namely hysteresis and creep [5]. Of the two effects, hysteresis has a much larger impact on the positioning precision of the motor, especially under dynamic operation. The purpose of this paper is to model this effect in order to correctly predict the response of the PAD.

Modeling hysteresis in the piezoelectric motor is a necessary step in developing compensation methods to negate the effects. The most encountered method of modeling hysteresis in literature remains the Preisach scalar model [6], which provides a straightforward method of representing the hysteretic effect. Although initially developed for the purpose of modeling magnetic hysteresis, due to its fenomenological nature, the method can be used to model any type of hysteresis [7]. This fact, combined with the generally predictable performance has

Fig. 1: The Piezoelectric Actuator Drive (PAD)

led the Preisach model to be the preferred method used when hysteresis is involved.

Many modifications and improvements to the original model have been proposed, such as accounting for dynamic input changes [8], [9] or reducing the computational complexity by simplifying the parameter identification process [10]. For this paper, simplicity and real-time execution are the most important factors in determining the method used. Therefore, the classical model enhanced through a least squares weight determination [6], [11], [12] is chosen.

The Preisach hysteresis model is a powerful method in black box-type phenomenological hysteresis modeling. It is capable of representing any hysteretic shape with complete disregard for the underlying physical phenomena involved. Nonetheless, one major disadvantage of the method is its incapability, in its standard form, of modeling temperature dependence, a limitation also identified in [13]. Therefore, an empirically-supported model for hysteresis dependence on temperature is introduced

Compensation of the effects of hysteresis is necessary in order to improve the positioning accuracy of piezoelectric devices in applications where open-loop control is desirable. Even in closed-loop applications, precompensation of hysteresis can help reduce requirements on control law dynamics and improve overall system behavior. In this respect, building an inverse Preisach model is necessary. One of the disadvantages exhibited by this model now becomes apparent, in that it does not have an analytical inverse. Therefore, an approximate inverse is calculated, based on a closest-match algorithm [11], [13]–[15].

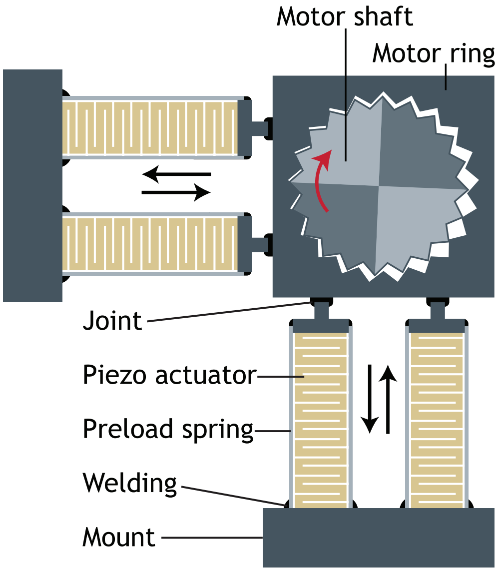

Fig. 2: PAD operating principle

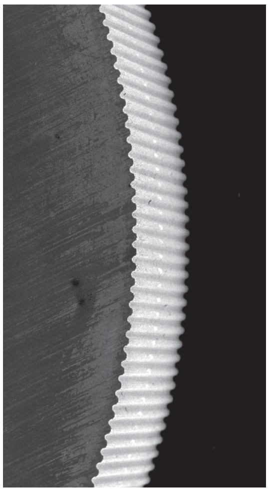

Fig. 3: Microtoothing on the motor shaft. Tooth distance is 120 µm and depth is 38 µm

The paper starts by presenting the underlying principle of the Preisach model of hysteresis in section II, followed by presenting temperature dependence in section III and model inversion in section IV. The experimental set-up is described in section V, while measurements and validation is presented in section IV. The conclusion follows in section VII.

II. The Preisach Model of Hysteresis

The idea behind the classical scalar Preisach model consists of describing the hysteretic effect through the use of an infinite number of parallel-connected relay-type two-state discontinuous operators $\gamma_{\alpha\beta}[u(t)]$, called basic hysterons. These elements represent relay-like loops on the input-output plane with two values, α and β, acting as the 'on' and 'off' thresholds, with $\beta \leq \alpha$. When the input signal $u(t)$ becomes

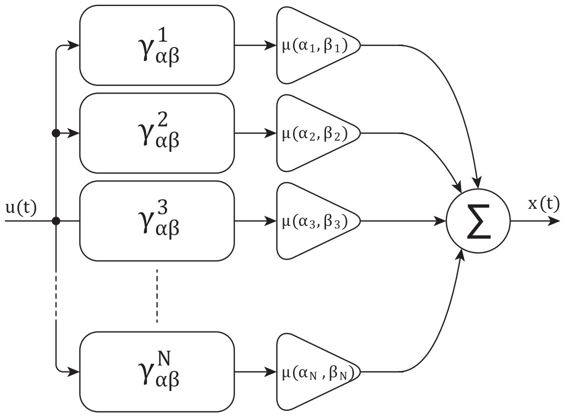

Fig. 4: Parallel connection of elementary Preisach hysterons with weighting gains

greater than α, the output of the operator becomes 'high' and goes to 'low' state only when the input becomes less than β. In between tresholds, the previous value is retained. More explicitly, in the case of piezoelectric devices this can be written mathematically as

$$\gamma_{\alpha\beta}[u(t)] = \begin{cases} -1 & u(t) \leq \beta; \\ \gamma_{\alpha\beta}[u,\gamma_0](t) & \beta \leq u(t) \leq \alpha; \\ 1 & u(t) \geq \alpha. \end{cases} \tag{1}$$

The hereby-defined hysteron output depends on both signal input and its initial output, defined in (1) as $\gamma_0|_{\gamma_0\in[+1;-1]}$. This representation of the basic hysteretic operator, represented graphically in Fig. 5, is in agreement with the property of a hsyteretic system where the output depends not only on the input, but past values of the input as well. In other words, hysteresis is a nonlinearity with a non-local memory effect.

In order to be able to reproduce a wide range of hysteresis curves, the outputs of the basic hysterons are then weighted with an experimentally-determined weighting function $\mu(\alpha,\beta)|_{\mu(\alpha,\beta)\geq 0,\forall(\alpha,\beta)\in T}$. Determining this function represents the major challenge in deriving and using the Preisach hysteresis model.

The structural block diagram of the Preisach model is shown in Fig. 4. It illustrates the parallel connection and weighting of individual elementary hysterons, whose sum produces the instantaneous output. Mathematically, for a given input $u(\cdot)$ this can be expressed as

$$x(t) = \iint\limits_{\alpha\geq\beta} \mu(\alpha,\beta)\gamma_{\alpha\beta}[u,\gamma_0](t)\,\mathrm{d}\beta\,\mathrm{d}\alpha \tag{2}$$

where $u(t)$ is the voltage input to the piezoelectric actuator, $x(t)$ represents the output displacement, $\mu(\alpha,\beta)$ is the experimentally-obtained weighting function and $\gamma_{\alpha\beta}[u(t)]$ is the hysteron state.

Thereby, an operator Γ can be defined that describes the dependence of the output on current and past inputs as expressed by (2):

$$x(t) = \Gamma[u,\gamma_0(\alpha,\beta)](t), \tag{3}$$

where $\gamma_0(\alpha,\beta)$ represents the initial state of each relay.

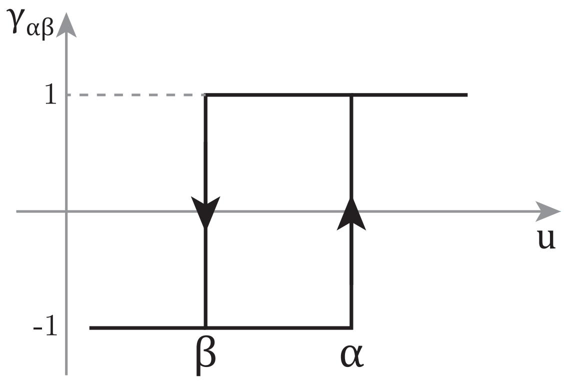

Fig. 5: The elementary Preisach hysteron with thresholds α and β. The arrows represent one-way state transitions

A geometrical interpretation of the hysteron plane (also called the $\alpha-\beta$ plane) greatly facilitates the understanding of (2) and the Preisach model in general. In this plane, a so-called Preisach triangle T_0 is defined, which represents the region of operation of the actuator, bordered by $\alpha_{max}, \beta_{max}, \alpha_{min}$ and β_{min}. Only the surface above the diagonal given by $\alpha = \beta$ has any physical meaning and therefore T_0 is an upper triangular surface. The elementary hysterons $\gamma_{\alpha\beta}[u,\gamma_0](t)$ have a direct correlation to the $\alpha-\beta$ half-plane in such a way that at any point in time T_0 is divided into two surfaces S^+ and S^-, representing the (α,β) pairs for which $\gamma_{\alpha\beta}[u,\gamma_0](t) = 1$ or -1, respectively.

Thereby, for a monotonic increase of the input $u(t)$, the input-output plane shows an ascending hysteresis branch, while the $\alpha-\beta$ half-plane 'fills up' from the bottom to the horizontal line defined by $\alpha = \{\alpha_1 | \alpha_1 \leq u(t)\}$. Similarly, a monotonic decrease in input will then determine the surface to 'empty', but this process is orthogonal to the one for increasing input. Therefore the 'filled' space T_0 will empty starting from the right towards the vertical line defined by $\beta = \{\beta_1 | \beta_1 \geq u(t)\}$. Thereby a stochastic input signal with several extrema will be represented as a combination of 'filled' and 'emptied' areas on the triangle, delimited by a boundary staircase layer, denoted L. The intersection point between this memory curve and the diagonal defined by $\alpha = \beta$ represents the current value of the input $u(t)$. The problem then boils down to finding the area under the obtained staircase curve. This process is visually exemplified in Fig. 6.

An important property of the Preisach model is the wipe-out feature, whereby the input history is erased when the input increases above (or decreases below) the previous points of extrema. Specifically, in Fig. 6d if the input were to increase beyond α_1, then the pair (α_1, β_2) would be removed from the history. Visually, the corner represented by (α_1, β_2) on the half-plane would be 'engulfed' by the vertically increasing S^+ surface. In time domain, this coincides with $u(t)$ increasing in amplitude beyond its previous extremum. This feature is important in order to prevent excessive history growth.

Using the presented geometric interpretation, the Preisach

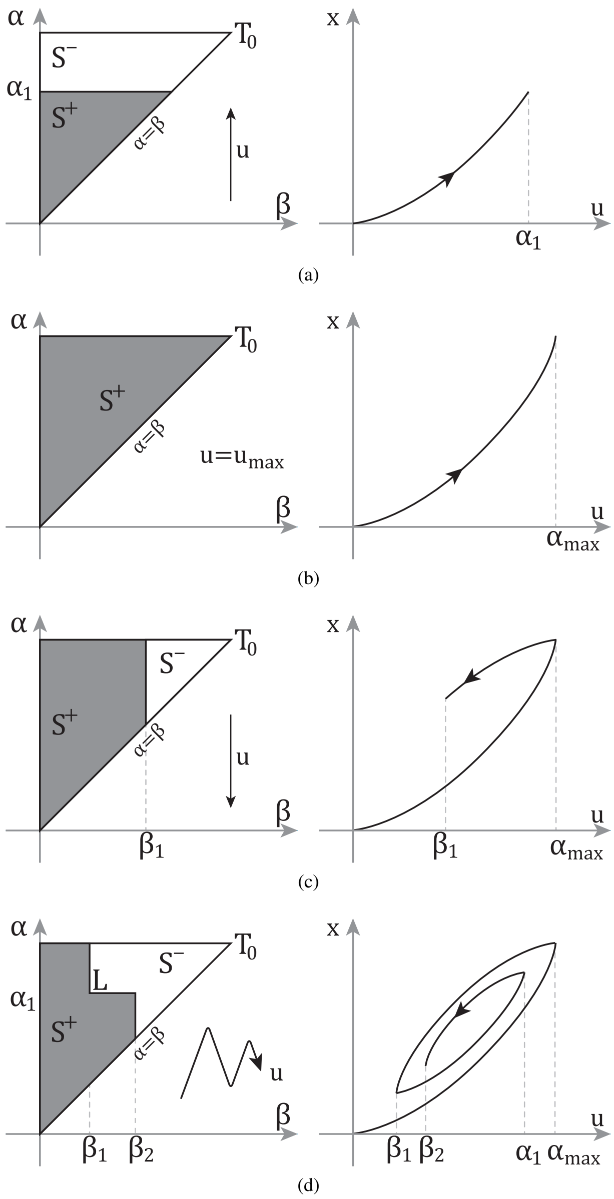

Fig. 6: Representation of the Preisach triangle, with examples for increasing (a), maximum (b), decreasing (c) and progressively decreasing amplitude (d) triangular input and their respective surface divisions.

model (2) can be rewritten as

$$\begin{aligned} x(t) = &\iint\limits_{S^+} \mu(\alpha,\beta)\gamma_{\alpha\beta}[u,\gamma_0(\alpha,\beta)](t)\,\mathrm{d}\beta\,\mathrm{d}\alpha \\ &+ \iint\limits_{S^-} \mu(\alpha,\beta)\gamma_{\alpha\beta}[u,\gamma_0(\alpha,\beta)](t)\,\mathrm{d}\beta\,\mathrm{d}\alpha \end{aligned} \tag{4}$$

Considering that $\gamma_{\alpha\beta}[u,\gamma_0(\alpha,\beta)](t) = -1|_{u(t)\leq\beta}$ and $\gamma_{\alpha\beta}[u,\gamma_0(\alpha,\beta)](t) = 1|_{u(t)\geq\alpha}$, (4) can be reduced to

$$x(t) = \iint\limits_{S^+} \mu(\alpha,\beta)\,\mathrm{d}\beta\,\mathrm{d}\alpha - \iint\limits_{S^-} \mu(\alpha,\beta)\,\mathrm{d}\beta\,\mathrm{d}\alpha \tag{5}$$

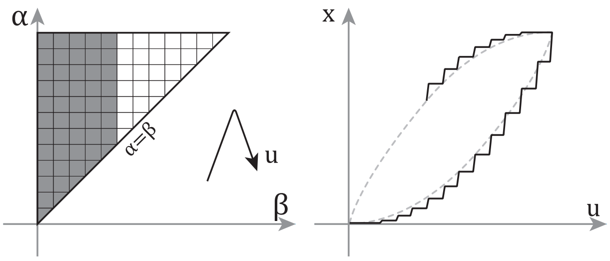

Fig. 7: Division of the Preisach plane into $N = 12$ equally-distanced values for α and β, and the resulting 12 discrete levels obtained on the hysteresis curve.

The next step in completing the Preisach hysteresis model is discretizing the half-plane and determining the $\mu(\alpha,\beta)$ weighting function. There are many ways in achieving this, both parametric and nonparametric, but a constrained least squares iterative minimization process is arguably the best suited nonparametric method for it [14] since no initial assumption is made on the distribution shape. Through this method, the square of the difference between actual and modeled outputs is iteratively minimized until the error is below a set threshold. The drawback is increased computational intensity for large amounts of data and high levels of discretization. Therefore, in the case of the Preisach model, $\mu(\alpha,\beta)$ will then be

$$\mu(\alpha,\beta) = \min_{\mu(\alpha,\beta)} \left\| \gamma_{\alpha\beta}[u, \gamma_0(\alpha,\beta)](t) \cdot \mu(\alpha,\beta) - x(t) \right\|^2 |_{\mu(\alpha,\beta) \geq 0} \tag{6}$$

In order map actual values for each hysteron weight to the Preisach plane, the previously-defined limiting triangle T_0 is now split up into a mesh containing values for the point pairs $\{(\alpha_i,\beta_j)|i=1..N, j=i..N\}$. Fig. 7 shows the geometrical interpretation of the discrete Preisach plane on the left hand side, together with the obtained input-output representation on the right-hand side, for an arbitrary value of $N = 12$. The number of α and β values equals the number of discrete steps on the hysteresis curve. Naturally, the higher N is chosen, the finer the mesh becomes and consequently, the finer the hysteresis representation will become. This is at the expense of exponentially increasing memory requirements to store all the values.

Through (5), a theoretical basis for modeling hysteresis in piezoelectric actuators is set. The PAD motor employs four piezoelectric stack actuators in order to generate rotational motion, as presented in Fig. 2. In order to be able to model the effects of hysteresis in the motor, the actuators need to be excited by a sufficiently rich input in order to activate all hysterons within the defined plane at least once [15]. In this respect, a biased receding amplitude sawtooth signal is used, whose envelope converges towards the bias value. This produces a spiral hysteretic response, as illustrated in Fig. 6d. By ensuring that the number of identification periods is at least equal to the discretization step, all hysterons can be excited.

The result of the identification process is a piecewise constant Preisach half-plane populated with the values of the weighting function $\mu(\alpha),\beta)$.

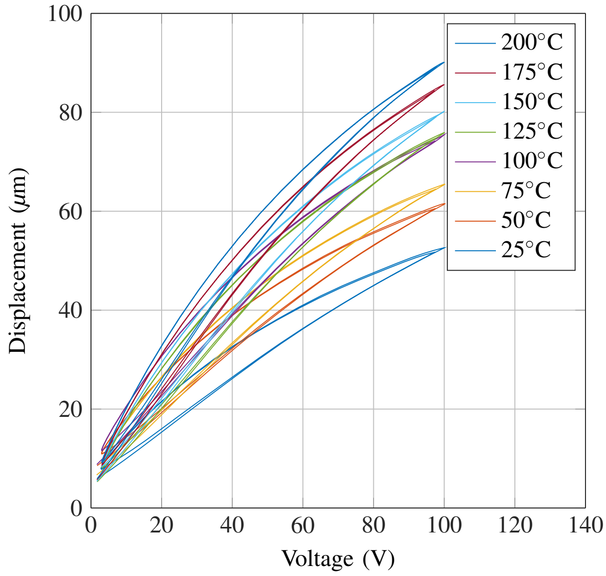

Fig. 8: Hysteresis versus voltage.

III. Inlfuence of Temperature on the Model

In order to analyze the effect of temperature on stack actuator operation and consequently on the modeling process, a set of measurements was performed using the identification signal described. Its response is then measured for 8 different temperature levels, ranging from 25 °C to 200 °C.

The previously presented Preisach identification procedure is then applied with a low discretization step of $N = 20$, in order to enable quicker interpretation of the results. Thereby, 8 separate weighting matrices are obtained that correspond to the 8 different temperature levels.

Fig. 8 shows one loop of the hysteresis behavior of the studied device for each temperature level. Herein, the maximum obtainable stroke of the piezoelectric actuator increases with temperature, with the free displacement obtained at 200 °C showing a 70 % increase over room temperature values.

The Preisach model is then used to obtain 8 sets of different distribution matrices. Fig. 8 shows that temperature changes the maximum stroke and at the same time the hysteretic behavior is reduced with temperature increase. This is also supported by an increase in the weights on the main diagonal of the Preisach plane, paired with a decrease in the off-diagonal terms. This is illustrated in Fig. 9.

While the increase in actuator output with increased temperature is significant, the relatively small change in the off-diagonal terms in the Preisach plane suggest that the effect of temperature on hysteresis opening is not significant compared to its influence on maximum stroke. Furthermore, the increase in stroke suggests a linear dependence to temperature.

The observations in this experiment support previous claims [16], [17] that the piezoelectric stroke increases with temperature. Moreover, in the range of measurement, a quasi-linear dependency between the two is observed. This previous research then explains this trend by introducing a set of temperature-dependent constitutive equations wherein the charge constant is directly proportional to temperature.

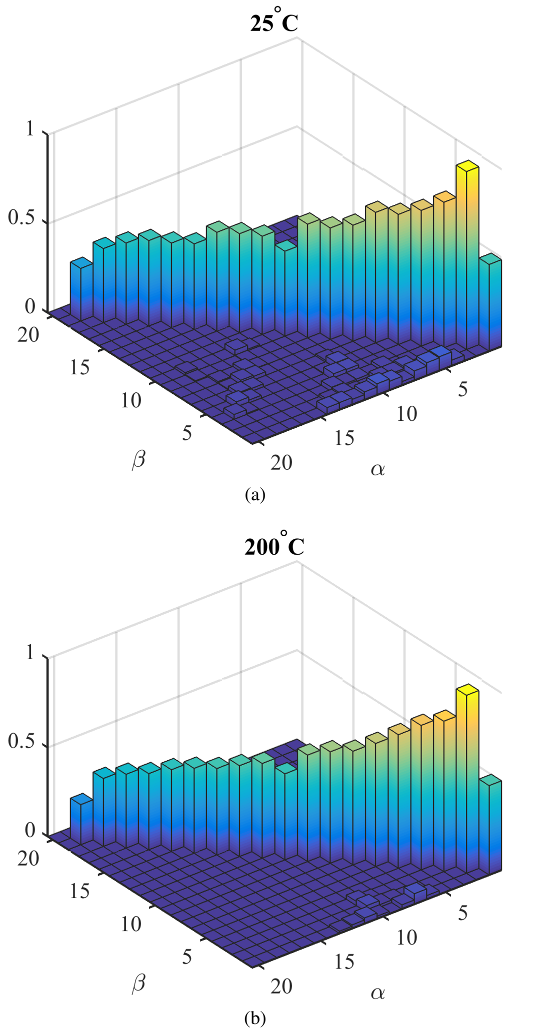

Fig. 9: Difference between identified Preisach weights at 25 °C (a) and 200 °C (b).

Since the Preisach model is phenomenological in nature, this physically-attributed temperature trend is not inherently useful. Therefore, a better approach is to augment the obtained weight function to include the temperature dependence as an added overall linear weighting factor.

Based on the expression for the Preisach operator Γ in (3), a new operator Γ_T can be introduced that takes temperature behavior into effect through a temperature proportionality factor κ_T. This can be expressed as

$$\Gamma_T[u, \gamma_0(\alpha, \beta), \kappa_T](t) = \kappa_T \Gamma[u, \gamma_0(\alpha, \beta)](t). \tag{7}$$

Therefore, the temperature-dependent Preisach model output becomes

$$\begin{aligned} x(t) &= \Gamma_T[u, \gamma_0(\alpha, \beta), \kappa_T](t) = \\ &= \kappa_T \iint_{S^+} \mu(\alpha, \beta)\, \mathrm{d}\beta\, \mathrm{d}\alpha - \kappa_T \iint_{S^-} \mu(\alpha, \beta)\, \mathrm{d}\beta\, \mathrm{d}\alpha \end{aligned} \tag{8}$$

IV. Preisach model inverse

Based on the notion of discretization illustrated in Fig. 7, the surface T contains $N(N+1)/2$ piecewise-constant weights μ, where the density in each cell is constant, but can vary from cell to cell. Similarly, model input sensitivity is now reduced to a minimum variation $\Delta u = (u_{max} - u_{min})/N$, by virtue of discretization. Therefore, the model output will only change for an input variation that is larger than Δu.

Now, given an initial memory curve L_0, the goal is to find an input value $\hat{u} \in T$ such that the model output is equal or close to a desired output x_d [13]. Written in terms of (3) discretized,

$$|\Gamma[\hat{u}, L_0] - x_d| = \min_{u \in T} |\Gamma[u, L_0] - x_d|. \tag{9}$$

In short, the algorithm compares a desired output to the output of the Preisach model and then successively increases or decreases the input to the model until the error between the two outputs is smaller than the discretization step.

The implemented algorithm is based on the original one provided in [13], but improves upon it by grouping conditions, minimizing branching and reducing looping in order to enhance clarity and reduce execution time. For purposes of completeness, the full algorithm is provided in Alg.1.

Algorithm 1 Closest-match algorithm

Require: $x_d, L_0, \Delta n$
Ensure: $\hat{u}, \hat{L}$
  $n = 0$
  if $x_d[n] - x[n] == 0$ **then**
    $(\hat{u}, \hat{L}) = (u[n], L_0[n])$
    return
  else
    while $\mathrm{abs}(x_d[n] - x[n]) > 0$ **do**
      if $u[n] = u_{max}$ **then**
        $(\hat{u}, \hat{L}) = (u[n], L_0[n])$
        return
      else
        $u[n+1] = u[n] + \Delta u \cdot \mathrm{sgn}(x_d[n] - x[n])$
        $n = n + 1$
        $x[n] = \Gamma(u[n], L_0[n-1])$
      end if
    end while
    if $abs(x_d[n] - x[n] \leq abs(x_d[n] - x[n+1]$ **then**
      $(\hat{u}, \hat{L}) = (u[n], L_0[n])$
      return
    else
      $(\hat{u}, \hat{L}) = (u[n-1], L_0[n-1])$
      return
    end if
  end if

The resulting estimated voltage $\hat{u}$ will now represent the inverse hysteretic input that will cancel out the system hysteresis. Due to discretization, $\hat{u}$ now contains high frequency components in the form of discrete steps which can excite system dynamics and cause unnecessary strain in the actuators. These can be partially removed through interpolation [13], [15]. The drawback of the method is that it only provides piecewise-smoothing from step to step, and therefore a better

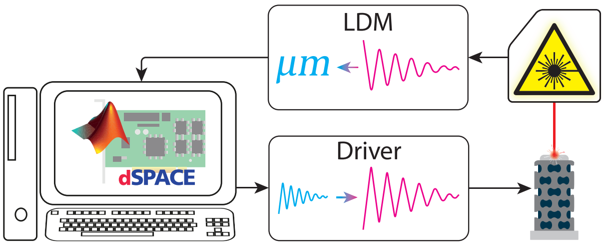

Fig. 10: Block diagram of the experimental set-up. A computer equipped with a PCI dSPACE board is used. The signal generated is amplified through a voltage amplifier. The unit under test is a Noliac custom piezoelectric stack actuator. Elongation is measured using a Keyence LC-2440 laser sensor connected to a Keyence LC-2400 laser displacement meter (LDM).

solution is to apply high order digital filtering. Normally, this would also introduce undesired phase shift in the input signal, thereby negating the applicability of the inverse.

To avoid undesired phase shift, use of a zero-phase filter is proposed [18]. Zero-phase filtering implies processing of the input data in both forward and reverse directions in order to eliminate phase lag. This implies a loss of causality and therefore impossibility of implementation in a closed-loop system. For the current application, this is not an issue since only forward compensation is desired.

This approximate inverse model can now be used in order to shape the input signal such that the desired output displacement trajectory is obtained. Thereby, forward hysteresis compensation is achieved. The results of this procedure will be presented in the results section of this paper, together with a verification process by which a signal other than the one used for identification is set as trajectory and the piezo output is measured to see the performance of the compensation.

V. Experimental set-up

The experimental setup is presented in Fig. 10 and consists of a computer with a dSPACE single-board PCI system, a linear voltage amplifier and a laser displacement sensor. The laser sensor is a Keyence LC-2440 sensor head connected to a Keyence LC-2400 controller. The measurement system has measuring range of ± 3 mm, maximum resolution of 0.2 µm and a bandwidth of 20 kHz. The unit under test is a Noliac custom piezoelectric stack actuator laser-welded into a spring-load casing with 750 N preloading. The actuator is rated for 200 V input voltage, producing a maximum elongation of 60 µm.

A Matlab script is used to produce a positively biased receding sawtooth waveform which is then amplified and drives the actuator. The waveform is adjustable in time, envelope slope and number of teeth. This type of waveform is chosen in order to eliminate the effects of creep while keeping all hysteresis information intact. Data acquisition of the position value is then performed and all data is stored into Matlab for processing.

VI. Measurements and Results

Results on the forward model of hysteresis

In order to identify the Preisach model and build the $\alpha-\beta$ plane, the system response is measured for a single piezoelectric actuator from the four existing ones in motor. The

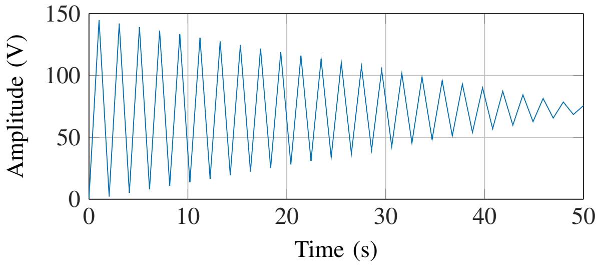

(a)

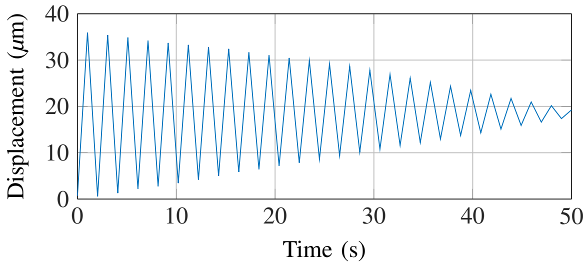

(b)

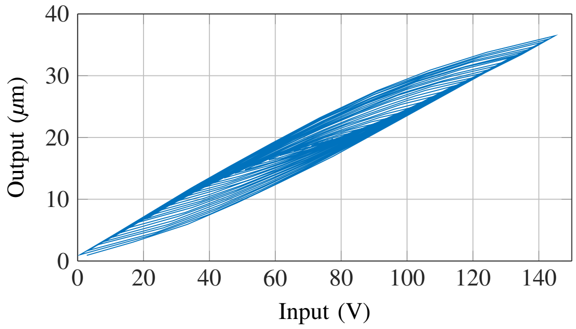

(c)

Fig. 11: Receding amplitude sawtooth identification signal (a), obtained response (b) and resulting hysteresis (c).

other actuators are assumed to be identical with the measured one. This assumption is reasonable, within the fabrication tolerances of the actuators themselves but it will of course impact the model accuracy.

The identification signal used together with its response are shown in Fig. 11(a) and (b), respectively, while (c) illustrates the hysteretic effect between the input and piezoelectric response. The input signal is a 1 Hz receding sawtooth that starts at maximum input amplitude and successively converges towards the bias point. There is a direct correlation between the number of input signal periods or inversions and the number of concentric hysteresis loops. For correct model identification, the number of reversals has to at least match the discretization level employed so that all hysterons are excited at least once.

The result of the identification procedure is then a weight matrix $\mu(\alpha,\beta)$, with each of its values assigned to a corresponding square in the Preisach plane.

Fig. 12a. illustrates the modeled versus measured responses, limited to the last 10 s of the signal to illustrate more

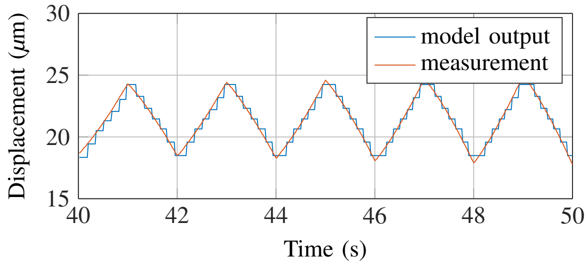

(a)

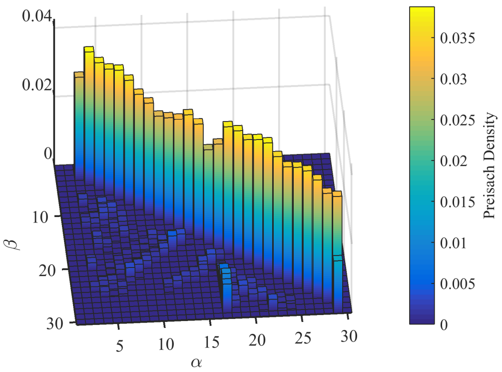

(b)

Fig. 12: Detail view of modeled versus measured responses (a) and corresponding weight matrix (b) for a discretization level of $N = 30$.

detail. The response estimated by the developed model is in agreement with the measured response. Therefore the model correctly estimates the actuator's exponential displacement response as a direct result of the triangular input excitation.

Fig. 12b. presents the mapping of the weights onto the plane for a discretization level of $N = 30$. The main diagonal elements account for the bulk of the response and correspond to the quasi-linear diagonal shape of the hysteretic curve.

Temperature effects on hysteresis

Fig. 8 illustrates a quasi-linear dependence between actuator temperature and its measured response. This is also reflected in the obtained distributions, as the effects of temperature are only prominent on the components situated on the main diagonal. Therefore, in order to visually illustrate the effects of temperature on the Preisach plane, only the main diagonals of the obtained matrices are analyzed. Fig. **??** shows the elements on these diagonals plotted in increasing temperature order. The figure exhibits the same type of quasi-linear increase in diagonal coefficients between temperature levels.

Fig. 13b. shows the mean relative trend of the weights on the main diagonal of the Preisach distribution matrix with respect to temperature. This linear fit, whose slope represents the value for the introduced temperature coefficient κ_T can now be used to extrapolate model weights for different temperatures. Plot 13c. then shows the evaluation of this approach by illustrating the maximum relative error obtained at each temperature level versus the real weights directly modeled. Although a deviation from the real weight by 22 % seems

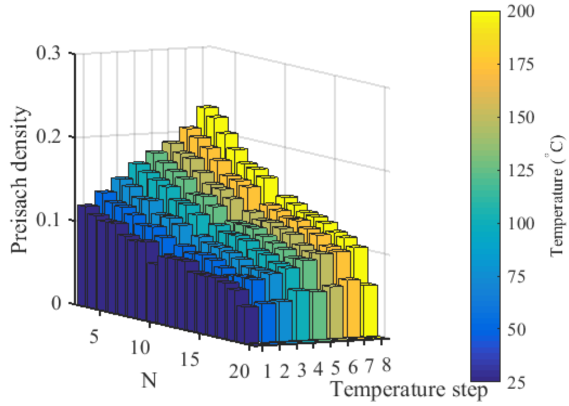

(a)

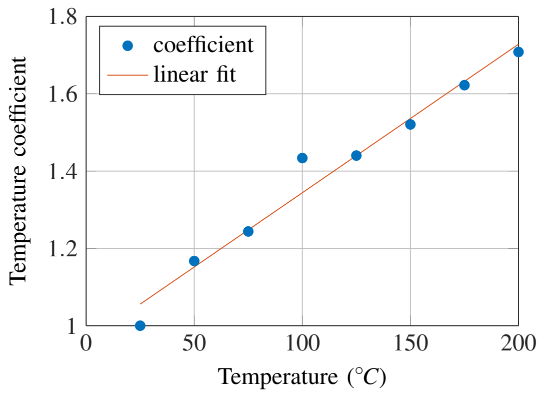

(b)

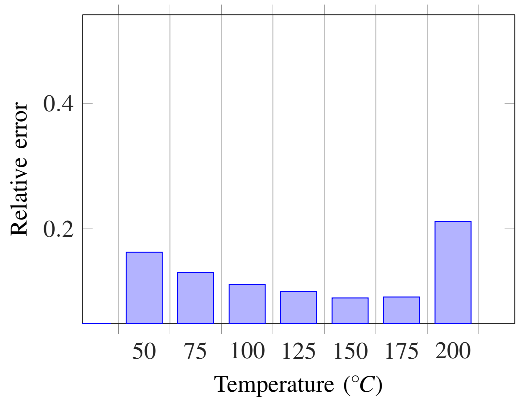

(c)

Fig. 13: Value of Preisach distribution diagonal elements versus temperature (a), linear fit of the temperature trend (b) and obtained maximum relative error for each temperature value (c).

significant, this is the worst-case scenario for one single value in the entire diagonal. The actual average error is 3 %.

Inverse model validation

Fig. 14a. shows the measured and desired responses of a piezoelectric device. The desired trajectory is used as an input to the Preisach inversion algorithm. The resulting input voltage is presented in (b), and the measured response in (a) is the result obtained for this input signal. The hysteresis plot in (c) shows a much more linear input-output response of the device compared to Fig. 11(c). This proves that hysteresis precompensation greatly reduces the nonlinear effects.

In order to further evaluate the performance of this compensation method, a pure sinusoidal displacement profile is set as the desired trajectory. The voltage signal obtained from the Preisach inversion is then fed to the piezo device again, with the results being shown in Fig. 15. Plot (a) shows a good match between desired and measured responses, with the nonlinearities almost completely eliminated. This is then reinforced by the x-y plot showing hysteresis between desired and measured responses in (b). In order to prove that the nonlinear effects have been transfered to the input voltage signal, plot (c) shows its hysteretic response with respect to the measured output.

From these results it can be concluded that the hysteresis inversion method used is effective in obtaining a more linear response in piezoelectric devices with respect to their output displacement. Through the improved closest-match inversion algorithm, an inverse hysteretic relationship is embedded into the piezo voltage input. A look-up table is then used to store input values and as a result, the direct and inverse effects cancel each other out.

VII. Conclusions

This paper models the effects of hysteresis in the piezoelectric stack actuators used in the Piezoelectric Actuator Drive motor. A discrete Preisach model was chosen due to its popularity as a hysteresis modeling tool, relative simplicity and ease of implementation. A modeling approach is chosen whereby the model weights are identified through a least squares algorithm.

Next, the effects of temperature on hysteresis response are shown, and a modification to the Preisach operator is proposed to include this dependence as a linear coefficient. The method is validated through comparison of the measured response at 200 °C and the extrapolated one from 25 °C, which shows an average error of 3 %.

A model inversion method is then implemented using an improved closest-match algorithm. The improvements brought on reduce algorithm looping and branching, leading to an overall reduction in computational time. Validation of the model inverse is performed on two sets of reference trajectories, whereby the mean relative errors between desired and measured outputs do not exceed 3 % in either case.

Therefore, the modeling, temperature dependence and inversion methods shown herein prove to be a practical tool in hysteresis forward compensation.

Future work will focus on investigating the effects of higher frequency dynamics on the model, as well as the influence of creep on static operation.

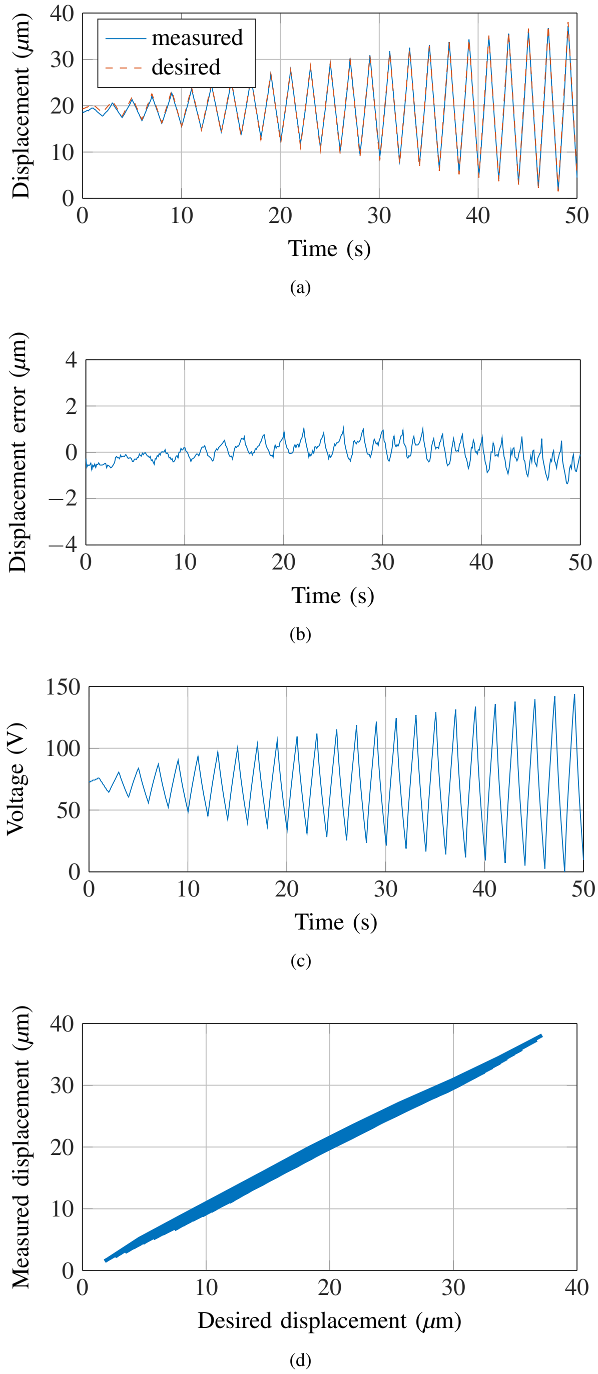

Fig. 14: Response of the system to an inverted identification input signal. The desired and measured trajectory (a), trajectory error (b), obtained inverse input voltage (c) and hysteresis between desired and measured trajectory (d).

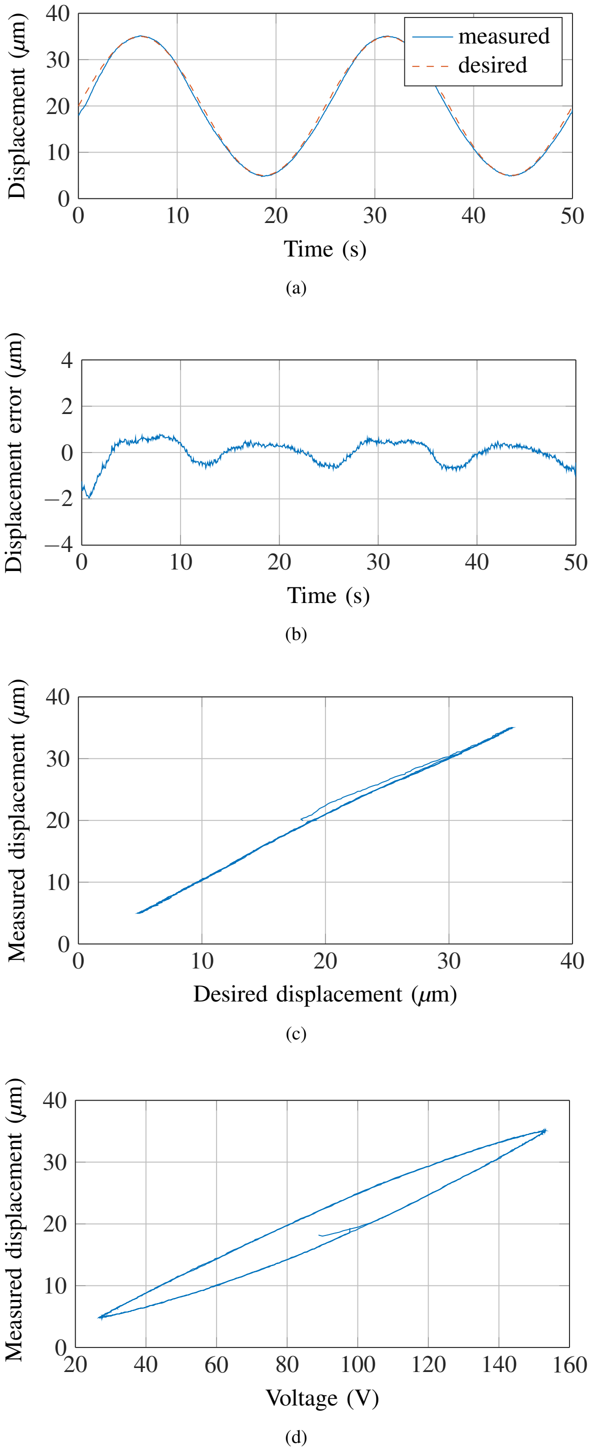

Fig. 15: Response of the system to a sinusoidal excitation. The desired and measured trajectory (a), trajectory error (b), hysteresis between the two (b) and hysteresis between inverted system input and measured output (c). The hysteresis shape is inverted in this case.

ACKNOWLEDGEMENTS

The authors would like to thank Noliac A/S for providing a PAD motor to be dissected and investigated, as well as the Danish National Advanced Technology Foundation for financial support. A special thanks to Charles Mangeot for providing the data on variation of hysteresis with temperature.

REFERENCES

[1] A. Kappel, B. Gottlieb, and C. Wallenhauer, "Piezoelectric actuator drive (pad)," *AT-AUTOMATISIERUNGSTECHNIK*, vol. 56, no. 3, pp. 128–135, 2008.

[2] J. Rucha, H. Liess, J. Heinzl, A. Kappel, T. Schwebel, and B. Gottlieb, "Applicability of a piezo actuator drive as a sensorless high precision drive," *10th International Conference on New Actuators*, 2006.

[3] R. Zeichfussl, B. Gottlieb, C. Wallenhauer, S. Herzig, A. Kappel, and T. Luth, "A method for auto-adjustment of a new piezoelectric drive," in *Mechatronics, 2009. ICM 2009. IEEE International Conference on*, April 2009, pp. 1–6.

[4] C. Wallenhauer, B. Gottlieb, A. Kappel, T. Schwebel, J. Rucha, and T. Lueth, "Accurate load detection based on a new piezoelectric drive principle employing phase-shift measurement," *Journal of Microelectromechanical Systems*, vol. 16, no. 2, pp. 344–350, 2007.

[5] T.-G. Zsurzsan, C. Mangeot, M. Andersen, Z. Zhang, and N. Andersen, "Piezoelectric stack actuator parameter extraction with hysteresis compensation," in *Power Electronics and Applications (EPE'14-ECCE Europe), 2014 16th European Conference on*, Aug 2014, pp. 1–7.

[6] T. Doong and I. D. Mayergoyz, "On numerical implementation of hysteresis models," *IEEE Transactions on Magnetics*, vol. MAG-21, no. 5, pp. 1853–1855, 1985.

[7] I. Mayergoyz and G. Friedman, "Generalized preisach model of hysteresis," *Magnetics, IEEE Transactions on*, vol. 24, no. 1, pp. 212–217, Jan 1988.

[8] R. B. Mrad and H. Hu, "Dynamic modeling of hysteresis in piezoceramics," vol. 1, pp. 510–515 vol.1, 2001.

[9] X. Wang, V. Pommier-Budinger, Y. Gourinat, and A. Reysset, "A modified preisach model for hysteresis in piezoelectric actuators," *Informal Proceedings of the 11th International Workshop of Electronics, Control, Measurement, Signals and Their Application To Mechatronics, Ecmsm 2013, Informal Proc. Int. Workshop Electron., Control, Meas., Signals Their Appl. Mechatronics, Ecmsm*, p. 6648956, 2013.

[10] F. Weibel, Y. Michellod, P. Mullhaupt, and D. Gillet, "Real-time compensation of hysteresis in a piezoelectric-stack actuator tracking a stochastic reference," *2008 AMERICAN CONTROL CONFERENCE, VOLS 1-12*, pp. 2939–2944, 2008.

[11] R. V. Iyer, X. Tan, and P. Krishnaprasad, "Approximate inversion of the preisach hysteresis operator with application to control of smart actuators," *Automatic Control, IEEE Transactions on*, vol. 50, no. 6, pp. 798–810, 2005.

[12] I. D. Mayergoyz and G. Friedman, "On the integral equation of the vector preisach hysteresis model," *IEEE Transactions on Magnetics*, vol. MAG-23, no. 5, pp. 2638–2640, 1987.

[13] X. Tan, R. Venkataraman, and P. Krishnaprasad, "Control of hysteresis: theory and experimental results," *Proc SPIE Int Soc Opt Eng, X-ray and Gamma-ray Instrumentation for Astronomy*, vol. 4326, pp. 101–112, 2001.

[14] R. V. Iyer and X. Tan, "Control of hysteretic systems through inverse compensation," *Control Systems, IEEE*, vol. 29, no. 1, pp. 83–99, 2009.

[15] J. Å. Stakvik, M. R. Ragazzon, A. A. Eielsen, and J. T. Gravdahl, "On implementation of the preisach model: Identification and inversion for hysteresis compensation," *Modeling, Identification and Control*, vol. 36, no. 3, p. 133, 2015.

[16] M. W. Hooker, "Properties of pzt-based piezoelectric ceramics between -150 and 250 c," 1998.

[17] D. Wang, Y. Fotinich, and G. Carman, "Influence of temperature on the electromechanical and fatigue behavior of piezoelectric ceramics," *Journal of Applied Physics, J. Appl. Phys, J Appl Phys, Jap*, vol. 83, no. 10, pp. 5342–5350, 1998.

[18] A. Oppenheim and R. Schafer, *Discrete-time signal processing*. Prentice-Hall, 1999.

E

Control and sensor techniques for PAD servo motor drive

2015 IEEE 50th International Universities Power Engineering Conference (UPEC2015)

Control and sensor techniques for PAD servo motor drive

Gabriel T. Zsurzsan*, Zhe Zhang, Michael M.A. Andersen and Nils A. Andersen
Department of Electrical Engineering, Technical University of Denmark
Denmark
E-mail: *tgzsur@elektro.dtu.dk

***Abstract*—The Piezoelectric Actuator Drive (PAD) is a new type of electrical motor that employs piezoelectric multilayer actuators coupled with a form-fitted micro-mechanical gearing to generate rotary motion. The PAD is precise, having a positioning error of less than 2 arc-seconds. Its typical output torque is 4 N·m, without any additional gearing. The whole motor is fully non-magnetic, enabling its use in applications where magnetic neutrality is of importance. The main challenges of the PAD are the hysteretic behavior of the ceramic actuators used and their highly capacitive nature. After compensating for the hysteretic behavior, the current waveforms of the motor can be used to extract all necessary parameters for sensorless operation. Moreover, these signals provide a qualitative information about the precision in motor centering and show any mismatch between the actuators used.**

***Index Terms*—Piezoelectricity, multilayer actuator, motor, hysteresis, compensation, control**

I. Introduction

THE Piezoelectric Actuator Drive (PAD) is a new type of electrical rotary machine that essentially uses special ceramic actuators to impart motion. The ceramics used have piezoelectric properties – this means they physically stretch when a voltage is applied to them. This linear motion is on the order of micrometers, and is very precise.

A micro-mechanical gearing is then employed to transform the linear motion of piezoelectric actuators into a precise rotational motion [1]. These micrometer-sized teeth enable the PAD to achieve high positioning accuracy, similar to stepper motors. The motor has a positioning accuracy of less than 2 arc-seconds without the use of any positioning sensors. At the same time, the PAD achieves high typical output torques of 4 N·m without extra gearing [2]. To give a relative idea of strength, this is enough to lift a 65 kg sack of cement attached to a rope that is winding around the shaft.

The main advantage of using the PAD as a replacement for conventional servo drives is the fact that the PAD is a fully non-magnetic motor. This allows the PAD to be used in applications where conventional drives are inadequate, such as operation in high radiation or strong magnetic fields. One such case is operation close to the bore of a magnetic resonance imaging (MRI) scanner, as a patient table positioning motor to enable patient positioning without disturbing the image produced by the scanner itself.

Despite the advantages of the PAD, there are some challenges associated with its operation. The piezoelectric actuators used act as large capacitors, having a capacitance of 3 µF. Therefore the power delivered to the motor is highly reactive. Since only the real part of the power delivered to the motor is effectively transformed into mechanical work, the power stage used to drive the motor needs to be able to cope with large amounts of return power in order to be efficient.

Furthermore, sensorless operation of the PAD is desired in order to reduce fabrication cost, improve reliability and maintain magnetic neutrality. This requires extracting information about rotor position, speed and motor torque from the motor signals without the use of expensive external sensors. Due to the stiff nature of the ceramic actuators, the load has very little influence on the motor signals and is therefore difficult to correctly estimate. Adding to this difficulty is the highly hysteretic behavior of piezoelectric ceramics in general [3]. This hysteresis needs to be compensated for in order to correctly estimate rotor position and speed.

While the micro-mechanical toothing combined with the large actuator stiffness make the PAD motor ideal for use in voltage-driven open-loop control [4], efficient operation and load-sensing capabilities can only be obtained in a closed-loop control structure. This requires overcoming the aforementioned challenges.

II. Piezoelectric stack actuators

Piezoelectricity has the property of being a bidirectional effect. The direct effect allows these ceramics to generate an electrical charge on their electrodes which is proportional to the force applied to their surface. The converse effect enables these materials to expand and contract a distance proportional to the voltage applied to their electrodes. The actuators employed in the motor use the converse piezoelectric effect to transform electrical energy to mechanical energy.

The range of elongation in piezoelectric ceramics is in the order of nano- to micrometers, and is therefore not inherently useful in transferring energy. Stacking many layers of piezoceramics on top of each other creates a piezoelectric multilayer actuator (PMA). These layers are connected electrically in parallel but mechanically in series, as shown in Fig. 1. The advantage of PMAs over their single layer counterparts is the ability to produce larger deflections and require a fraction of the voltage levels of its single layer counterparts. The cost comes in the form of larger exhibited capacitances and therefore higher currents for the same actuation speed.

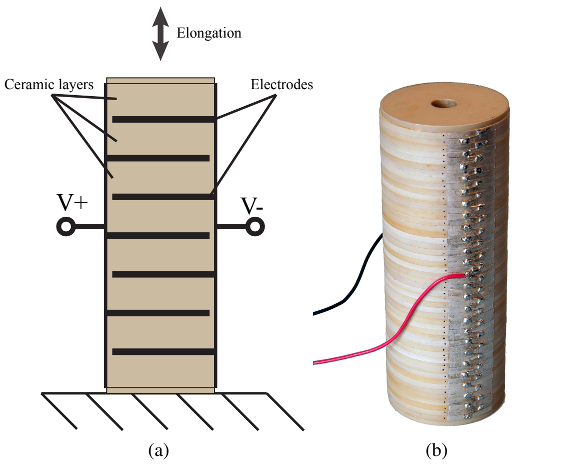

Fig. 1: Piezoelectric multilayer actuator (PMA) structure diagram (a) and actual image (b). The electrodes (black lines in (a) and silver surface with connection points in (b)) are inserted with an alternating polarity into the ceramic structure. Application of a voltage on these electrodes produces a vertical expansion of the structure.

III. PAD OPERATING PRINCIPLE

The PAD and its internal structure are shown in Fig. 2a and Fig. 2b. Four PMAs are placed inside the motor housing – two sets of parallel actuators, with the sets having a 90° angle between them. The PMAs are fixed to the motor housing on one side and to the motor ring on the other. This ring has a square exterior profile with a circular cutout in its center which houses the motor shaft. This shaft is fixed to the motor housing through ball bearings, allowing only rotation. Both the surface on the inside of the motor ring and the circumference of the shaft are machined into micro-mechanical teeth with a pitch of 100 µm. Fig. 2c shows a microscope image of the motor shaft teeth. The ring and shaft have 313 and 312 teeth, respectively, with the shaft having one tooth less than the ring. This forms a robust contact point between surfaces, suited for power transfer while also gives the PAD the ability to output high levels of torque through the inherent gearing ratio.

The multilayer actuators expand and contract linearly along their length and thereby push and pull against the motor ring. This creates two axes of actuation within the plane of the stack actuators, the motor ring and shaft, thereby enabling the motor ring to exhibit movement around the shaft. By applying a sinusoidal voltage to the actuators on one axis and a phase-shifted version of the same signal with a 90° phase shift to the other actuators, the resulting space-vector and trajectory will be circular. Fig. 3a shows the voltages applied to the actuators normalized to their sinusoidal periods, while Fig. 3b illustrates the resulting spatial trajectory. Thereby, the motor ring exhibits an off-center circular motion around the shaft which is rotated in the opposite direction through the contact point between them.

Each full period of the applied sinusoidal voltage determines the motor ring to do a full revolution around the shaft and this, in turn, makes the shaft rotate in the opposite direction for the distance equivalent to one tooth step. This is due to the inherent 312 gearing ratio present through the micro-mechanical toothing. Therefore a 360° rotation of the contact point between the motor ring and shaft produces a 1.15° rotation in the output shaft of the motor. This principle is illustrated in Fig. 4 Moreover, the frequency of the applied signals determines the speed of rotation, reduced by the same gearing ratio, such that

$$\nu = \frac{N_{ring} - N_{shaft}}{N_{ring}} \cdot \frac{f}{60}, \tag{1}$$

where ν is the shaft rotation speed in RPM, N_{ring} and N_{shaft} represent the number of teeth on the motor ring and shaft, respectively, and f is the frequency in Hz of the applied sinusoidal voltage signals.

IV. HYSTERESIS EFFECTS AND COMPENSATION METHODS

As mentioned in the introduction, a disadvantage of piezoelectric ceramics is the high level of hysteresis they exhibit between the applied voltage signal and the resulting displacement. This is even more pronounced in PMAs, where the real elongation of the actuator can vary by over 20% through the middle of the stroke [5], as shown in Fig. 5a. Since hysteresis has no effect on the actual displacement amplitude of the PMAs, it does not impact open-loop positioning accuracy when motion is executed along integer number of teeth. Since one electrical revolution equals to one tooth step, a fraction of that will result in sub-tooth motion. But since this implies partial actuator expansion, this type of motion will be heavily affected by hysteresis and in turn negatively affect sub-tooth positioning accuracy. Thereby, the absolute motor accuracy is reduced significantly.

A simple way of eliminating PMA hysteresis is to measure the extent of the effect and forward-compensate for it by adapting the driving signals, as proposed in [5]. This method was proven to reduce the absolute positioning error of the actuator under test by a factor of 10. The effects of hysteresis compensation on displacement are shown in Fig. 5a and Fig. 5b. Due to the manufacturing process of the actuators which involves chemical, thermal and polarization processes, the tolerance of their parameters is high, even for PMAs produced in the same batch. Therefore, although showing good results, the presented method requires measuring the characteristics of every actuator individually. While this might be feasible for low and very low volume manufacturing of PADs, a different method would be required for a feasible manufacturing line assembly process.

Therefore, a more feasible way of compensating for PMA hysteresis is a closed-loop approach. Methods for achieving this are currently under investigation.

V. SENSORLESS CONTROL

Sensorless control of electrical motors implies measuring the motor response only through its electrical signals and using these measurements to estimate all necessary motor quantities: position, speed, acceleration and torque. This allows the motor to be fully controlled without the use of external positioning or torque sensors, which represent a large part of the overall motor cost.

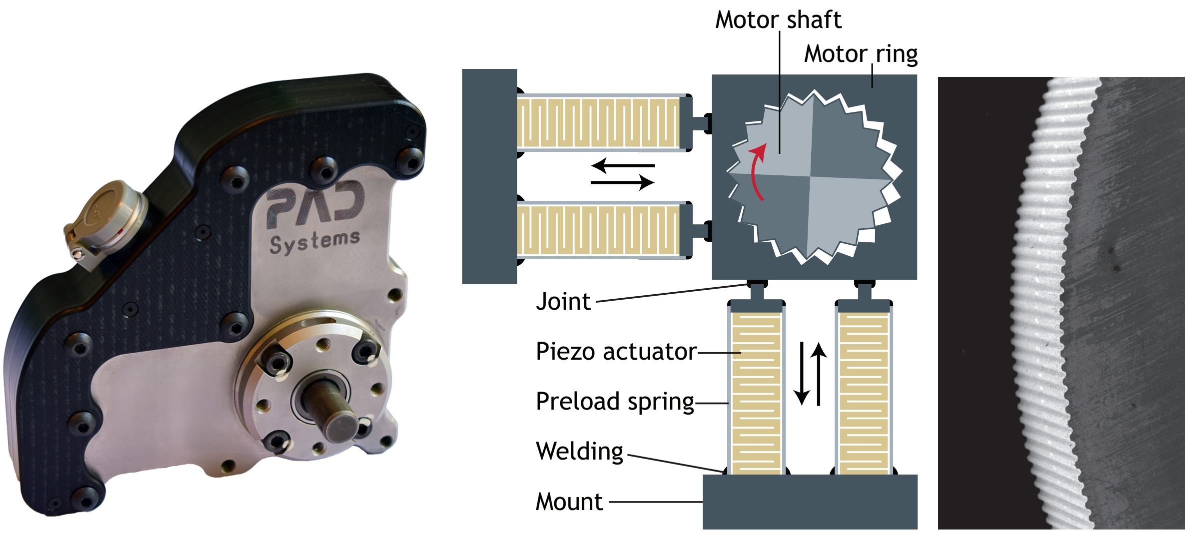

(a) (b) (c)

Fig. 2: PAD motor (a), internal structure (b) and micro-mechanical gearing (c). The internal structure of the PAD is made up of 4 PMA actuators acting against a motor ring, which in turn is coupled to the shaft through a micromechanical gearing. The pitch of the gears is 100 µm.

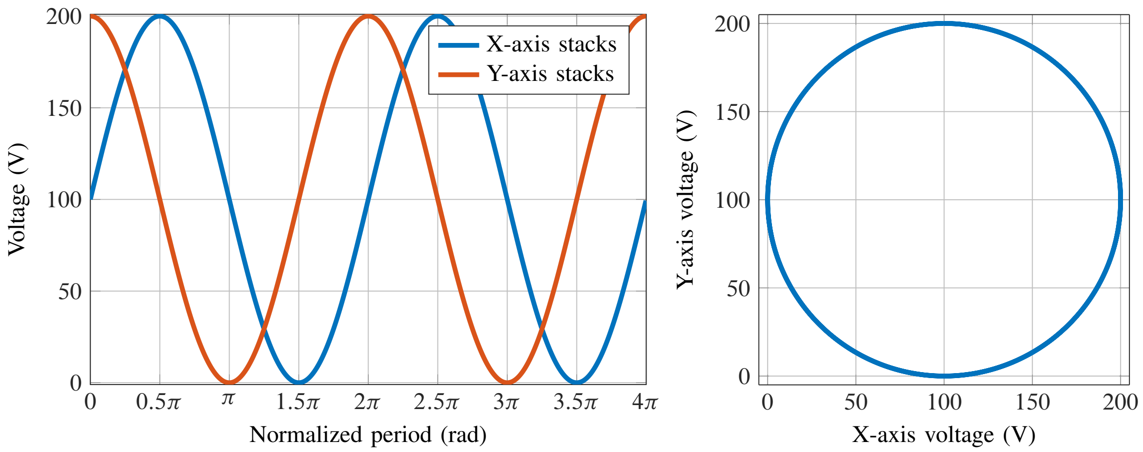

(a) (b)

Fig. 3: Sine and cosine voltage signals applied to the actuators, normalized to their period (a) and ideal spatial trajectory obtained (b)

Due to its inherent structure, the PAD motor behaves like a fully capacitive, voltage-driven rotary machine. The piezoelectric stack actuators forming the basis of motion in this motor give it a capacitive nature. This, coupled with the reversibility of the piezoelectric effect enable the stacks to act as both actuators and sensors [6]. The current flow to and from the motor provides information about rotor speed and position, but it also indicates the quality of mechanical contact between stator and rotor through electromechanical coupling between the shaft and the stacks. In order to qualify this coupling, the motor was driven in open-loop and the current waveforms were measured and plotted against each other to form a spatial trajectory plot. Analysis of the measured data yields interesting results. Fig. 6a and Fig. 6b show the trajectory of the traveling contact point between the motor ring and shaft during a pass over 15 teeth in the rotor, under conditions of 3 N·m load and no load, respectively. Each blue curve represents one electrical revolution of the ring and one tooth step of the shaft. The red pegs each represent a rotation of one tooth on the shaft and help with visually keeping track of shaft position. The dotted black circles represent the ideal, undistorted trajectory.

These data show that position and speed can both be estimated from the measured current waveforms, although sub-tooth precision cannot be guaranteed due to hysteresis strongly affecting the measurement. Moreover, a resonance can be observed in the case of the loaded motor which cannot be seen in the unloaded case. This effect is the result of hard electromechanical coupling between the actuators and

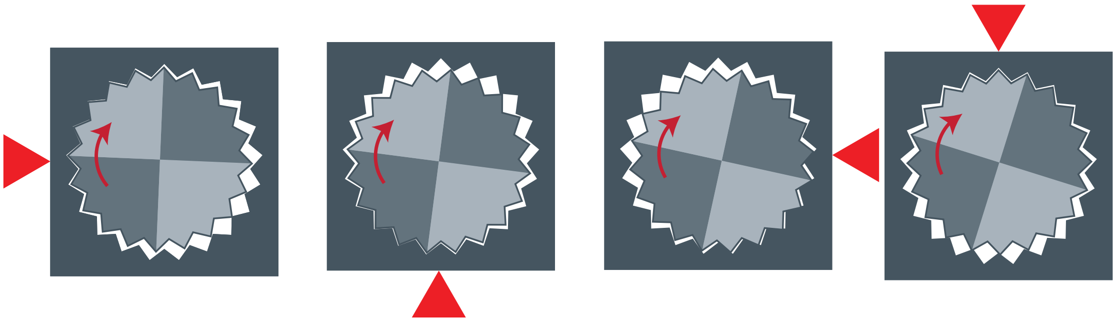

Fig. 4: The principle of rotation in the PAD motor. The red arrow represents the direction of actuation, which is the same as the position of the contact point. The shaft is fixed by a bearing while the ring is free to rotate around it. One revolution of the contact point will cause the motor shaft to turn the distance equivalent to one tooth.

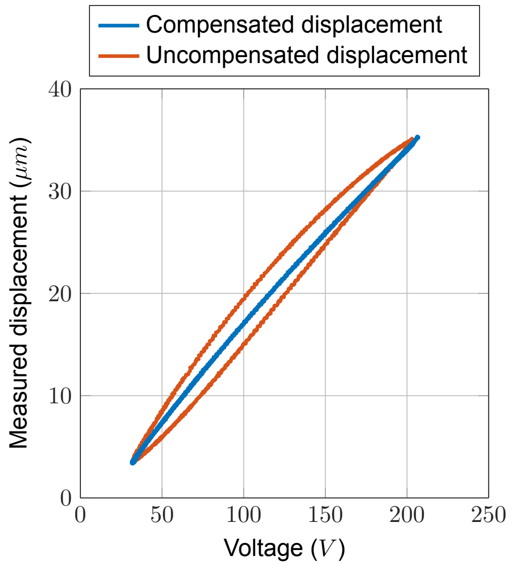

(a)

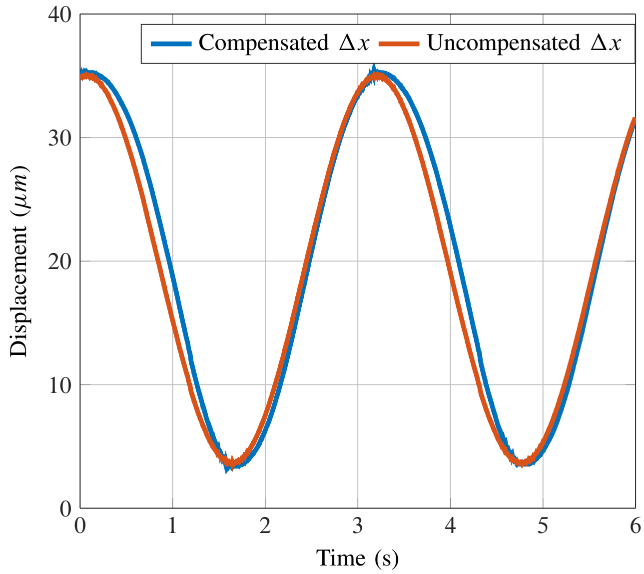

(b)

Fig. 5: Effects of hysteresis on PMA displacement versus input voltage (a), and time (b) uncompensated and compensated. Through compensation, the hysteresis exhibited between the input voltage signal and actual PMA elongation is almost fully eliminated.

the shaft, induced by the high load on the motor. This is an indication that the motor is very close to its power limit. If load or speed is increased further, a tooth skip will occur at the point of resonance.

Furthermore, a lack of symmetry along the first diagonal of the trajectory plot is observed. This indicates that the loading on the stack actuators is not symmetrical. Specifically, the flattened region visible in both the loaded and unloaded cases in the lower right area of the figures suggests a lack of proper centering between the ring and shaft. The current does not increase as it should, therefore the stacks are blocked and cannot expand properly in that quadrant.

Thus, the performed measurements provide valuable information about the motor itself without the use of any external sensors. Therefore, sensorless operation based only on the motor current is deemed possible, but only after proper compensation of any hysteretic effects. This is the next natural step in the project.

VI. Conclusion

The Piezoelectric Actuator Drive is a rotary motor that employs the micrometer precision of piezoelectric multilayer actuators coupled with a form-fit micro-mechanical gearing in order to produce a precise, powerful rotary motion. These features, coupled with the added benefit of complete magnetic neutrality make the PAD an ideal motor to be used in harsh, radiation-heavy environments or large magnetic fields. One direct application is patient positioning in an MRI scanner where the motor has to cope with magnetic fields of up to 7 Tesla and at the same time ensure that the sensitive imaging process is not disturbed. Therefore, achieving sensorless operation is a requirement since by eliminating all external positioning and torque sensors both the cost and impact on the imaging are reduced.

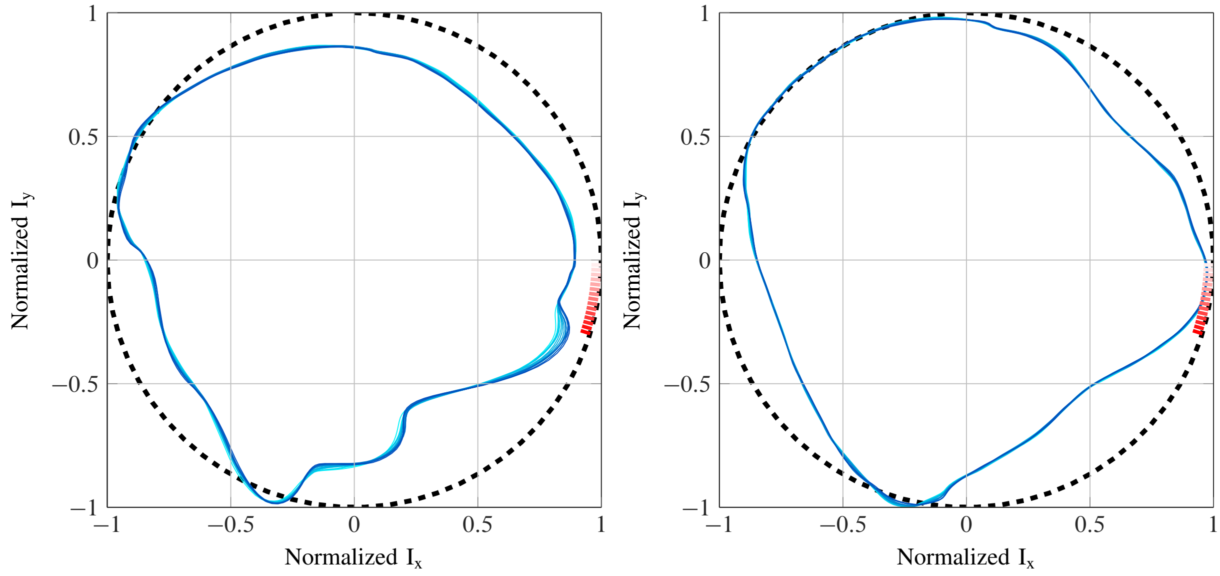

(a) (b)

Fig. 6: Normalized contact point trajectory plot under load (a) and no load (b). In both images, the black dashed circle represents the ideal, desired trajectory. Dark blue and dark red denote a more recent revolution and tooth step, while lighter colors are used to represent the 'history' of the trajectory point in time.

A first step in improving the dynamic operation of the motor is to compensate for the hysteretic behavior of the PMAs, which form the basis of the motion in the motor. Some good results have been achieved through precompensation, but this method is limited in practicality and therefore a feedback-based compensation method is being investigated.

The preliminary analysis of the information contained in the motor current waveforms shows the quality of the mechanical contact point between the motor ring and shaft. A first observation is the major impact PMA hysteresis has on the measurements performed. Nonetheless, the trajectory plot of the ring-shaft contact point extracted from the normalized current measurements indicate rotor-ring misalignment as well as show the absolute position of the weakest point of contact between the two.

Future work will encompass a full removal of all the effects of hysteresis, followed by a new set of current measurements in order to better analyze the behavior of the actuators. This will eventually lead to estimating the desired motor quantities – position, speed and torque – from the measured current waveforms and thereby achieving closed-loop sensorless operation.

Acknowledgements

The authors would like to thank Noliac A/S for providing a PAD motor to be dissected and investigated, as well as the Danish National Advanced Technology Foundation for financial support.

References

[1] A. Kappel, B. Gottlieb, and C. Wallenhauer, "Piezoelectric actuator drive (pad)," *AT-AUTOMATISIERUNGSTECHNIK*, vol. 56, no. 3, pp. 128–135, 2008.

[2] J. Rucha, H. Liess, J. Heinzl, A. Kappel, T. Schwebel, and B. Gottlieb, "Applicability of a piezo actuator drive as a sensorless high precision drive," *10th International Conference on New Actuators*, 2006.

[3] "Standard on piezoelectricity," *IEEE*, 1988.

[4] R. Zeichfussl, B. Gottlieb, C. Wallenhauer, S. Herzig, A. Kappel, and T. Luth, "A method for auto-adjustment of a new piezoelectric drive," in *Mechatronics, 2009. ICM 2009. IEEE International Conference on*, April 2009, pp. 1–6.

[5] G. T. Zsurzsan, C. Mangeot, M. A. E. Andersen, Z. Zhang, and N. A. Andersen, "Piezoelectric stack actuator parameter extraction with hysteresis compensation," *Power electronics and applications, 16th European Conference on*, in press.

[6] C. Wallenhauer, B. Gottlieb, A. Kappel, T. Schwebel, J. Rucha, and T. Lueth, "Accurate load detection based on a new piezoelectric drive principle employing phase-shift measurement," *Journal of Microelectromechanical Systems*, vol. 16, no. 2, pp. 344–350, 2007.

F

Investigating the Electromechanical Coupling in Piezoelectric Actuator Drive Motor Under Heavy Load

2014 IEEE International Power Electronics and Application Conference and Exposition (PEAC2014)

Investigating the Electromechanical Coupling in Piezoelectric Actuator Drive Motor Under Heavy Load

Tiberiu-Gabriel Zsurzsan, Michael A.E. Andersen, Zhe Zhang, Nils A. Andersen
DTU Electrical Engineering
Technical University of Denmark
Oersteds Plads, bld. 349
Kgs. Lyngby, Denmark
Email: tgzsur@elektro.dtu.

Abstract — **The Piezoelectric Actuator Drive (PAD) is an accurate, high-torque rotary piezoelectric motor that employs piezoelectric stack actuators and inverse hypocycloidal motion to generate rotation. Important factors that determine motor performance are the proper concentric alignment between the motor ring and shaft and the similarity of the stack actuators used. This paper investigates the electromechanical coupling of these factors into the motor current through experimental means.**

Keywords* — *motor, actuator, piezoelectric, piezo, stack, multi-layer

I. Introduction

The Piezoelectric Actuator Drive (PAD) which can be seen in Fig. 1 is a type of rotary motor that transforms the linear motion of piezoelectric stack actuators into a precise rotational motion [1]. The operating principle is illustrated in Fig. 2. The micro-mechanical toothing present in the ring and shaft, shown in Fig. 3, enables high positioning accuracy and output torque [2]. This type of toothing combined with the inherent large stiffness of the piezoelectric stack actuators makes the PAD appropriate for voltage-driven open-loop control [3].

Due to its inherent structure, the PAD motor behaves like a fully capacitive, voltage-driven rotary machine. The piezoelectric stack actuators forming the basis of motion in this motor give it a capacitive nature. This, coupled with the reversibility of the piezoelectric effect enable the stacks to act as both actuators and sensors [4]. The current flow to the motor provides information about rotor speed and position, but also indicates the quality of mechanical contact between stator and rotor through electromechanical coupling between the shaft and the stacks.

The aim of this paper is to use current measurement from the piezoelectric stack actuators to describe and qualify the mechanical coupling between the motor ring and shaft under both heavy and no load conditions.

II. Motor operation principle

A piezoelectric stack actuator comprises of hundreds of individual piezoelectric layers separated by thin electrodes. A voltage applied to the stack produces a proportional mechanical elongation. The layers are in a parallel configuration electrically, enabling a reduced voltage level to produce the necessary electric field. Mechanically, they are in a series configuration and therefore the elongation of each layer adds up to produce larger displacement than a single element would.

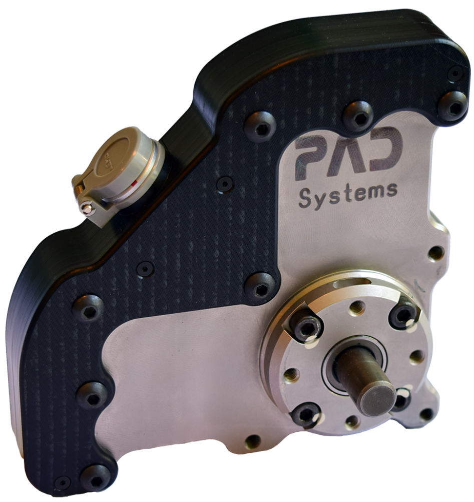

Fig. 1: The Piezoelectric Actuator Drive (PAD)

A widely-used model for piezoelectric structures is described in the IEEE Standard on Piezoelectricity [5]. A simplified version of the second alternative form of the constitutive equations given by the IEEE Standard are shown in (1) and (2), particularized for the dimension of actuation of a stack actuator. Stress in other directions is assumed to be null. Table I shows the quantities, their names and their units of measurement.

$$\Delta x = D_{33} \cdot V - \frac{1}{k} \cdot F \tag{1}$$

$$Q = C \cdot V + D_{33} \cdot F \tag{2}$$

TABLE I: List of constitutive equation symbols and their units

Symbol	Name	SI Unit
Δx	Displacement	m
Q	Stack charge	C
V	Applied voltage	V
F	Applied force	N
D_{33}	Piezoelectric constant	m/V or C/N
k	Stack spring constant	N/m^2

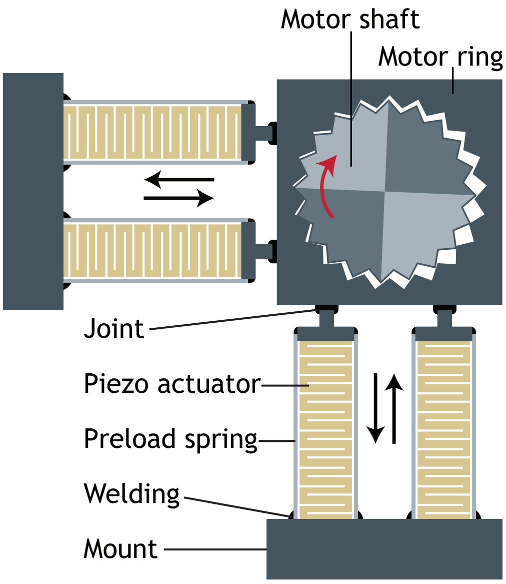

Fig. 2: PAD operating principle

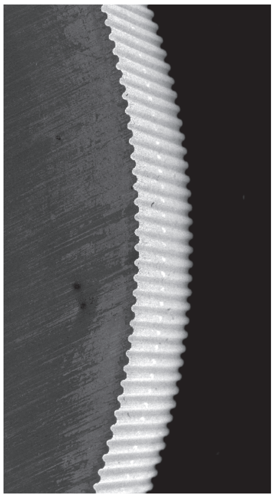

Fig. 3: Microtoothing on the motor shaft. Tooth distance is 120 µm and depth is 38 µm

Two sinusoidal voltages with a 90° phase shift between them are applied to stack actuators placed orthogonally, as shown in Fig. 2. Thereby the motor ring moves in a circular trajectory defined by Cartesian coordinate pair (r_x, r_y), expressed by the parametric equations (3) and (4). This will, in turn, produce a rotation in the motor shaft in the opposite direction to the ring.

$$r_x = x_1 \cdot sin(2\pi f \cdot t + \phi_1) \tag{3}$$

$$r_y = x_2 \cdot sin(2\pi f \cdot t + \phi_2) \tag{4}$$

Where x_1 and x_2 represent the elongation of the orthogonal stacks in m, f is the frequency of rotation in Hz and ϕ_1 and ϕ_2 are the phases in rad, with the restriction that $\phi_1 - \phi_2 = \pm\pi/2$. The trajectory produced is perfectly circular only if $x_1 = x_2$. This requires that the stack actuators are identical. Stack mismatch, improper shaft centering, hysteresis effects, and mechanical effects coupling into the motion will all produce deviations from circularity and in practice this will always be the case.

Every full rotation of the ring will cause the shaft to step one tooth. Therefore the relationship between the electrical and mechanical angular velocities ω_{el} and ω_m is shown in (5), with N_{shaft} and N_{ring} representing the number of teeth on the motor shaft and ring, respectively.

$$\omega_m = \omega_{el} \cdot \frac{N_{shaft} - N_{ring}}{N_{shaft}} \tag{5}$$

III. Experimental Setup

The experiments were conducted using a PAD7220 produced by Noliac A/S, shown in Fig. 5. It contains two piezoelectric stack actuators on each actuation axis. They are represented by the red and blue rectangles in the figure. Their capacitance is rated at 3.5 µF. The rated motor speed is 56.7 rpm with a gearing ratio between ring and shaft of 312. Rated torque is 4 N·m. The applied sinusoidal voltages have an amplitude of 100 V and an offset of 100 V.

An oscilloscope and current clamps with a bandwidth of 50 MHz were used to acquire and log the motor current. Measurements were taken with the motor running at 60 Hz electrical speed, under conditions of no load and 3 N·m of load torque. A data acquisition window of 5 seconds together with a sampling rate of 200 kSa/s were used in order to capture accurate data for a full mechanical revolution. The block diagram of the test setup is presented in Fig. 4.

IV. Measurement Results

Analysis of the measurement data yields interesting results. The acquired data was first normalized for easier comparison between the loaded and unloaded cases. Fig. 6 and Fig. 7 show

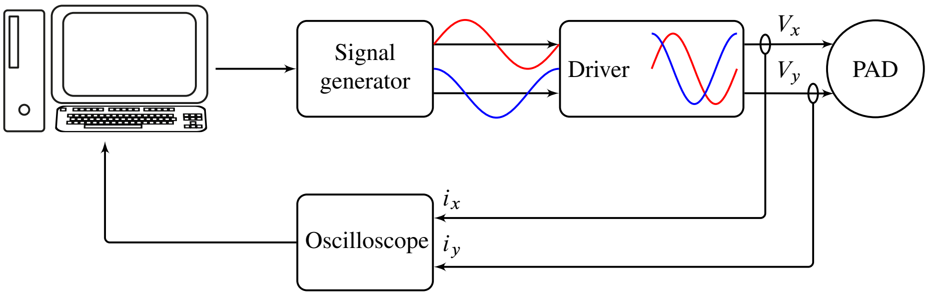

Fig. 4: Block diagram of the experimental setup

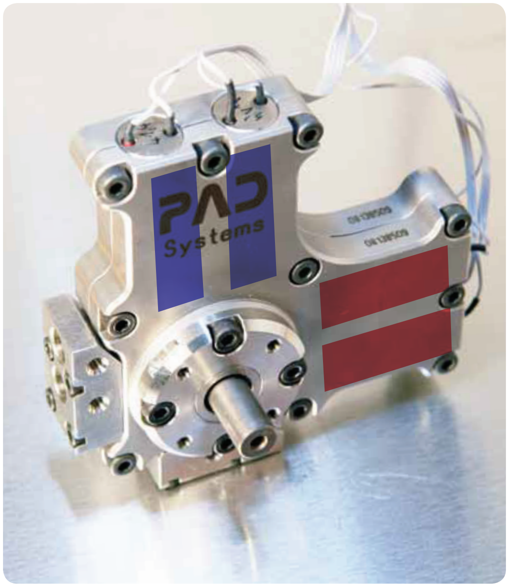

Fig. 5: The PAD7720 without the black cover. The stack ends are exposed: two on the X axis (red rectangles) and two on the Y axis (blue rectangles).

the trajectory of the traveling contact point between the motor ring and shaft during a mechanical quarter-circle motion. Each blue curve represents one electrical revolution and tooth step. The red pegs each represent one tooth on the shaft and help with visually keeping track of shaft position. The dotted black circles represent the ideal, undistorted trajectory.

The first observation is a pronounced deviation from circularity of the trajectory which is caused by lack of hysteresis compensation. Piezoelectric stack actuators are highly hysteretic [6] [7] and this effect can readily be seen in the contact point trajectory.

A second observation is the presence of a resonance in the case of the loaded motor which cannot be seen in the unloaded case. This resonance is the result of hard electromechanical coupling between the actuators and the shaft due to the high load applied to the motor shaft. This indicates that the motor is very close to its output torque limit, while also showing the absolute position of the weakest contact point – the starting point of the resonance. If load is increased further, a tooth skip will occur at that point.

The lack of symmetry along the first diagonal of the trajectory plot further indicates that the loading on the stack actuators is not symmetrical. Specifically, the flattened region visible in both the loaded and unloaded cases in the lower right area of Fig. 6 and Fig. 7 suggests a lack of proper centering between the ring and shaft. The current does not increase as it should, therefore the stacks are blocked and cannot expand properly in that quadrant.

More information can be obtained by analyzing the single-sided amplitude spectra of the currents on both actuation axes with and without motor load. The input signals to the motor are ideally pure-tone phase-shifted sinusoids. Therefore, the ideal actuator response is also sinusoidal. The spectra, shown in Fig. 8 and Fig. 9 were computed over a full mechanical revolution of the motor shaft, meaning 312 electrical signal periods. By analyzing these signals, it becomes quickly obvious that a lot of energy is contained in the signal harmonics. The fundamental frequency mirrors the motor electrical speed (60 Hz), but harmonic components can be detected all the way down to the 92nd harmonic. This confirms the highly nonlinear response of the motor to input voltages.

Furthermore, since the input signals are purely sinusoidal, the quality of the motor response can be evaluated through signal-to-noise ratio (SNR), total harmonic distortion (THD) and signal-to-noise and distortion ratio (SINAD) analyses [8]. Table II presents the values obtained for each actuator axis, with the motor both loaded and unloaded. The SNR is higher under load than in the unloaded case. This is attributed to an increase in signal value while the noise floor is constant. The difference between the two axes in each case is consistent and further enforces the conclusion that the stacks are unevenly loaded. In all cases, the absolute values of the THD and SINAD measurements are approximately equal. This suggests that most of the distortion in the signals is harmonic distortion.

V. Conclusion

The present paper uses empirical methods to investigate the effects of the electromechanical coupling between motor shaft and actuators in a PAD motor, under no load and loads of $3\,\mathrm{N \cdot m}$. The information contained in the trajectory plot of the ring-shaft contact point extracted from the normalized current

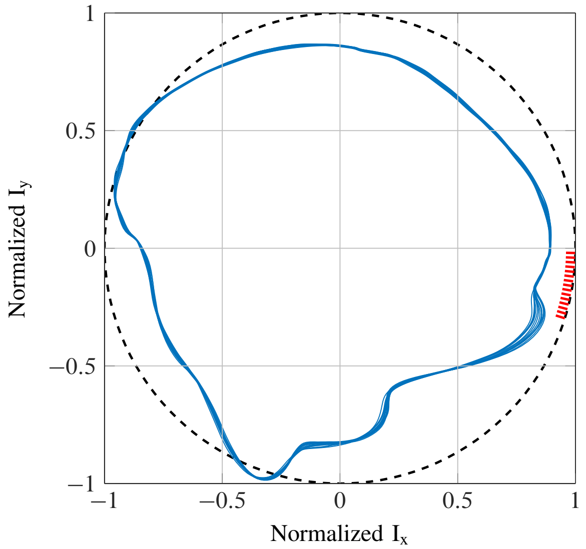

Fig. 6: Normalized contact point trajectory plot under heavy load (blue). The dotted circle is the ideal trajectory while the red pegs represent the number of teeth passed.

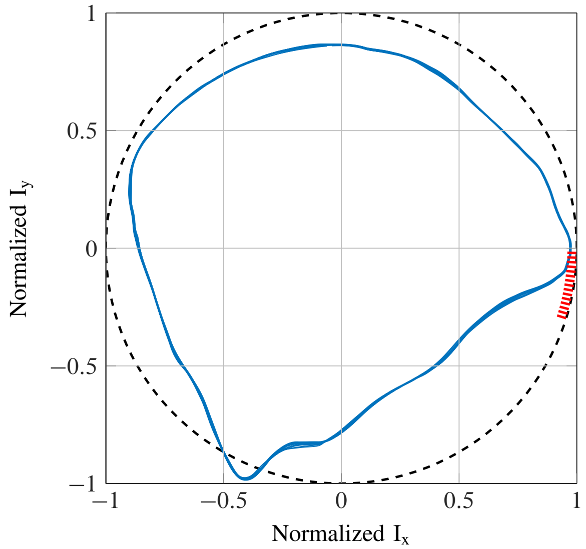

Fig. 7: Normalized contact point trajectory plot under no load (blue). The dotted circle is the ideal trajectory while the red pegs represent the number of teeth passed.

TABLE II: Values for SNR, THD and SINAD in loaded and unloaded cases

Case	**Heavy load**		**No load**	
Axis	***X***	***Y***	***X***	***Y***
SNR (dB)	37.895	40.625	35.079	35.897
THD (dB)	-17.367	-18.503	-17.638	-20.139
SINAD (dB)	17.365	18.543	17.561	20.059

measurements indicate rotor-ring misalignment as well as show the absolute position of the weakest point of contact.

Further analysis of the single-sided amplitude spectra of the stack actuators together with the current signal-to-noise ratio (SNR), total harmonic distortion (THD) and signal-to-noise and distortion ratio (SINAD) calculations enforce the conclusions drawn from the time and spatial plots of the current signals. These metrics also state that most of the distortion in the signals is harmonic distortion.

It was shown that the motor current carries a wealth of information about not only the loading effects on the shaft, but the quality of the mechanical assembly procedure. Moreover, the analysis can be conducted on any readily-assembled motor and therefore this a potentially useful tool in production quality assurance.

References

[1] A. Kappel, B. Gottlieb, and C. Wallenhauer, "Piezoelectric actuator drive (pad)," *AT-AUTOMATISIERUNGSTECHNIK*, vol. 56, no. 3, pp. 128–135, 2008.

[2] J. Rucha, H. Liess, J. Heinzl, A. Kappel, T. Schwebel, and B. Gottlieb, "Applicability of a piezo actuator drive as a sensorless high precision drive," *10th International Conference on New Actuators*, 2006.

[3] R. Zeichfussl, B. Gottlieb, C. Wallenhauer, S. Herzig, A. Kappel, and T. Luth, "A method for auto-adjustment of a new piezoelectric drive," in *Mechatronics, 2009. ICM 2009. IEEE International Conference on*, April 2009, pp. 1–6.

[4] C. Wallenhauer, B. Gottlieb, A. Kappel, T. Schwebel, J. Rucha, and T. Lueth, "Accurate load detection based on a new piezoelectric drive principle employing phase-shift measurement," *Journal of Microelectromechanical Systems*, vol. 16, no. 2, pp. 344–350, 2007.

[5] "Standard on piezoelectricity," *IEEE*, 1988.

[6] L. Juhasz, J. Maas, and B. Borovac, "Parameter identification and hysteresis compensation of embedded piezoelectric stack actuators," *Mechatronics*, vol. 21, no. 1, pp. 329–338, 2011.

[7] G. T. Zsurzsan, C. Mangeot, M. A. E. Andersen, Z. Zhang, and N. A. Andersen, "Piezoelectric stack actuator parameter extraction with hysteresis compensation," *Power electronics and applications, 16th European Conference on*, in press.

[8] C. Karandjeff, C. Hannaford, R. Liggiero, S. Max, and S. J. Tilden, "Measuring snr, sinad, and thd quickly," *EE Evaluation Engineering*, vol. 50, no. 10, pp. 18, 20–1, 2011.

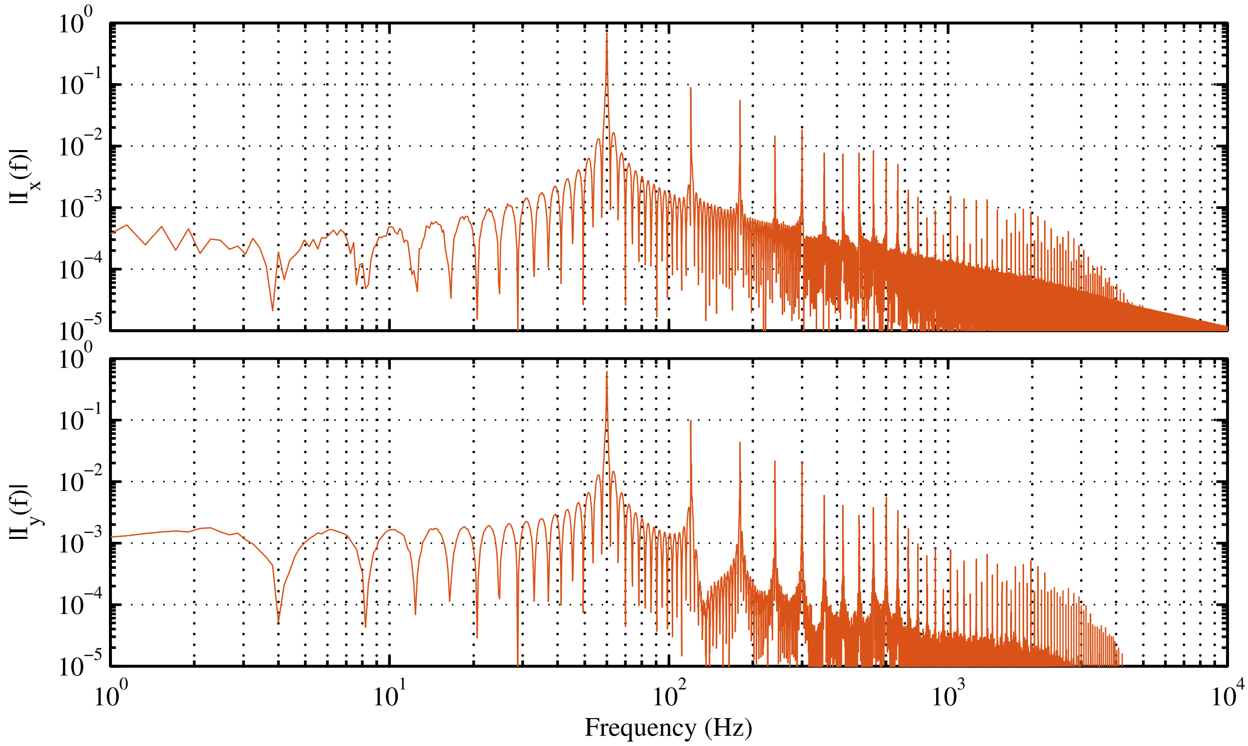

Fig. 8: Single-Sided Amplitude Spectra of $I_x(t)$ and $I_y(t)$ under heavy load

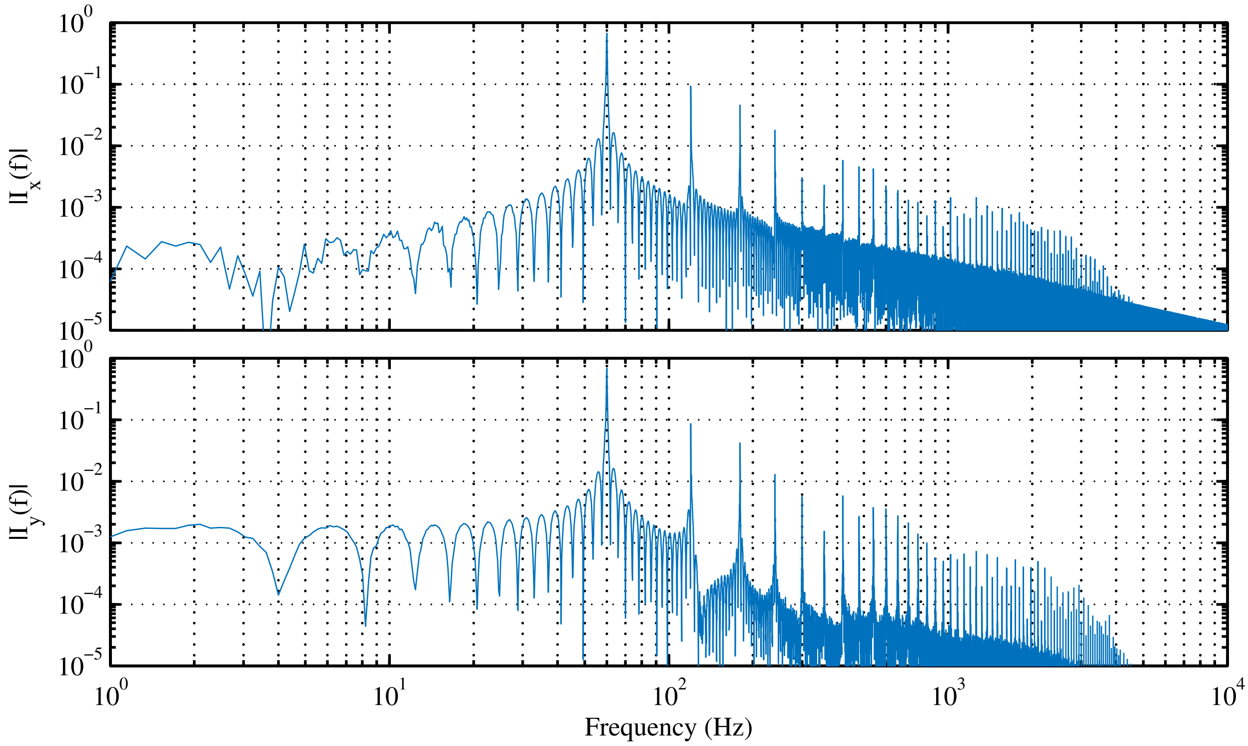

Fig. 9: Single-Sided Amplitude Spectra of $I_x(t)$ and $I_y(t)$ with no load

G

Class-D amplifier design and performance for driving a Piezo Actuator Drive servomotor

2016 IEEE International Conference on Industrial Technology (ICIT2016)

Class-D amplifier design and performance for driving a Piezo Actuator Drive servomotor

Gabriel T. Zsurzsan*, Zhe Zhang, Michael M.A. Andersen and Nils A. Andersen
Department of Electrical Engineering, Technical University of Denmark
Denmark
E-mail: *tgzsur@elektro.dtu.dk

***Abstract*—This paper investigates the behavior of piezoelectric stacks in a Piezoelectric Actuator Drive (PAD) motor, which shows non-linear equivalent impedance and has a dramatic impact on the overall system performance. Therefore, in this paper, the piezo stackt's model is discussed and an improved large signal model is proposed and verified by measurement. Finally, a Class-D amplifier as a power driver and its associated closed-loop control are implemented and tested to control PAD drive effectively.**

***Index Terms*—Piezoelectricity, motor, control**

I. Introduction

THE The Piezoelectric Actuator Drive (PAD) is a new type of electrical motor that employs piezoelectric multilayer actuators which have inherent capacitive behavior [1]–[5]. The PADs internal structure is shown in Fig. 1. Through voltage excitation, the multilayer actuators expand and contract linearly along their length [6]–[8]. Therefore, by applying a sinusoidal voltage to the actuators on one axis and a 90° phase-shift version to the other actuators, the resulting space-vector and trajectory will be circular, and the corresponding waveforms are illustrated in Fig. 2 respectively. In order to control PAD drives effectively and efficiently, in this paper, besides small signal model, an improved large signal model of piezoelectric actuators equipped in PADs is proposed to estimate the apparent power transferring through the power driver accurately. A switched-mode Class-D power amplifier [9], [10] i.e. a synchronous Buck converter is employed as the driver generating the needed two channel phase-shifted sinusoidal outputs. The analysis and design of the power driver and its associated average current mode closed-loop controller implemented digitally are presented. Finally, the analysis is verified by the measurement results from a laboratory prototype.

II. Piezoelectric stack actuators

Considering piezoelectric stack a constant load capacitance allows for designing the power amplifier in terms of component stresses, switching frequency and efficiency. However, neglecting the non-linear nature of the piezo stack impedance hides many important phenomena. To better describe the piezo stacks behavior, both small signal (SS) and large signal (LS) impedance are measured, which can be used for a mathematical analysis of system and more importantly for power driver design. The SS capacitance and loss tangent of a

(a)

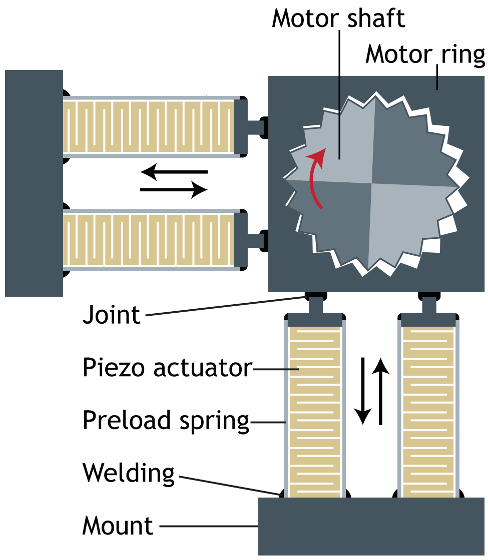

(b)

Fig. 1. PAD motor (a) and its internal structure (b). The internal structure of the PAD is made up of 4 PMA actuators acting against a motor ring, which in turn is coupled to the shaft through a micromechanical gearing. The pitch of the gears is 100 µm.

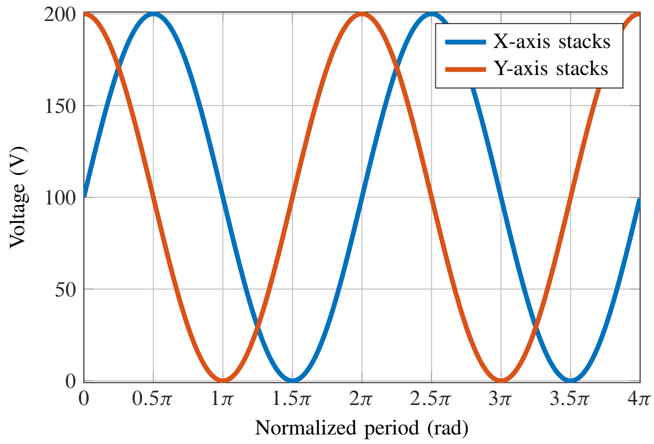

(a)

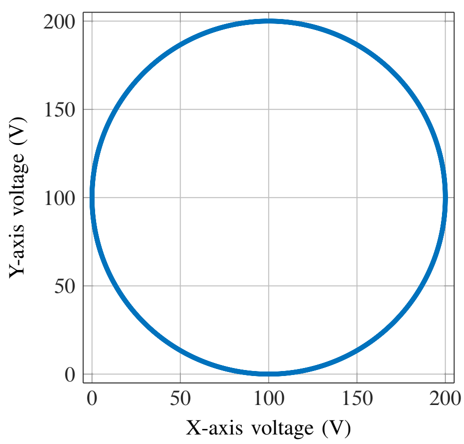

(b)

Fig. 2. Sine and cosine voltage signals applied to the actuators, normalized to their period (a) and ideal spatial trajectory obtained (b)

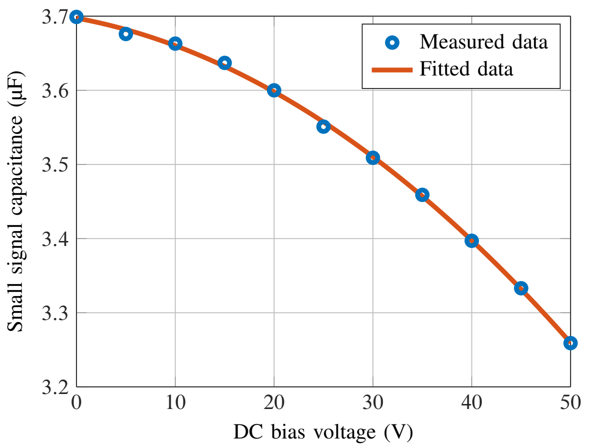

Fig. 3. Derating of small-signal capacitance with the increase of dc voltage.

free standing piezo stack is measured with a 100 Hz, 1 V rms excitation signal by OMICRON Lab Bode 100 and Picotest J2130A DC Bias Injector. The result, which shows a similar small signal feature with ceramic capacitors, can be seen in Fig. 3. The normally used LS model is given in (1), where the current (RMS) of piezo stack is approximated by simple linear function of the SS signal capacitance C_{ss} and applied RMS voltage V_{rms}. However, from Fig. 4a, the measured piezo stack rms currents deviate from the estimated ones based on (1). Therefore, an improved LS model is presented in (2) with an exponential function rather than a linear one, which can more actually predict the load current, as shown in Fig. 4b. The exponential curve is based off of empirical observations of stack behavior. This can then more accurately be used to specify the power driver design.

$$i_{rms} = 2\pi \cdot f \cdot C_{ss} \cdot V_{rms} \tag{1}$$

$$i_{rms} = 2\pi \cdot f \cdot C_{ss} \cdot (a \cdot e^{b \cdot V_{rms}} - c) \tag{2}$$

TABLE I
EMPIRICAL EXPONENTIAL FITTING COEFFICIENTS

	25 Hz	50 Hz	75 Hz	100 Hz	Avg.
a	51.26	45.02	45.72	42.65	46.16
b	0.013	0.014	0.014	0.015	0.014
c	51.62	45.31	46.03	42.87	46.46

where the coefficients a, b and c are obtained by averaging the fitted parameter with four diverse operating frequencies as listed in Table I.

III. Driver Stage

A bidirectional Buck converter illustrated in Fig. 5 is adopted as the power driver in this study. The specifications are listed in Table II. Therefore, based on the LS model given above, the output power per axis as a function of torque and output frequency, and equivalent load resistance as a function of output power are plotted in Fig. 6. Then the maximal delivered power of the driver can be calculated, from which the switching devices and the output inductor can be selected. With the output inductor L of 270 μH, the inductor current ripple-to-average ratio (RAR) at $f = 200\,\text{Hz}$ and $\tau = 2\,\text{N}\cdot\text{m}$ is shown in Fig. 7, where the factor 2 is marked with a red line. With output frequency f decreasing, the RAR will much larger than 2. In this case the inductor current direction reverses twice during every switching period and the power switches can operate under ZVS condition.

IV. Control

The control strategy is an average current control mode. An inner current loop regulates the inductor current while an outer voltage loop regulates the output voltage, where G_{id} and G_{vi} represent the SS transfer functions of duty cycle to inductor current and inductor current to output voltage, respectively. The current compensator is a PID controller to achieve an

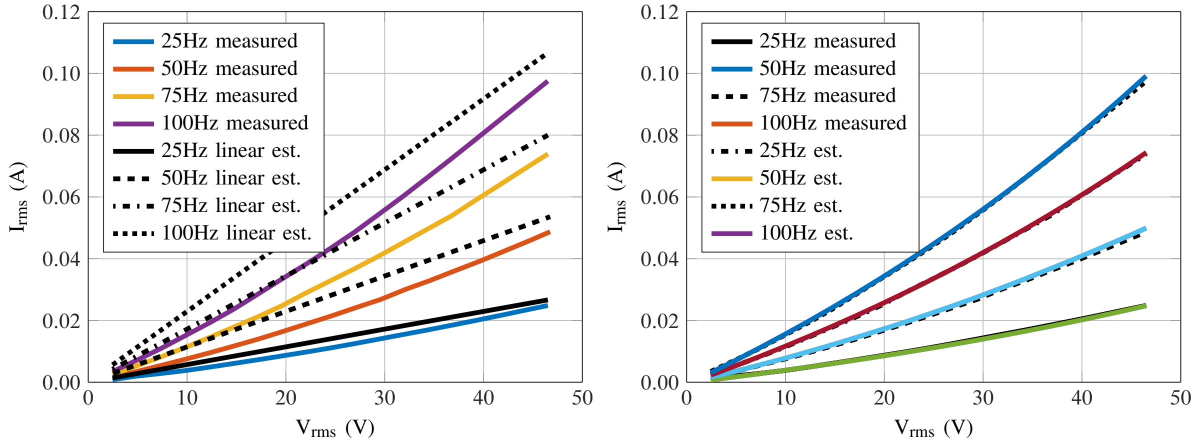

(a) (b)

Fig. 4. large signal model of the stacks: normal model (a), and the proposed improved model (right).

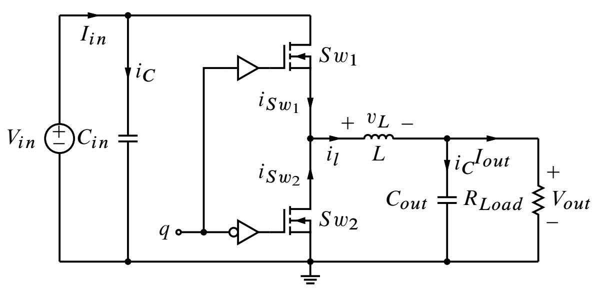

Fig. 5. Synchronous buck converter.

TABLE II
DRIVER DESIGN SPECIFICATIONS

Specification	Value
Input voltage	200 Vdc
Modulation index M	0.1 – 0.9
Output voltage	20 V – 180 V
Switching frequency f_s	100 kHz
Output frequency	0 Hz – 200 Hz
Maximum motor torque τ	2 N·m

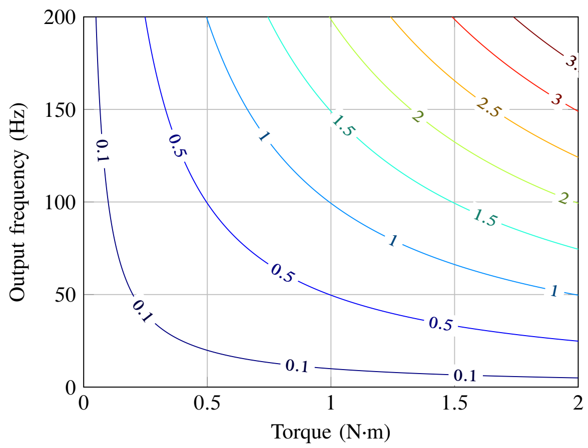

(a)

Fig. 6. Output power of the driver versus frequency and torque.

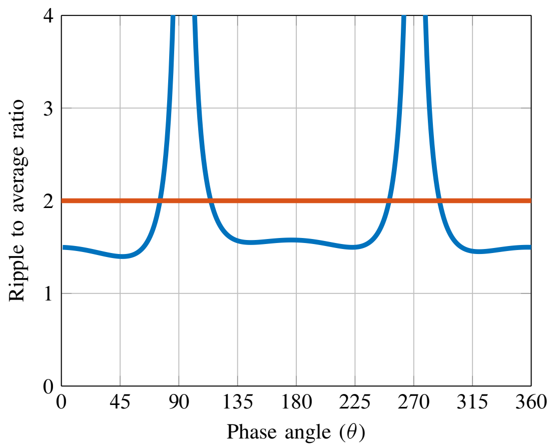

Fig. 7. Inductor current ripple-to-average ratio.

adequate phase margin, since the sampling and hold process as well as the computational delay contributes a negative effect on phase response. The outer voltage compensator is simply a P controller to avoid overshoot. The transfer functions of the controllers are shown in (3) and (4)

$$G_{ci} = \frac{0.1393 - 0.1748z^{-1} + 0.0548z^{-2}}{1 - 1.043z^{-1} + 0.0432z^{-2}} \tag{3}$$

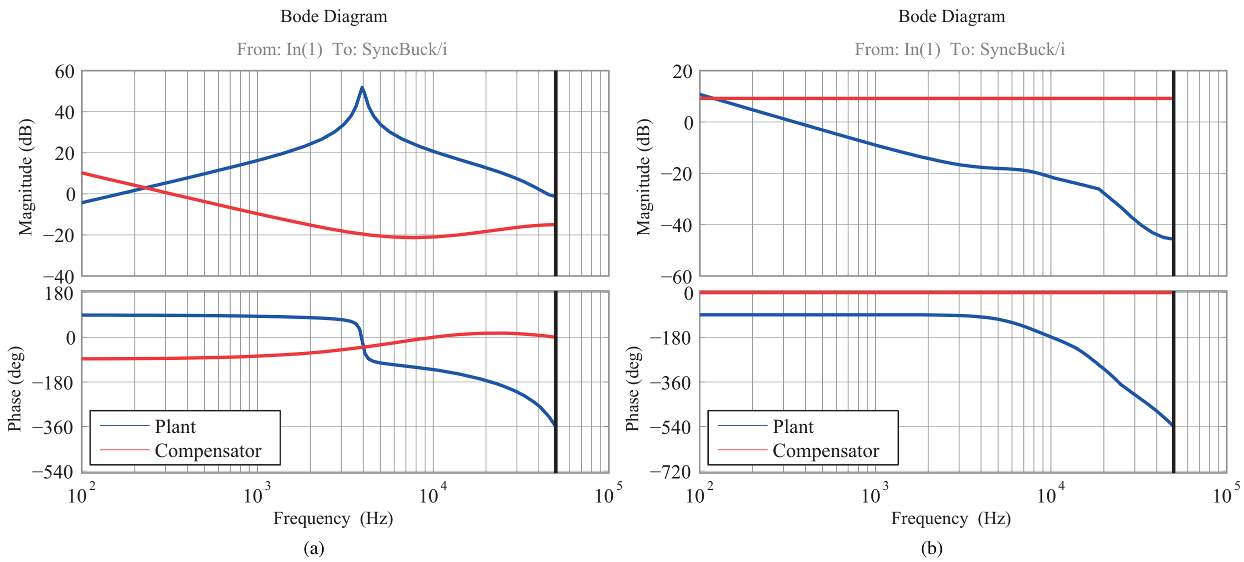

Fig. 8. Open loop response of uncompensated current loop (blue) and designed compensator (red) (a) and response of uncompensated voltage loop (blue) and designed compensator (red) (b).

$$G_{cv} = 2.875 \tag{4}$$

The frequency responses of the plant and the designed controllers are presented in Fig. 8.

V. Experimental results

In order to verify the analysis, a prototype is built, and also the thermal measurement under full load from an infrared camera is presented in Fig. 9, where the maximum temperature stays below $60\,°C$. Output voltage waveforms at lowest and highest frequencies tested are shown in Fig. 10. Moreover, a X-Y voltage plot of the two outputs under frequencies ranging from 10 Hz – 250 Hz is shown, which verifies the voltage control performance of the driver. To verify that the motor is truly working in closed loop, its response to signal disturbances is tested. As the system is only tested without external load the only disturbances that can be tested are changes in input voltage. Fig. 11 shows the output response to the input voltage step from 200 V to 250 V, and there is no significant voltage change in output voltage which means the control loop works effectively. Finally, the power loss in the PAD system including the driver and the motor has been measured and shown in Fig.12. It can be seen clearly that the converter loss increases with increasing output frequency.

VI. Conclusion

This work presents the implementation of a digitally controlled Class-D switch mode driver to drive a PAD motor. The piezo elements of the motor have been analyzed with both small and large signals. The motor is a highly capacitive load with a capacitance increase of up to 100% at large signals. Due to the capacitive nature of piezo actuators, the power driver has to been designed physically large relative to the active power it processes. A discrete closed loop controller is implemented on the digital signal controller. Measurement results show that the PAD has been driven with up to 250 Hz and the THD over the entire frequency range is from 0.9% to 1.4%. The PAD was not pushed any further in frequency due to the high loss on the piezoelectric stacks. It would be interesting to optimize the driver in terms of size and power efficiency in future research work.

References

[1] A. I. Colli-Menchi and E. Sanchez-Sinencio, "A high-efficiency self-oscillating class-d amplifier for piezoelectric speakers," *IEEE Trans. Power Electron.*, vol. 30, no. 9, pp. 5125–5135, 2015.

[2] B. Ducharne, L. Garbuio, M. Lallart, D. Guyomar, G. Sebald, and J.-Y. Gauthier, "Nonlinear technique for energy exchange optimization in piezoelectric actuators," *IEEE Trans. Power Electron*, vol. 28, no. 8, pp. 3941–3948, 2013.

[3] R.-J. Wai and C.-H. Tu, "Design of total sliding-mode-based genetic algorithm control for hybrid resonant-driven linear piezoelectric ceramic motor," *IEEE Trans. Power Electron.*, vol. 22, no. 2, pp. 563–575, 2007.

[4] E. Goenaga, J.-P. Ferrieux, and J. Barbaroux, "Contactless power transfer system for high power piezoelectric actuators in aeronautical applications," *IEEE Applied Power Electronics Conf. and Exhibition, Proc.*, pp. 3172–3179, 2013.

[5] S. Ben-Yaakov, E. Rozanov, T. Wasserman, T. Rafaeli, L. Shiv, and G. Ivensky, "Resonant driver for a piezoelectric motor with single transistor direction switches," *IEEE Applied Power Electronics Conf. and Exposition, Proc.*, vol. 2, pp. 1037–1043, 2000.

[6] P. A. Sente, F. M. Labrique, and P. J. Alexandre, "Efficient control of a piezoelectric linear actuator embedded into a servo-valve for aeronautic applications." *IEEE Trans. Ind. Electron.*, vol. 59, no. 4, p. 1971, 2011.

[7] N. Bonnail, D. Tonneau, F. Jandard, G. Capolino, and H. Dallaporta, "Variable structure control of a piezoelectric actuator for a scanning tunneling microscope," *IEEE Trans. Ind. Electron.*, vol. 51, no. 2, pp. 354–363, 2004.

[8] S. Huang, K. K. Tan, and T. H. Lee, "Adaptive sliding-mode control of piezoelectric actuators," *IEEE Trans. Ind. Electron.*, vol. 56, no. 9, pp. 3514–3522, 2009.

[9] M. C. W. Hoyerby and M. A. E. Andersen, "Carrier distortion in hysteretic self-oscillating class-d audio power amplifiers: Analysis and optimization," *IEEE Trans. Power Electron*, vol. 24, no. 3-4, pp. 714–729, 2009.

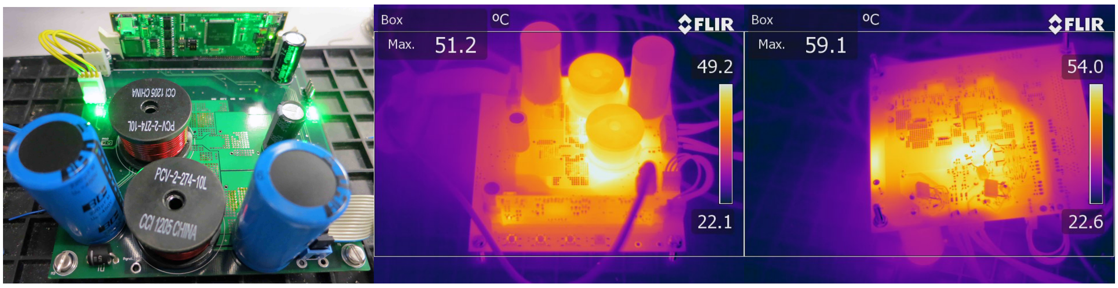

(a) (b) (c)

Fig. 9. Image of the designed prototype (a) and thermal image of converter running at full load. Top (b) and bottom (c) views show maximum operating temperature to be below 60 °C.

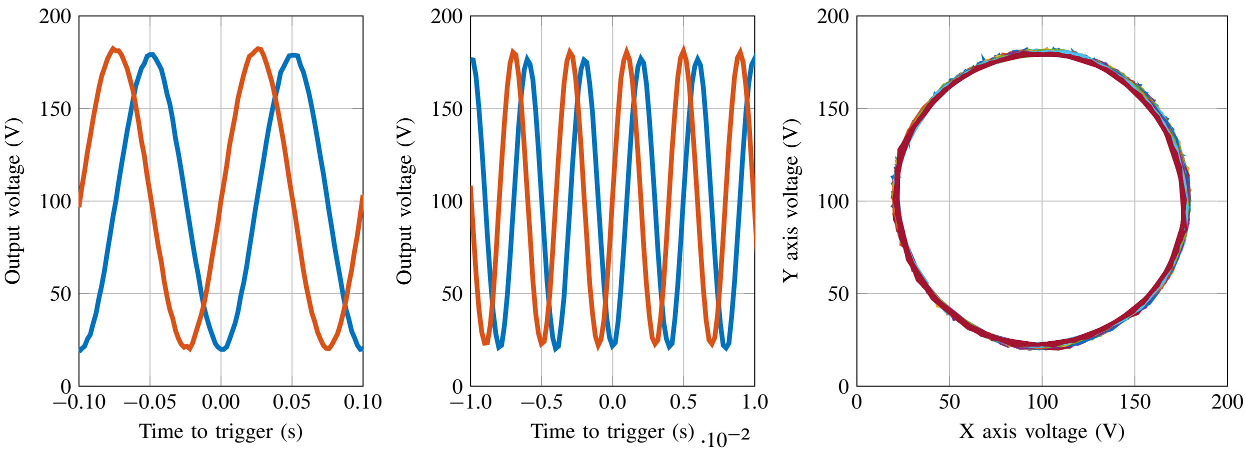

(a) (b) (c)

Fig. 10. Plot of voltage waveforms versus time at 10 Hz (a) and 250 Hz (b).

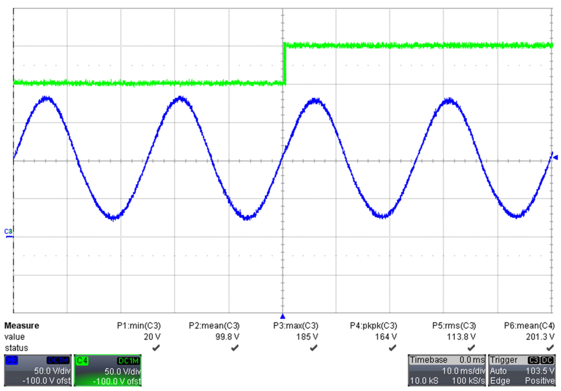

Fig. 11. Response to input voltage step.

[10] A. Oliva, S. Ang, and G. Bortolotto, “Digital control of a voltage-mode synchronous buck converter,” *IEEE Trans. Power Electron*, vol. 21, no. 1, pp. 157–163, 2006.

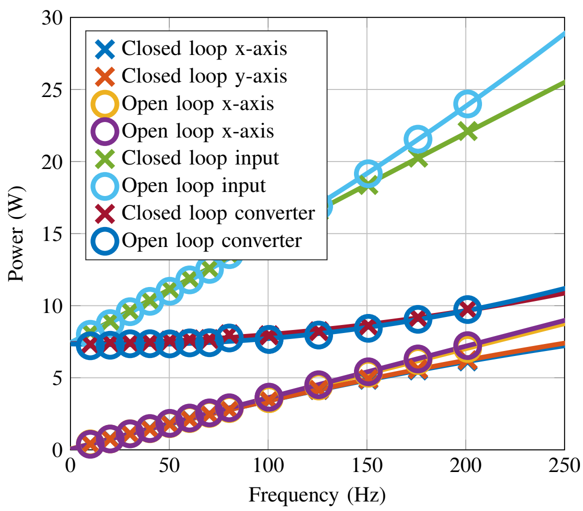

Fig. 12. Total power and loss versus frequency.

H

RESONANT POWER CONVERTER COMPRISING ADAPTIVE DEAD-TIME CONTROL

Patent application

RESONANT POWER CONVERTER COMPRISING ADAPTIVE DEAD-TIME CONTROL

The invention relates in a first aspect to a resonant power converter comprising: a first power supply rail for receipt of a positive DC supply voltage and a second power supply rail for receipt of a negative DC supply voltage. The resonant power converter comprises a resonant network with an input terminal for receipt of a resonant input voltage from a driver circuit. The driver circuit is configured for alternatingly pulling the resonant input voltage towards the positive and negative DC supply voltages via first and second semiconductor switches, respectively, separated by intervening dead-time periods in accordance with one or more driver control signals. A dead-time controller is configured to adaptively adjusting the dead-time periods based on the resonant input voltage.

BACKGROUND OF THE INVENTION

A sub-group of resonant power converter comprises a piezoelectric transformer as a resonant circuit or resonant tank. Piezoelectric power converters are a viable alternative to traditional magnetics based resonant power converters in numerous voltage or power converting applications such as AC/AC, AC/DC, DC/AC and DC/DC power converter applications. Piezoelectric power converters are capable of providing high isolation voltages and high power conversion efficiencies in a compact package with low EMI radiation. The piezoelectric transformer is normally operated in a narrow frequency band around its fundamental or primary resonance frequency with a matched load coupled to the output of the piezoelectric transformer. The optimum operating frequency or excitation frequency shows strong dependence on different parameter such as temperature, load, fixation and age. So-called zero-voltage-switching (ZVS) operation, or soft-switching, of a driver circuit, coupled to the input terminal of a resonant network, which may comprise a piezoelectric transformer, may be achieved via the intrinsic input impedance characteristics of the resonant network or may be achieved by coupling an external inductor in series or parallel with the output signal supplied by the driver circuit. In both cases an input impedance of the resonant network may appear inductive across a relatively large frequency range such that capacitances at the output of the driver circuit can be alternatingly charged and discharged by resonant current during dead-time periods of the driver circuit without inducing prohibitive power lossess. The driver circuit may comprise a half-bridge or full-bridge MOS transistor circuit.

For obtaining the desired zero voltage switching (ZVS), a dead-time period or interval (DT) of the driver circuit needs to be sufficiently large to allow charging and discharging of the input terminal of the resonant network. The present inventors have discovered that a dead-time period shorter than required for zero voltage switching causes hard switching of the driver circuit. Likewise, a dead-time period longer than required for zero voltage switching may either cause hard switching of the driver circuit or may cause soft switching of the driver circuit with sub-optimum efficiency. However, prior art resonant power converters have been provided with a fixed dead-time period, for example tailored to characteristics of a particular piezoelectric transformer at fixed operating conditions. The fixed dead-time period is unable to account for manufacturing tolerances and drift of active and passive electronic components of the resonant power converter, in particular those of a piezoelectric transformer. Hence, the use of fixed dead-time period leads to increased power consumption of practical resonant power converters where the above-mentioned manufacturing tolerances and drift of active and passive electronic components are inevitable.

Hence, it would be advantageous to provide adjustable dead-time periods of appropriate length or duration to secure zero voltage switching of the driver circuit of a resonant power converter in general and in piezoelectric power converters specifically.

SUMMARY OF THE INVENTION

A first aspect of the invention relates to a resonant power converter comprising:
a first power supply rail for receipt of a positive DC supply voltage and a second power supply rail for receipt of a negative DC supply voltage,
a resonant network comprising an input section and an output section wherein the input section comprises an input terminal for receipt of a resonant input voltage and the output section comprises an output terminal for providing a resonant output voltage in response to the resonant input voltage,
a driver circuit comprising a first semiconductor switch coupled to the positive DC supply voltage and a second semiconductor switch coupled to the negative DC sup-

ply voltage and a driver output connected to the input terminal for supply of the resonant input voltage;
wherein the driver circuit is configured for alternatingly pulling the resonant input voltage towards the positive and negative DC supply voltages via the first and second semiconductor switches, respectively, separated by intervening dead-time periods in accordance with one or more driver control signals,
a dead-time controller configured to adaptively adjusting the dead-time periods based on the resonant input voltage.

The dead-time controller is able to provide adequate length or duration of the dead time periods of the driver circuit to deliver sufficient energy for charging and discharging the input capacitance at the input terminal of the resonant network for example an input electrode of a piezoelectric transformer. This feature enables zero voltage switching (ZVS) and/or zero current switching (ZCS) of the driver circuit and minimizes the energy consumption involved in the switching activity of the first and second semiconductor switches of driver circuit. The dead-time controller of the resonant power converter may utilize various features of the resonant input voltage for detecting an optimum dead time period and adaptively adjusting the dead-time period. The dead-time controller may be configured to adjust the dead-time period during every switching cycle of the resonant input voltage based on an instantaneous value thereof. The switching cycle is determined by a switching frequency of the resonant power converter. Alternatively, the dead-time controller may be configured to adjust the dead-time period during a specific operating condition of the power converter for example solely during a start-up phase or initialization time of the resonant network or solely during steady state operation of the resonant network as discussed in further detail below with reference to the appended drawings. The adaptive adjustment of the dead-time period may hence result in a decrease of energy loss and consequently increased efficiency of the resonant power converter both during the start-up phase and during steady state operation.

If the resonant network comprises a piezoelectric transformer which may possess a zero-voltage-switching factor (ZVS factor) larger than 100%, preferably larger than 120%, such as larger than 150% or 200%. This means the piezoelectric transformer possesses native ZVS properties or characteristics as discussed in further detail for example in U.S. patent application No. 14/237,432. A number of highly useful piezoelectric transformers suitable for application in the present piezoelectric power converters with high power conversion efficiencies and native ZVS properties are disclosed in European patent application No. 11176929.5.

The driver circuit may comprise a half-bridge or H-bridge driver. The half-bridge driver circuit may comprise a first semiconductor switch and a second semiconductor switch coupled in series between the positive DC supply voltage and the negative DC supply voltage. A midpoint node between the first and second semiconductor switches may be deliver the driver output voltage or signal to the input terminal of the resonant network such as an input electrode or electrodes of a primary/input section of the piezoelectric transformer. Each of the first and second semiconductor switches may comprise a MOSFET for example a DMOS, PMOS or NMOS device. Each of the first and second semiconductor switches further comprises a control terminal or input such as a gate terminal for receipt of the driver control signal. A first driver control signal of the first semiconductor switch is configured to switch the first semiconductor switch between a conducting/ON state and a non-conducting/OFF state. A second driver control signal of the second semiconductor switch is likewise configured to switch the second semiconductor switch between a conducting/ON state and a non-conducting/OFF state. The first and second driver control signals are preferably non-overlapping such that the first semiconductor switch pulls the resonant input voltage towards the positive DC supply voltage via its relatively small on-resistance in the conducting state and the second semiconductor switch after the intervening dead-time period pulls the resonant input voltage towards the negative DC supply voltage via its relatively small on-resistance in the conducting state. Hence, during the dead time period the resonant input voltage or signal is alternatingly charged and discharged from the positive DC supply voltage to the negative DC supply voltage and vice versa by resonant current flowing through an intrinsic input impedance of the piezoelectric transformer and/or by resonant current flowing through, or out of, a series inductor of the resonant network as discussed in further detail below with reference to the appended drawings. The resonant input signal is clamped to the positive DC supply voltage in a first time period where the first semiconductor switch is conducting and the second semiconductor switch non-conducting. Likewise, the resonant input signal is clamped to the negative DC supply voltage in a second time period where the second semiconductor switch is conducting and the first semiconductor switch non-conducting.

Hence, according to one embodiment of the resonant power converter, the first semiconductor switch comprises a conducting state where the input terminal is connected to the positive DC supply voltage and the second semiconductor switch comprises a conducting state where the input terminal is connected to the negative DC supply voltage; and where the first semiconductor switches is in a non-conducting state during the dead-time periods and the second semiconductor switch is in a non-conducting state during the dead-time periods.

The switching frequency of the resonant power converter may lie between 75 kHz and 500 kHz such as between 100 kHz and 150 kHz. The resonant power converter may comprise a feedback loop which induces self-oscillation of the resonant power converter. The feedback loop ensures that the switching or excitation frequency automatically tracks changing characteristics of a piezoelectric transformer and electronic circuitry of the input side of the power converter.

According to one embodiment, the dead-time controller utilizes a level or amplitude of the instantaneous resonant input voltage to detect the respective time instant to switch the first or the second semiconductor switch to its conducting state. According to another embodiment, the dead-time controller utilizes a waveform shape of the instantaneous resonant input voltage to detect the respective time instants or phases at which to switch the first or second semiconductor to the conducting state as discussed in further detail below with reference to the appended drawings.

The dead-time controller may be configured to adjust a phase or timing of the first driver control signal of the first semiconductor switch and a phase or timing of the second driver control signal of the second semiconductor switch to adaptively adjust the duration of the dead-time periods as discussed in further detail below with reference to the appended drawings.

The dead-time controller may comprise a steady-state controller comprising:
a first comparator configured to compare the instantaneous resonant input voltage

to the positive DC supply voltage and supply a first comparator output signal (Z_{HS}) for adjusting the phase of the first driver control signal in accordance with the first comparator output signal. A second comparator of the steady-state controller may be configured to compare the instantaneous resonant input voltage to the negative DC supply voltage and supply a second comparator output signal (Z_{LS}) for adjusting the phase of the second driver control signal in accordance with the second comparator output signal.

The dead-time controller may comprise a start-up controller configured to detect a waveform shape of the instantaneous resonant input voltage; and
generating a first control signal (Z_{MH}) for adjusting the phase of the first driver control signal in accordance with the waveform shape; and/or
generating a second control signal (Z_{ML}) for adjusting the phase of the second driver control signal in accordance with the waveform shape.

The dead-time controller may be configured to detect the waveform shape of the resonant input voltage by comparing the instantaneous resonant instantaneous transformer input voltage with a delayed replica of the resonant input voltage as discussed in further detail below with reference to the appended drawings. The waveform shape of the resonant input voltage may be utilized by the dead-time controller to:
detect a local maximum of the waveform of the instantaneous resonant input voltage in response to the delayed replica of the resonant input voltage exceeds the instantaneous resonant input voltage; and/or
detect a local minimum of the waveform of the instantaneous resonant input voltage in response to the delayed replica of the resonant input voltage falls below the instantaneous resonant input voltage.

The dead-time controller may be configured to limit the instantaneous resonant input voltage between a lower threshold voltage and an upper threshold voltage before detecting the local maximum and/or detecting the local minimum. The lower threshold voltage may for example lie between 0.05 and 0.2 times the positive DC supply voltage and the upper threshold voltage may lie between 0.75 and 0.95 times the positive DC supply voltage if the negative DC supply voltage is ground or zero volt.

The dead-time controller may comprise a first digital OR circuit configured to logically OR the first comparator output signal and the first control signal; and
a second digital OR circuit configured to logically OR the second comparator output signal and the second control signal.

As discussed above, the driver circuit and the resonant network are preferably configured for ZVS operation or ZCS operation at the switching frequency of the resonant power converter to charge and discharge the resonant input voltage during the dead-time periods with minimal power consumption.

As discussed previously, the resonant network may comprise a piezoelectric transformer wherein the primary or input section of the piezoelectric transformer is coupled to the resonant input voltage to supply a transformer input voltage. The secondary section of the piezoelectric transformer may generate the resonant output voltage.

A second aspect of the invention relates to a method of adaptively controlling a dead-time interval of a driver circuit of a resonant power converter. The method may comprise steps of:
generating first and second non-overlapping driver control signals for the driver circuit in accordance with a switching frequency signal of the resonant power converter, wherein the driver circuit is coupled between positive and negative DC supply voltages for supply of power,
applying the first and second non-overlapping driver control signals to the driver circuit to generate a driver output signal alternating between the positive DC supply voltage and negative DC supply voltage separated by intervening dead-time periods or intervals,
applying the driver output voltage to an input terminal of the resonant network to generate a resonant input voltage,
generating a resonant output voltage in response to the resonant input voltage at an output side or terminal of the resonant network ,
detecting a feature of the resonant input voltage,

adjusting a duration of the dead-time interval or period of the driver circuit based on the detected feature of the resonant input voltage.

The method may comprise detecting the instantaneous resonant input voltage in each switching cycle of the switching frequency of the resonant power converter and adjusting the dead-time period adjusted accordingly in response. Other embodiments, may be adjusting the dead-time periods less frequently for example during every second, third or fourth switching cycle of the resonant input voltage. The resonant power converter may comprise a rectification circuit coupled to the resonant output voltage of the resonant network for example an output signal of the secondary side of a transformer such as the piezoelectric transformer. The rectification circuit may comprise a half-wave rectifier or a full-wave rectifier.

BRIEF DESCRIPTION OF THE DRAWINGS

Preferred embodiments of the invention are described in more detail in connection with the appended drawings, in which:

FIG. 1 shows a simplified schematic block diagram of a prior art piezoelectric power converter,

FIGS. 1A, 1B and 1C show respective plots of equivalent circuits and resonant current flow of the piezoelectric transformer of the piezoelectric power converter during eight separate time sub-intervals of a switching cycle,

FIG. 2A) shows corresponding waveforms of transformer input voltage and resonant current during one switching cycle of the prior art piezoelectric power converter in steady state operation where ZVS is achieved,

FIG. 2B) shows corresponding waveforms of transformer input voltage and resonant current during one switching cycle of the prior art piezoelectric power converter in steady state operation where ZVS is achieved,

FIG. 3A) shows a first example of corresponding waveforms of the transformer input voltage and resonant current during one switching cycle of the prior art piezoelectric power converter during a start-up phase or period of the converter,

FIG. 3B) shows a second example of corresponding waveforms of the transformer input voltage and resonant current during one switching cycle of the prior art piezoelectric power converter in steady state operation,

FIG. 4A) shows corresponding waveforms of the resonant input voltage and resonant current during one switching cycle of a resonant power converter, based on a piezoelectric transformer, in accordance with a first embodiment of the invention in steady state operation where the dead-time period is optimum and ZVS is achieved,

FIG. 4B) shows corresponding waveforms of the resonant input voltage and resonant current during one switching cycle of the piezoelectric power converter in accordance with the first embodiment during a start-up phase or period where the dead-time period is optimum,

FIG. 5 is a simplified schematic circuit diagram of the resonant power converter in accordance with the first embodiment of the invention,

FIG. 5A is a simplified schematic circuit diagram of a resonant power converter based on a LCC power converter in accordance with a second embodiment of the invention,

FIG. 6 is a schematic block diagram of a preferred embodiment of the dead-time controller of the first and second embodiments of the resonant power converter; and

FIG. 7 shows experimentally measured normalized voltage and current waveforms of the transformer input voltage and resonant current of the piezoelectric power converter captured through several switching cycles of the start-up phase and corresponding waveforms of a prior art piezoelectric power converter.

DETAILED DESCRIPTION OF PREFERRED EMBODIMENTS

The below-appended description of preferred embodiments of the piezoelectric power converters uses the following:

NOMENCLATURE:

V_F: Transformer input voltage or switching voltage.

i_{res}: Resonant current of piezoelectric transformer.

I_{pk} : Peak value of the resonant current of the piezoelectric transformer.

ω : Switching angular frequency.

Cd1: Input electrode capacitance of the piezoelectric transformer.

Cd2: Output electrode capacitance of the piezoelectric transformer.

R: Dielectric losses inside the piezoelectric transformer.

C: Resonant capacitance of the piezoelectric transformer.

L: Internal inductance of the piezoelectric transformer.

C_{oss}: Output capacitance of MOSFETs of a driver circuit.

C_{in}: Equivalent input capacitance of the piezoelectric transformer attached to a driver circuit.

DT: Dead time.

ODT: Optimum dead time.

FIG. 1 shows a simplified schematic block diagram of a prior art resonant power converter 100 based on a piezoelectric transformer 104. The piezoelectric transformer, PT, 104 is represented by a simplified equivalent electric circuit diagram inside box 104. A lower waveform plot 101 of FIG. 1 shows various voltage and current waveforms of the prior art piezoelectric power converter 100 during operation at a certain switching or excitation frequency as discussed in further detail below. The piezoelectric power converter 100 additionally comprises an input driver circuit 103 electrically coupled to an input electrode of the piezoelectric transformer 104 for receipt of transformer input voltage V_F. Hence, the transformer input signal applies an ac input drive signal to the input or primary section of the piezoelectric transformer 104. A driver control circuit (not shown) may be generating appropriately timed gate control signals for NMOS transistors S_1 and S_2 of the input driver 103. A second input electrode of the piezoelectric transformer 104 may be connected to a negative DC supply rail such as ground, GND, as illustrated. An electrical load R_L may be coupled between a pair of output electrodes of the piezoelectric transformer 104. The pair of pair of output electrodes is electrically coupled to a secondary or output section of the piezoelectric transformer 104 as indicated by the 1:N transformer symbol.

In piezoelectric power converters switches are normally semiconductor devices such as MOSFETs with a build-in delay time. This delay time applies to a gate drive signal to start up a switching of the state of the semiconductor switch. Typically, the turn on and turn off delay time of the semiconductor switch differs. Therefore, an amount of delay is given to the gate drive signal to prevent simultaneous conducting states on of the semiconductor switches. Therefore, a dead time period or interval is usually defined as a time interval during a switching transition where both semiconductor switches, e.g. MOSFETs, are in non-conducting states, i.e. turned off. A driver circuit with a half-bridge topology, coupled to an input electrode of the piezoelectric transformer, should preferably have a dead-time period arranged in-between the conducting state periods of the semiconductor switches in order to avoid cross-conduction or shoot through between the semiconductor switches. In piezoelectric power converters, the semiconductor switches of the driver circuit need to supply reactive energy to an input capacitor or capacitance associated with the primary section of the piezoelectric transformer. However, the dead-time period provides appropriate time for charging and discharging this input capacitance of the primary section of the piezoelectric transformer. In contrast only MOSFET's output capacitances need to be charged by resonant current of LCC resonant power converters. These MOSFET's output capacitances are typically around hundreds of pF.

In piezoelectric power converters, the output capacitances of the semiconductor switches and the input capacitance associated with the primary section of the piezoelectric transformer must be charged by resonant current to raise the resonant input voltage at input electrode from the negative DC supply voltage or rail, e.g. ground 0 (V), to the positive DC supply voltage or rail as previously discussed. Since the input capacitance associated with the primary section of the piezoelectric transformer is normally in the range of nF it requires longer time for the resonant current to provide enough charge to the capacitances. Hence, the dead-time of the input driver of a piezoelectric power converter is normally longer or larger than the dead-time of the input driver of a LCC resonant converter. It is often advantageous to keep the dead-time of the input driver of a piezoelectric power converter as short as possible in order to increase power conversion efficiency. Furthermore, this feature will prolong injection of energy to the piezoelectric transformer during turn on time of a high side switch pulling the input the output of the driver circuit towards the positive DC supply voltage. The behaviour of input inductor less piezoelectric power converters where ZVS operation of the input driver circuit is achieved is analysed in the following with reference to the different operating modes illustrated on the plots of FIGS. 1A, 1B and 1C. The present analysis is generally carried out for 8 different operating modes which are divided into 4 intervals. Each of these 4 intervals comprises 2 subintervals as discussed below. Therefore, voltage waveforms of the transformer input voltage V_F through a switching cycle of the input voltage are shown as $t_0 – t_{12}$ with respect to V_F. FIG. 2 shows both the transformer input voltage V_F and corresponding resonant current I_{res} waveforms during one switching cycle in steady state of the piezoelectric power converters where ZVS operation is achieved. The plots a-h of FIGS. 1A), 1B) and 1C) show eight different operating modes. The below-appended analysis is based on the following three assumptions:

1) The converter's input capacitor is considered as summation of the input capacitance C_{d1} of the piezoelectric transformer 104 and the sum of output capacitances of the first and second semiconductor switches S_1 and S_2, typically MOSFETs,

$$C_{in} = 2\,C_{oss}+C_{d1} \tag{1}$$

2) Negligible parasitic components;

3) Fundamental resonating of the piezoelectric transformer due to its high quality factor.

Therefore, Mason's lumped circuit is used to demonstrate operation of the piezoelectric power converter in terms of resonant current and switching voltages of the semiconductor switches S_1 and S_2 of the input driver 103. Resonant current is also illustrated to allow detailed investigation of the operating modes. Output capacitors of S_1 and S_2 and C_{d1} are considered to be the input capacitance of the input section of piezoelectric transformer 104 since parasitic capacitances of a MOSFET based semiconductor switch is typically much lower than C_{d1} or in the other hand they would be charged and discharged together in the dead-time period. Furthermore, the dead-time period is studied in detail below.

1) S_2 is in a conducting switch state or ON while S_1 is in a non-conducting switch state or OFF state: Time interval t_{12} – t_2. The input capacitance of the piezoelectric transformer 104 is fully discharged and essentially short circuited through the relatively small on-resistance of semiconductor switch S_2 which is a low-side switch of the input driver. At t_{12} S_2 is turned on and resonant current I_{res} freewheels through S_2 and changes direction at some point in time which is labelled as t_{1I}. There is a minor voltage difference across S_2 while it is conducting. At time instant t_{1I} the resonant current has crossed zero and changes direction from forward to reverse and the operation of the piezoelectric power converter is illustrated in two subintervals by plots a and b of FIG. 1A. Plot a and plot b show an equivalent circuit and a resonant current flow during each of these time intervals. The below listed set of equations (2) formulates the resonant current and the switching voltage at this interval.

$$\begin{cases} V_F(t) = 0 \\ i_{res}(t) = I_{pk} \sin(\omega t - \phi_I) \end{cases} \qquad (2)$$

2) Both S_2 and S_1 are in a non- conducting switch state or OFF: Time interval $t_2 - t_5$. During this time interval both semiconductor switches are OFF and the resonant current keeps its direction in the reverse orientation going through C_{d1} to a voltage slightly above the positive DC supply voltage V_{DC} until a high-side body diode, i.e. the body diode 113a of MOSFET switch S_1, clamps the transformer input voltage V_F at $V_{DC.}$ Plot c of FIG. 1A shows the equivalent circuit and current flow in this time interval and the set of equations (3) below describes the voltage and current wave-forms.

$$\begin{cases} V_F(t) = \frac{I_{pk}}{C_{in}} \left(\cos(\omega t - \phi_I) - \cos(\omega t_2 - \phi_I)\right) + 0 \\ i_{res}(t) = I_{pk} \sin(\omega t - \phi_I) \end{cases} \qquad (3)$$

During time interval t_5 – t6, the high-side body diode 113a of MOSFET switch S_1 starts to conduct reverse resonant current. Therefore, the transformer input voltage V_F is clipped to the sum of diode voltage drop across the body diode and V_{DC}. This time interval is not requisite because C_{d1} is already charged sufficiently to produce ZVS or soft switching. Plot d of FIG. 1B shows the equivalent circuit and current flow in this time interval and the set of equations (4) below describes the voltage and current waveforms.

$$\begin{cases} V_F(t) = V_{DC} + V_d \\ i_{res}(t) = I_{pk}\ sin(\omega t\ -\ \phi_I) \end{cases} \qquad (4)$$

3) S_1 is in a conducting switch state or ON while S_2 is in a non-conducting switch state or OFF: Time interval $t_6 – t_8$. The high side MOSFET S_1 is conducting and the resonant current I_{res} freewheels through S_1 to be provided to the piezoelectric transformer. There is in practice a minor voltage difference across the finite on-resistance of S_1 while conducing. At t_{2I} the resonant current I_{res} has crossed zero or ground and changes direction from reverse to forward. The operation of the piezoelectric power converter is therefore illustrated in two subintervals by plots e and f of FIG. 1B. The plots e and f show an equivalent circuit and current flow during each of these time intervals. The below listed set of equations (5) formulates the resonant current and the switching voltage V_F during this time interval.

$$\begin{cases} V_F(t) = V_{DC} \\ i_{res}(t) = I_{pk}\ sin(\omega t\ -\ \phi_I) \end{cases} \qquad (5)$$

4) Both S_2 and S_1 are in a non- conducting switch state or OFF: Time interval $t_8 – t_{12}$. At time instant t_8 the high-side switch S_1 is turned off. During this interval both S_2 and S_1 are in OFF states and the resonant current I_{res} keeps its direction in the forward orientation by being fed through the input capacitance C_{d1}. The input capacitance C_{d1} is discharged and the voltage across C_{d1} drops to a level slightly below ground until a low side body diode 113b of S_2 clamps at time instant t_{1I}. Plot g of FIG. 1C shows the equivalent circuit and current flow in this time interval and the set of equations (6) below describes the voltage and current waveforms of I_{res} and V_F.

$$\begin{cases} V_F(t) = \frac{I_{pk}}{C_{in}}\ (cos(\omega t\ -\ \phi_I) - cos(\omega t_8\ -\ \phi_I))\ +\ V_{DC} \\ i_{res}(t) = I_{pk}\ sin(\omega t\ -\ \phi_I) \end{cases} \qquad (6)$$

Time interval $t_{1l} – t_{12}$: At t_{1l} the low side body diode of S_2 starts to conduct forward the resonant current. Therefore, the transformer input voltage V_F is clipped at a level of one diode voltage drop below ground. This time interval is not requisite because C_{d1} is already discharged completely to produce ZVS or soft switching. Plot h of FIG. 1C shows the equivalent circuit and current flow in this time interval and the set of equations (7) below describes the resonant current and the switching voltage V_F during this time interval.

$$\begin{cases} V_F(t) = -V_d \\ i_{res}(t) = I_{pk}\, sin(\omega t - \phi_l) \end{cases} \tag{7}$$

As previously mentioned it is important to have a sufficient duration or length of the intervening dead-times periods between the alternatingly conducting switch states of the first and second semiconductor switches S_1 and S_2. The duration of each of these dead time periods have often been shorter or longer than required to provide optimal ZVS operation for the reasons discussed above. This situation causes so-called hard switching of the first and and/or second semiconductor switches S_1 and S_2 and leads to a marked increase of the power consumption of the driver circuit. FIGS. 2A) and 2B) show these situations in the steady state operation of the prior rat piezoelectric power converter 100 depicted schematically on FIG. 1.

In contrast, the piezoelectric power converter 500 in accordance with the first embodiment of the present invention provides soft-switching of the first and and/or second semiconductor switches S_1 and S_2 of the driver circuit 503 by making an appropriate adaptation of the dead-time period of the driver circuit. In this manner, the dead-time may be adaptively adjusted to charge and discharge the input capacitance C_{d1} of the piezoelectric transformer 504 to the positive DC supply voltage V_{DC} and the negative DC supply voltage - for example ground or 0 V. FIG. 5 shows one embodiment of a piezoelectric power converter 500 in accordance with the present invention where a dead-time controller is configured to adaptively adjust a duration of the dead-time periods based on the transformer input voltage V_F as discussed in further detail below. In addition, FIG. 5A shows a magnetics based LCC topology of resonant power converter 500a in accordance with a second embodiment of the present invention where a dead-time controller is configured to adaptively adjust durations of the dead-time periods based on the resonant input voltage V_F as discussed in further detail below.

FIG. 2A) shows the situation where the dead-time period is shorter than optimum because the first and second semiconductor switches S_1 and S_2 are turned ON too early before the input capacitance C_{d1} is fully charged or discharged, respectively, to the DC supply voltage in question. This situation leads to hard switching of the driver circuit as shown by the respective waveforms 222a, 222b of the instantaneous transformer input voltage V_F and the corresponding resonant current I_{res}.

FIG. 2B) shows the situation where the dead-time period is longer than optimal because the first and second semiconductor switches S_1 and S_2 are turned ON too late. This situation also leads to hard switching of the driver circuit as shown by the respective waveforms 223a, 223b of the instantaneous transformer input voltage V_F and the corresponding resonant current I_{res}. In this case when the resonant current changes direction, the body diodes of the first and second semiconductor switches S_1 and S_2 are not conducting. This causes the input capacitance C_{d1} to discharge at time instant t_{2l} or being charged at t_{1l} before the semiconductor switches are turned on.

In prior art resonant power converters, such as piezoelectric power converters, the dead-time period has been a fixed time or value for the purpose of ensuring that ZVS operation is achieved in the steady state operation of the resonant power converter. This fixed dead-time period is normally longer than the optimal dead-time period discussed above. Another disadvantage of this fixed dead-time period is the build-up of resonant current is delayed during initialization or start-up of the prior art resonant power converter and it takes longer time for the converter to reach steady state operation. While this prolonged start-up time may seem rather insignificant in general, it becomes an important source of excess power consumption in resonant power converters that are turned on and turned off very frequently. This pattern of frequent turn off and turn off of the resonant power converter is for example utilized in so-called burst-mode control or quantum-mode control of the output voltage of the resonant power converter.

The present resonant power converter embodiments eliminate the cases shown in FIGS. 2A) and 2B) with too short or too long dead-time periods, compared to the optimal dead-time period. The piezoelectric power converter embodiment 500 depicted on FIG. 5 comprises the previously discussed dead-time controller OTD 514 which may dynamically detect and set an optimized dead time during every switching cycle of the transformer input voltage V_F. The operation of dead-time controller 514 optimizes, for example during each switching cycle, the time instants where the semiconductor switches S_2 and S_1 are switched from OFF to ON, i.e. turned on, to be placed substantially where the instantaneous transformer input voltage V_F reaches either the positive DC supply voltage or reaches the negative DC supply voltage during steady-state operation of the power converter. Furthermore, the dead-time controller 514 may also be configured to optimize the switching instants of the semiconductor switches S_2 and S_1 during the previously discussed initialization or start-up phase of the power converter. In the latter case, the operation of dead-time controller 514 optimizes, during each switching cycle, the time instants where the semiconductor switches S_2 and S_1 are switched from OFF to ON, i.e. turned on, to be placed substantially where the instantaneous transformer input voltage V_F reaches either a minima level or a maxima level. This may be accomplished by detecting or monitoring the waveform shape of the instantaneous transformer input voltage V_F as discussed in additional detail below. FIG. 4A) shows exemplary waveforms of the transformer input voltage V_F and resonant current I_{res} of the piezoelectric power converter 500 during steady-state operation of the power converter 500. The two consecutive dead-time periods of the depicted single switching cycle of the transformer input voltage V_F are indicated by legend ODT. As shown by the waveform segment 422a, the transformer input voltage V_F increases monotonically from the negative DC supply voltage for ground (0 V) to the positive DC supply voltage $V_{DC.}$ This increase of voltage is caused by the conducting state of the first semiconductor switch S_1 (and hence non-conducting state of S_2) which is pulling the transformer input voltage V_F towards V_{DC} via the small on-resistance of switch S_1. Likewise, the monotonically decreasing waveform segment 422b of the transformer input voltage V_F from the positive DC supply voltage V_{DC} to the negative DC supply voltage (0 V) is caused by the small on-resistance of switch S_2 which is pulling the transformer input voltage V_F towards 0 V or ground.

As shown in FIG. 1B), there are two dead time period periods or intervals in each switching cycle and these dead-time periods correspond to the time intervals $t_2 – t_6$ and $t_8 – t_{12}$ described above. Two time subintervals $t_2 – t_4$ and $t_8 – t_{10}$ are necessary to reach voltage across C_{d1} to the positive and negative DC supply voltage for obtaining ZVS operation of the driver circuit. In effect, the optimum dead time period is may reasonably be defined as a minimum time required for the resonant input voltage V_F to travel from one of the positive and negative DC supply voltages or rails to the other. Therefore, by detecting the time instants or points where the resonant input voltage V_F reaches either the positive or the negative DC supply voltage the time intervals $t_4 – t_6$ and $t_{10} – t_{12}$ can be reduced to a minimum possible time. This is utilized in one embodiment of invention. On the other hand, optimizing the respective time intervals $t_2 – t_4$ and $t_8 – t_{10}$ is achieved by detection of time instant t_4 and detection of of time instant t_{10} as shown in Fig. 4A). The latter detection allows the dead-time controller 514 to turn on the first and second semiconductor switches S_1 and S_2 at these time instants or points, respectively. This results in the setting of the optimum dead time period during each switching cycle of the resonant input voltage V_F. This feature results in fast and power efficient start-up of the resonant current I_{res} by maximizing respective conducting state time periods of the first and second semiconductor switches S_1 and S_2 in order to feed energy into the resonant tank, e.g. including a primary side of the piezoelectric transformer, and build up resonant current.

The skilled person will appreciate that the detection of the time instants or points where the instantaneous transformer input voltage V_F reaches either the positive or negative DC supply voltage under steady state operation may be accomplished by different types of analog, digital or mixed-signal circuitry as discussed below in further detail. The previously discussed start-up phase or time period of the power converter designates the time period from power-on of the power converter to the time instant where the resonant current in the piezoelectric transformer reaches the maximum amplitude in the operating point of the power converter. During this start-up phase, the resonant current is growing continuously, but it does not reach the highest possible amplitude. Therefore, the input capacitance C_{d1} will not be charged all the way up to the level of the positive DC supply voltage or discharged all the way down to the level of the negative DC supply voltage.

FIGS. 3A) and 3B) show exemplary voltage and current waveforms of V_F and I_{res} during the start-up phase or period of the prior art power converter 100.

Accordingly, two different situations may be encountered during the dead time period DT in the start-up period: In a first situation, the instantaneous transformer input voltage V_F may pass through local maximum/minimum before the semiconductor switches are turned on. FIG 3B) shows waveforms 323a, 323b of V_F and I_{res} for this situation. The presence of the maximum/minimum or extrema in V_F at time instant t_{2I} of the waveform 323a is caused by a change of direction of the resonant current I_{res} during the first dead time period DT as indicated by the zero-crossing of I_{res} at the time instant t_{2I}. Therefore, the resonant current I_{res} changes from charging to discharging the input capacitance C_{d1}. In the second situation, the transformer input voltage V_F is still increasing or decreasing until the first or second semiconductor switch S_1 or S_2 is turned on. This means that the transformer input voltage V_F will not pass through any local extrema. In this situation, the amplitude of the resonant current I_{res} is too small to fully charge the input capacitance C_{d1}. This second situation is illustrated by the waveforms 322a, 322b of V_F and I_{res} of FIG. 3A). The resonant current I_{res} is changing direction during a switching cycle. The amplitude of the resonant current leads to the difference between the first and second situations which may be encountered during the start-up period. The resonant current I_{res} is build up after power-on of the power converter and gradually increases in amplitude until the resonant current I_{res} reaches a steady state amplitude. During steady state operation, the amplitude of the resonant current I_{res} remains essentially constant provided the input voltage, temperature and load of the power converter also remain essentially constant. At the beginning of the start-up time period, the amplitude of the resonant current I_{res} is so small that I_{res} is unable to fully charge the the input capacitance C_{d1} during the dead time period to the positive DC supply voltage. This deficiency applies to both of the charging processes illustrated by FIG. 3A) and FIG. 3B). The optimal charging process may reasonably be considered reached by adapting the charging process of the input capacitance C_{d1} as illustrated by FIG.

4B). In the latter charging process the resonant current I_{res} is near its peak amplitude at time instant t_2 when dead time period starts.

It can be shown that the total amount of energy provided to the input capacitance C_{d1} in the dead time period, defined as $\Delta t = t_6 - t_2$, is:

$$\Delta E = \frac{I_{pk}^2}{4C_{in}}\left(1 - \frac{1}{2\omega\Delta t} sin(2\omega\Delta t)\right) \quad (15)$$

Therefore, it is important to turn on the first semiconductor switch S_1 or the second semiconductor switch S_2 at the zero crossing of the resonant current I_{res} depicted on FIG. 4B). Consequently, to optimize the dead time period either during the start-up phase of the power converter or during the steady state operation thereof, one embodiment of the dead-time controller 514 may be configured to switch the first or second semiconductor switch to its conducting state either when the transformer input voltage V_F reaches one of the positive and negative DC supply voltages or when the resonant current I_{res} crosses zero which ever condition occurs first. If neither of these conditions are detected the dead-time controller 514 may apply a fixed dead time period to facilitate build-up of the resonant current I_{res}. The skilled person will understand that there is no direct access to detect or measure the resonant current I_{res} inside the piezoelectric transformer 513. Therefore, the transformer input voltage V_F may conveniently be used by the dead-time controller 514 as a reference for detecting the dead time period in the piezoelectric power converter 500.

The LCC resonant power converter 500a of FIG. 5A in accordance with the second embodiment of the present invention likewise eliminates cases corresponding to those shown in FIGS. 2A) and 2B) with too short or too long dead-time periods of the resonant input voltage, compared to the optimal dead-time period. The LCC power converter 500a comprises a resonant network or circuit comprising first capacitor C and a first inductor L connected in series to the resonant input voltage V_F applied at the input terminal 507a of the resonant network. The resonant network additionally comprises a second capacitor C_p coupled in parallel across a primary side of a magnetic transformer with conversion ratio 1:N. Hence, the resonant voltage across the primary side of the magnetic transformer may be an output voltage of the resonant network. A secondary side of the magnetic transformer is coupled to a load R_L. Other embodiments of the resonant power converter 500a may comprise a rectification circuit coupled to the secondary side of the magnetic transformer to generate a DC output voltage of the LCC power converter 500a. A resonant current I_{res} is flowing through the first inductor L of the resonant network to alternatingly charge and discharge the resonant input voltage V_F during successive dead-time periods of the half-bridge driver 503a. The LCC power converter 500a comprises a dead-time controller OTD 514a which may be configured to dynamically detect and set an optimized dead time period during every switching cycle of the resonant input voltage V_F. The operation of the dead-time controller 514a may optimize, during each switching cycle or at least a majority of switching cycles, the time instants where the semiconductor switches S_2 and S_1 of the driver 501a are switched from OFF to ON to be placed substantially where the instantaneous resonant input voltage V_F reaches either the positive DC supply voltage or reaches the negative DC supply voltage during steady-state operation of the LCC power converter 500a. This may be accomplished by adjusting the phase or timing of the first and second driver control signals HS_G, LS_G as discussed in detail below with reference to FIG. 6. Furthermore, the dead-time controller 514a may also be configured to optimize the switching instants of the semiconductor switches S_2 and S_1 of the driver circuit 503a during an initialization or start-up phase of the LCC power converter 500a. In the latter case, the operation of dead-time controller 514 optimizes, during each switching cycle, the time instants where the semiconductor switches S_2 and S_1 are switched from OFF to ON, i.e. turned on, to be placed substantially where the instantaneous resonant input voltage V_F reaches either a minima level or a maxima level during a dead-time period. This may be accomplished by detecting or monitoring the waveform shape of the instantaneous resonant input voltage V_F in a manner correspond to the one discussed in additional detail below with reference to FIG. 6. The operation and characteristics of the gate driver 501a and driver circuit 503a are also discussed in additional detail below with reference to the corresponding gate driver 501 and driver circuit 503 of the first embodiment of the resonant power converter 500.

FIG. 6 is a schematic block diagram of a preferred embodiment of the dead-time controller 514 of the piezoelectric power converter 500. The dead-time controller

514 comprises *inter alia* a steady-state controller 624 and a start-up controller 634 and a control circuit 644 (OTD C). The steady-state controller 624 is adapted to generate appropriately timed first and second driver control signals HS_G, LS_G for the for the half-bridge driver 503, delivered through the optional gate drive 501, and during steady-state operation of the power converter 500 and the corresponding first and second driver control signals HS_G, LS_G for the half-bridge driver 503a during steady-state operation of the LCC resonant power converter 500a. The start-up controller 634 is adapted to generate appropriately timed first and second driver control signals HS_G, LS_G for the half-bridge drivers 503, 503a during the initialization time or start-up time of the power converters 500, 500a. Hence, the first driver control signal HS_G switches the first or high side semiconductor switch S_1 between its conducting state and non-conducting state and the second driver control signal LS_G switches the second semiconductor switch S_2 between its conducting state and non-conducting state. Body diodes D_1 and D_2 are associated with the semiconductor switches S_1 and S_2, respectively, and may have the same function as the previously discussed body diodes 113a, 113b. Each of the first and second semiconductor switches S_1 and S_2 preferably comprises a MOSFET. The output of the driver circuit 503 supplies the transformer input voltage V_F since the output node of the driver circuit 503, i.e. the mid-point node between respective drain terminals of the MOSFET semiconductor switches S_1 and S_2, is coupled directly to a first input electrode 507a of an input section or primary side of the piezoelectric transformer 513. A second input electrode 507b of the primary side of the piezoelectric transformer 513 may be coupled to GND. The dead-time controller 514 is electrically connected to the transformer input voltage V_F and to the second input electrode 507b. The piezoelectric transformer 513 may further comprise a pair of output electrodes 508a, 508b electrically coupled to a secondary or output section of the piezoelectric transformer 513 and supply a transformer output voltage to an input of a rectification circuit 508. The rectification circuit 508 may comprise a half wave or full wave rectifier, and possibly output capacitor(s), to provide a smoothed DC voltage at an output node or terminal V_{OUT} of the piezoelectric power converter 500.

The steady-state controller 624 comprises a first comparator 625 configured to compare the instantaneous level or value of the transformer input voltage V_F to the positive DC supply voltage V_{DC}, fed through terminal or line 622, and supply a first comparator output signal Z_{HS}. The first comparator output signal Z_{HS} is utilized for adjusting the phase of the first driver control signal HS_G (please refer to FIG. 5) via the logic control circuit 644. The first driver control signal HS_G is applied to a control or gate terminal of the first semiconductor switch S_1 of the driver circuits 503, 503a. The steady-state controller 624 additionally comprises a second comparator 627 configured to compare the instantaneous level or amplitude of the transformer input voltage V_F to the negative DC supply voltage, which is ground or 0 V in the present embodiment, fed through terminal or line S, 623, and supply a second comparator output signal Z_{LS}. The second comparator output signal Z_{LS} is utilized for adjusting a phase of a second driver control LS_G (please refer to FIG. 5) via the logic control circuit 644. The second driver control signal LS_G is applied to the control or gate terminal of the second semiconductor switch S_2 of the half-bridge driver 503, optionally via the gate drive 501.

The start-up controller 634 is configured to detect a waveform shape of the transformer input voltage V_F and generate a first control signal Z_{MH} for adjusting the timing or phase of the first driver control signal HS_G via the logic control circuit 644 in accordance with the waveform shape of the transformer input voltage $V_{F.}$ The start-up controller 634 is preferably also configured to detect a waveform shape of the transformer input voltage V_F and generate a second control signal Z_{ML} for adjusting the timing or phase of the second driver control signal LS_G via the logic control circuit 644 in accordance with the waveform shape of the transformer input voltage V_F. During the initialization period or start-up phase or period of the piezoelectric power converter 500, the instantaneous transformer input voltage V_F is applied at line or terminal 620, signal S, and compared with a delayed replica of the transformer input voltage S_d. The delayed replica of the transformer input voltage S_d is applied to a negative input of a third comparator 639 of the circuit 514. A local local maximum of the waveform of the instantaneous transformer input voltage is detected when $S_d >$ signal S. Hence, the local maximum of the waveform of the instantaneous transformer input voltage during a dead-time period with increasing resonant input voltage is detected in response to, or when, the voltage of the delayed replica S_d exceeds signal S. Likewise, a local minimum of the waveform of V_F during a dead-time period with decreasing or falling resonant input voltage is detected when signal S < signal S_d (the delayed replica of the transformer input voltage).

The start-up controller 634 may furthermore limit the instantaneous transformer input voltage V_F between a predefined lower threshold voltage and a predefined upper threshold voltage before detecting the above-discussed local local maximum and minimum of the waveform of the instantaneous transformer input voltage. In the present embodiment, the start-up controller 634 is configured to set an intermediate or middle voltage range (M) between the predefined lower threshold voltage V_{Low} and the predefined upper threshold voltage V_{Hi} via the corresponding reference voltages applied through input lines or terminals 616 and 618 of the start-up controller 634. The predefined lower threshold voltage V_{Low} may for example be around 10 % of the positive DC supply voltage V_{DC} such as between 0.05 and 0.2 times V_{DC} when the negative DC supply voltage is ground as in the present embodiment. The predefined upper threshold voltage V_{Hi} may for example be around 90 % of the positive DC supply voltage V_{DC} such as between 0.75 and 0.95 times V_{DC}. These value ranges for the predefined lower and upper threshold voltages will provide a suitable noise margin for local extrema detection and prevent undesired triggering by noise impulses of the transformer input voltage. A fourth comparator 636 indicates whether the instantaneous transformer input voltage on line S is above the predefined lower threshold voltage V_{Low}. A fifth comparator 638 indicates whether the instantaneous transformer input voltage on line S is below the predefined upper threshold voltage V_{Hi}. The third comparator 639 may comprise a high precision dual/differential output comparator. As mentioned above, the output signals $HS_{G,}$ LS_G of the ODT C block are controlled by the control circuit or block 644 in accordance with logic states of the input signals Z_{MH}, Z_{ML}, Z_{HS} and Z_{LS}. The first semiconductor switch S_1 is switched ON in response to either Z_{HS} or Z_{HM} is asserted such that HS_G is logically “1”. The second semiconductor switch S_2 is turned/switched ON in response to either Z_{LS} or Z_{ML} is asserted or digitally “1” such that LS_G is logically “1”. A reset control signal "R" through line 645 of the control circuit or block 644 is configured to selectively switching off the first and second semiconductor switches S_1 and S_2 after the allocated ON time period of the semiconductor switch in question. Finally, an optional enable signal "En" and function received through line 647 may enable/disable the operation of the dead-time controllers 514, 514a in the resonant power converters 500, 500a. The skilled person will understand that the respective voltage levels of references voltages such as V_{Hi}, V_{DC} and V_{Low} utilized in the dead-time controller 514 may be scaled to a voltage level of the comparators 625, 627, 639, 636, 638. The particular

Boolean functions implemented in the dead-time controller 514 for the outputs of the steady-state controller 624 and the start-up controller 634 are:

$$\begin{cases} Z_{ML} = (S < V_{Hi}) \cdot (S > S_d) \\ Z_{MH} = (S > V_{Low}) \cdot (S < S_d) \\ Z_{HS} = (S > V_{DC}) \\ Z_{LS} = (S < 0) \end{cases} \qquad (16)$$

$$\begin{cases} HS_G = (Z_{HS} + Z_{MH}) \cdot En \cdot \overline{R} \\ LS_G = (Z_{LS} + Z_{ML}) \cdot En \cdot \overline{R} \end{cases} \qquad (17)$$

The steady-state controller 624 comprises the first comparator 625 which is configured to comparing the transformer input voltage V_F to the positive DC supply voltage V_{DC} via the positive and negative inputs of the first comparator 625. The positive input of the first comparator 625 receives the transformer input voltage V_F via line or terminal 620. The second comparator 627 is configured to comparing the transformer input voltage V_F to the negative DC supply voltage, i.e. 0 V via the positive and negative inputs of the second comparator 627.

Overall, the first and second semiconductor switches S_1 and S_2 are turned on, i.e. switched to the conducting state, by a rising edge of Z_{HS} and Z_{LS}, respectively, in the steady state operation of the resonant power converters 500, 500a. Likewise, the first and second semiconductor switches S_1 and S_1 are turned off, i.e. switched to the non-conducting state, by a falling edge of Z_{HS} and Z_{LS}, respectively, in the steady state. The same control scheme applies during the start-up or initialization period of the resonant power converters 500, 500a and the logic control block 644 determines whether first and second driver control signal $HS_{G,}$ LS_G for the first and second semiconductor switches S_1 and S_2 are derived from the outputs of the steady-state controller 624 or the outputs of the start-up controller 634. Hence, each of the driver circuits 501, 503, 501a, 503a is configured to alternatingly pulling the resonant or transformer input voltage V_F towards the positive and negative DC supply voltages or rails via the first and second semiconductor switches S_1 and S_2, respectively, separated by intervening dead-time periods during each switching cycle in accordance the first and second driver control signals HS_G, LS_G.

The lower plot 1020 of FIG. 7 shows experimentally measured normalized voltage and current waveforms of the transformer input voltage V_F and resonant current I_{res} captured through several switching cycles of a start-up phase or state of the piezoelectric power converter 500 in comparison with the corresponding waveforms on the upper plot 1010 of the exemplary prior art piezoelectric power converter 100 depicted on FIG. 1A. The measurements were performed on a radial mode piezoelectric transformer with the following parameters:

Parameter	Value	Parameter	Value
C_{d1}	3.8 nF	C_{d2}	626 pF
C	565 nF	R	5.6 Ω
L	3.5 mH	N	3.5

Furthermore, the fundamental resonance frequency of the radial mode piezoelectric transformer was 116.3 kHz and the load Z_L was a resistive load corresponding to 300 W of output power.

CLAIMS

1. A resonant power converter comprising:
a first power supply rail for receipt of a positive DC supply voltage and a second power supply rail for receipt of a negative DC supply voltage,
a resonant network comprising an input section and an output section wherein the input section comprises an input terminal for receipt of a resonant input voltage and the output section comprises an output terminal for providing a resonant output voltage in response to the resonant input voltage,
a driver circuit comprising a first semiconductor switch coupled to the positive DC supply voltage and a second semiconductor switch coupled to the negative DC supply voltage and a driver output connected to the input terminal for supply of the resonant input voltage;
wherein the driver circuit is configured for alternatingly pulling the resonant input voltage towards the positive and negative DC supply voltages via the first and second semiconductor switches, respectively, separated by intervening dead-time periods in accordance with one or more driver control signals,
a dead-time controller configured to adaptively adjusting the dead-time periods based on the resonant input voltage.

2. A piezoelectric power converter according to claim 1, wherein the first semiconductor switch comprises a conducting state where the input terminal is connected to the positive DC supply voltage and the second semiconductor switch comprises a conducting state where the input terminal is connected to the negative DC supply voltage; and
where the first semiconductor switches is in a non-conducting state during the dead-time periods and the second semiconductor switch is in a non-conducting state during the dead-time periods.

3. A resonant power converter according to claim 1 or 2, wherein the dead-time controller is configured to adjust a phase of a first driver control signal of the first semiconductor switch and a phase of a second driver control signal of the second semiconductor switch to adaptively adjust the duration of the dead-time pe-

riods.

4. A resonant power converter according to claim 1, wherein the driver circuit comprises a half-bridge wherein the first semiconductor switch and the second semiconductor switch are coupled in series between the positive DC supply voltage and the negative DC supply voltage.

5. A resonant power converter according to claim 3 or 4, wherein the dead-time controller comprises a steady-state controller comprising:
a first comparator configured to compare the instantaneous resonant input voltage to the positive DC supply voltage and supply a first comparator output signal (Z_{HS}) for adjusting the phase of the first driver control signal in accordance with the first comparator output signal,
a second comparator configured to compare the instantaneous resonant input voltage to the negative DC supply voltage and supply a second comparator output signal (Z_{LS}) for adjusting the phase of the second driver control signal in accordance with the second comparator output signal.

6. A resonant power converter according to claim 3 or 4, wherein the dead-time controller comprises a start-up controller configured to detect a waveform shape of the instantaneous resonant input voltage; and
generating a first control signal (Z_{MH}) for adjusting the phase of the first driver control signal in accordance with the waveform shape; and/or
generating a second control signal (Z_{ML}) for adjusting the phase of the second driver control signal in accordance with the waveform shape.

7. A resonant power converter according to claim 6, wherein the dead-time controller is configured to detect the waveform shape of the instantaneous resonant input voltage by comparing the instantaneous resonant instantaneous transformer input voltage with a delayed replica of the resonant input voltage.

8. A resonant power converter according to claim 7, wherein the dead-time controller is configured to:
detect a local maximum of the waveform of the instantaneous resonant input

voltage in response to the delayed replica of the resonant input voltage exceeds the instantaneous resonant input voltage; and/or
detect a local minimum of the waveform of the instantaneous resonant input voltage in response to the delayed replica of the resonant input voltage falls below the instantaneous resonant input voltage.

9. A resonant power converter according to claim 7 or 8, wherein the dead-time controller is configured to limit the instantaneous resonant input voltage between a lower threshold voltage and an upper threshold voltage before detecting the local maximum and/or detecting the local minimum.

10. A resonant power converter according to claim 9, wherein the lower threshold voltage lies between 0.05 and 0.2 times the positive DC supply voltage and the upper threshold voltage lies between 0.75 and 0.95 times the positive DC supply voltage.

11. A resonant power converter according to claim 5 and 6, wherein the dead-time controller comprises a first digital OR circuit configured to logically OR the first comparator output signal and the first control signal; and
a second digital OR circuit configured to logically OR the second comparator output signal and the second control signal.

12. A method of adaptively controlling a dead-time interval of a driver circuit of a resonant power converter, comprising steps of:
generating first and second non-overlapping driver control signals for the driver circuit in accordance with a switching frequency signal of the resonant power converter, wherein the driver circuit is coupled between positive and negative DC supply voltages for supply of power,
applying the first and second non-overlapping driver control signals to the driver circuit to generate a driver output signal alternating between the positive DC supply voltage and negative DC supply voltage separated by intervening dead-time periods or intervals,
applying the driver output voltage to an input terminal of the resonant network to generate a resonant input voltage,

generating a resonant output voltage in response to the resonant input voltage at an output side or terminal of the resonant network ,
detecting a feature of the resonant input voltage,
adjusting a duration of the dead-time interval or period of the driver circuit based on the detected feature of the resonant input voltage.

13. A method of adaptively controlling a dead-time period according to claim 12, wherein the instantaneous resonant input voltage is detected in each switching cycle of the switching frequency of the resonant power converter and the dead-time period adjusted accordingly in response.

14. A resonant power converter according to any of the preceding claims, wherein the driver circuit and the resonant network are configured for ZVS operation or ZCS operation at the switching frequency of the resonant power converter.

15. A resonant power converter according to any of the preceding claims, wherein the resonant network comprises a piezoelectric transformer;
wherein a primary section of the piezoelectric transformer is coupled to the resonant input voltage to supply a transformer input voltage and a secondary section of the piezoelectric transformer generates the resonant output voltage.

ABSTRACT

The invention relates in a first aspect to a resonant power converter comprising: a first power supply rail for receipt of a positive DC supply voltage and a second power supply rail for receipt of a negative DC supply voltage. The resonant power converter comprises a resonant network with an input terminal for receipt of a resonant input voltage from a driver circuit. The driver circuit is configured for alternatingly pulling the resonant input voltage towards the positive and negative DC supply voltages via first and second semiconductor switches, respectively, separated by intervening dead-time periods in accordance with one or more driver control signals. A dead-time controller is configured to adaptively adjusting the dead-time periods based on the resonant input voltage.

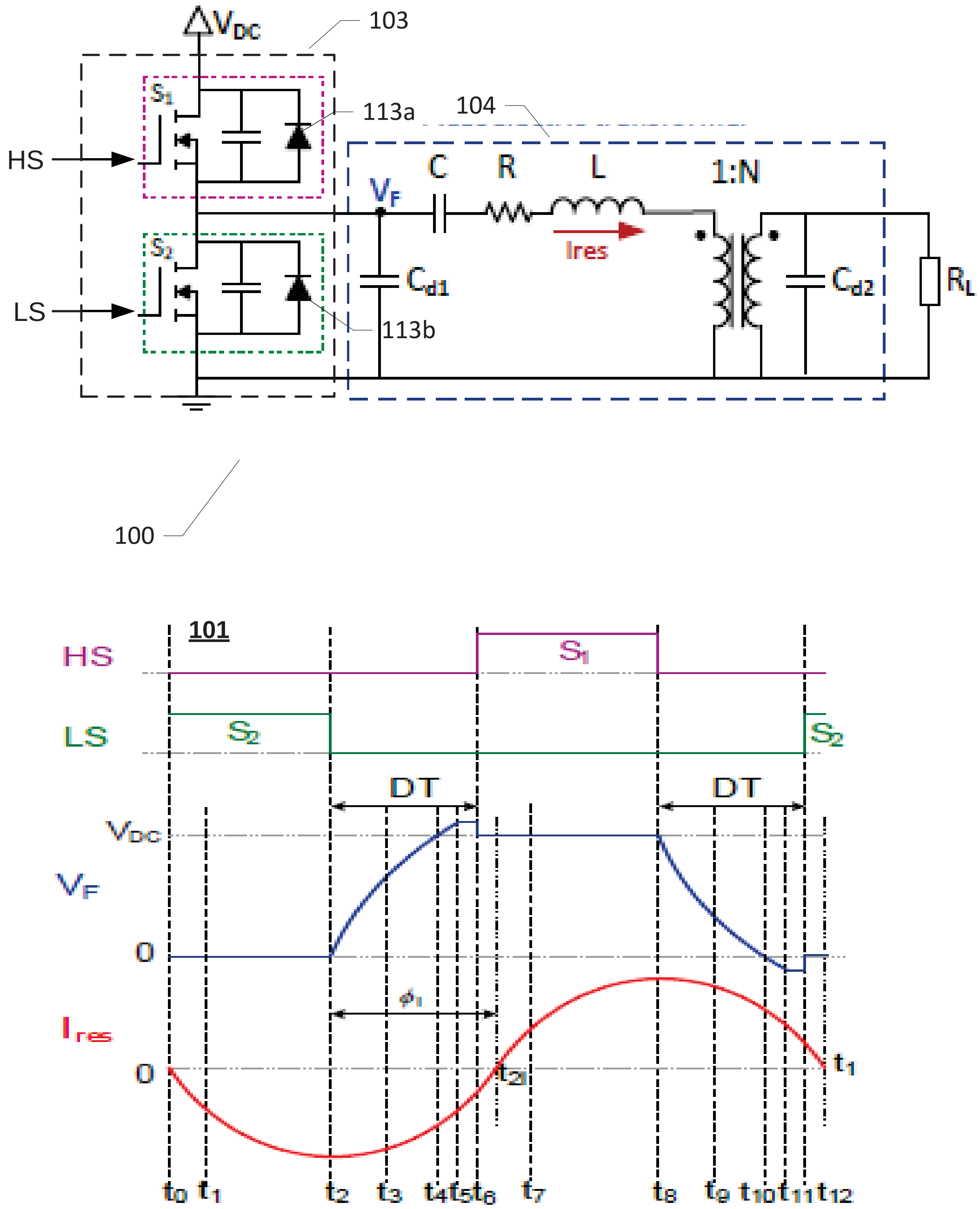
VDC
103
S1
113a
104
HS
C
R
L
1:N
VF
Ires
Cd1
Cd2
RL
S2
LS
113b
100
101
HS
S1
LS
S2
S2
DT
DT
VDC
VF
0
φ1
Ires
0
t2
t1
t0 t1
t2
t3
t4 t5 t6
t7
t8
t9 t10 t11 t12

FIG. 1

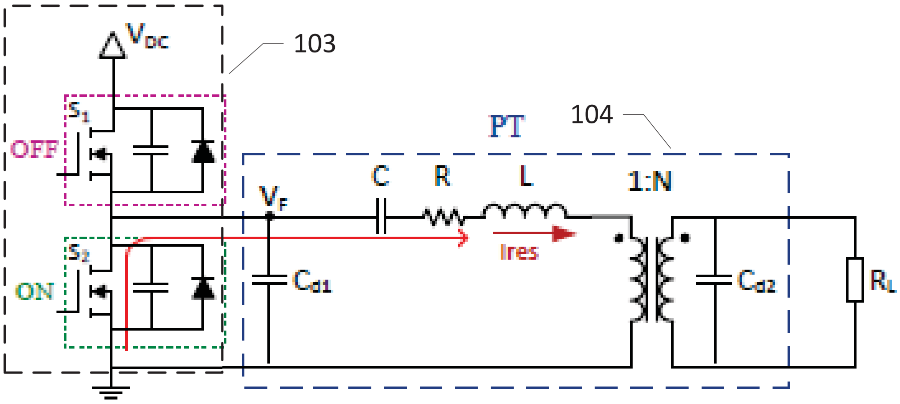

a: Subinterval $t_{12} - t_{1'}$

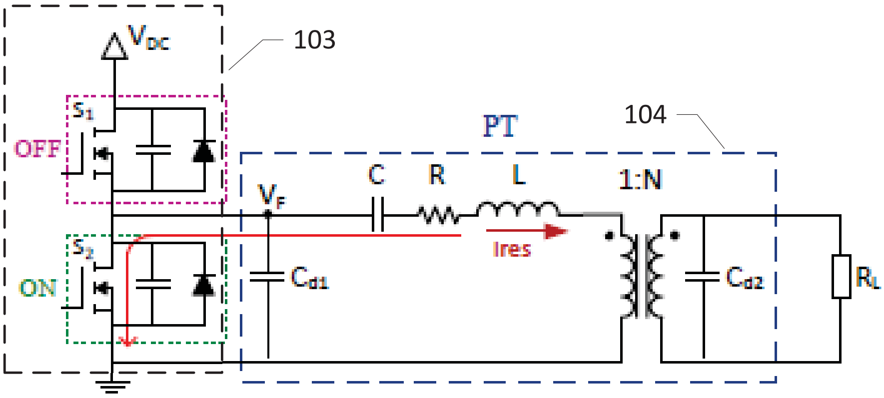

b: Subinterval $t_{1'} - t_2$

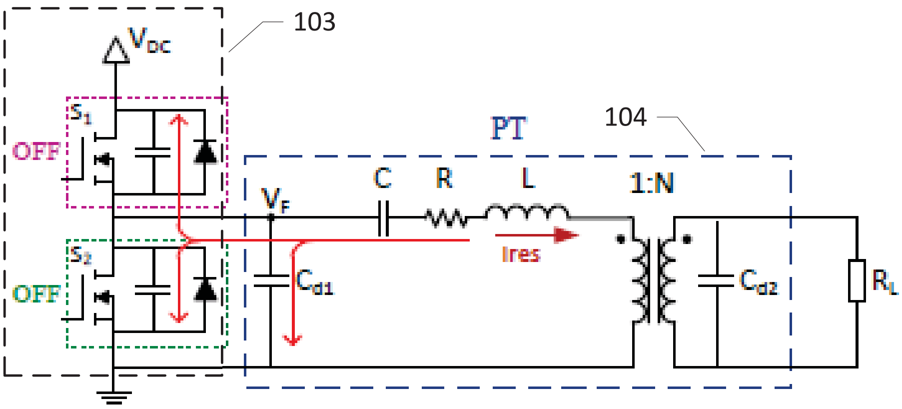

c: Subinterval $t_2 - t_5$

FIG. 1A

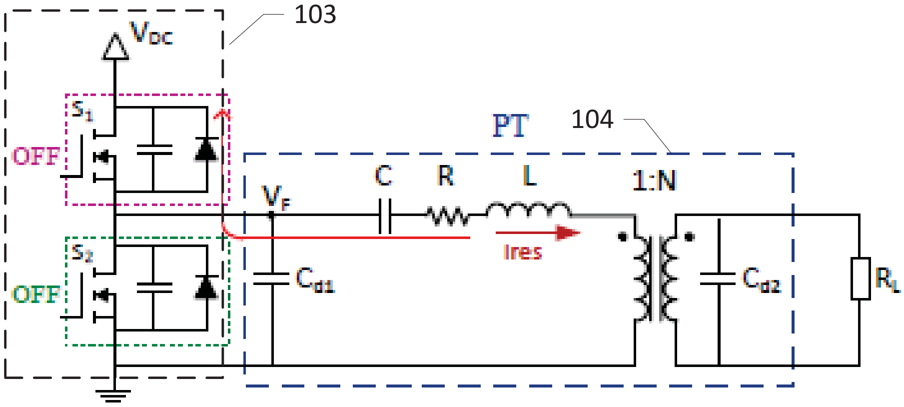

d: Subinterval $t_5 - t_6$

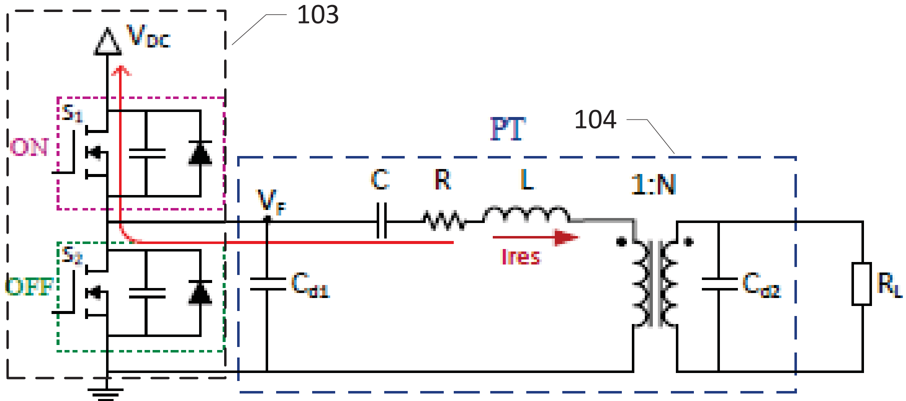

e: Subinterval $t_6 - t_{21}$

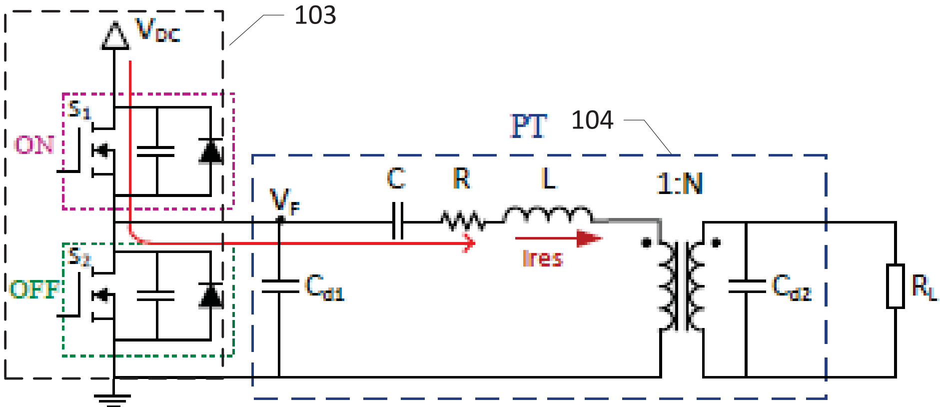

f: Subinterval $t_{21} - t_8$

FIG. 1B

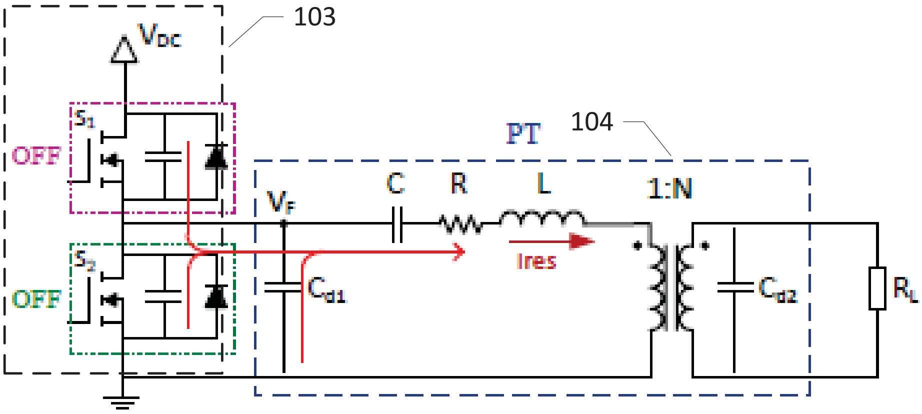

g: Subinterval $t_8 - t_{11}$

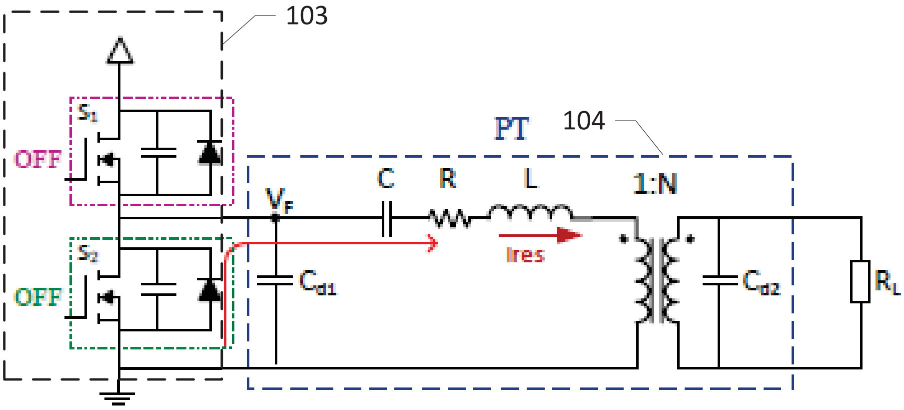

h: Subinterval $t_{11} - t_{12}$

FIG. 1C

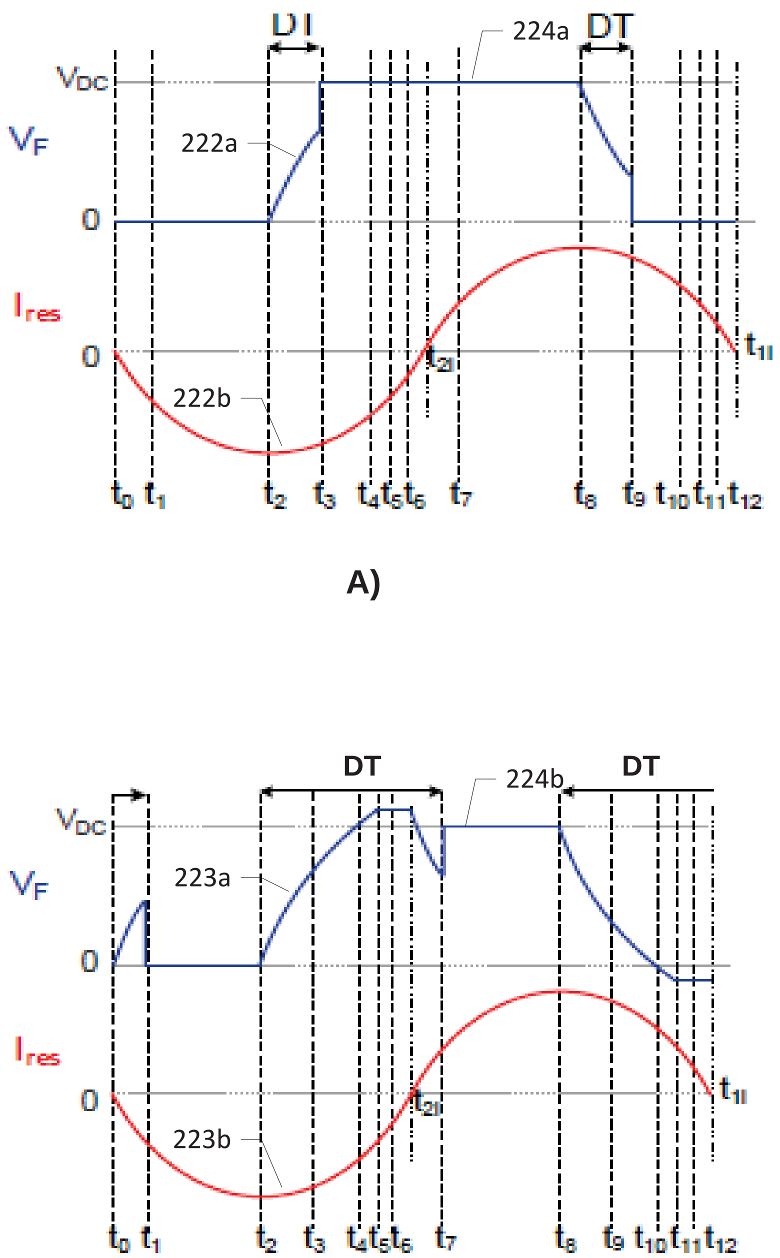
DT
224a
DT
VDC
VF
222a
0
Ires
0
222b
t0 t1 t2 t3 t4 t5 t6 t7 t8 t9 t10 t11 t12
t2I
t1I
A)
DT
224b
DT
VDC
VF
223a
0
Ires
0
223b
t0 t1 t2 t3 t4 t5 t6 t7 t8 t9 t10 t11 t12
t2I
t1I

B)

FIG. 2

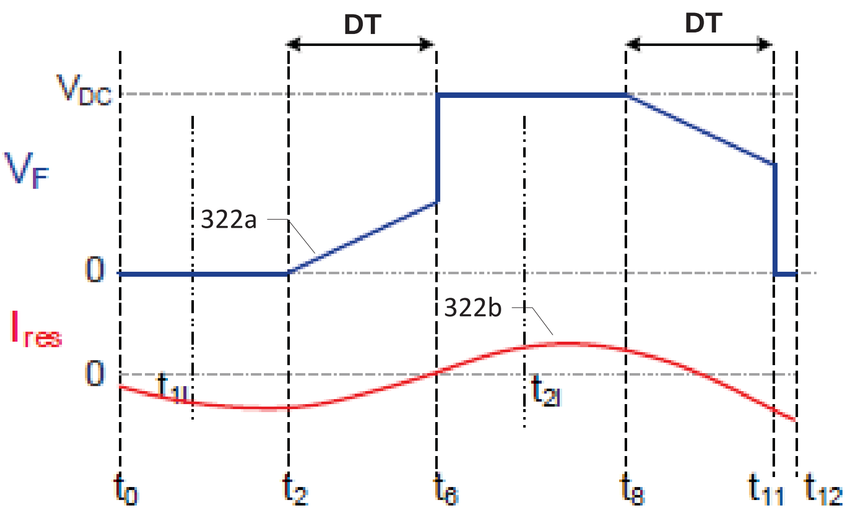
DT
DT
V_{DC}
V_F
322a
0
322b
I_{res}
0
t_{1I}
t_{2I}
t_0
t_2
t_6
t_8
t_{11}
t_{12}

A)

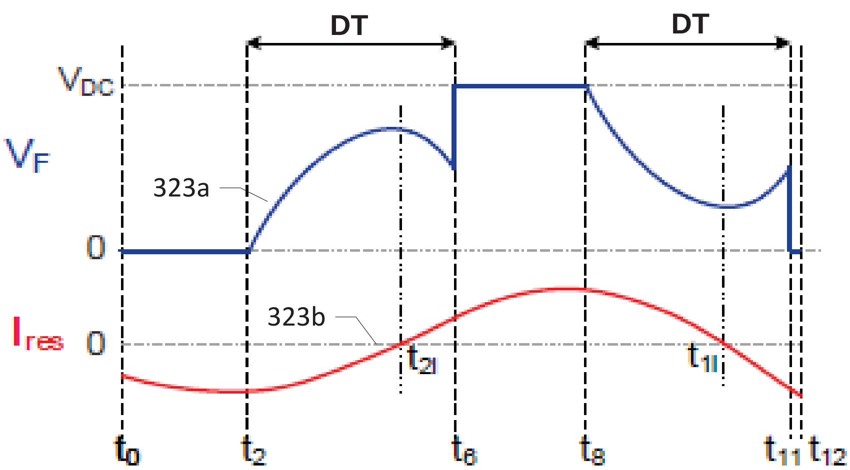
DT
DT
V_{DC}
V_F
323a
0
323b
I_{res}
0
t_{2I}
t_{1I}
t_0
t_2
t_6
t_8
t_{11}
t_{12}

B)

FIG. 3

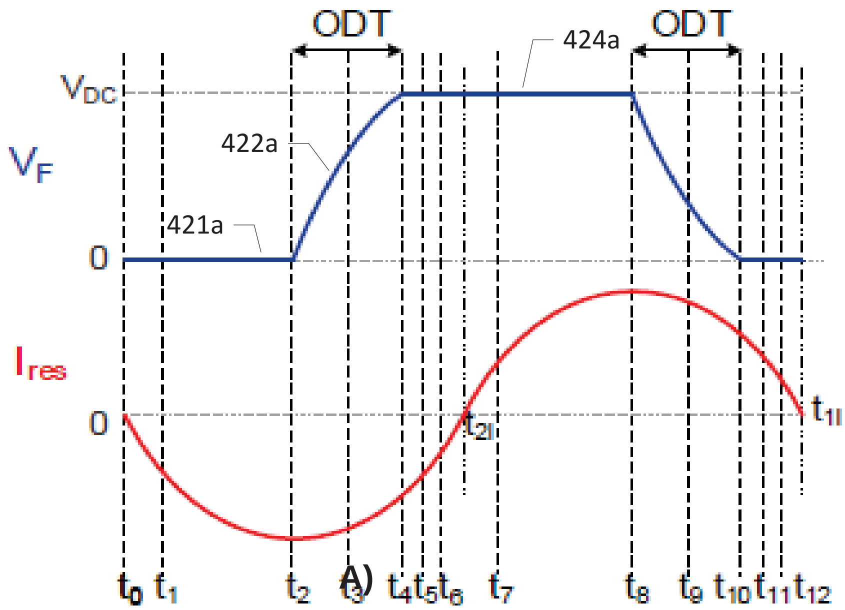
ODT
ODT
424a
V_{DC}
422a
V_F
421a
0
I_{res}
0
t_{2I}
t_{1I}
t_0 t_1 t_2 t_3 t_4 t_5 t_6 t_7 t_8 t_9 t_{10} t_{11} t_{12}
A)

A)

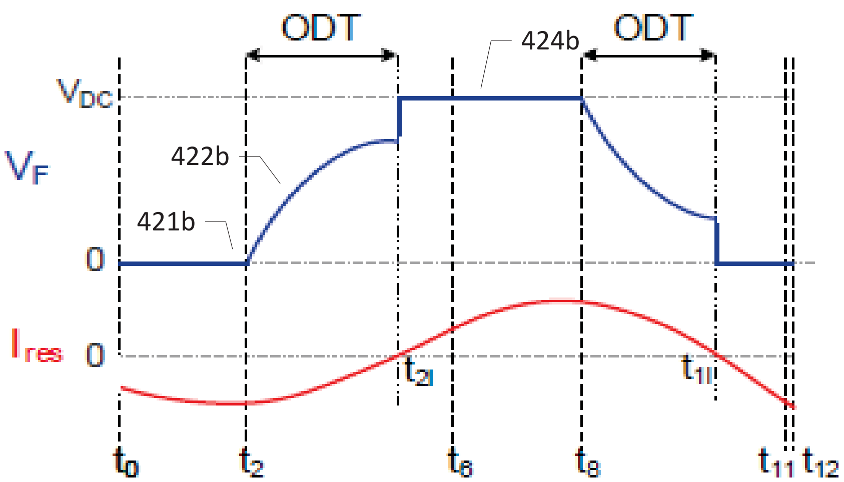
ODT
ODT
424b
V_{DC}
422b
V_F
421b
0
I_{res} 0
t_{2I}
t_{1I}
t_0 t_2 t_6 t_8 t_{11} t_{12}

B)

FIG. 4

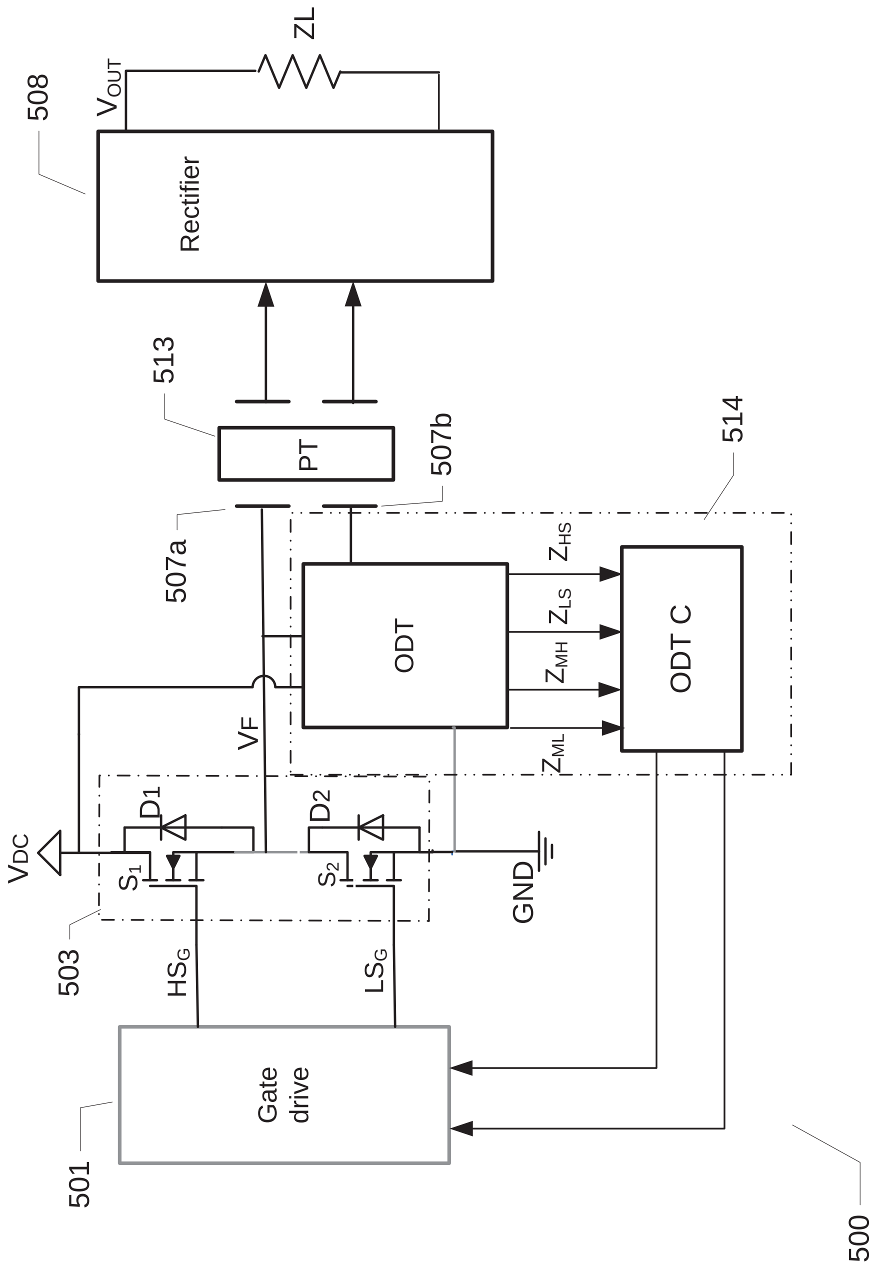

508
VOUT
ZL
Rectifier
513
PT
507a
507b
514
ODT
ODT C
ZHS
ZLS
ZMH
ZML
VF
VDC
D1
D2
S1
S2
GND
503
HSG
LSG
Gate drive
501
500

FIG. 5

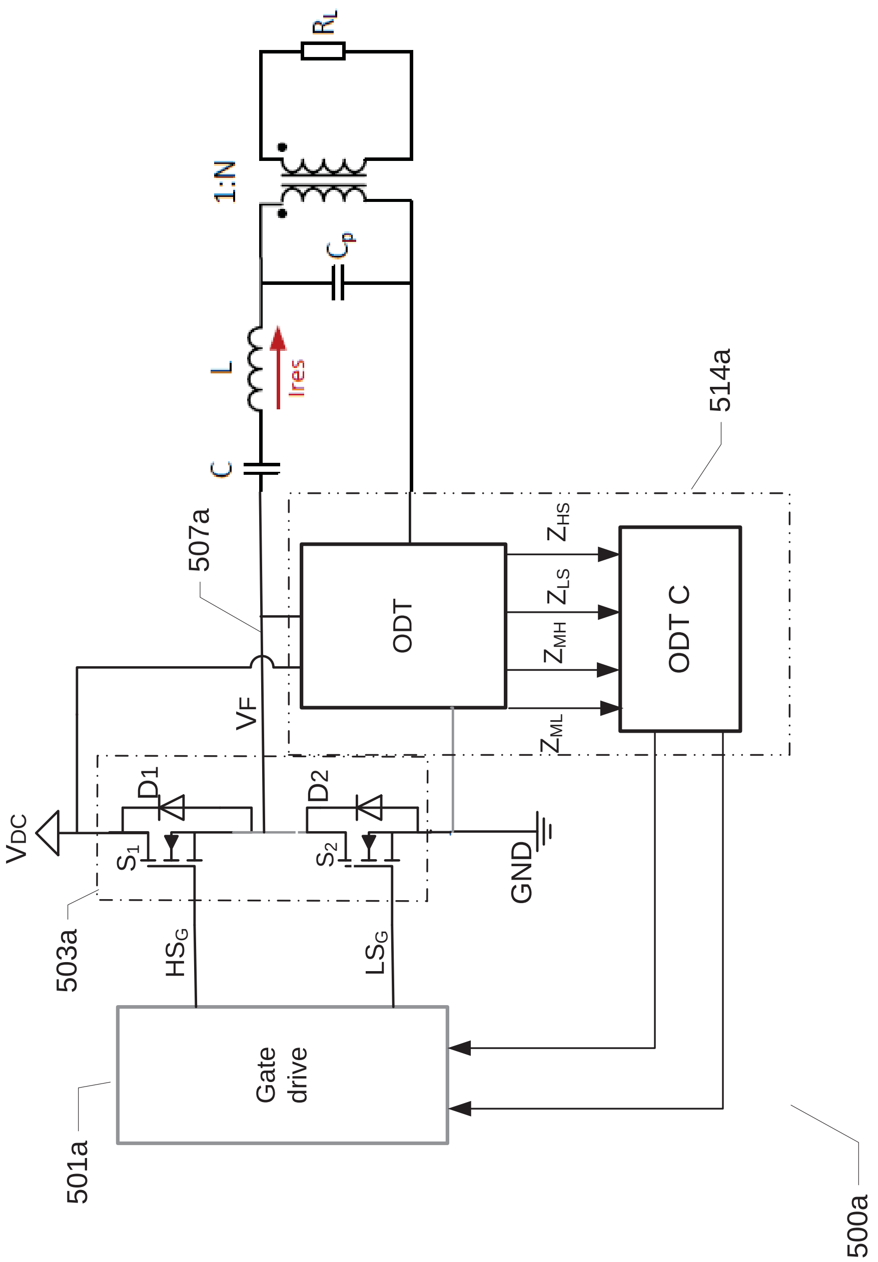
R_L
1:N
C_p
L
Ires
C
514a
507a
ODT
ODT C
Z_{HS}
Z_{LS}
Z_{MH}
Z_{ML}
VF
D1
D2
S_1
S_2
V_{DC}
GND
503a
HS_G
LS_G
Gate drive
501a
500a

FIG. 5A

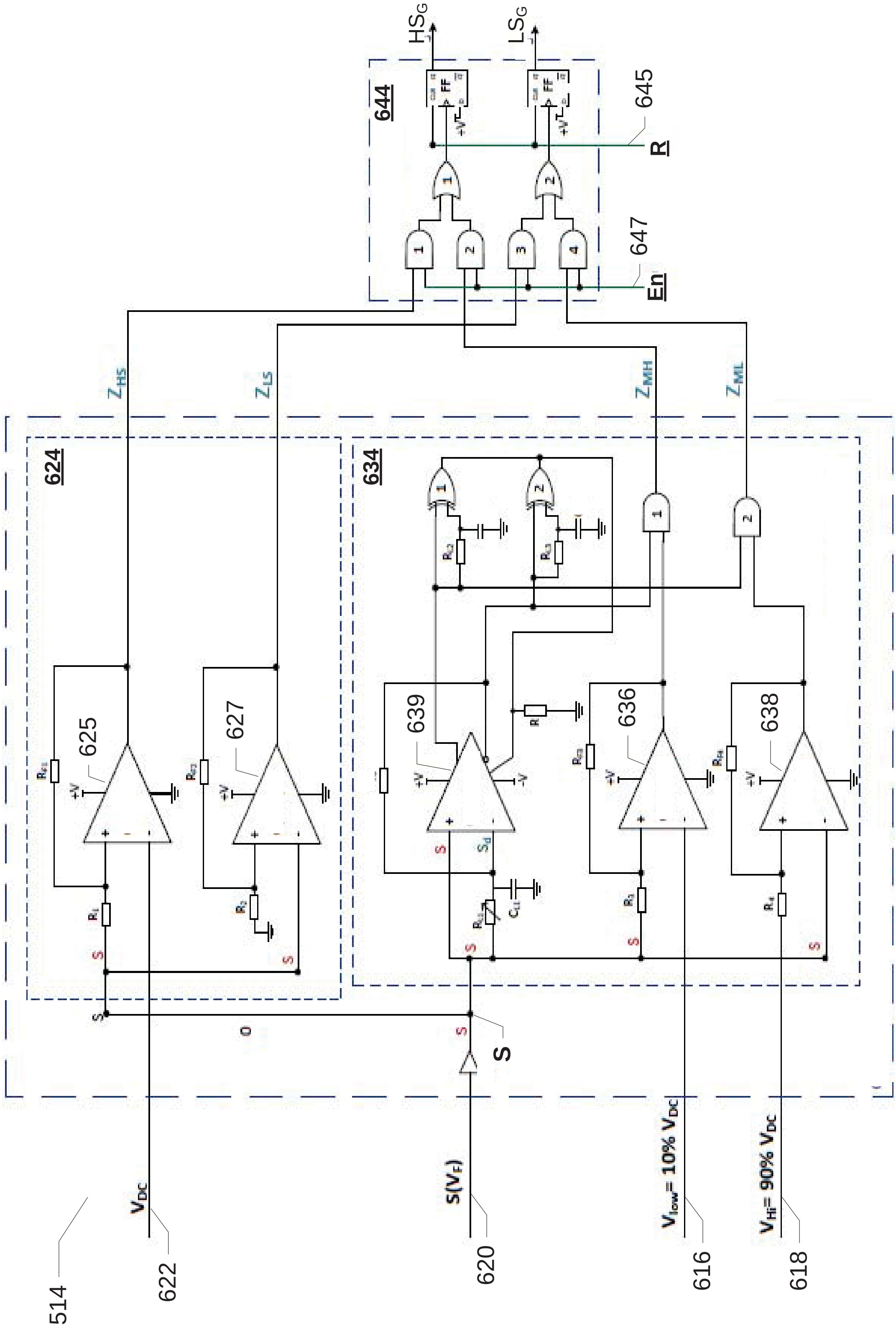

HS$_G$
LS$_G$
644
645
647
R
En
Z_{HS}
Z_{LS}
Z_{MH}
Z_{ML}
624
634
625
627
639
636
638
S
S_d
S(V_F)
V_{DC}
V_{low}= 10% V_{DC}
V_{Hi}= 90% V_{DC}
514
622
620
616
618

FIG. 6

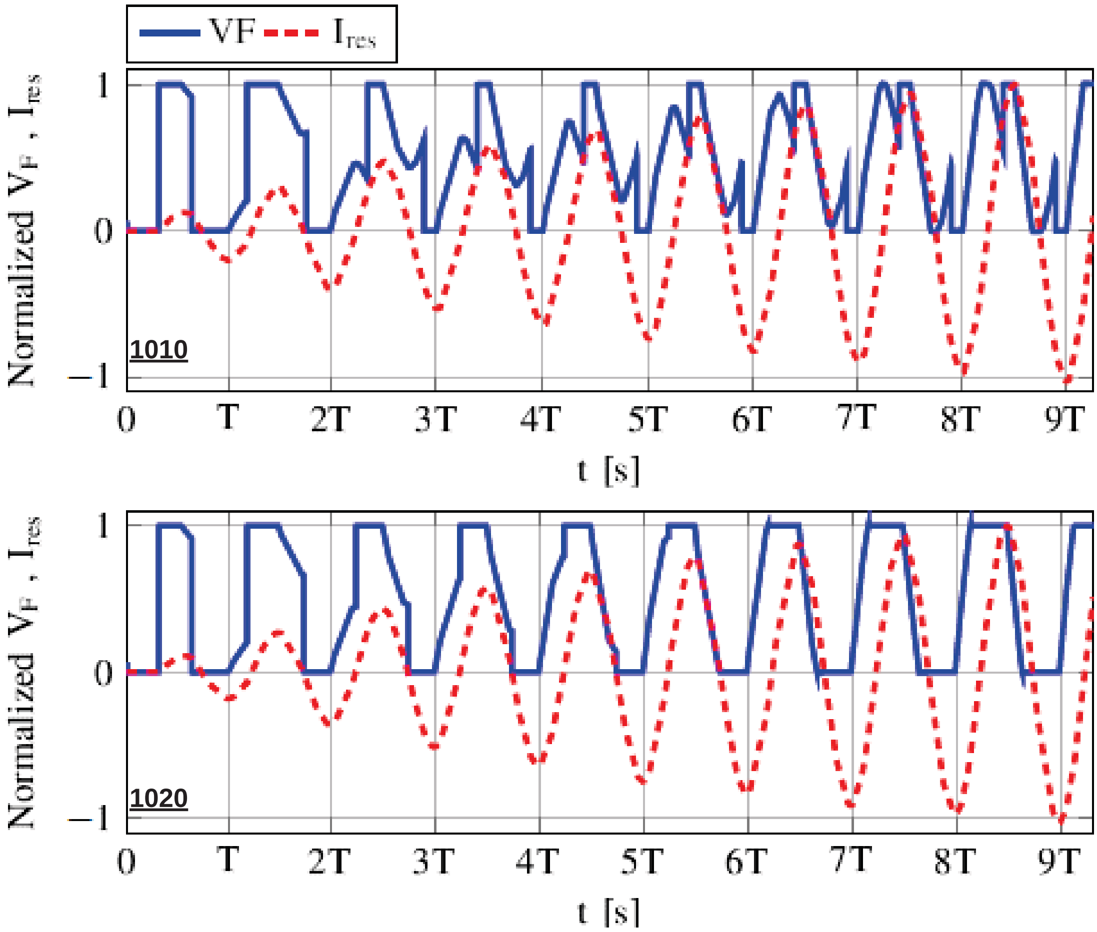
VF
I res
Normalized V F , I res
1
0
−1
1010
0
T
2T
3T
4T
5T
6T
7T
8T
9T
t [s]
1020

FIG. 7

I

RESONANT POWER CONVERTER WITH DEAD-TIME CONTROL OF SYNCHRONOUS RECTIFICATION CIRCUIT

Patent application

RESONANT POWER CONVERTER WITH DEAD-TIME CONTROL OF SYNCHRONOUS RECTIFICATION CIRCUIT

The invention relates in a first aspect to a resonant power converter comprising a synchronous rectifier for supplying a DC output voltage. The synchronous rectifier is configured for alternatingly connecting a resonant output voltage to positive and negative DC output nodes via first and second semiconductor switches, respectively, separated by intervening dead-time periods in accordance with first and second rectification control signals. A dead-time controller is coupled to the resonant output voltage or the resonant input voltage and configured for adaptively adjusting lengths of the dead-time periods via the first and second rectification control signals.

BACKGROUND OF THE INVENTION

A sub-group of resonant power converter comprises a piezoelectric transformer as a resonant circuit or resonant tank. Piezoelectric power converters are a viable alternative to traditional magnetics based resonant power converters in numerous voltage or power converting applications such as AC/AC, AC/DC, DC/AC and DC/DC power converter applications. Piezoelectric power converters are capable of providing high isolation voltages and high power conversion efficiencies in a compact package with low EMI radiation. The piezoelectric transformer is normally operated in a narrow frequency band around its fundamental or primary resonance frequency with a matched load coupled to the output of the piezoelectric transformer. The optimum switching frequency or excitation frequency of the piezoelectric power converter shows strong dependence on different parameter such as temperature, load, fixation and age. So-called zero-voltage-switching (ZVS) operation, or soft-switching, of an input driver and/or a synchronous rectification circuit of the piezoelectric power converter is important to avoid prohibitive power losses associated with the respective switching activities of the input driver and/or synchronous rectification circuit. However, synchronous rectification circuits of prior art resonant power converters have utilized a fixed length of the dead-time period, for example tailored to characteristics of a particular piezoelectric transformer at fixed operating conditions. The fixed dead-time period is unable to account for manufacturing tolerances and drift of active and passive electronic components of the resonant power converter, in particular those of a piezoelectric transformer. ´

Hence, the use of fixed dead-time periods leads to increased power consumption of practical resonant power converters where the above-mentioned manufacturing tolerances and drift of active and passive electronic components are inevitable. Hence, it would be advantageous to provide mechanisms for maintaining the desired zero voltage switching (ZVS) properties of the input driver and/or synchronous rectification circuit.

SUMMARY OF THE INVENTION

A first aspect of the invention relates to a resonant power converter comprising:

a first power supply rail for receipt of a positive DC supply voltage and a second power supply rail for receipt of a negative DC supply voltage,

a resonant network comprising an input section for receipt of a resonant input voltage and an output section for supplying a resonant output voltage generated in response to the resonant input voltage,

an input driver configured for supplying the resonant input voltage;

a synchronous rectifier comprising:

a rectifier input coupled to the resonant output voltage,

first and second semiconductor switches controlled by first and second rectification control signals, wherein the synchronous rectifier is configured for alternatingly connecting the resonant output voltage to positive and negative DC output nodes via the first and second semiconductor switches, respectively, separated by intervening dead-time periods in accordance with the first and second rectification control signals;

a first dead-time controller coupled to the resonant output voltage or the resonant input voltage and configured for adaptively adjusting lengths of the dead-time periods via the first and second rectification control signals.

The first dead-time controller is configured to provide adequate length or duration of the dead time periods of the synchronous rectifier to deliver sufficient energy for charging and discharging various capacitances at the output section of the resonant network with the resonant current alternatingly flowing into and out of the resonant network. The capacitances at the output section of the resonant network may comprise a capacitance of a secondary section of a piezoelectric transformer and various intrinsic capacitances of the first and second semiconductor switches.

The first dead-time controller is able to maintain zero voltage switching (ZVS) and/or zero current switching (ZCS) of the synchronous rectifier despite temperature drift and variation of component values or parameters of the resonant power converter by adaptively adjusting lengths or durations of the dead-time periods of the synchronous rectifier. Maintaining proper ZVS operation over time minimizes energy consumption involved in the switching activity of the first and second semiconductor switches of the synchronous rectifier. The present inventors have discovered that a dead-time period shorter than required for zero voltage switching causes hard switching of the synchronous rectifier. Likewise, a dead-time period longer than required for zero voltage switching may either cause hard switching of the synchronous rectifier or may cause soft switching of the synchronous rectifier with sub-optimum efficiency. The synchronous rectifier may comprise a half-wave rectifier or a full-wave rectifier.

The resonant power converter may comprise an AC-DC or DC-DC converter topology. The positive and negative DC output nodes of the synchronous rectifier may provide the DC output voltage of the resonant power converter for connecting to a load device, load resistor or load circuit.

The first dead-time controller of the resonant power converter may utilize various features of the resonant output voltage for detecting an optimum length of the dead time period and adaptively adjusting the length of the dead-time period. The dead-time controller may be configured to adjust the length of the dead-time period during every switching cycle of the resonant output voltage based on an instantaneous value thereof. Alternatively, the dead-time controller may be configured to adjust the lengths of dead-time periods during a specific operating condition of the resonant power converter - for example solely during a start-up or initialization phase of the resonant network or solely during steady state operation of the resonant network.

The switching cycle is determined by a selected switching frequency of the resonant power converter. The switching frequency of the resonant power converter may be set by certain characteristics or tuning of a self-oscillating feedback loop connected around a secondary side circuit of the resonant power converter as discussed in further detail below with reference to the appended drawings.

The synchronous rectifier may comprise a half-bridge or H-bridge driver. The half-bridge driver circuit may comprise a first semiconductor switch and a second semiconductor switch coupled in series between the positive DC supply voltage and the negative DC supply voltage. A midpoint node between the first and second semiconductor switches may be connected to an input of the synchronous rectifier. Hence, according to one embodiment of the resonant power converter, the first semiconductor switch comprises a conducting state connecting the resonant output voltage to the positive DC supply voltage and the second semiconductor switch comprises a conducting state connecting the resonant output voltage to the negative DC supply voltage. In addition, each of the first and the second semiconductor switches resides in a non-conducting or off state during the dead-time periods of the rectification circuit.

According one embodiment of the present resonant power converter, the input driver comprises third and fourth semiconductor switches controlled by first and second driver control signals, respectively. The input driver is configured for alternatingly connecting the resonant input voltage to the positive and negative DC supply voltages through the third and fourth semiconductor switches, respectively, separated by intervening dead-time periods in accordance with the first and second driver control signals. The first driver control signal is configured to switch the third semiconductor switch between a conducting/ON state and a non-conducting/OFF state. The second driver control signal is likewise configured to switch the fourth semiconductor switch between a conducting/ON state and a non-conducting/OFF state. The first and second driver control signals are preferably non-overlapping such that the third semiconductor switch pulls the resonant input voltage towards the positive DC supply voltage via its relatively small on-resistance in the conducting state and the fourth semiconductor switch, subsequent to the intervening dead-time period, pulls the resonant input voltage towards the negative DC supply voltage via its relatively small on-resistance in the conducting state. Hence, during the dead time period of the input driver the resonant input voltage or signal is alternatingly charged and discharged from the positive DC supply voltage to the negative DC supply voltage and vice versa by resonant current flowing through an intrinsic input impedance of the piezoelectric transformer and/or by resonant current flowing through, or out of, a series inductor of the resonant network as discussed in further detail below with reference to the appended drawings. The resonant input signal is effectively clamped to the positive DC supply voltage in a first time period where the third semiconductor switch conducts and the fourth semiconductor switch is non-conducting. Likewise, the resonant input signal is clamped to the negative DC supply voltage in a second time period where the fourth semiconductor switch is conducting and the third semiconductor switch is non-conducting. During the dead-time periods, both the third semiconductor switch and the fourth semiconductor switch are non-conducting. Each of the first, second, third and fourth semiconductor switches may comprise a MOSFET for example a DMOS, PMOS or NMOS device. Each of the first, second, third and fourth semiconductor switches further comprises a control terminal or input such as a gate terminal for receipt of the respective driver control signal or rectification control signal.

As discussed previously, the resonant network may comprise a piezoelectric transformer wherein the input section of the resonant network comprises a primary section of the piezoelectric transformer coupled to the resonant input voltage and the output section of the resonant network comprises a secondary section of the piezoelectric transformer for generating the resonant output voltage.

The switching frequency of the resonant power converter may lie between 75 kHz and 500 kHz such as between 100 kHz and 150 kHz. The resonant power converter may comprise a feedback loop configured to induce self-oscillation around the primary side circuit and/or secondary side circuit of the resonant power converter as discussed in additional detail below. The feedback loop may ensure that a switching frequency of the resonant power converter automatically tracks changing characteristics of the resonant network, e.gl based on a piezoelectric transformer, and electronic circuitry of the primary side or secondary side of the power converter.

According to one embodiment, the dead-time controller utilizes a level or amplitude of the resonant input voltage to detect the respective time instant to switch the first or the second semiconductor switch to its conducting state. According to another embodiment, the dead-time controller utilizes a waveform shape of the instantaneous resonant input voltage to detect the respective time instants or phases at which to switch the first or second semiconductor to their respective conducting states as discussed in further detail below with reference to the appended drawings.

The dead-time controller may be configured to adjust a phase or timing of the first driver control signal of the first semiconductor switch and a phase or timing of the second driver control signal of the second semiconductor switch to adaptively adjust the duration of the dead-time periods as discussed in further detail below with reference to the appended drawings.

A number of useful embodiments of the present resonant power converter comprise a self-oscillating feedback loop for setting or controlling the switching frequency of the power converter. The self-oscillating feedback loop may be connected around either the primary section or the secondary section of the power converter. The primary side or secondary side self-oscillating feedback loop is efficient in maintain a proper operating point of the resonant power converter despite drift or variation of component values and parameters of the power converter - for example those caused by ageing and temperature variations. The self-oscillating feedback loop may be designed or configured to oscillate at, or proximate to, a fundamental resonance frequency of the resonant network as discussed in further detail below with reference to the appended drawings.

The first dead-time controller may be coupled to the resonant output voltage in one embodiment of the resonant power converter. The resonant power converter further comprises a first self-oscillating feedback loop which comprises a first resonant voltage or current detector coupled to the output section of the resonant circuit and configured to derive a first feedback signal from a resonant voltage or resonant current of the output section. The resonant power converter further comprises a first adjustable delay circuit configured for generating the first and second rectification control signals based on the first feedback signal. The piezoelectric transformer may comprise a separate electrode for supplying the first resonant voltage or current detector with a resonant voltage or current proportional to the resonant output voltage. Hence, the piezoelectric transformer may comprise:

- a first secondary electrode connected to the secondary section of the piezoelectric transformer for supplying the resonant output voltage; and
- a second secondary electrode embedded in the secondary section for supplying the first feedback signal to the first adjustable delay circuit.

One embodiment of the resonant power converter comprises a first phase shift circuit configured to derive the first and second drive control signals from the first and second rectification control signals by adding respective phase shifts to the first and second rectification control signals. This feature is advantageous in certain applications because the first and second drive control signals are derived/generated in a relatively simple manner from the first and second rectification control signals, respectively, using a small amount of additional components and signal routing as discussed in further detail below with reference to the appended drawings.

In an alternative embodiment, the first dead-time controller is coupled to the resonant input voltage and a self-oscillating feedback loop is connected around the primary section of the power converter. The self-oscillating feedback loop comprises a resonant voltage or current detector coupled to the input section of the resonant circuit and configured to derive a first feedback signal from a resonant voltage or resonant current of the input section; The self-oscillating feedback loop further comprises a first adjustable delay circuit configured for generating the first and second drive control signals based on the first feedback signal. In some of these embodiments, the resonant network comprises a piezoelectric transformer which comprises:

- a first primary electrode connected to the primary section of the piezoelectric transformer for supplying the resonant input voltage; and
- a second primary electrode embedded in the primary section of the piezoelectric transformer for supplying the first feedback signal to the first adjustable delay circuit. One such embodiment comprises a first phase shift circuit configured to derive the first and second drive control signals from the first and second rectification control signals by adding respective phase shifts to the first and second rectification control signals as discussed in further detail below with reference to the appended drawings.

Another alternative embodiment of the resonant power converter comprises two separate and independent self-oscillating feedback loops connected around the primary section or the secondary section, respectively, of the power converter. The presence of such separate self-oscillating feedback loops in the present piezoelectric resonant power converter provides numerous advantages such as an adjustable bi-directional power flow between the DC input voltage and the DC output voltage. The characteristics of this bi-directional power flow can furthermore be very accurately and flexibly controlled by independent digital control or setting of the respective time delays of the first and second adjustable delay circuits as discussed in further detail below with reference to the appended drawings.

One such embodiment of the resonant power converter therefore comprises, in addition to the first self-oscillating feedback loop:

- second self-oscillating feedback loop comprising:

a second resonant voltage or current detector coupled to the input section of the resonant circuit and configured to derive a second feedback signal from a resonant voltage or resonant current of the input section; and a second adjustable delay circuit configured for generating the first and second drive control signals based on the second feedback signal; and

- a second dead-time controller coupled to the resonant input voltage and configured for adaptively adjusting lengths of the dead-time periods of the input driver via the first and second driver control signals. The first adjustable delay circuit may comprise a first digital delay line and a first digital control input for adjusting respective time delays between the first feedback signal and the first and second rectification control signals. The second adjustable time delay circuit may in addition or alternative comprise a second digital delay line and a second digital control input for adjusting respective time delays between the second feedback signal and the first and second driver control signals. Various construction details, programming interfaces etc. of the first and second digital delay lines are discussed in further detail below with reference to the appended drawings.

Each of the first and second adjustable time delay circuits may comprise a digital control input for setting the time delay in the digital domain by a digital processor such as a microprocessor. For this purpose the resonant power converter may

therefore comprise:
a digital processor comprising a first data communication interface connected to at least one of the first and second digital control inputs of the first and second adjustable time delay circuits;
said digital processor being configured to repeatedly compute and apply time delay settings for at least one of:
the first digital delay line for adapting a switching frequency of the first self-oscillating feedback loop to a fundamental resonance frequency of the output section of the resonant circuit; and
the second digital delay line for adapting a switching frequency of the second self-oscillating feedback loop to a fundamental resonance frequency of the input section of the resonant circuit.

The digital processor is configured to:
compute the time delay settings of the first digital delay line to maintain a loop phase shift of substantially 360 degrees, or an integer multiple of 360 degrees, in the first self-oscillating feedback loop; and/or
compute the time delay settings of the second digital delay line to maintain a loop phase shift of substantially 360 degrees, or an integer multiple of 360 degrees, in the second self-oscillating feedback loop.

One embodiment of the first and/or second adjustable time delay circuits has a time step resolution of the first or second digital delay line greater than 10 ns such as greater than 2 ns, or greater than 1 ns, as discussed in further detail below with reference to the appended drawings.

The first dead-time controller may be configured to adjust a phase of the first rectification control signal based on a waveform shape of the resonant output or input voltage and a phase of the second rectification control signal based on the waveform shape of the resonant output or input voltage to adaptively adjust the lengths of the dead-time periods.

A second aspect of the invention relates to a method of adaptively controlling dead-time periods of a synchronous rectifier of a resonant power converter, said method comprising steps of:

a) generating first and second non-overlapping rectification control signals of the synchronous rectifier in accordance with a resonant output voltage or a resonant input voltage of a resonant network of the resonant power converter, wherein the synchronous rectifier is coupled between positive and negative DC output voltage nodes of the converter,

b) applying the first and second non-overlapping rectification control signals to control inputs of the synchronous rectifier to generate a DC output voltage by alternatingly connecting the resonant output voltage to the positive and negative DC output voltage nodes separated by intervening dead-time periods,

c) monitoring at least one of the resonant output voltage and the resonant input voltage,

d) detecting a feature of a waveform of the resonant output voltage or the resonant input voltage,

f) adjusting lengths of the dead-time periods of the synchronous rectifier based on the detected feature.

According to one embodiment of the present methodology of adaptively controlling dead-time periods, step d) may comprise:

detecting the feature of the waveform in each cycle of the resonant input voltage waveform or detecting the feature of the waveform in each cycle of the resonant output voltage waveform.

BRIEF DESCRIPTION OF THE DRAWINGS

Preferred embodiments of the invention are described in more detail in connection with the appended drawings, in which:

FIG. 1 shows a simplified schematic circuit diagram of a piezoelectric resonant power converter in accordance with a first embodiment of the invention,

FIG. 2 shows a simplified schematic circuit diagram of an exemplary adjustable delay circuit for application in various embodiments of the present piezoelectric resonant power converters,

FIG. 2A shows a schematic circuit diagram of an exemplary embodiment of the adjustable delay circuit of FIG. 2 based on a digital delay line for application in various embodiments of the present piezoelectric resonant power converters,

FIG. 3 shows a simplified schematic circuit diagram of a piezoelectric resonant power converter in accordance with a second embodiment of the invention,

FIG. 4 shows a schematic block diagram of an exemplary dead-time controller for use in resonant power converters in accordance with various embodiments of the present invention; and

FIG. 5 is a simplified schematic circuit diagram of a piezoelectric resonant power converter in accordance with a third embodiment of the invention,

DETAILED DESCRIPTION OF PREFERRED EMBODIMENTS

In the following sections various exemplary embodiments of the present resonant power converter are described with reference to the appended drawings. The skilled person will understand that the accompanying drawings are schematic and simplified for clarity and therefore merely show details which are essential to the understanding of the invention, while other details have been left out. Like reference numerals refer to like elements throughout. Like elements will, thus, not necessarily be described in detail with respect to each figure.

FIG. 1 shows a simplified schematic block diagram of a resonant power converter 100 based on a piezoelectric transformer 104 operating as a resonant network of the power converter. The piezoelectric resonant power converter 100 additionally comprises an input driver 103 electrically coupled to an input section or primary section of the piezoelectric transformer 104 for receipt of a resonant input voltage V_{FP}. The resonant input voltage V_{FP} is supplied at an output node or terminal 102 of the input driver 103. Hence, the resonant input voltage V_{FP} is an ac input drive signal at a switching frequency of the power converter. The resonant input voltage V_{FP} may be applied to the input or primary section of the piezoelectric transformer 104 via first and second physical input electrodes of the transformer 104. A driver control circuit 101 is configured to generate appropriately timed gate control signals for the first and second semiconductor switches S_{D1} and S_{D2} of the input driver 103. Each of the first and second semiconductor switches S_{D1} and S_{D2} may comprise a FET for example a NMOS or PMOS transistor. The first and second semiconductor switches S_{D1} and S_{D2} are coupled in cascade such that they jointly form a half-bridge topology of the input driver 103. The second input electrode of the piezoelectric transformer 104 may be connected to a negative DC supply rail of the power converter 100 such as ground, GND, shared with the input driver 103 as illustrated. The input driver 103 additionally comprises a first power supply rail for receipt of a positive DC supply voltage V_{DD}. Hence, the waveform of the resonant input voltage V_{FP} is determined by a first driver control signal LS_P and a second driver control signal HS_P supplied to the first and second semiconductor switches S_{D1} and S_{D2} through the driver control circuit 101. The first and second input control signals LS_P, HS_P are derived via time delay or phase shift imparted by an optional phase shifter 126 coupled to a first and second rectification control signals LS_S, HS_S of a synchronous rectifier 123 of a secondary side circuit of the resonant power converter as discussed below in further detail. The first and second driver signals LS_P, HS_P are non-overlapping and separated by intervening off periods as discussed below in further detail.

The above-mentioned secondary side circuit of the piezoelectric resonant power converter 100 comprises an output section of the piezoelectric transformer 104, the synchronous rectifier 123, a smoothing capacitor C_L and a converter load R_L connected to a DC output voltage V_{OUT} of the piezoelectric power converter. The output section of the piezoelectric transformer 104 generates the resonant output voltage V_{FS} at an output electrode or electrodes coupled to the secondary section of the piezoelectric transformer 104 in response to the previously discussed application of the resonant input voltage V_{FP} to the primary section of the piezoelectric transformer 104. The resonant output voltage V_{FS} is applied to an input node 122 of the synchronous rectifier 123. The synchronous rectifier 123 comprises first and second semiconductor switches S_{R1} and S_{R2} controlled by the first and second non-overlapping rectification control signals LS_S, HS_S, respectively. The first and second rectification control signals LS_S, HS_S are generated by a self-oscillating feedback loop extending around the secondary circuit of the piezoelectric resonant power converter 100. The non-overlapping property of LS_S, HS_S forces the synchronous rectifier 123 to alternatingly connect the resonant output voltage V_{FS} to the DC output voltage V_{OUT} and ground (GND), serving as the negative DC output voltage in the present embodiment, separated by intervening dead-time periods as controlled by the timings of the first and second rectification control signals LS_S, HS_S. The skilled person will understand that the resonant output voltage V_{FS} is alternatingly connected to the DC output voltage V_{OUT} through a relatively small on-resistance of semiconductor switch S_4 and GND through a relatively small on-resistance of semiconductor switch S_{R1}. During the dead-time periods, semiconductor switches S_{R1} and S_{R2} are both placed in non-conducting states or off states to let the resonant output voltage V_{FS} essentially float such that the resonant currents flowing into, or out of, an intrinsic output inductance of the output section of the piezoelectric transformer 104 charges or discharges the input node 122 of the synchronous rectifier 123 either towards V_{OUT} or towards GND. During the dead-time period, the resonant current must charge and discharge output capacitances of the first and second semiconductor switches S_{R1} and S_{R2} and an output capacitance of the secondary section of the piezoelectric transformer 103 as these all are coupled to the input node 122 of the synchronous rectifier 123. The output capacitance associated with the secondary section of the piezoelectric transformer is normally in the range of nF while the output capacitances of typical MOSFETs used as switches S_{R1} and S_{R2} may be around hundreds of pF. Therefore, the dead time period or interval of the synchronous rectifier 123 or the input driver 103 is defined as the time interval of a switching cycle of the resonant input voltage or resonant output voltage where both semiconductor switches, e.g. MOSFETs, are in non-conducting states, i.e. turned off.

The skilled person will understand that the present invention may be applied to magnetics based resonant power converter in a corresponding manner. In such magnetics based resonant power converter, the piezoelectric transformer 104 is replaced by a resonant network typically comprising a number of interconnected capacitors and inductors in accordance with a particular converter topology. The magnetics based resonant power converter may comprise a magnetic transformer galvanically insulating the primary section and the secondary side circuitry of the resonant power converter. The magnetics based resonant power converter may for example comprise a LCC converter topology.

As previously mentioned it is important to have a sufficient duration or length of the intervening dead-time periods between the alternatingly conducting switch states of the first and second semiconductor switches S_{R1} and S_{R2} to provide optimal ZVS operation of the synchronous rectifier 123 for the reasons discussed in significant detail in the applicant’s co-pending European patent application No. 15174592.4. In the latter co-pending patent application, optimal ZVS operation is discussed in the context of adjusting the corresponding dead-time periods of the semiconductor switches of the input driver 103. The ZVS operation eliminates so-called hard switching of the first and and/or second semiconductor switches S_{R1} and S_{R2} of the rectifier which hard switching would lead to a marked increase of the power consumption of the synchronous rectifier 123.

The secondary side circuit of the resonant power converter 100 comprises a dead-time controller comprising an ODT-s block 114 and a cooperating DB-s block 124 which jointly are configured to adaptively adjusting lengths of the dead-time periods of the synchronous rectifier 123 by controlling state switching of the first and second rectifications control signals LS_S, HS_S based on the resonant output voltage $V_{FS.}$ The dead-time controller 114, 124 is capable of adjusting the lengths or durations of the dead-time periods by individually controlling timing or phase of the state transitions of the first and second rectifications control signals LS_S, HS_S applied to the control inputs of the synchronous rectifier 123. The ODT-s block 114 generates a set of control signals to the DB-s block 124 via a signal bus or connection 115. The dead-time controller exploits these control signals to provide adequate length or duration of the dead time periods of the driver circuit to deliver sufficient energy for charging and discharging the output capacitance at the output terminal or node of the output section of the piezoelectric transformer 104. This feature enables zero voltage switching (ZVS) and/or zero current switching (ZCS) of the synchronous rectifier 123 such that energy consumption imparted by the switching activity of the first and second semiconductor switches S_{R1} and S_{R2}.

The dead-time controller 114, 124 may utilize various features of the resonant output voltage V_{FS} for detecting an optimum dead time period of each of the first and second semiconductor switches S_{R1} and S_{R2} and adaptively adjusting the dead-time period. The dead-time controller 114, 124 may in some embodiments be configured to adjust the length of the dead-time period during substantially every switching cycle of the resonant output voltage based on an instantaneous value thereof. This switching cycle is determined by a switching frequency of the resonant power converter. Alternatively, the dead-time controller may be configured to adjust the length of the dead-time period during a specific operating condition of the piezoelectric power converter 100 for example solely during a start-up phase or initialization time of the resonant network or solely during steady state operation of the resonant network as discussed in further detail below with reference to FIG. 4 illustrating an exemplary embodiment of the ODT-s block 114. The adaptive adjustment of the lengths or durations of the dead-time periods reduces energy losses and consequently leads to increased power conversion efficiency of the piezoelectric resonant power converter both during the start-up phase and during steady state operation. The self-oscillating feedback loop of the piezoelectric resonant power converter 100 extends around the secondary side circuit of the power converter. The self-oscillating feedback loop comprises a first resonant voltage or current detector 120 coupled to the output/secondary section of the piezoelectric transformer 104. The first resonant voltage or current detector 120 may be coupled to the piezoelectric transformer 104 via an auxiliary, or second secondary, electrode 121 which provides a resonant voltage or current proportional to the resonant output voltage V_{FS}. The auxiliary, or second secondary, electrode 121 may be embedded in the secondary section of the piezoelectric transformer. The output 119 of the resonant voltage or current detector 120 is digital or binary feedback signal with a frequency corresponding to, or proportional, to the resonant output voltage V_{FS}.

The binary feedback signal is applied to an adjustable delay circuit 125 of the self-oscillating feedback loop. The adjustable delay circuit 125 is configured for deriving the previously discussed first and second rectification control signals LS_S, HS_S of the synchronous rectifier 123 from the first feedback signal. The adjustable delay circuit 125 accomplishes this task by generating a pair of intermediate control signals ODL_{on} and ODL_{off} for the DB-s block 124 as discussed in further detail below with reference to the exemplary embodiment of the adjustable delay circuit 125 and DB-s block 124 depicted on FIGS. 2 and 2A.

The skilled person will understand that the characteristics of the secondary side self-oscillating feedback loop discussed above must satisfy two requirements to produce sustained oscillation in the closed loop. One is that the phase shift through the entire feedback loop should be an integer multiple of 360°; the other requirement is that the loop gain must be greater than unity to start-up oscillation. The former condition is fulfilled by adjusting phase shift through the loop. The latter condition is preferably fulfilled by using a suitable comparator in the resonant voltage or current detector 120. The gain of this comparator can reasonably be considered infinite and therefore its output voltage, i.e. the first feedback signal, possesses a square wave shape alternatingly saturated to the positive DC supply voltage V_{DD} and the negative DC supply voltage GND.

The first and second drive control signals LS_P, HS_P of the input driver 103 are derived from the first and second rectification control signals LS_S, HS_S via the time delay or phase shift imparted by the phase shifter 126 as previously discussed. In this manner, the first and second drive control signals L_{SP}, H_{SP} may be essentially identical to the first and second rectification control signals, respectively, except for a predetermined phase shift $\Delta\phi$. In this manner, the switching frequency of the resonant input voltage V_{FP} generated by the input driver 103 is forced to, or locked to, the switching frequency of the secondary side self-oscillating feedback loop. The latter feature is advantageous in certain applications because the first and second drive control signals LS_P, HS_P are derived/generated in a relatively simple manner from the first and second rectification control signals, respectively, using a small amount of additional components and signal routing. However, this method of deriving the first and second drive control signals LS_P, HS_P may lead to sub-optimal ZVS properties of the input driver 103 because the timing of the first and second drive control signals LS_P, HS_P is based on the adaptive optimization of the first and second rectification control signals LS_S, HS_S carried out by the dead-time controller 114, 124 and the adjustable delay circuit 125. The optimum timing of the first and second drive control signals LS_P, HS_P may differ from that of the first and second rectification control signals LS_S, HS_S for numerous reasons for example different intrinsic input and output capacitances of the piezoelectric transformer 104, different intrinsic output capacitances between the pair of semiconductor switches S_{D1} and S_{D2} of the input driver and the pair of semiconductor switches S_{R1} and S_{R2} of the synchronous rectifier 123.

The skilled person will appreciate that the dead-time controller 114, 124 is coupled to the resonant output voltage V_{FS} in the present piezoelectric power converter 100 to derive the set of control signals, transmitted via bus 115, to the DB-s block 124 for adjusting the lengths of the dead-time periods of the synchronous rectifier 123. According to the alternative embodiment discussed below with reference to FIG. 3, a corresponding dead-time controller is coupled to the resonant input voltage V_{FP} rather than the resonant output voltage V_{FS}. In the latter embodiment, the first and second rectification control signals LS_S, HS_S are derived from the first and second drive control signals LS_P, HS_P via an optional phase shifter 326 coupled to the first and second rectification control signals LS_S, HS_S of the input driver. The use of the secondary side self-oscillating feedback loop to control the switching frequency of the present piezoelectric power converter 100 has several advantages. The closed loop control efficiently compensates for the drift or variation of component values and parameters of the power converter for example those caused by ageing and temperature variations. This is achieved because the closed loop control scheme is efficient in keeping the switching frequency of the piezoelectric power converter 100 at a proper operating point of the power converter. This switching frequency typically lies slightly above a fundamental resonant frequency of the piezoelectric transformer 104.

The adjustable delay circuit 125 of the present piezoelectric power converter 100 utilizes a digital delay line to apply a digitized phase shift compensation to the feedback signal to maintain a full feedback loop phase shift of 360° (or a multiple thereof) despite the previously discussed component and parameters variations over time. The time delay imparted by the digital delay line to the binary feedback signal (at the output 119 of the resonant voltage/current detector 120) is digitally controllable via a digital control input of the adjustable delay circuit 125 through a data communication interface 135. The data communication interface 135 is connected to a digital controller 130 that is configured to program or write a desired time delay to the adjustable delay circuit as discussed in further detail below with reference to FIG. 2A. The digital controller 130 may comprise a software programmable device such as a microprocessor or hard-wired digital logic circuitry for example comprising a digital sequential and combinational logic. The digital controller 130 may be programmed or implemented by a FPGA device or fabricated as an ASIC - for example using sub-micron CMOS technology.

FIG. 2 shows a simplified schematic circuit diagram of an exemplary embodiment of the adjustable delay circuit 125 and the DB-s block 124 which also forms part of the dead-time controller 124 as discussed above. The skilled person will appreciate that the adjustable delay circuits of the other embodiments of the present resonant power converters 300, 500 as discussed below in connection with FIG. 3 and FIG. 5 may be substantially identical to the adjustable delay circuit 125. The ODL block 125 is composed of two sub-blocks 201, 203 designated ODL_{on} and ODL_{off}, respectively. The previously discussed binary feedback signal is applied to the input of the adjustable delay circuit 125 and gets delayed by ODL_{on} to turn on, i.e. switching to the conducting state, each of the first and second semiconductor switches S_{R1} and S_{R2} at its rising edge. The output of the ODL_{on} sub-block 201 is tied to the ODL_{off} and imposes additional time delays to the binary feedback signal to turn off, i.e. switching to a non-conducting state, each of the first and second semiconductor switches S_{R1} and S_{R2} at each rising edge of its output pulses. The time delay applied by the ODL_{off} sub-block 203 defines the on-time or conducting time period of the first and second semiconductor switches S_{R1} and S_{R2}. The DB-s block 124 is controlling the final waveforms of the first and second rectification control signals LS_S, HS_S. The time delay span of the adjustable delay circuit 125 may correspond to at least one half–cycle of the either the resonant input voltage or the resonant output voltage. In the present embodiment, signal Ref applied to the input of an optional fixed time delay (FTD) circuit increases the time delay of the adjustable delay circuit 125 in certain predetermined steps to ensure that the time delay span of the circuit 125 covers at least the one half–cycle of the either the resonant input voltage or the resonant output voltage.

The configuration or topology of the adjustable delay circuit 125 provides a digitally programmable or settable time delay of the dead-time periods with very high resolution as explained in further detail below with reference to the detailed schematic of FIG. 2A. The inventors have achieved a time resolution down to 1 ns in an experimental prototype of the present piezoelectric power converter 100. The high time resolution makes it possible to accurately control the time delay added to the secondary side self-oscillating feedback loop and/or to the primary side self-oscillating feedback loop as discussed below. In return, this feature allows the digital controller 130 to very accurately adapt or adjust the switching frequency of the self-oscillating loop to changes of the operating point, e.g. the fundamental resonance frequency, of the piezoelectric transformer 104.

FIG. 2A shows a schematic circuit diagram 205 of an exemplary embodiment of the adjustable delay circuit blocks DDL-ON 205a and DDL-OFF 205b of FIG. 2 based on the digital delay line. The adjustable delay circuit block 205 comprises a resettable integrator build around operational amplifier 211 generating a saw tooth waveform to the inverting input of a comparator 213. The resettable integrator uses capacitor C_F as integration element and is reset by switch D1 via a control network steered by an inverting output. The non-inverting input of the comparator 213 is supplied with an adjustable reference voltage V_{Ref} generated by a programmable D/A converter 207. The programmable D/A converter 207 may have a resolution between 12 and 18 bits for example 16 bits as illustrated. The level of the reference voltage V_{Ref} is set by a digital control input 215 of the programmable D/A converter 207. This digital control input 215 is connected to the previously discussed digital controller 130 via the data communication/programming interface or bus 135. The data communication bus 135 may comprise a SPI compatible data bus or any other suitable data bus. The high resolution of the programmable D/A converter 207 enables a very small step size of the level of the reference voltage V_{Ref} such that the latter can be very accurately set to a desired voltage. The small step size of the level of the reference voltage V_{Ref} allows the delay time of the output signal DDL_{out} to in response be adjusted in very small time steps such as time steps of 10 ns or smaller or 1 ns or smaller depending *inter alia* on the selected resolution of the programmable D/A converter 207.

Waveform graph 250 shows respective exemplary waveforms of the input signal DDL_{in} and output signal DDL_{out} of the adjustable delay circuit block DDL-ON 205. The graph 250 finally shows a corresponding waveform of the internal control signal $EDDL_{in}$.

FIG. 3 shows a simplified schematic block diagram of a piezoelectric resonant power converter 300 in accordance with a second embodiment of the invention. The piezoelectric resonant power converter 300 largely comprises corresponding circuit blocks and features to those of the first embodiment of the piezoelectric resonant power converter 100 discussed above. However, the piezoelectric resonant power converter 300 comprises a self-oscillating feedback loop connected around a primary side circuit of the power converter 100 in contrast to the self-oscillating feedback loop of the previous piezoelectric resonant power converter 100 which was connected around the secondary circuit of the converter.

The primary side circuit of the resonant power converter 300 comprises a dead-time controller comprising an ODT-p block 314 and a cooperating DB-p block 324 which jointly are configured to adaptively adjusting lengths of the dead-time periods of the input driver 303 by controlling state switching of first and second driver control signals LS_P, HS_P based on the resonant output voltage $V_{FS.}$ The dead-time controller 314, 324 is thereby capable of adjusting the lengths or durations of the dead-time periods of input driver 303 by individually controlling timing or phase of the state transitions of the first and second driver control signals LS_P, HS_P applied to the control inputs of the input driver. The input driver 303 comprises semiconductor switches S_{D1} and S_{D2} which are both placed in non-conducting states, or off states, during each dead-time period to let the resonant input voltage V_{FP} essentially float such that resonant currents flowing into, or out of, an intrinsic input inductance of the primary section of the piezoelectric transformer 304 charges or discharges the resonant input voltage V_{FP} either towards V_{DC} or towards GND. During each the dead-time period, the resonant current must either charge or discharge the output capacitances of the first and second semiconductor switches S_{D1} and S_{D2} and an input capacitance of the primary section of the piezoelectric transformer 303 as these all are coupled to the deriver output node 102. The role of the ODT-p block 314 and cooperating DB-p block 324 is provide an adaptable and optimum length of the dead-time periods of the input driver 303 in a manner largely similar to the adaptable and optimum dead-time period of the synchronous rectifier 123 of the previous embodiment of the resonant power converter 100. As mentioned previously, the operation theory and principles of the dead-time controllers are discussed in significant detail in the applicant's co-pending European patent application No. 15174592.4. FIG. 4 is illustrating an exemplary embodiment of the ODT-p block 314.

The primary side self-oscillating feedback loop comprises a resonant voltage or current detector 320 coupled to the input /primary section of the piezoelectric transformer 304. The first resonant voltage or current detector 320 may be coupled to the piezoelectric transformer 304 via an auxiliary, or second primary, electrode 321 which provides a resonant voltage or current proportional to the resonant input voltage V_{FP}. The output 319 of the resonant voltage or current detector 320 is digital or binary feedback signal with a frequency corresponding to, or proportional, to the resonant output voltage V_{FP}. The binary feedback signal is applied to an adjustable delay circuit 325 of the primary side self-oscillating feedback loop. The adjustable delay circuit 125 derives the previously discussed first and second drive control signals LS_P, HS_P from the binary feedback signal in a similar manner to the operation of the previously discussed adjustable delay circuit 125 of the first embodiment of the power converter 100. The skilled person will understand that the characteristics of the primary side self-oscillating feedback loop must satisfy same two requirements as those discussed above in respect of the secondary side self-oscillating feedback loop discussed above to produce and maintain sustained oscillation in the closed loop. The resonant power converter 300 furthermore comprises a digital controller 330 that is configured to program or write a desired time delay to the adjustable delay circuit 325 via a data bus or interface 335 in a similar manner to the one discussed above in connection with the previous embodiment of the invention.

The first and second rectification control signals LS_S, HS_S of the synchronous rectifier 323 are derived from the first and second drive control signals LS_P, HS_P of the input driver 303 via a time delay or phase shift imparted by a phase shifter 326. In this manner, the first and second rectification control signals LS_S, HS_S are derived by the primary side connected dead-time controller 325 which is coupled to the resonant input voltage V_{FP} rather than the resonant output voltage V_{FS}. The first and second rectification control signals may be essentially identical to the first and second drive control signals, respectively, except for a predetermined phase shift $\Delta\phi$ generated by the phase shifter 326. Thereby, the switching frequency of the resonant output voltage V_{FS} applied to the input of the synchronous rectifier 323 is forced to, or locked to, the switching frequency of the primary side self-oscillating feedback loop. The latter feature is advantageous in certain applications because the first and second rectification control signals LS_S, HS_S are derived/generated in a relatively simple manner from the first and second drive control signals, respectively, using a small amount of additional components and signal routing. The role of the primary side self-oscillating feedback loop of the present converter 300 is to control the switching frequency of the piezoelectric power converter 300 and preferably maintain the switching frequency of the converter at a substantially optimal frequency of the piezoelectric transformer 304 despite drift and variation of component values and parameters of the power converter 300 - for example caused by ageing and/or temperature variations.

FIG. 4 shows a schematic block diagram of an exemplary embodiment of the dead-time controllers 114, 314, 514 of the piezoelectric power converters 100, 300, 500. The dead-time controller 414 comprises *inter alia* a steady-state controller 624 and a start-up controller 634 and a control circuit 644 (OTD C). The steady-state controller 624 is adapted to generate appropriately timed first and second driver control signals HS_G, LS_G for the either the input driver 103 or the synchronous rectifier 323 of the piezoelectric power converters 100, 300. The start-up controller 634 is adapted to generate appropriately timed first and second driver control signals HS_G, LS_G or first and second rectification control signals LS_S, HS_S during the initialization time or start-up time of the piezoelectric power converters 100, 300. The operation theory and operation principles of the dead-time controller 514 are discussed in significant detail in the applicant's co-pending European patent application No. 15174592.4 and will not be repeated here.

FIG. 5 is a simplified schematic circuit diagram of a piezoelectric resonant power converter 500 in accordance with a third embodiment of the invention. The piezoelectric resonant power converter 500 comprises two separate self-oscillating feedback loops connected around the primary section of the converter and the secondary section of the converter, respectively. The piezoelectric resonant power converter 500 furthermore comprises two separate dead-time controllers. A first dead-time controller is connected to the resonant output voltage and comprises an ODT-s block 514 and a cooperating DB-s block 524 which jointly are configured to adaptively adjusting lengths of the dead-time periods of the synchronous rectifier 523 by controlling state switching of first and second driver control signals LS_P, HS_P based on the resonant output voltage $V_{FS.}$ The primary side circuit of the resonant power converter 500 comprises a second dead-time controller comprising an ODT-p block 514 and a cooperating DB-p block 524p which jointly are configured to adaptively adjusting lengths of the dead-time periods of the input driver 503 by controlling state switching of first and second driver control signals LS_P, HS_P based on the resonant input voltage $V_{FP.}$ The skilled person will understand that the first dead-time controller may be substantially identical to the dead-time controller discussed above in connection with the first embodiment of the piezoelectric power converter 100 and that the second dead-time controller may be substantially identical to the dead-time controller discussed above in connection with the second embodiment of the piezoelectric power converter 300. The use of two separate dead-time controllers in the present piezoelectric resonant power converter 500 provides separate optimization of the lengths of the dead-time periods of synchronous rectifier 523 and the lengths of the dead-time periods of the input driver 503. This may be a significant advantage for numerous types of resonant power converters because the optimum lengths of these different dead-time periods typically differ for example due to different intrinsic input and output capacitances of the piezoelectric transformer 504 etc. as briefly discussed above.

The first self-oscillating feedback loop of the piezoelectric resonant power converter 500 comprises a first resonant voltage or current detector 520s coupled to an output/secondary section of the piezoelectric transformer 504. The first resonant voltage or current detector 520s may be coupled to the piezoelectric transformer 504 via an auxiliary, or second secondary, electrode as discussed above in connection with FIG. 1. The output of the resonant voltage or current detector 520s is a digital or binary feedback signal with a frequency corresponding to, or proportional, to the resonant output voltage V_{FS}. The binary feedback signal is applied to a first adjustable delay circuit 525s of the self-oscillating feedback loop which may be identical to the previously discussed adjustable delay circuit 125 of the first power converter embodiment 100. The second, or primary side, self-oscillating feedback loop comprises a second resonant voltage or current detector 520p coupled to the input/primary section of the piezoelectric transformer 504. The second resonant voltage or current detector 520p may be coupled to the piezoelectric transformer 504 via an auxiliary, or second primary, electrode as discussed above in connection with FIG. 3. The output of the resonant voltage or current detector 520p is a digital or binary feedback signal with a frequency corresponding to, or proportional, to the resonant input voltage V_{FP}. The binary feedback signal is applied to a second adjustable delay circuit 525p of the primary side self-oscillating feedback loop. The second adjustable delay circuit 525p derives the previously discussed first and second drive control signals LS_P, HS_P from the binary feedback signal in a similar manner to the operation of the previously discussed adjustable delay circuit 325 of the second embodiment of the power converter 300. The skilled person will understand operational characteristics and features of the first self-oscillating feedback loop may be substantially identical to those of the self-oscillating feedback loop discussed above in connection with the first embodiment of the piezoelectric power converter 100 and that the operational characteristics and features of the second self-oscillating feedback loop may be substantially identical to those of the self-oscillating feedback loop discussed above in connection with the second embodiment of the piezoelectric power converter 300.

The presence of two separate self-oscillating feedback loops within the present piezoelectric resonant power converter 500 provides numerous advantages such as an adjustable bi-directional power flow between the DC input voltage and the DC output voltage. This bi-directional power flow can furthermore be very accurately and flexibly controlled by the digital control, via the digital controller 530s, of the time delay through programming of the first adjustable delay circuit 525s, e.g. with 10 ns or better resolution such as better than 1 ns. The control of the bi-directional power flow is a significant advantage because this feature allows efficient driving of inductive loads and seamless integration in numerous smart-grid applications and networks. The piezoelectric resonant power converter 500 furthermore comprises first and second digital controllers 530s, 530p. The first digital controller 530s is configured to program or write a desired time delay to the first adjustable delay circuit 525s via a first data bus or interface 535s in a similar manner to the one discussed above in connection with FIG. 1. The second digital controller 530p is configured to program or write a desired time delay to the first adjustable delay circuit 525s via a second data bus or interface 535p in a similar manner to the one discussed above in connection with FIG. 3. The first and second digital controllers 530p, 530s may be physically separate circuits or devices which has the advantage of enabling galvanic isolation between the primary side and secondary side circuits of the piezoelectric resonant power converter 500. However, in alternative embodiments of power converter 500, the first and second digital controller 530p, 530s may be integrated or fused to form a single physical circuit or device connected to both of the first and second data busses or interfaces 535s, 535p. This embodiment of the power converter 500 may lower component costs and space requirements of the power converter.

CLAIMS

1. A resonant power converter comprising:
a first power supply rail for receipt of a positive DC supply voltage and a second power supply rail for receipt of a negative DC supply voltage,
a resonant network comprising an input section for receipt of a resonant input voltage and an output section for supplying a resonant output voltage generated in response to the resonant input voltage,
an input driver configured for supplying the resonant input voltage;
a synchronous rectifier comprising:
a rectifier input coupled to the resonant output voltage,
first and second semiconductor switches controlled by first and second rectification control signals, wherein the synchronous rectifier is configured for alternatingly connecting the resonant output voltage to positive and negative DC output nodes via the first and second semiconductor switches, respectively, separated by intervening dead-time periods in accordance with the first and second rectification control signals;
a first dead-time controller coupled to the resonant output voltage or the resonant input voltage and configured for adaptively adjusting lengths of the dead-time periods via the first and second rectification control signals.

2. A resonant power converter according to claim 1, wherein the input driver comprises third and fourth semiconductor switches controlled by first and second driver control signals; wherein the input driver is configured for alternatingly connecting the resonant input voltage to the positive and negative DC supply voltages through the third and fourth semiconductor switches, respectively, separated by intervening dead-time periods in accordance with the first and second driver control signals.

3. A resonant power converter according to any of the preceding claims, wherein the resonant network comprises a piezoelectric transformer;
wherein the input section of the resonant network comprises a primary section of the piezoelectric transformer coupled to the resonant input voltage and the output section of the resonant network comprises a secondary section of the piezoelectric

transformer for generating the resonant output voltage.

4. A resonant power converter according to any of the preceding claims, wherein the first dead-time controller is coupled to the resonant output voltage; said resonant power converter further comprising:
a first self-oscillating feedback loop comprising:
a first resonant voltage or current detector coupled to the output section of the resonant circuit and configured to derive a first feedback signal from a resonant voltage or resonant current of the output section; and
- a first adjustable delay circuit configured for generating the first and second rectification control signals based on the first feedback signal.

5. A resonant power converter according to claims 3 and 4, wherein the piezoelectric transformer comprises:
- a first secondary electrode connected to the secondary section of the piezoelectric transformer for supplying the resonant output voltage; and
- a second secondary electrode embedded in the secondary section for supplying the first feedback signal to the first adjustable delay circuit.

6. A resonant power converter according to claim 5, further comprising:
a first phase shift circuit configured to derive the first and second drive control signals from the first and second rectification control signals by adding respective phase shifts to the first and second rectification control signals.

7. A resonant power converter according to any of claims 1-3, wherein the first dead-time controller is coupled to the resonant input voltage; said resonant power converter further comprising:
a self-oscillating feedback loop comprising:
a resonant voltage or current detector coupled to the input section of the resonant circuit and configured to derive a first feedback signal from a resonant voltage or resonant current of the input section; and
- a first adjustable delay circuit configured for generating the first and second drive control signals based on the first feedback signal.

8. A resonant power converter according to claims 3 and 7, wherein the piezoelectric transformer comprises:
- a first primary electrode connected to the primary section of the piezoelectric transformer for supplying the resonant input voltage; and
- a second primary electrode embedded in the primary section of the piezoelectric transformer for supplying the first feedback signal to the first adjustable delay circuit.

9. A resonant power converter according to claim 8, further comprising:
a first phase shift circuit configured to derive the first and second drive control signals from the first and second rectification control signals by adding respective phase shifts to the first and second rectification control signals.

10. A resonant power converter according to any of claims 4-6, further comprising:
- second self-oscillating feedback loop comprising:
a second resonant voltage or current detector coupled to the input section of the resonant circuit and configured to derive a second feedback signal from a resonant voltage or resonant current of the input section; and
- a second adjustable delay circuit configured for generating the first and second drive control signals based on the second feedback signal; and
- a second dead-time controller coupled to the resonant input voltage and configured for adaptively adjusting lengths of the dead-time periods of the input driver via the first and second driver control signals.

11. A resonant power converter according to any of claims 4-10, wherein the first adjustable delay circuit comprises a first digital delay line and a first digital control input for adjusting respective time delays between the first feedback signal and the first and second rectification control signals; and/or
the second adjustable time delay circuit comprises a second digital delay line and a second digital control input for adjusting respective time delays between the second feedback signal and the first and second driver control signals.

12. A resonant power converter according to claim 11, further comprising:
- a digital processor comprising a first data communication interface connected to at

least one of the first and second digital control inputs of the first and second adjustable time delay circuits;
said digital processor being configured to repeatedly compute and apply time delay settings for at least one of:
the first digital delay line for adapting a switching frequency of the first self-oscillating feedback loop to a fundamental resonance frequency of the output section of the resonant circuit; and
the second digital delay line for adapting a switching frequency of the second self-oscillating feedback loop to a fundamental resonance frequency of the input section of the resonant circuit.

13. A resonant power converter according to claim 12, wherein the digital processor is configured to:
compute the time delay settings of the first digital delay line to maintain a loop phase shift of substantially 360 degrees, or an integer multiple of 360 degrees, in the first self-oscillating feedback loop; and/or
compute the time delay settings of the second digital delay line to maintain a loop phase shift of substantially 360 degrees, or an integer multiple of 360 degrees, in the second self-oscillating feedback loop.

14. A method of adaptively controlling dead-time periods of a synchronous rectifier of a resonant power converter, said method comprising steps of:
a) generating first and second non-overlapping rectification control signals of the synchronous rectifier in accordance with a resonant output voltage or a resonant input voltage of a resonant network of the resonant power converter, wherein the synchronous rectifier is coupled between positive and negative DC output voltage nodes of the converter,
b) applying the first and second non-overlapping rectification control signals to control inputs of the synchronous rectifier to generate a DC output voltage by alternatingly connecting the resonant output voltage to the positive and negative DC output voltage nodes separated by intervening dead-time periods,
c) monitoring at least one of the resonant output voltage and the resonant input voltage,
d) detecting a feature of a waveform of the resonant output voltage or the resonant

input voltage,

f) adjusting lengths of the dead-time periods of the synchronous rectifier based on the detected feature.

15. A method of adaptively controlling dead-time periods of a synchronous rectifier according to claim 15, wherein step d) comprises:

detecting the feature of the waveform in each cycle of the resonant input voltage waveform or detecting the feature of the waveform in each cycle of the resonant output voltage waveform.

ABSTRACT

The invention relates in a first aspect to a resonant power converter comprising a synchronous rectifier for supplying a DC output voltage. The synchronous rectifier is configured for alternatingly connecting a resonant output voltage to positive and negative DC output nodes via first and second semiconductor switches, respectively, separated by intervening dead-time periods in accordance with first and second rectification control signals. A dead-time controller is coupled to the resonant output voltage or the resonant input voltage and configured for adaptively adjusting lengths of the dead-time periods via the first and second rectification control signals.

(FIG. 1 for publication)

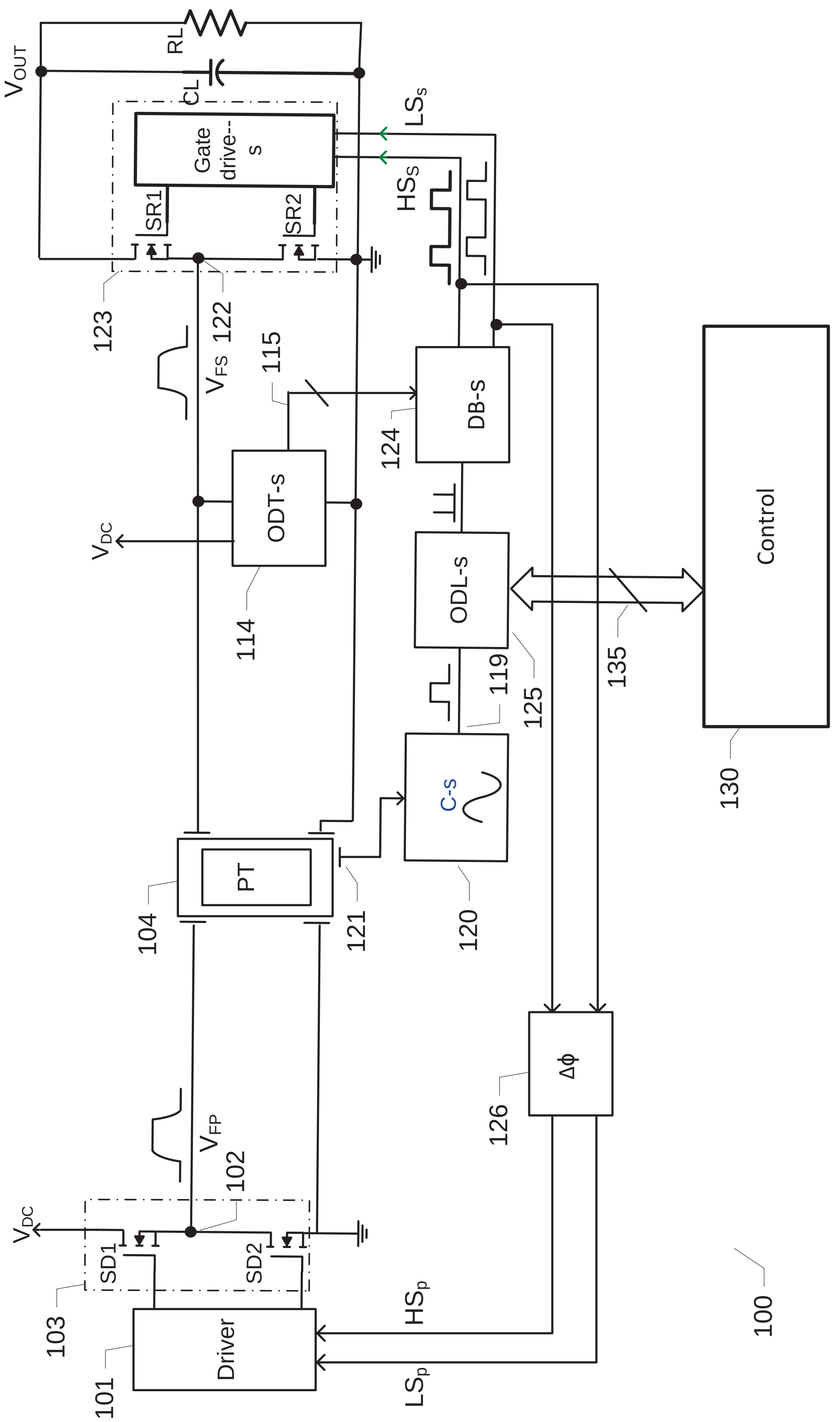

VOUT
RL
CL
Gate drive-s
SR1
SR2
123
122
VFS
115
LSs
HSs
124
DB-s
ODT-s
VDC
114
ODL-s
119
125
135
Control
130
C-s
120
PT
104
121
VFP
102
VDC
SD1
SD2
103
Driver
101
HSp
LSp
Δϕ
126
100

FIG. 1

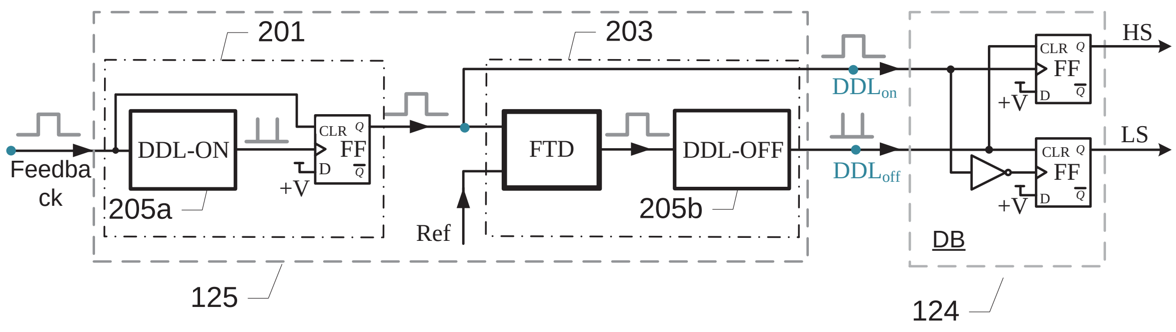
201
203
DDL-ON
CLR
Q
FF
D
Q
+V
Feedback
205a
FTD
DDL-OFF
205b
Ref
DDLon
DDLoff
125
CLR
Q
FF
D
Q
+V
HS
CLR
Q
FF
D
Q
+V
LS
DB
124

FIG. 2

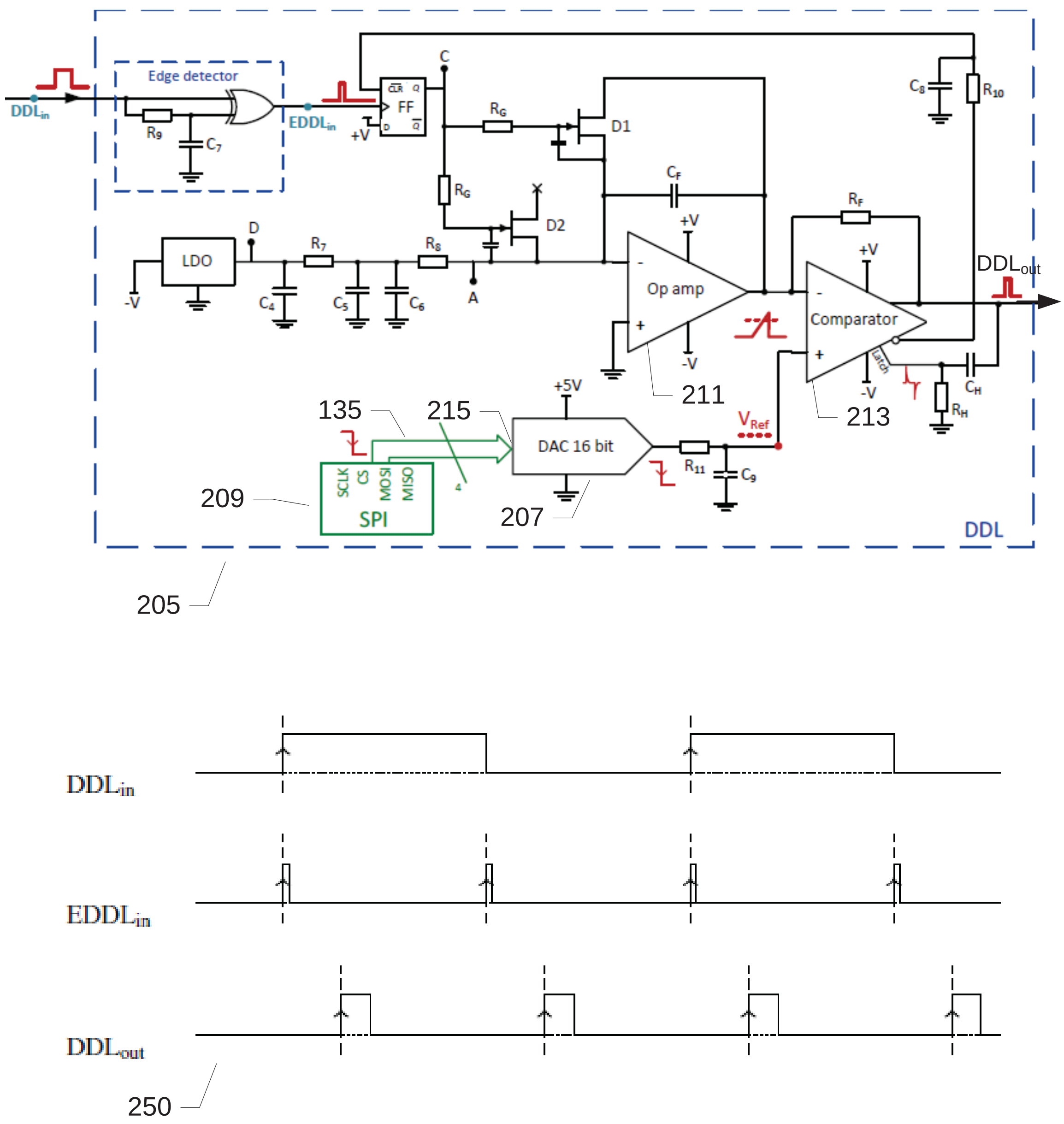
Edge detector
DDLin
EDDLin
R9
C7
CLR
Q
FF
D
+V
C
RG
D1
CF
RG
D2
D
LDO
R7
R8
-V
C4
C5
C6
A
+V
Op amp
-V
RF
+V
Comparator
-V
Latch
C8
R10
DDLout
CH
RH
211
213
VRef
135
215
+5V
DAC 16 bit
R11
C9
SCLK
CS
MOSI
MISO
SPI
209
207
4
DDL
205
DDLin
EDDLin
DDLout
250

FIG. 2A

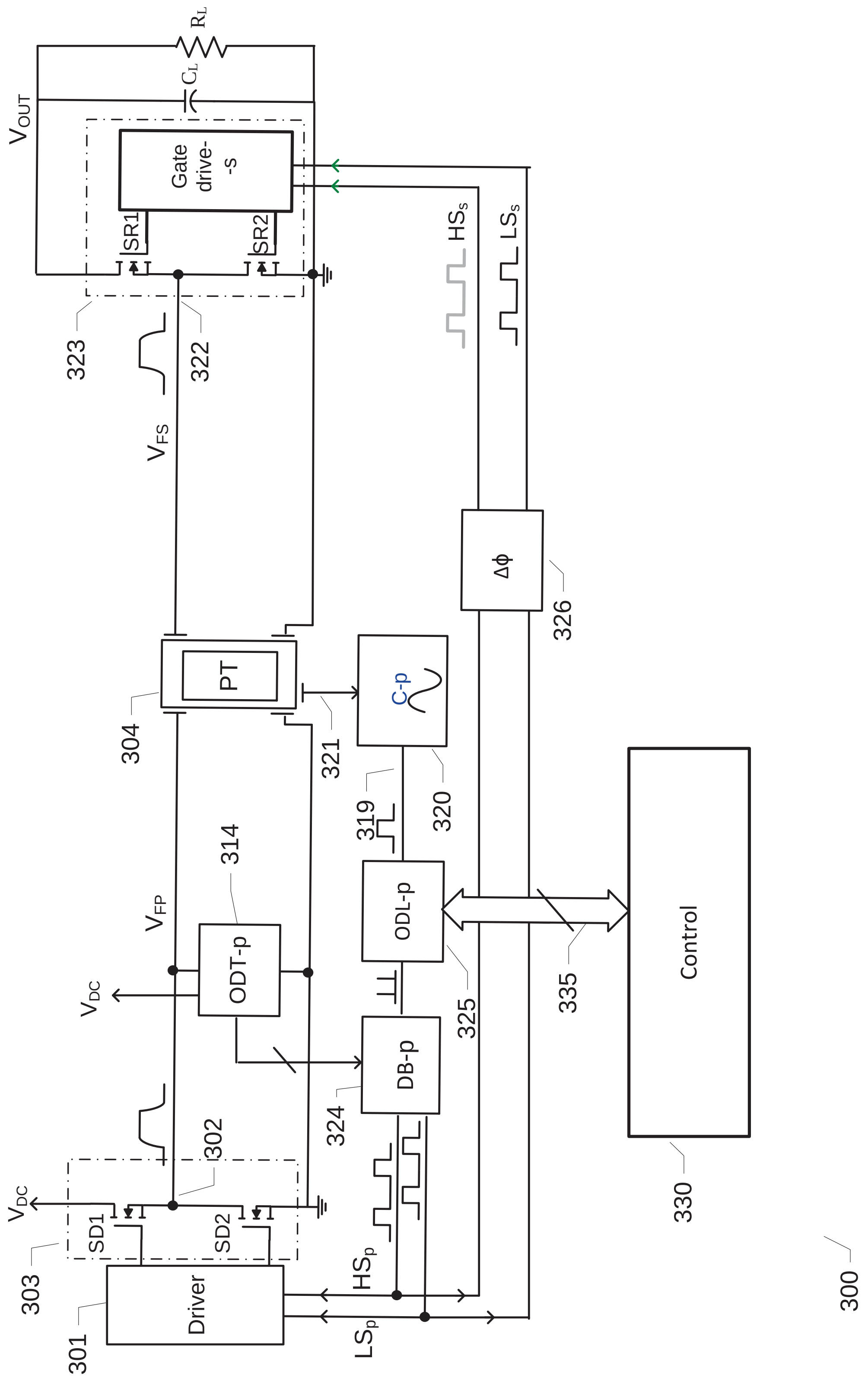

V_{OUT}
C_L
R_L
Gate drive--s
SR1
SR2
323
322
V_{FS}
HS_s
LS_s
Δϕ
326
PT
304
C-p
321
320
319
314
V_{FP}
ODT-p
ODL-p
V_{DC}
DB-p
325
335
Control
324
302
SD1
SD2
303
Driver
301
HS_p
LS_p
330
300

FIG. 3

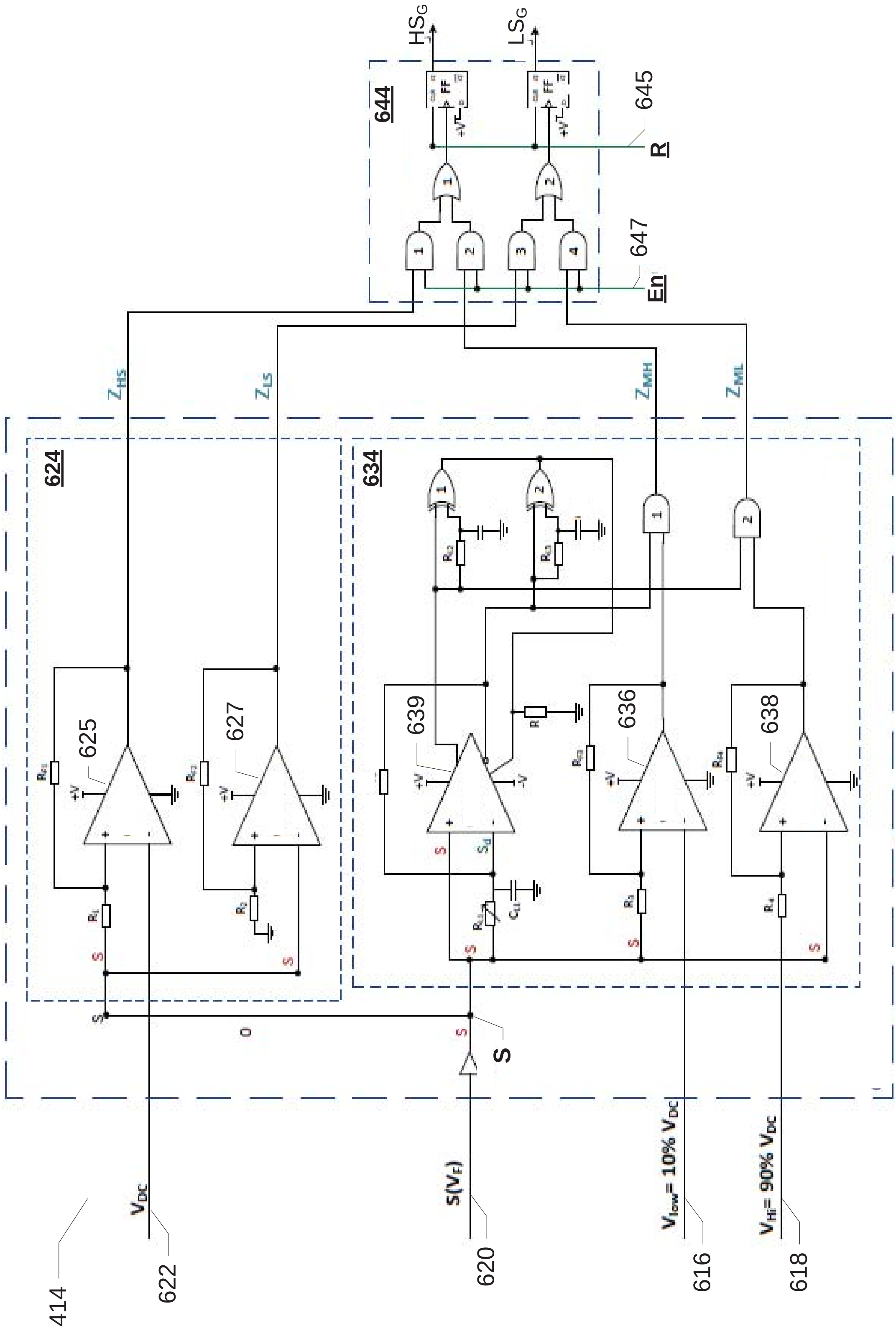

HSG
LSG
644
645
R
647
En
ZHS
ZLS
ZMH
ZML
624
634
625
627
639
636
638
S
0
VDC
S(VF)
Vlow= 10% VDC
VHi= 90% VDC
414
622
620
616
618

FIG. 4

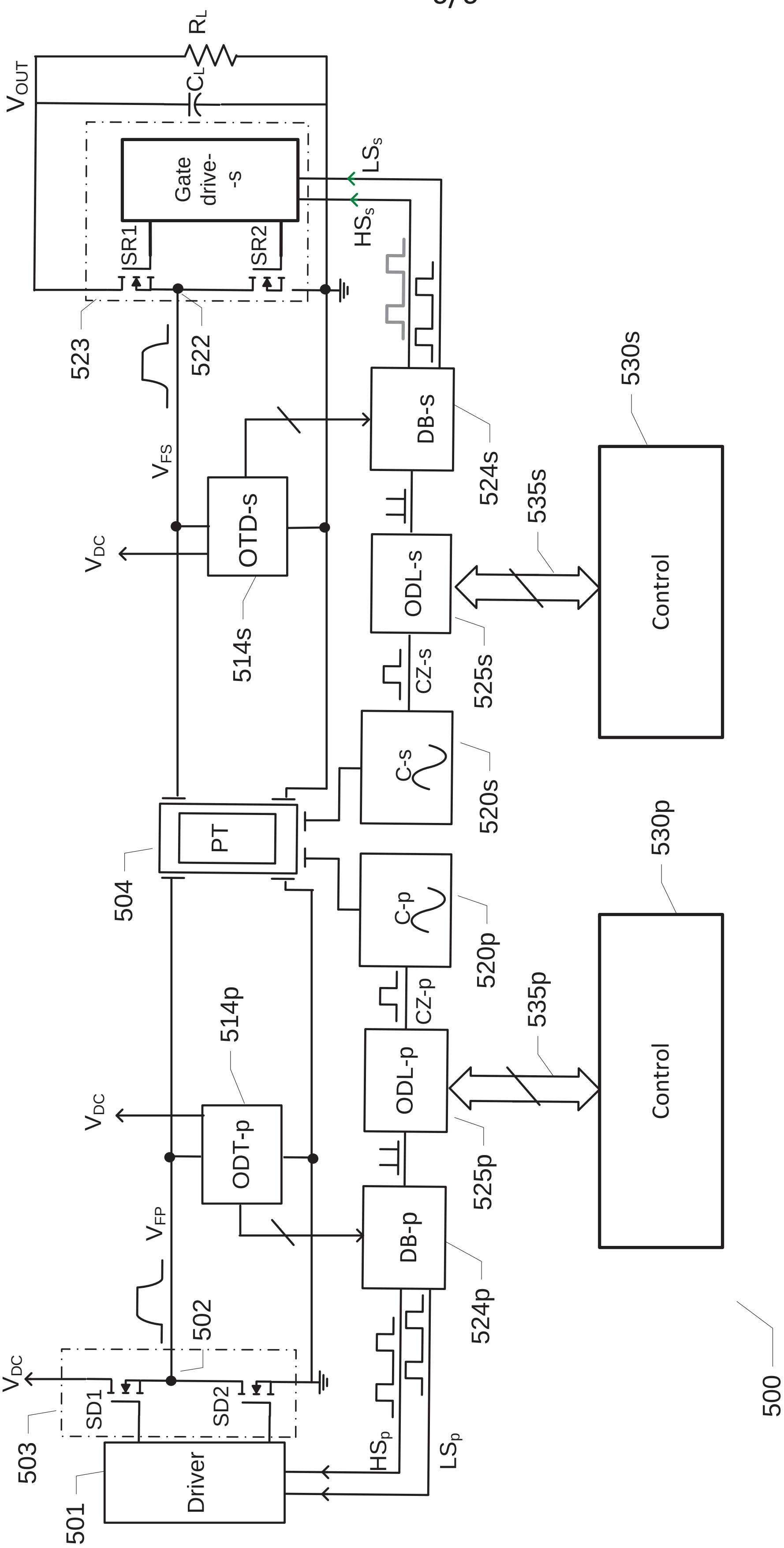

VOUT
CL
RL
Gate drive-s
SR1
SR2
LSs
HSs
523
522
VFS
VDC
OTD-s
514s
DB-s
524s
535s
ODL-s
525s
CZ-s
C-s
520s
Control
530s
PT
504
C-p
520p
CZ-p
530p
ODL-p
535p
525p
Control
514p
VDC
ODT-p
VFP
DB-p
524p
502
VDC
SD1
SD2
503
Driver
501
HSp
LSp
500

FIG. 5

J

Optimum phase in the self-oscillating loop for piezoelectric transformer-based power converters

IEEE Transactions on Power Electronics

1

1

Optimum phase in the self-oscillating loop for piezoelectric transformer-based power converters

Marzieh Ekhtiari, *Student Member, IEEE,* Tiberiu-Gabriel Zsurzsan, *Student Member, IEEE,* Michael A. E. Andersen, *Member, IEEE,* and Zhe Zhang, *Member, IEEE*

Abstract

A new method is implemented in designing of self-oscillating loop for driving piezoelectric transformers. This method can also be used for other types of converters, e.g. resonant converters. The implemented method is based on combining both analog and digital control systems. Digitized time delay, or in other words digitized phase shift through the self-oscillating loop results in very precise frequency control and ensures optimum operation of the piezoelectric transformer in terms of gain and efficiency. In this work, additional time delay is implemented digitally for the first time through a 16 bit digital-to-analog converter in the self-oscillating loop. Delay control setpoints updates at a rate of 417 kHz. The new design of the optimum delay circuit provides 1ns time resolution for the control in the self-oscillating loop. This allows the control loop to dynamically follow frequency changes of the transformer in each resonant cycle. Ultimately, by selecting the optimum phase shift, maximum efficiency under the load, and temperature condition is achievable. In this work efficiency improvement of 9% in the experiments is achieved. The operation principle behind self-oscillating is also discussed in this paper.

All authors are with the Electronics Group, Department of Electrical Engineering, Technical University of Denmark, Richard Petersens Plads, bld. 325, Kgs. Lyngby,DK-2800, Denmark.
E-mail: maekh@elektro.dtu.dk, tgzsur@elektro.dtu.dk, ma@elektro.dtu.dk, zz@elektro.dtu.dk.

Index Terms

Optimum delay line; self-oscillating loop; phase shift; switch mode power supply; zero-voltage switching; piezoelectric transformer.

NOMENCLATURE

ADL-CEZC	Adjustable delay line circuit added to the CEZC block.
C	Resonant capacitance of the piezoelectric transformer.
C_{d1}	Input electrode capacitance of the piezoelectric transformer.
C_{d2}	Output electrode capacitance of the piezoelectric transformer.
CEZC	Current estimation zero crossing.
DDL	Dynamic delay line.
DDL_{in}	Input signal of the DDL block.
DDL_{out}	Output signal of the DDl block.
EDDL_{in}	Input signal of the digitized delay line block passed through the edge detector.
FF	Flip-flop.
FPGA	Field-programmable gate array.
FTD	Fixed time delay.
HS	High-side gate voltage.
i_{res}	The resonant current of the piezoelectric transformer.
L	Internal inductance of the piezoelectric transformer.
LS	Ligh-side gate voltage.
MOSFET	Metal-oxide-semiconductor field-effect transistor.
ODL	Optimum delay line circuit block.
ODL_{out}	Output signal of the optimum delay line circuit block.
R	Dielectric losses inside the transformer.

R_m	Matched load for the piezoelectric transformer.
v_F	Switching voltage.
ZCi_{res}	Zero crossed signal of the estimated resonant current.
ZVS	Zero-voltage switching.
ω	Switching angular frequency.
ϕ_I	Phase shift of the resonant current with reference to the turn-off time of the low-side switch.

I. Introduction

Piezoelectric transformers' (PT) voltage gain, resonance frequency and efficiency change with variation of their load and temperature [1]–[4]. Therefore, in order to operate a PT in its optimum point, located slightly above the resonant frequency [5], it is necessary to follow changes in the resonance frequency [1], [6]–[8].

When the inductorless topology is employed for the PT-based converters, the operating frequency of the PT is reduced to a narrow band in which PT shows an inductive behavior. Therefore, a very small variations in the resonant frequency can easily cause instability in the converter. However, keeping operating frequency in a proper point which is slightly above resonant frequency is hard to be attained by open loop. As a consequence, closed loop control is indispensable for compensating influence of parameters such as frequency and temperature, in order to have stable operation of PT and consequently accurate performance of the converter [9]–[13].

The options for the closed-loop are phased locked loop (PLL) and self-oscillating loop control methods. The PLL approach which is also a controlled oscillator is not a good option for the inductorless PT-based converters [5]. Therefore, the self-oscillating loop is used for the closed-loop control of the PT's operating point.

The self-oscillating loop is able to adjust its phase shift to follow the PT's resonant frequency. Therefore, implemented adjustable phase shift compensates for the rest of the phase shift in the loop for frequency variations. This is more important when a PT-based converter is operating in bi-directional mode for energy recovery [10]. As an example, when the energy transfered by the converter needs to be controlled to maintain DC output voltage at different voltage levels, the PT's load changes [8], [10]. Any changes in the PT's load causes a change in its operating point [8]. In order to keep the PT operating at its most efficient point, its operating frequency should be changed. This is performed by changing the converter's switching frequency. The switching frequency is controlled through a self-oscillating loop [9], [14]. Therefore, by changing the predesigned phase shift, the switching frequency follows variations in the PT's resonant current.

Phase shift compensation with high resolution becomes necessary especially when the load of the converter is variable. Notably, the PT's transfer function also differs by temperature rise [1], [15]. These variations directly translates to PT's load variations. If the total phase shift of the loop is not properly adjusted to an integer factor of 360°, it causes a damping of the resonant current. Therefore, closed-loop operation cannot be achieved and basically the converter will not start working. Thereby, very fine resolution for phase shift adjustment is required. A more thorough explanation of the self-oscillating loop is provided in the Section II.

Several attempts have done for closing the feedback loop in the PT-based switch-mode power supply (SMPS) [9], [11], [12], [16]. In previous research, an adjustable time delay block that controls the total loop phase has been implemented for a bi-directional converter through an analog circuit. This was done by detecting peaks in the PT's resonant current [10], [17]. In the closed-loop operation, 360° phase difference cannot be ensured for the load or temperature variations of the PT, particularly in bi-directional operation [10]. The principle behind self-oscillation obtained in the prior art is explained in the Sub-section II-A and experimental results are provided inthe Sub-section II-C.

The analog implementation becomes unstable when approaching 0° in the real implementation [10].

To solve this problem, a digitalized phase shift compensation is applied in this paper. Changes in the PT's resonant frequency are compensated for the closed-loop by detecting and adding required phase shift in order to obtain a full loop phase shift of 360°. Furthermore, digital implementation allows for fine changes in time delay inside the loop for frequency tracking. Compensation is performed by adding a finely-controlled time delay to the feedback chain. Resolution of the applied time delay is 1 ns. This ensures that the added time delay is finely controllable in order to precisely adapt the frequency of the self-oscillating loop and match changes in the PT's operating point. More explanation about the proposed method is provided in the Sub-section III-A and experimental results are provided in the Sub-sections II-C and IV. This further ensures soft switching operation of the PT and therefore, the highest efficiency attainable.

II. Self-oscillating loop for PT-based converters

A. Principle and design considerations

Essentially, two requirements need to be satisfied in order to produce sustained oscillation in closed-loop. One is that phase angle of the entire loop should be an integer multiple of 360°; the other requirement is that the loop gain should be greater than unity to start-up oscillation. The former condition is fulfilled by adjusting phase shift through the loop. The latter condition is fulfilled by designing through a comparator since the comparator's gain can be considered infinite and therefore its input becomes saturated to the rail voltages, generating square waves in the output. In the designed circuit there is a hysteresis controller which operates as an oscillator during start-up with a frequency close to or lower than the PT's resonance frequency. The frequency of square waves can be designed to be slightly lower than the resonance frequency. In this case, it is ensured that oscillation does not lock into the second or higher resonance frequencies of the PT. Furthermore, it is close to the PT's fundamental resonance frequency and this helps minimizing time for the loop to be locked. Fig. 1 shows the block diagram for the self-oscillating

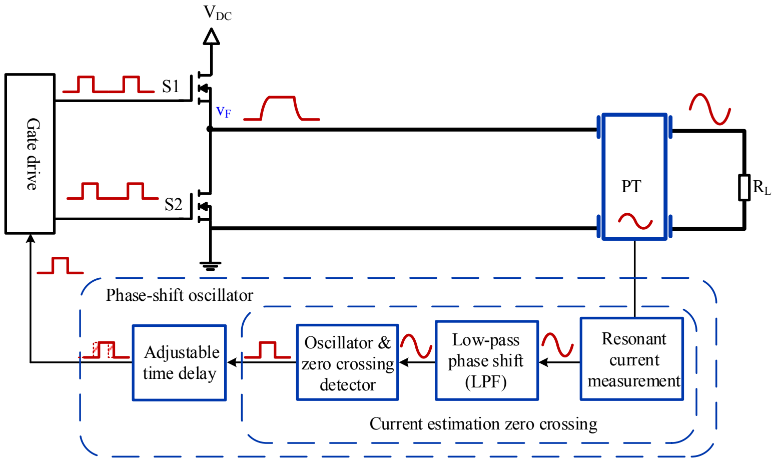

Fig. 1: Block diagram of prior art self-oscillating loop.

loop [9], and Fig. 2 shows the circuit for the self-oscillating loop together with the PT-based power stage with matched load. Equation (1) represents the time period of this self-induced oscillation.

$$T = R'_F C_3 \, ln(1 + \frac{2R_4}{R_5}) \tag{1}$$

where R'_F is equivalent resistance of two parallel resistors, R_F and R_3. The resistor R_5 is used in order to provide an initial condition for the capacitor and helps with oscillation start-up. The ratio of R_4/R_5 forms the hysteresis window to specify a voltage range and to build the appropriate level of noise immunity.

Thereby, small perturbations in the loop start the self-induced oscillation. This results in self-excitation of the resonant current inside the PT during the start-up. Self-excited square waves with a frequency lower than or close to the resonant frequency of the PT will excite resonant modes inside the transformer. This is achieved by the fundamental frequency of the square waves and its higher order harmonics. Since the PT is operating as a high Q band-pass filter (BPF), it filters higher order harmonics out and transfers the fundamental component to its output. The electrical quality factor of the PT is derived as:

$$Q = \frac{1}{\omega C_{d2} R_L} \tag{2}$$

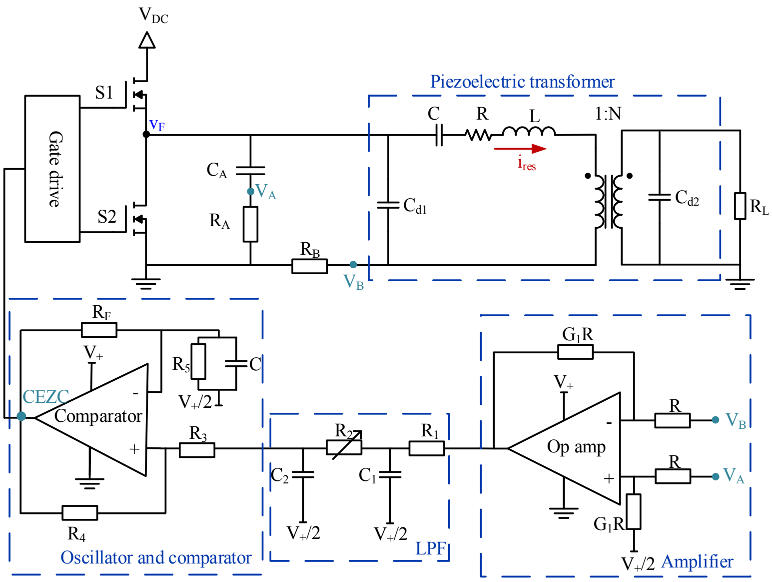

Fig. 2: Circuit design demonstrates principle of self-oscillating loop in PT-based SMPS.

where $\omega = 1/\sqrt{LC}$ is the series-resonance angular frequency of the PT [18], [19]. Therefore, resonant current is considered as sinusoidal waveform described in (3).

$$i_{res}(t) = I_{pk}(t)\, sin(\omega t \;-\; \phi_I) \tag{3}$$

where $\phi_I \in [0, \pi]$ is the current phase angle.

The amplitude of the fundamental resonant current grows with time, until its level is large enough compared to the self-induced oscillator. Since the amplitude of the sinusoidal waveform at the output of low-pass filter (LPF), shown in Fig. 1, is greater than the amplitude of the self-induced oscillation waveform, the oscillator operates as a comparator. This allows the comparator's behavior to change from that of an oscillator to that of a true comparator. Therefore, it compares resonant current with a DC level in order to mark the zero crossing of the current. The loop is designed for the case where the PT is connected to the resistive matched load [9] by considering Mason's equivalent parameters [20], [21].

$$R_{matched} = \frac{1}{\omega C_{d2}} \tag{4}$$

The reasoning behind this design choice is that a matched load is considered to be the worst-case scenario for a PT, in terms of achieving soft switching [22]. Zero-voltage switching (ZVS) is a form of soft switching considered in this work. Fig. 3 shows the trend of load resistance versus ZVS factor [22]. At the matched load, the energy transfer through the PT is maximum and therefore its efficiency is maximized as well. This results in a point of minima on the ZVS factor axis [8], [21]. The role of the ZVS factor is to provide the worst-case scenario for analyzing PTs in terms of soft switching capability. Therefore, if ZVS is achieved for the matched load, it will be obtained for other loads as well [22]. The worst-case explanation of approximated ZVS factor is expressed based on empiric analysis of ZVS in the following equation [23]:

$$V_p' = (0.304\ \frac{1}{n^2}\frac{C_{d2}}{C_{d1}} + 0.538) \cdot (0.585\eta + 0.414) \tag{5}$$

where η is the efficiency of the transformer. V_p' is ZVS factor and should be roughly above 1 in order to obtain soft switching. Therefore, the ZVS region is a narrow frequency range above the resonance frequency, where the PT behaves as an inductor and $V_p' > 1$. Furthermore, the ZVS bandwidth of the PT is a ratio of L/C for a constant resonance frequency [22]. Equation (5) and Fig. 4 are based on a primary analysis of ZVS in order to justify the necessity to design a driver and self-oscillating loop for the matched load, where Fig. 4 shows the soft switching factor for a PT as an example [22].

B. Current estimation zero crossing (CEZC)

The resonance current in the PT is reconstructed within two time intervals. Voltage V_B across R_B shown in Fig. 2 measures this resonance current while the switches are on. Voltage V_A across R_A measures the resonant current during dead time, while both switches are off. The resonance current in this period is

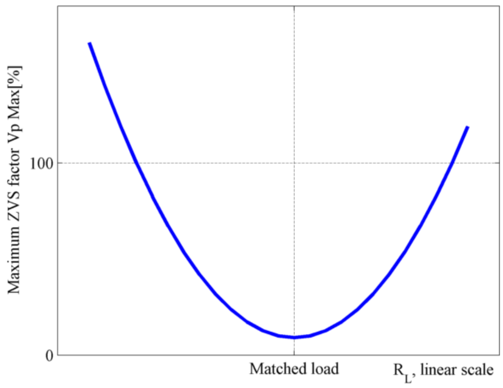

Fig. 3: Soft switching factor for PT as a function of load resistance.

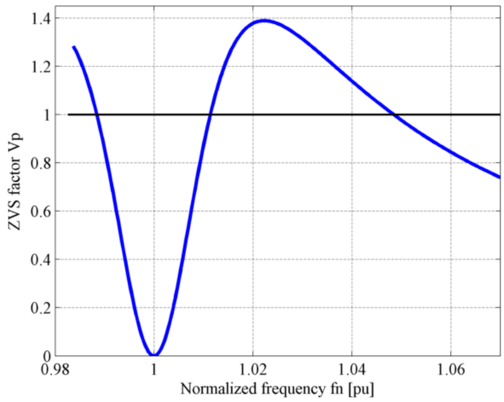

Fig. 4: Normalized frequency vs. normalized soft switching factor for PT; $R = 98\ m\Omega$, $C = 11.27\ nF$, $L = 733$ µH, $C_{d1} = 112\ nF$, $C_{d2} = 14.6\ pF$, $N = 112$.

supplied by the PT's input capacitor C_{d1}. Therefore, the current passing through C_{d1} follows the resonant current and can be measured by differentiating the voltage across C_{d1}. This is performed by using C_A and R_A as a differentiator. C_A should be approximately 10 times lower than C_{d1} in order not to affect the input capacitance of the PT and, subsequently, dead time and ZVS factor of the transformer. R_A and R_B are also chosen to have low values and in order to set a ratio between V_A and V_B for the input of the op-amp. By subtraction of these two voltage waveforms through the op-amp, an approximate sine waveform representing the resonant current will be reconstructed in the output [5], [9], [24]. Fig. 2 shows the voltages V_A and V_B. Therefore, voltage in the output of the op-amp is:

$$V_{out}|_{opamp} = G_1(V_A - V_B) = G_1(R_A \overbrace{C_A \frac{d}{dt} V_{C_{d1}}}^{i_{res}|_{sw:off}} - R_B\, i_{res}|_{sw:on}) \tag{6}$$

The estimated current has a 180° phase shift compared to the resonance current which results in the same zero-crossing points. Thereafter, the estimated resonance current is transmitted to a second order low-pass filter (LPF) which provides an additional phase shift through the feedback loop. In order to have adequate phase shift through the LPF, its cut-off frequency is adjusted to be around the resonance

TABLE I: PT EQUIVALENT PARAMETERS

Parameter	Value	Parameter	Value
C_{d1}	3.83 nF	C_{d2}	626 pF
C	565 nF	R	5.63Ω
L	3.5 mH	N	3.57

TABLE II: Phase shift during one switching cycle in the self-oscillating loop; switching frequency is 118.3 kHz with time period of 8.45μs.

Delay	Time[μs]	Phase[°]	Duty cycle%
HS→HSGD	1.59	67.8	18.85
HSGD→I_{est}	0.27	11.5	3.19
I_{est}→LPF	6.09	259.4	72.04
LPF→CEZC	0.5	21.3	5.92
Total	8.45	360	100

frequency. Furthermore, some harmonics are eliminated by the LPF, resulting in a smoother waveform which contains the fundamental harmonic of the resonance current. The filtered signal is transmitted to the comparator and generates a square wave indicating the zero crossing of the input signal. The square wave signal is fed into the adjustable time delay in order to compensate for the rest of the phase shift to have a total of 360° in the whole loop from the input of the gate driver to the output of feedback loop. In case the switching frequency needs to be decreased, the total phase shift should be increased.

C. Experimental results

Fig. 5 shows experimental waveforms. The designed board is shown in Fig. 6. A radial mode PT with Mason's equivalent circuit, shown in Fig. 2, is used, driven by square wave signals with a switching frequency of 118.3 kHz, while driving a resistive load of 300 Ω. Moreover, reconstructed resonant current from voltages V_A and V_A is shown in Fig. 5. Furthermore, the equivalent parameter values of the PT are measured and shown in Table I. Phase shifts and corresponding time delays between stages are measured and shown in Table II.

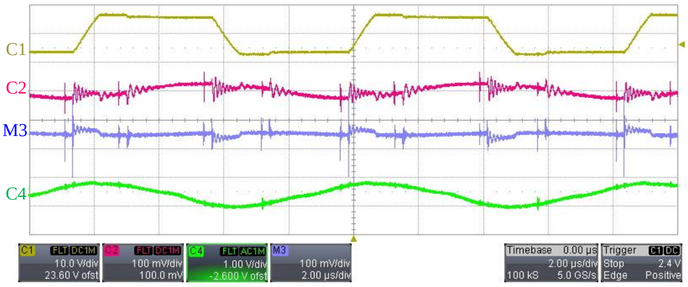

Fig. 5: Reconstruction of the resonant current. C1: switching voltage v_F, C2: V_A, M3: V_A, C4: G1 (V_A-V_B)

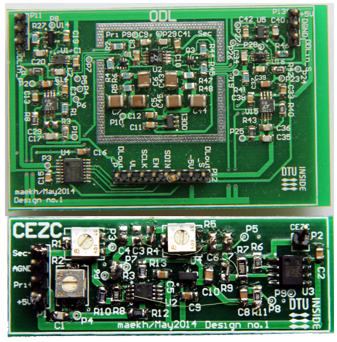

Fig. 6: ODL and CEZC-A boards

III. Phase-shift self-oscillating loop with optimum delay line

A. Digitized delay line (DDL)

Initial investigation of the time step resolution which required finely adjustment of the total phase shift in the loop. This investigation was performed by mapping relative changes in the frequency to the output voltage variations. The result of this investigation shows that there is an measurable change in the amplitude of the PT's output voltage for every 10 Hz change in switching frequency. For example, if the operating frequency of 100 kHz increases by 10 Hz, the output voltage shows a considerable change in the amplitude e.g. 6 V. This output voltage variation depends on the transformer and the range of the operating frequency. Therefore, a precision of minimum 10 Hz in the frequency is required for dynamic time delay which is equivalent to 1ns time delay resolution. Thereby, a phase shift self-oscillating closed loop is designed together with the contribution of the digital-to-analog converter (DAC) and field-programmable gate array (FPGA). These are used to implement a high-resolution time delay inside the dynamic time delay block.

Fig. 7 shows the circuit designed for the dynamic time delay (DDL) together with the drawing of the input and output waveforms of the DDL circuit block. In this block, the input signal (DDL_{in}) is first transformed into edge-detecting one-shot pulses ($EDDL_{in}$) which are then used as a clock source for the flip-flop (FF). The signal froms this FF is then used to reset the hardware integrator present in the circuit. Namely, when the input signal edge-triggers the FF, the feedback capacitor in the op-amp feedback starts charging, thereby creating a fixed voltage slope. This is then compared to the variable reference voltage provided by the DAC. Thereafter, the complementary output of the comparator resets the FF which consequently turns the metal-oxide-semiconductor field-effect transistor (MOSFET) D1 on and discharges the feedback capacitor, thereby resetting the integrator. Since the input pulse triggers the start of the integration, the variable reference provided to the comparator by the DAC coupled with the voltage slope work together to create a time-delayed version of the input pulse which is proportional to the DAC output value. The output of the comparator is then latched for a short time by its own output through a high-passed signal to its latch pin, resulting in one-shot pulses at the output of the DDL (DDL_{out}).

B. Self-oscillating loop based on the optimum time delay

A new phase shift self-oscillating loop for the PT-based converter is designed and proposed with the combination of the analog and digital designs. Fig. 8 shows the simplified block diagram of the proposed closed-loop with main blocks. The output signal of the current estimation zero-crossing (CEZC) block is a 50% duty cycle square wave signal, having the same frequency as the PT. For the closed-loop operation the reference signal is considered as high-side gate voltage (HS). For tracking the PT's frequency the reference is considered as the output of the CEZC block. In this design rising edge of the CEZC is used for turning on the high-side switch. By working on the different operating frequency ranges, there is need to adjust the phase shift of the LPF inside the CEZC analog block to synchronize the CEZC and HS signals. In order to avoid adjusting phase shift in the hardware, a digital time delay circuit is added to the CEZC block, named adjustable delay line (ADL-CEZC). The delayed estimated resonant current is then tied to the optimum delay line block (ODL). The output of the ODL is then capable of prolonging the switching period by changing the on time of the switches (Ton). The output of the ODL is fed into

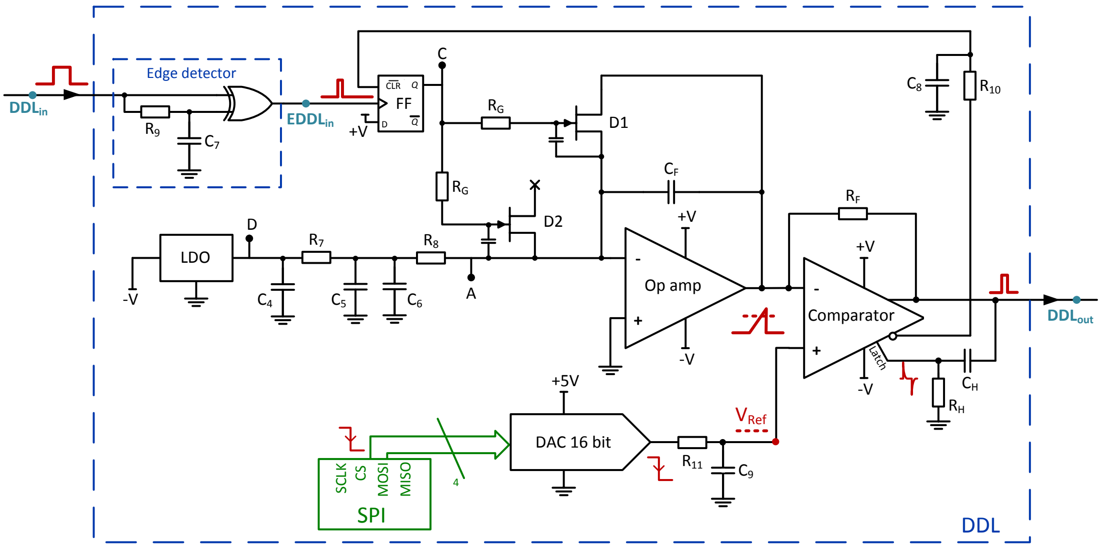

a: Digitized time delay circuit (DDL).

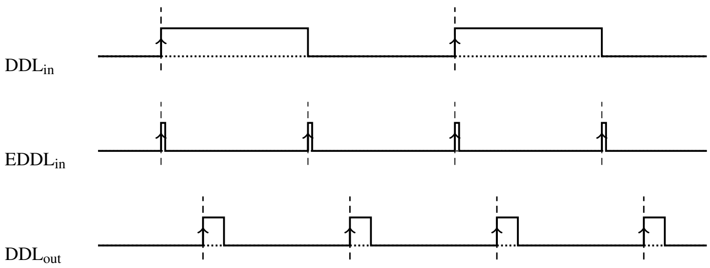

b: The input and output signals of the DDL block shows an arbitrary delay with 1 ns step resolution.

Fig. 7: DDL circuit and input and output signals.

the control block in order to generate the high-side and low-side signals as an input of the gate driver. In addition to the hardware control gates, commands from the FPGA are also have contribution in the control block.

Fig. 9 decomposes the main blocks in the Fig. 8 into sub-blocks also shows a detailed drawing of the main input and output signals inside the block diagram. The voltage $v_F(t)$ is the transformer's primary-side voltage while exhibiting soft switching. $i_{res}(t)$ shows the resonance current of the PT. However, in the PT-based SMPS the resonant current is dependent on the characteristic parameters of the PT and

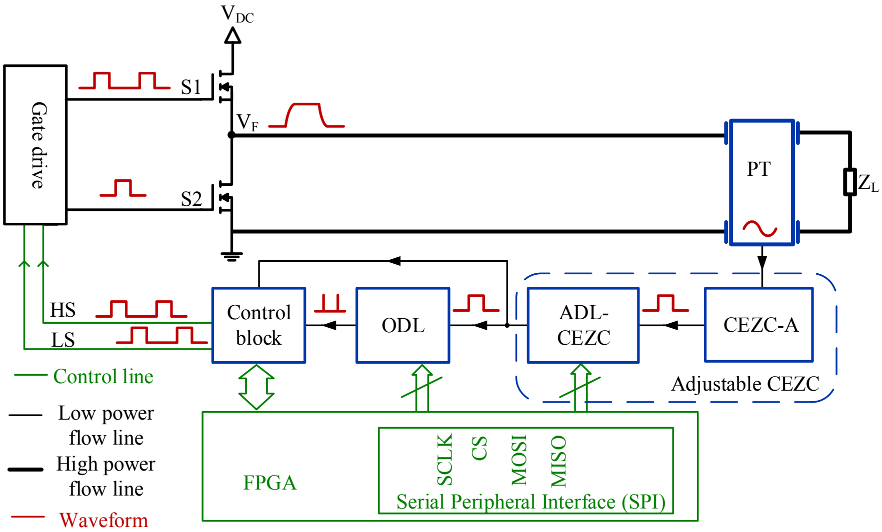

Fig. 8: Block digram of self-oscillating loop with optimum phase.

it changes its polarity when either the switches are turned on or their body diodes conduct. Therefore, depending on the operating frequency and temperature of the PT, there is a phase shift between the resonance frequency and the switching voltage, that is defined as ϕ_I in (3), [21]. The signal ZCi_{res} shows the zero crossing resonant current. The CEZC implies a 180° phase shift to the real resonant current. The output of the adjustable delay line (ADL-CEZC) turns on the half-bridge switches. This block is composed of a digitized delay circuit (DDLon) and a FF with 50% square waves in its input and output. The 50% square wave signal fed into to the ODL is delayed by a certain value adjustable with a reference signal. In the end the one-shot pulse signal generated by DDLoff in the output of the ODL turns off the MOSFETs. The high-side and low-side switches are turned on by rising edges of DL-CEZC and $\overline{\text{DL-CEZC}}$ signals, respectively, which are used as clock inputs to the control block FFs. The output of the ODL block is then used to reset the FFs, thereby turning the switches off.

DT is first adjusted for a specific design regarding a certain PT and switching frequency. By adjusting the time-delay for turning the switches off, the frequency of self-oscillation changes. The propagation delay in the control block is assumed negligible in the waveforms shown in Fig. 9.

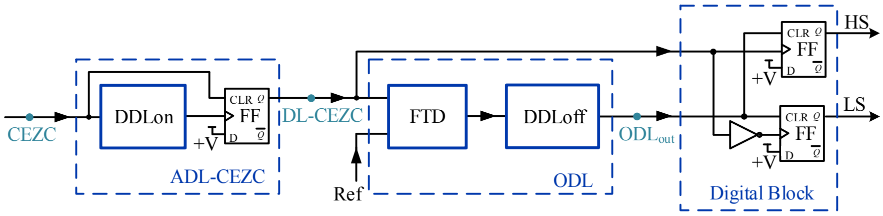

a: Block digram of self-oscillating loop with optimum phase.

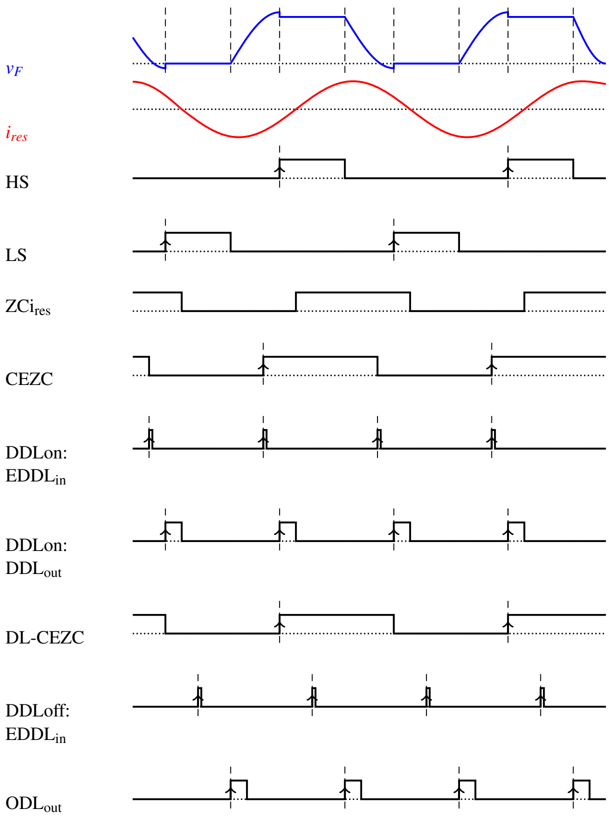

b: Signals with proportional delay for demonstrating the functionality of the optimum phase control method.

Fig. 9: Optimum phase self-oscillating loop and signal waveforms

IV. Results

A prototype has been built and analyzed shown in Fig. 10. Fig. 6 shows designed modular boards for DDL and CEZC blocks. The circuit implemented for CEZC is very similar to one explained in

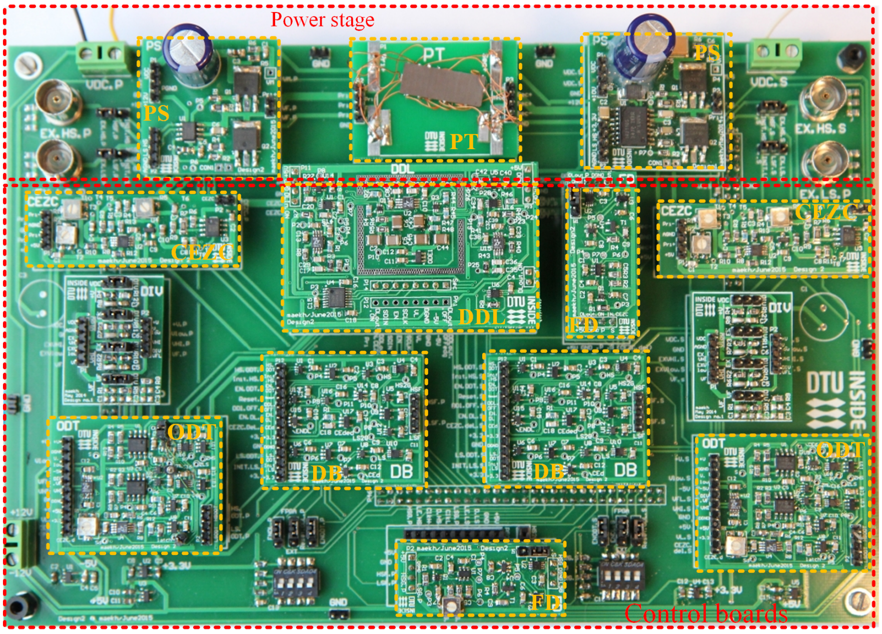

Fig. 10: Prototype buit; bidirectional board.

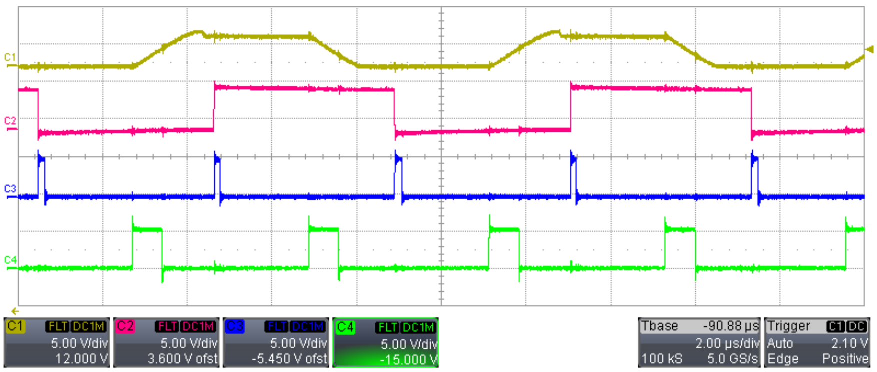

Fig. 11: Signal waveforms where dynamic delay is applied; C1: switching waveform ($v_F(t)$); C2: CEZC as input of DDL block; C3: one-shot pulse as input of DDL block (EDDL_{in}); C4: output of DDL (DDL_{out}).

section II-B. Fig. 11 shows signals in the input and output of the DDL module in the setup.

Fig. 12 shows efficiency improvement. The input voltage is 24 V and the load is a 225 Ω resistor in parallel with a 470 μF capacitance. For each specific output voltage the delay has been swept from a minimum value to the maximum value in the range that ZVS is obtained. The starting point for the

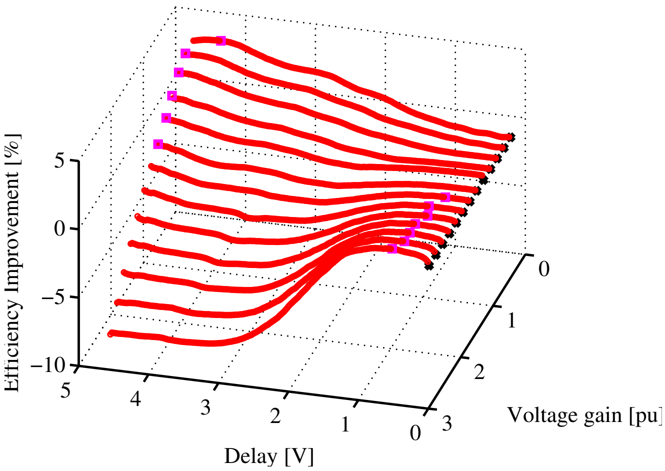

Fig. 12: Experimental results: Efficinecy improvement as a function of voltage gain.

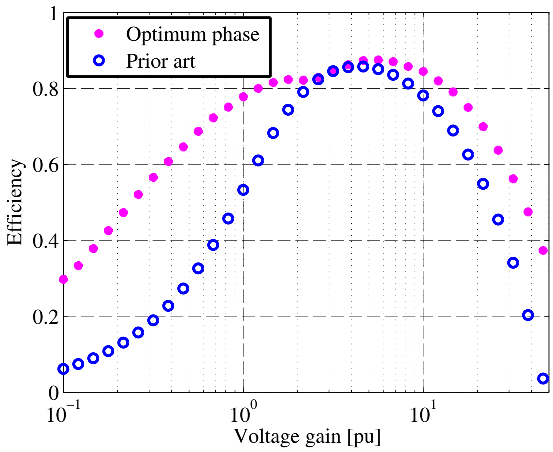

Fig. 13: Simulation results: Efficiency improvement vs. sweep of delay in order to detect the optimum phase (OP) for voltage gains.

delay sweep is set to 115.6 kHz in each voltage gain. Therefore, the best phase shift or frequency can be chosen to achieve the maximum possible efficiency as are shown in Fig. 12 with square markers.

Simulation results shown in Fig. 13 for both step-up and step-down converters which shows efficiency improvement by choosing the best phase shift in the loop.

V. Conclusion

General operation of a self-oscillating loop for piezoelectric transformer-based power converters was explained. The designed circuit for operating the transformer together with experimental results were provided. The circuit is based on a new idea for compensating and controlling the total loop phase shift for the self-oscillating PT loop through digital means, in order to achieve and maintain soft switching. This is combined with a resonance current estimation that is able to start and maintain the circuit oscillation. The operation of and cooperation between the analog resonance current estimator and digital phase shift adjustment were presented in detail, together with some insight into the performance of the designed circuit. The concept was proven through the experimental results. 1 ns time step resolution is sufficient for adjusting the phase shift of the loop. The designed circuit is able to follow changes in the resonance frequency of the PT in every cycle. Experimental results showed proof of the concept. Although this method was applied for the PT-based power converters but it has a general application and can also be used for other types of resonant converters. One of the advantages of the presented approach is that the designed hardware can be utilized for different PTs where in previous research; analog self-oscillating loop; the loop should be individually designed for each PT. Another advantage is that implemented method has flexibility for phase shift compensation, but the disadvantage is a complex control method.

Acknowledgment

The authors would like to thank Noliac A/S for supplying the prototype of a piezoelectric transformer as well as "The Danish National Advanced Technology Foundation" for their financial support.

References

[1] M. Ekhtiari, Z. Zhang, and M. A. E. Andersen, “State-of-the-art piezoelectric transformer-based switch mode power supplies,” *40th Annual Conference of the IEEE Industrial Electronics Society, IECON2014*, pp. 5072–5078, in press, 2014.

[2] E. Horsley, M. Foster, and D. Stone, “State-of-the-art piezoelectric transformer technology,” in *Power Electronics and Applications, 2007 European Conference on*, Sept 2007, pp. 1–10.

[3] A. V. Carazo, “50 years of piezoelectric transformers. Trends in the technology,” in *Symposium D âĂŞ Materials and Devices for Smart Systems*, ser. MRS Proceedings, vol. 785, 2003.

[4] A. M. Flynn and S. R. Sanders, “Fundamental limits on energy transfer and circuit considerations for piezoelectric transformers,” *Power Electronics, IEEE Transactions on*, vol. 17, no. 1, pp. 8–14, 2002.

[5] M. S. Rodgaard, “Piezoelectric transformer based power converters; design and control,” *Ph.D. Thesis, Department of Electrical Engineering, Technical University of Denmark*, 2012.

[6] S. Bronstein, “Piezoelectric transformers in power electronics,” Ph.D. dissertation, Ben-Gurion University of the Negev, 2005.

[7] A. M. Sánchez, M. Sanz, R. Prieto, J. A. Oliver, P. Alou, and J. A. Cobos, “Design of piezoelectric transformers for power converters by means of analytical and numerical methods,” *Industrial Electronics, IEEE Transactions on*, vol. 55, no. 1, pp. 79–88, 2008.

[8] C. y. Lin, “Design and analysis of piezoelectric transformer converters,” *PhD Dissertation, Virginia Tech*, 1997.

[9] M. Rodgaard, M. A. E. Andersen, T. Andersen, and K. Meyer, “Self-oscillating loop based piezoelectric power converter,” *US patent 61/638,883 and WIPO, WO2013083678-A2*, 2011.

[10] M. S. Rodgaard, “Bi-directional piezoelectric transformer based converter for high-voltage capacitive applications,” *30th Applied Power Electronics Conference and Exposition, 2015,Charlotte, NC*, 2015.

[11] M. Prieto, J. Diaz, J. Martin-Ramos, and J. Nufio, “Closing a second feedback loop in dc/dc converters based on piezoelectric transformers,” in *Power Electronics Specialists Conference, 2004. PESC 04. 2004 IEEE 35th Annual*, vol. 6, June 2004, pp. 4682–4688 Vol.6.

[12] J. Diaz, J. Martin-Ramos, M. Prieto, and F. Nuno, “A double-closed loop dc/dc converter based on a piezoelectric transformer,” in *Applied Power Electronics Conference and Exposition, 2004. APEC ’04. Nineteenth Annual IEEE*, vol. 3, 2004, pp. 1423–1428 Vol.3.

[13] J. Díaz, F. Nuño, J. M. Lopera, and J. A. Martín-Ramos, “A new control strategy for an ac/dc converter based on a piezoelectric transformer,” *IEEE Transactions on Industrial Electronics*, pp. 850–856, 2004.

[14] B. Putzeys, “Simple self-oscillating class D amplifier with full output filter control,” *Audio Engineering Society - 118th Convention Spring Preprints 2005*, pp. 1908–1915, 2005.

[15] T. Andersen, M. A. Andersen, O. C. Thomsen, M. Foster, and D. Stone, “Nonlinear effects in piezoelectric transformers explained by thermal-electric model based on a hypothesis of self-heating,” in *IECON 2012-38th Annual Conference on IEEE Industrial Electronics Society*. IEEE, 2012, pp. 596–601.

[16] J. Alonso, C. Ordiz, and M. Dalla Costa, “A novel control method for piezoelectric-transformer based power supplies

assuring zero-voltage-switching operation," *Industrial Electronics, IEEE Transactions on*, vol. 55, no. 3, pp. 1085–1089, March 2008.

[17] M. A. E. Andersen, K. Meyer, M. S. Rodgaard, and T. Andersen, "Piezoelectric power converter with bi-directional power transfer," *US patent 61/567,924 and 2013, WIPO, WO2013083679-A1*, 2011.

[18] G. Ivensky, I. Zafrany, and S. Ben-Yaakov, "Generic operational characteristics of piezoelectric transformers," *Power Electronics, IEEE Transactions on*, vol. 17, no. 6, pp. 1049–1057, Nov 2002.

[19] A. V. Mezheritsky, "Quality factor concept in piezoceramic transformer performance description," *Ultrasonics, Ferroelectrics, and Frequency Control, IEEE Transactions on*, vol. 53, no. 2, pp. 429–442, 2006.

[20] E. M. Syed, "Analysis and modeling of piezoelectric transformer," *M.Sc. Thesis, Department of Electrical and Computer Engineering, University of Toronto*, 2001.

[21] R. L. Lin, "Piezoelectric transformer characterization and application of electronic ballast," *Ph.D. Dissertation, Virginia Polytechnic Institute and State University*, 2001.

[22] K. Meyer, M. Andersen, and F. Jensen, "Parameterized analysis of zero voltage switching in resonant converters for optimal electrode layout of piezoelectric transformers," *Power Electronics Specialists Conference. PESC 2008. IEEE*, pp. 2543–2548, June 2008.

[23] M. Rodgaard, T. Andersen, and M. Andersen, "Empiric analysis of zero voltage switching in piezoelectric transformer based resonant converters," *Power Electronics, Machines and Drives (PEMD 2012), 6th IET International Conference on*, p. 63, March 2012.

[24] T. Andersen, "Piezoelectric transformer based power supply for dielectric electro active polymers," *Ph.D. Thesis, Department of Electrical Engineering, Technical University of Denmark*, 2012.

K

Using squeeze-film effect to reduce surface friction in electrostatic actuators

2015 6th International Conference on Advanced Mechatronics (ICAM2015)

No.15-210 Proceedings of the 6th International
Conference on Advanced Mechatronics (ICAM2015),
Tokyo, Japan, December 5-8, 2015

Using squeeze-film effect to reduce surface friction in electrostatic actuators

Gabriel Zsurzsan*1, Akio Yamamoto*2, Zhe Zhang*1, Nils A. Andersen*1, Michael A.E. Andersen*1
*1 DTU Electrical Engineering, Technical University of Denmark
Richard Petersens Plads byg. 325, Kgs. Lyngby, Denmark
*2 Department of Precision Engineering, Graduate School of Engineering, The University of Tokyo
7-3-1 Hongo, Bunkyo-ku, Tokyo, 113-8656 Japan

This paper presents a method of reducing load friction in two degrees-of-freedom (2-DOF) transparent electrostatic induction actuator by using vibration-induced squeeze film effect. An experimental set-up was built to prove the concept. An overall 70% reduction in required driving voltage was obtained when the squeeze film is present.

1 Introduction

Electrostatic film actuators are thin, lightweight and flexible actuators composed of fully transparent plastic films etched with fine-pitched electrodes. They have very wide areas of application such as particle transportation or flexible muscle actuation, but feature most prominently in haptcis and human-machine interfaces where their transparency allows them to be overlaid onto any traditional display surface or game board. This allows enhancing these interfaces with actuation, motion and feedback capabilities [1–4].

Despite their usefulness, a disadvantage of electrostatic actuators is the fact that they require a layer of very small glass beads between stator and slider films to act as both gap material and friction reducer. This reduces the feasibility of the actuators since the glass beads require periodic reapplication and also create a mess around the area in use.

The necessity for glass beads can be reduced or totally eliminated by inducing a squeeze film between the contact surfaces through controlled piezoelectric vibration. This vibration traps a very thin layer of air (or any other gas) between parallel plate surfaces thereby creating the squeeze film effect [5–12]. This thin air layer can successfully substitute the use of glass beads in electrostatic film actuators.

2 Study of glass plate vibration

The transparent electrostatic actuator consists of a layer of film with electrodes printed onto a large glass plate substrate. A large voltage is applied to the electrodes, whereby an electrostatic force is exerted upon a dielectric sheet placed on top. This controllable force enables the dielectric sheet to move across the surface. Small glass beads need to be spread onto the actuator surface in order to both provide an air gap and reduce friction between actuated sheet and actuator surface.

In order to eliminate the need for these beads, squeeze film effect is employed. The squeeze film effect is the effect whereby a very thin layer of gas gets trapped between relatively large, parallel plate surfaces if these are kept in relative motion versus one another. This effect is the result of an overpressure phenomenon present between the surfaces.

The design methodology closely follows the one presented in [13], with a significant difference in the size scope of the application. While Giraud et al. employ the effect for tactile friction modulation on a relatively small 4.3 inch LCD, the plate used as base for the electrostatic actuator measures 345 mm in length, its width is 250 mm with a thickness of 1.8 mm. A full modal, frequency and time analysis of the vibration of such a size plate is performed in order to size the required actuators to excite the correct mode of vibration, beyond human hearing range. One such mode obtained is at 21.7 kHz. The resulting vibration half-wavelength is 15 mm. This is shown in Fig. 1.

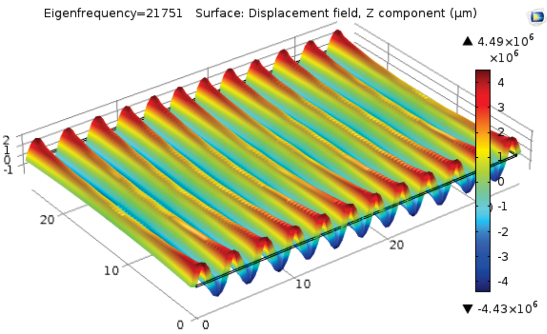

Fig. 1 Snapshot of time-domain vibration propagation analysis in the glass plate subjected to sinusoidal excitation at 21.7 kHz.

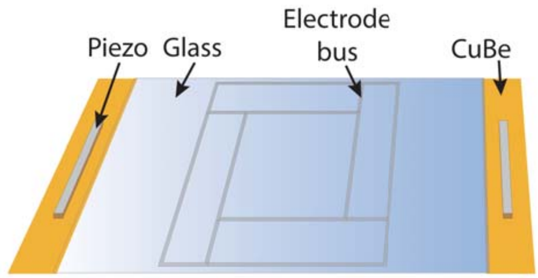

Fig. 2 Resonating glass-base electrostatic actuator system sketch.

3 System design

In order to excite the glass plate to vibrate at the obtained resonant frequency, two copper-berylium resonators with attached piezoelectric actuators were sized and glued to the glass plate through epoxy resin. The resonators measure 250 mm x 50 mm x 2 mm, where the long edge has to fit the glass plate while the width is determined by the desired resonance frequency. The initial design used six 11 mm x 50 mm x 1 mm piezos on each resonator, designed to operate in d31

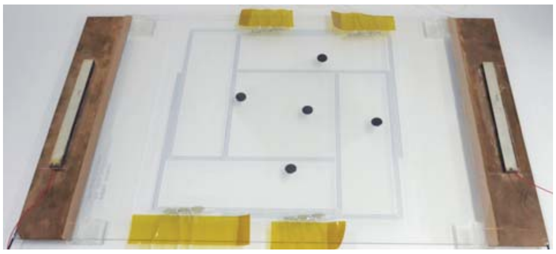

Fig. 3 Photo of the final system, with plastic actuated sheet shown on top of the actuator surface.

mode. Due to long delivery time of the desired piezos, these were substituted with two 120 mm x 10 mm x 5 mm actuators which were readily available. The difference in size with respect to the original design resulted in a resonance frequency shift of the entire system into the audible range. The sketch of the designed system is shown in Fig. 2, while the actual final system is presented in Fig. 3.

4 Results and conclusion

In order to generate a sizable electrostatic force that can overcome stick-slip of the chosen dielectric sheet (visible on top of the actuator surface in Fig. 3) without using any glass beads or squeeze film, a voltage of 500 V needs to be applied to the electrodes. With the vibration system turned on, this minimum voltage is reduced to only 150 V. That equates to a 70% reduction in electrostatic voltage requirements to overcome stick-slip, which can be attributed a corresponding reduction in friction between the actuated sheet and actuator surface. Moreover, using the originally-designed piezoelectric actuators would push the system resonance frequency to above hearing range, making it more suitable for human interaction.

All in all, squeeze film effect is successfully employed in order to eliminate the need for glass beads in transparent rigid-plate surface electrostatic actuators, but the actual operation of the actuator seems to depend on other influencing factors, such as humidity. Therefore, the overall system will be the subject of further analysis and improvement.

5 Acknowledgement

This work was partly supported by Grant-in-Aid for Scientific Research KAKENHI (B) (No. 26280069) from JSPS, Japan, and partly supported by the Danish High Technology Foundation grant number 054-2011-1.

References

[1] K. Amano and A. Yamamoto, "Tangible interactions on a flat panel display using actuated paper sheets," *ITS 2012 - Proceedings of the ACM Conference on Interactive Tabletops and Surfaces*, pp. 351–354, 2012.

[2] T. Hosobata, A. Yamamoto, and T. Higuchi, "2-dof synchronous electrostatic actuator with transparent electrodes arranged in checkerboard patterns," *IEEE International Conference on Intelligent Robots and Systems*, pp. 6 697 066, 4919–4924, 2013.

[3] R. Iguchi, T. Hosobata, and A. Yamamoto, "Transparent electrostatic actuator with mesh-structured electrodes for driving tangible icon in tabletop interface," in *Proceedings of the 2014 ACHI International Conference on Advances in Computer-Human Interactions*. IARIA, 2014, pp. 288–293.

[4] N. Yamashita, K. Amano, and A. Yamamoto, "Interaction with real objects and visual images on a flat panel display using three-dof transparent electrostatic induction actuators," in *Proceedings of the 2014 ACHI International Conference on Advances in Computer-Human Interactions*. IARIA, 2014, pp. 294–299.

[5] R. Pratap, S. Mohite, and A. K. Pandey, "Squeeze film effects in mems devices," *Journal of the Indian Institute of Science*, vol. 87, no. 1, pp. 75–94, 2007.

[6] S. Bharadwaj and M. J. Dapino, "Effect of load on active friction control using ultrasonic vibrations," *Proceedings of SPIE - the International Society for Optical Engineering, Industrial and Commercial Applications of Smart Structures Technologies 2009*, vol. 7290, no. 1, p. 72900G, 2009.

[7] M. Biet, F. Giraud, and B. Lemaire-Semail, "Squeeze film effect for the design of an ultrasonic tactile plate," *IEEE-ACM Transactions on Networking*, vol. 15, no. 6, pp. 2678–2688, 2007.

[8] R. Capozza, A. Vanossi, A. Vezzani, and S. Zapperi, "Suppression of friction by mechanical vibrations," *Physical Review Letters*, vol. 103, no. 8, p. 085502, 2009.

[9] C. Hudin, J. Lozada, and V. Hayward, "Localized tactile stimulation by time-reversal of flexural waves: case study with a thin sheet of glass," *2013 World Haptics Conference*, pp. 67–72, 2013.

[10] V. Levesque, L. Oram, K. MacLean, A. Cockburn, N. D. Marchuk, D. Johnson, J. E. Colgate, and M. A. Peshkin, "Enhancing physicality in touch interaction with programmable friction," *Conference on Human Factors in Computing Systems - Proceedings*, pp. 2481–2490, 2011.

[11] L. Winfield, J. Glassmire, J. E. Colgate, and M. Peshkin, "T-pad: Tactile pattern display through variable friction reduction," *Proceedings - Second Joint Eurohaptics Conference and Symposium on Haptic Interfaces for Virtual Environment and Teleoperator Systems, World Haptics 2007*, pp. 4 145 211, 421–426, 2007.

[12] W. Littmann, H. Storck, and J. Wallaschek, "Reduction of friction using piezoelectrically excited ultrasonic vibrations," *Proceedings of SPIE - the International Society for Optical Engineering, Smart Structures and Materials 2001: Damping and Isolation*, vol. 4331, pp. 302–311, 2001.

[13] F. Giraud, M. Amberg, B. Lemaire-Semail, and G. Casiez, "Design of a transparent tactile stimulator," *Haptics Symposium 2012 - Proceedings*, pp. 6 183 835, 485–489, 2012.

L

Evaluation of Breaking Performance in Vibration-Assisted Electrostatic Surface Induction Actuator

2015 6th International Conference on Advanced Mechatronics (ICAM2015)

No.15-210 Proceedings of the 6th International
Conference on Advanced Mechatronics (ICAM2015),
Tokyo, Japan, December 5-8, 2015

Evaluation of Breaking Performance in Vibration-Assisted Electrostatic Surface Induction Actuator

Takeru Nemoto*1, Gabriel Zsurzan*1,2, Akio Yamamoto*1
*1 Department of Precision Engineering, Graduate School of Engineering, The University of Tokyo
7-3-1 Hongo, Bunkyo-ku, Tokyo, 113-8656 Japan
*2 Department of Electrical Engineering, Technical University of Denmark
Richard Petersens Plads byg. 325, Kgs. Lyngby, Denmark

This paper evaluates breaking performance of an electrostatic surface induction actuator. The actuator is equipped with piezoelectric vibrators such that the friction between the slider and the stator electrodes can be dramatically reduced by squeeze-film effect. In such an actuator, the friction force can be changed by turning on and off the vibrator. The friction change can be utilized for high-performance slider motion control; for example, friction can be increased by switching off the vibrator when the slider needs to stop. In this paper, we evaluated how fast the slider can stop in several conditions. The result clearly shows the effect of friction change in breaking performance of the actuator.

1 Introduction

Table top displays with electrostatic surface actuators enable users to interact with computers through real physical objects placed on the display [1, 2]. The electrostatic surface actuators can be fabricated thin and transparent by utilizing screen printing; printing fine-pitch electrodes using transparent (or translucent) conductive paste on a transparent plastic sheet or glass plate can realize thin and transparent actuator. Such an actuator can be quite easily mounted on off-the-shelf LCD monitors. For example, in [1], electrostatic surface induction actuator was placed on LCD monitor to realize physical interaction with computer-animated objects; the user can move a paper sheet placed on the LCD to play with a computer-animated object inside the monitor.

One of the technical challenges in the electrostatic surface actuators is the reduction of friction between the slider and the stator electrodes. The electrostatic force that drives the slider in horizontal direction also works in vertical direction as attraction force. The attraction force is much larger than the lateral driving force, and therefore, the interface surface between the slider and the stator must have very low surface friction; otherwise the slider does not move due to large friction force. One common method to reduce friction coefficient is to spread tiny glass beads between slider and stator [1, 2]. However, use of glass beads raises a maintenance problem. Another method is to use special surface coating for both surfaces of the slider and the stator [3]. The surface coating, however, limits the slider material.

Recently, another method of friction reduction has been tried, which utilizes squeeze film effect caused by vibration [4]. By vibrating the stator surface using piezoelectric elements, a thin air layer is produced between the slider and the stator, which dramatically reduces the friction.

The use of squeeze film effect brings us a new function that does not exist in the previous means of friction reduction. The new function is modulation of friction force; by turning on and off the piezoelectric vibrator, friction coefficient can virtually be changed. For example, friction can be reduced for acceleration of the slider, whereas friction can be enhanced for sudden stop of the slider. Such characteristic is quite important for the above-mentioned application of the electrostatic actuator. In the interactive system reported in [1], the slider needs to stop instantly when it hits the virtual object rendered in the LCD.

Toward such goal, this paper investigates the breaking performance of the electrostatic actuator with squeeze-film effect. The performance was compared in three different conditions, where either or both of vibration and electrostatic driving force are turned off to stop the slider.

2 Experiment

The experimental setup is shown in Fig. 1. The electrostatic actuator was made by screen printing. Translucent conductive paste was printed on a glass plate to form fine-pitch electrodes. The electrode pattern consists of 16 sub-areas arranged in 4-by-4 matrix, as same as in [2]. Each sub-area contains three-phase electrode arrangements in x- or y-direction. Such electrode pattern can realize rotation of the slider at some fixed points, in addition to 2-DOF translational motion [2]. On both edges of the glass plate, vibration sources are attached, consisting of beryllium copper plates and piezoelectric elements. The detail of the actuator design is reported in [4].

The breaking performance was evaluated for rotation motion of the slider, as there is no stroke limitation for rotational motions. Transparent slider (OHP sheet) was cut into circular form with a diameter of 80 mm and placed on the stator surface such that the slider covers four electrode

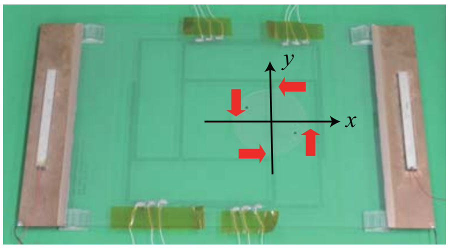

Fig. 1 Experimental setup.

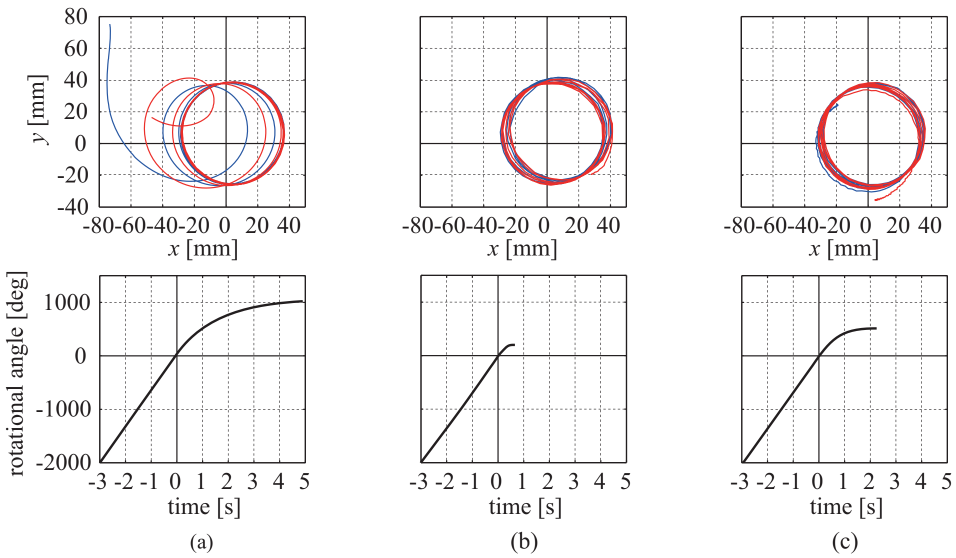

Fig. 2 Trajectories of two fiducial markers and rotational angle of the slider.

sub-areas. The electrodes were fed three-phase voltage such that they generate electrostatic driving force in the directions illustrated in Fig. 1 using red arrows. The motion of the slider was recorded by high speed camera (VW-6000, Keyence). To facilitate it, the slider was equipped with two fiducial markers (black dots in Fig. 1).

The slider was rotationally accelerated using electrostatic driving force until it reaches a steady-state. The vibration was kept on during the acceleration. Then, either electrostatic driving force or vibration, or both, was suddenly turned off to investigate breaking performance. The driving conditions for the piezo elements were 290 V_{p-p} and 17.9 kHz, and those for electrostatic driving were 500 V_{p-p} and 200 Hz.

Fig. 2 shows the results. The plots on the top show the motion trajectories of the fiducial markers on the slider, recorded from three seconds before the breaking started until the slider stopped. The plots on the bottom show the time-course of the rotational angle of the slider. The breaking conditions are

(a) only electrostatic driving force was cut off,
(b) only vibration was cut off (electrostatic driving force was kept active), and
(c) both electrostatic driving force and vibration were cut off.

In case (a), the slider lost control and drifted away due to too small friction force. It hit some obstacles, such as electrical terminals, before it completely stopped in about 5 seconds. In case (b), the slider stopped the rotation in about 0.5 second, even though there was still electrostatic driving force. This stopping time was much shorter than the case (c) where the slider needed about two seconds to stop. In case (b), it seems that the electrostatic attraction force became dominant due to the increased friction coefficient after the cut off of the vibration. Comparison of these three cases clearly shows the effect of friction changes for slider breaking performance. This time, in case (b), the voltages for the electrostatic actuator was kept the same even after the cut-off of the vibration. The breaking performance would be much enhanced if we apply different voltage pattern for breaking, such as voltage pattern for reversed motion or DC voltages.

3 Conclusion

Friction reduction between the slider and the stator electrodes was one of the technical challenges in electrostatic surface actuators. Use of squeeze-film effect is one promising mean for friction reduction. In this paper, we focused on another interesting aspect of the squeeze-film effect; the friction between the slider and the stator can be changed. The effect of friction change was evaluated in breaking performance for the rotating slider. The results clearly shows that the breaking performance was enhanced by cutting off the vibration for the squeeze film effect.

Acknowledgement

This work was supported in part by KAKENHI B (No. 26280069) from JSPS, Japan.

References

[1] K. Amano and A. Yamamoto, "Tangible interactions on a flat panel display using actuated paper sheets", *Proc. 2012 ACM int'l conf. Interactive tabletops and surfaces*, pp. 351-354 (2012).
[2] N. Yamashita, et al., "Interaction with Real Objects and Visual Images on a Flat Panel Display using Three-DOF Transparent Electrostatic Induction Actuators", *Proc. 7-th International Conference on Advances in Computer-Human Interactions*, pp. 294-299 (2014)
[3] "Electrostatic Actuator", Japanese Unexamined Patent Application Publication, No. JP-A-Hei-238484 (1997)
[4] G. Zsurzsan, et al., "Using squeeze-film effect to reduce surface friction in electrostatic actuators", to appear in *Proc. JSME/RMD International Conference on Advanced Mechatronics 2015*

M

Improved Kayaking Ergometer Using a Switch-mode Converter Driven Alternator

2016 IEEE International Conference on Industrial Technology (ICIT2016)

Improved Kayaking Ergometer Using a Switch-mode Converter Driven Alternator

Chris Cornaby, Jeppe Friberg, Nikolaj B. Søndergaard, Kristian Lindberg-Poulsen, Tiberiu-Gabriel Zsurzsan
Institute of Electrical Engineering
Technical University of Denmark

***Abstract*—This paper describes the implementation of a generator as a source of resistance in a modern kayaking ergometer. This ergometer can function as a platform for emulation of the athlete-kayak-paddle system. The system was considered and described. A possible model for digital regulation has also been described. A synchronous-rectified buck converter has been designed to control the current through the rotor and, by extension, the mechanical resistance felt by the oarsman. The circuit was designed to function with a 12V car battery as a supply. Necessary specifications for efficiency and output stability were set, measured and met. The prototype without regulation was presented at the 2015 Kayaking World Cup, and was met with appreciation and positive feedback.**

I. Introduction

Currently indoor rowing machines, known as kayaking ergometers, are being used by professionals and amateurs alike for convenient training. Many different versions of kayaking ergometers exist. The idea of this paper is to replace the ordinary sources of mechanical resistance with an alternator delivering a variable resistance. The issue with a the mechanical approach to the emulation of kayaking, lies in the dynamics of the stroke through water. The drag through the water will initially be high, but as it is broken into laminar flow resistance and turbulent flow resistance, the drag of the water changes through the stroke. This can be emulated more accurately by use of digital regulation and a computer model of the athlete-kayak-paddle system. An overview of the controller circuit is provided along with results on how well the circuit performs.

This paper also discusses potential improvements to the existing system, as the design described in this paper is meant as a platform for further work on advanced emulation of kayaking.

II. System Dynamics

The main reason that the traditional ergometers are insufficient is their inability to accurately emulate the dynamics of a athlete-kayak-paddle system. In all modern ergometers the machine is separated from any large bodies of water and the fluid dynamics of water are unsuccessfully recreated.
There are two forces acting on the system in the anteroposterior direction; F_P, the forward element of the blade force F_B, also known as the force of propulsion, and R_T, the total aerodynamic and hydrodynamic drag forces[1]. M is the total mass of our system.
The equations governing the change of velocity in the anteroposterior direction are:

$$dv_x = \frac{F_P + R_T}{M} dt \tag{1}$$

Where the total resistance can be broken down into the aerodynamic and hydrodynamic resistance. The hydrodynamic resistance can further be broken into viscous (R_V) and wave (R_W) resistance[1]. These can be calculated from the coefficient of viscosity (C_V) and wave drag (C_W) as:

$$R_V = \frac{1}{2} \cdot \rho_W \cdot C_V \cdot S_W \cdot v_{/W}^2 \tag{2}$$

$$R_W = \frac{1}{2} \cdot \rho_W \cdot C_W \cdot \frac{\sigma}{L} \cdot v_{/W}^2 \tag{3}$$

Where $v_{/W}$ is the hull velocity relative to the water, ρ_W the density of water, S_W the submerged surface area of the hull, σ the maximum sectional area of the hull and L the length of the waterline[1].
The aerodynamic drag is expressed as:

$$R_A = \frac{1}{2} \cdot \rho_A \cdot C_A \cdot S_A \cdot v_{/A}^2 \tag{4}$$

Where ρ_A is the density of air, C_A is the aerodynamic drag coefficient, S_A is the forward frontal area of the system above water and $v_{/A}$ is the velocity of the air relative to the system. The estimation of constants is not the subject of this paper.

There are also vertical forces to consider; B, the buoyancy of the kayak and w, the weight of the system. When the kayak is in motion the blade force F_B will likely have a vertical component, causing the system to become less submerged the faster it goes. This implies that the surface area of the submerged part of the system will wary with speed and/or stroke technique, something to consider for advanced modelling. These vertical forces will not be considered in the following section, as that would increase the degrees of freedom and complexity of the system considerably while adding very little to the emulation.

III. Regulator Design

There are a few things to consider before a regulator can be designed. The "load" felt by the paddle in accelerating the system is proportional to the difference in velocity between the paddle and the kayak, assuming that the user is rowing in still water. Due to the string based force transfer method of the mechanical system, we cannot simulate the push of the water on the paddle in those cases where the kayak is moving at a higher velocity than the paddle. Furthermore there is a torque constant relating the force the paddle is acting on the water with and the current magnitude in the rotor of the generator, to correlate the simulated load and the load in the generator. This proportionality factor will be dependent on the generator used. The model of the system and a possible design for the regulator can be seen in Fig. 1. There are two transfer functions in the model. One is for the change in speed of the kayak and should correlate to the inertia of the system. The second is for the simulated load, and should be adjusted to give a correct feeling of a paddle through water. In-depth consideration of these transfer functions will be addressed in future work.

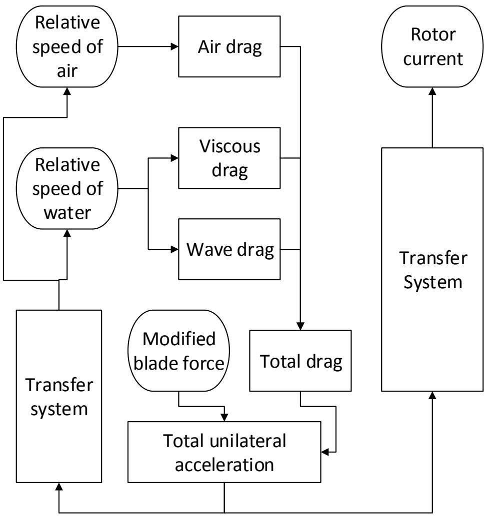

Fig. 1. Block diagram of the system model.

IV. Controller Design

The control circuit has been designed from a list of initial goals:

- Efficiency should be greater that 85%.
- Maximum output ripple should be less that 10% at max I_{Out}.
- Passive cooling should keep the circuit below 75 °C

The converter chosen for our control circuit is a synchronous-rectified buck converter. This converter topology has been chosen due to the demand of zero output without shutting down the circuitry. A synchronous rectified version of the buck has been chosen to reduce the losses in the circuit. The alternator winding resistance is estimated to 2Ω. 12V across the windings will result in a 6A rotor current when the rotor is not moving. This current is sufficient to produce the required maximum resistance.

When the circuit is turned on, it amplifies the output current and dampens output voltage as a linear function of duty cycle[2]:

$$I_{out} = \frac{I_{in}}{D} \tag{5}$$

$$V_{out} = V_{in} \cdot D \tag{6}$$

The linear nature of this type of converter makes it easy to change the output current I_{out}, and hereby change the magnetic resistance in the alternator. The control circuit is designed with a voltage-controlled pulse width modulator (PWM) that has a controllable duty cycle. The prototype has a manually changeable duty cycle, which is achieved by using a potentiometer in a voltage division to control the input voltage. The PWM signal is used to control a gate driver which then controls the two MOSFETs.

The efficiency of the converter depends on the conduction losses and switching losses. To minimise the conduction losses, the $R_{DS(on)}$ in the MOSFET's, as well as the resistance in the copper wire of the inductor, should be as low as possible. These losses are reduced primarily by choosing the right components.

The switching losses are a combination of the internal MOSFET loss, and the loss resulting from parasitic inductance due to gate and switching loops.

V. Mechanical Implementation

A kayaking ergometer was provided with a resistance fan which was replaced with a cogwheel. A smaller cogwheel was mounted on the alternator, and a chain was fitted to the appropriate length, as seen on Fig. 2. The force put into the strokes, also known as the blade force F_B, is converted into torque, which in turn drives the alternator with a gearing of 1:1.5. A low gearing is used to reduce the minimum resistance, so that operation with very low resistance is possible.

A. Alternator Functionality

As a given specification, an oarsman produces up to 600W of continuous power. The alternator acquired is therefore specified to handle at least 1kW. The alternator used in the prototype is a standard Lundell type car alternator, which requires a current through the rotor to generate the magnetic field required to induce an output. The alternator has been refitted, so that this rotor current is controlled by the controller circuit. The Lundell type alternator is designed to work with a car engine, and generates power in the interval 900 - 10,000 RPM[3]. With our gearing of 1:1.5, this requires the user to row a minimum of 600 RPM to generate power as our battery supplies 12V. By Faraday's law:

$$|\epsilon| = |\frac{d\Phi_B}{dt}| \tag{7}$$

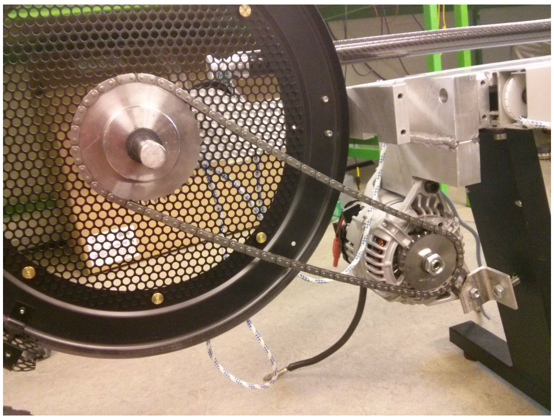

Fig. 2. Ergometer fitted with a cogwheel, alternator and a chain connecting the two

The induced voltage ϵ is proportional to the change of the magnetic field Φ_B over time. This means that the induced voltage is proportional to both the angular velocity of the rotor and the strength of the magnetic field in the rotor. At a constant velocity and magnetic field strength, the output of the alternator can be measured as a sinusoidal wave. This is then rectified by a full-wave rectifier in the alternator. Fig. 3 shows a simplified version of this circuit.

VI. Sensor Implementation

A six axis gyroscope and accelerometer (in a MPU-6050 chip) were fitted at each end of the paddle. In this way we can measure and calculate the kinematics of each blade, and use it as the modified blade force seen in Fig. 1.

IR diodes were fitted at the ends of the paddle and sensors were fitted below the seat of the user, for measuring if the paddle was below the waterline or not. Changing the placement of the sensors decide waterline height in relation to the user. By reading the blade force and waterline sensors into an Arduino UNO, the Arduino calculates the needed load for a given speed of the kayak compared to the momentum of the stroke, and sets the control signal to the power converter, which in turn adjusts the rotor current giving a greater sense of resistance to the rower. The emulation is in this way controlled digitally by the Arduino, where constants and transfer functions can be adjusted to give a better emulation, though this is not the focus of this paper. The complete setup of sensors and Arduino can be seen on Fig. 3.

VII. Measurements

To further reduce the switching losses, the circuitry has been constructed on a printable circuit board (PCB). The final PCB design can be seen in Fig. 5. In the design, large heat sinks have been included for both of the MOSFETs' drains for better heat dissipation. A thermal picture after two hours of continuous maximum output can be seen on Fig. 4. The greatest temperature is reached by the gate driver at 42,1 °C.

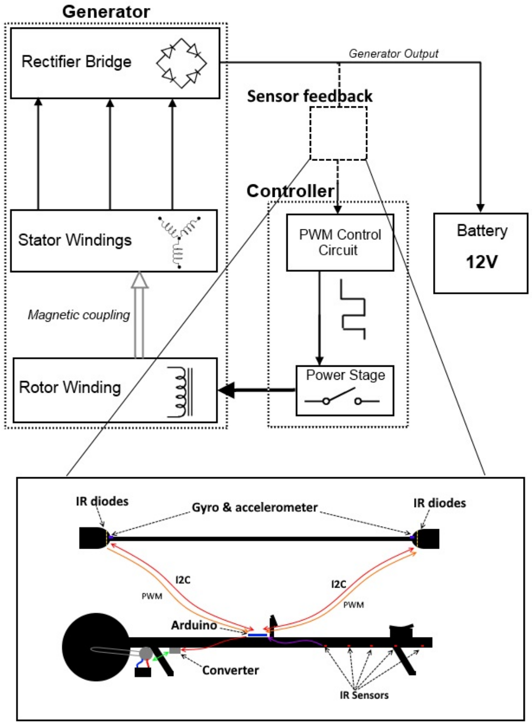

Fig. 3. Complete block diagram showing significant interconnections

The gate driver is rated for an absolute maximum temperature of 150 °C.

Implementing the PCB greatly reduced switching losses due to reduced parasitic inductances from loops. A PCB also reduces conduction losses in the copper wire since the size of the circuit is greatly reduced.

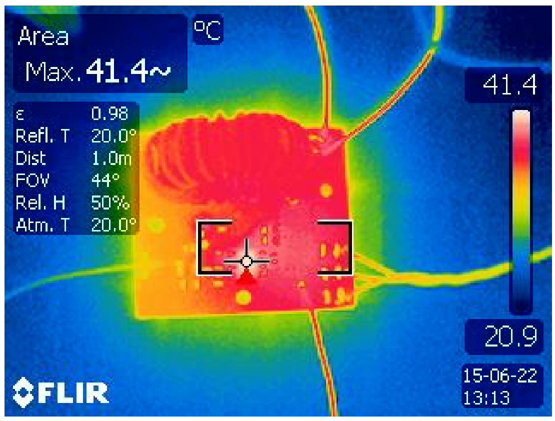

Fig. 4. Thermal picture at maximum power dissipation.

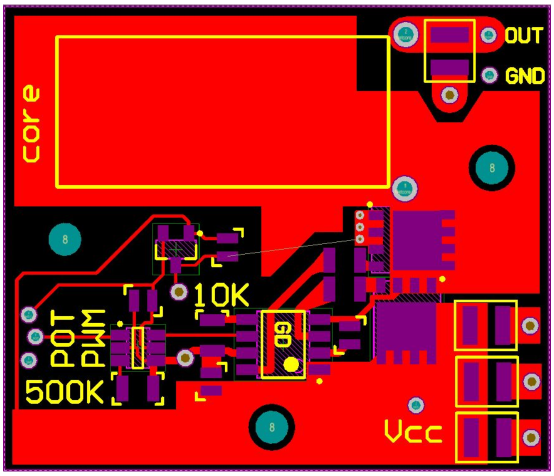

Fig. 5. Final Printed Circuit Board (PCB)

A. *Efficiency*

The efficiency of the circuit has been measured at differing duty cycles and with different ohmic loads. These measurements can be seen in Fig. 6. As previously mentioned the alternator winding resistance is estimated to be 2Ω, which means that the actual efficiency of the ergometer in use should be slightly better than or close to the measurements at 2.5Ω load.
The measurements shows an efficiency of above the targeted 85%, as soon as a duty cycle of 20% is reached. This threshold of 20% duty cycle is acceptable due to the relatively low output at this stage.

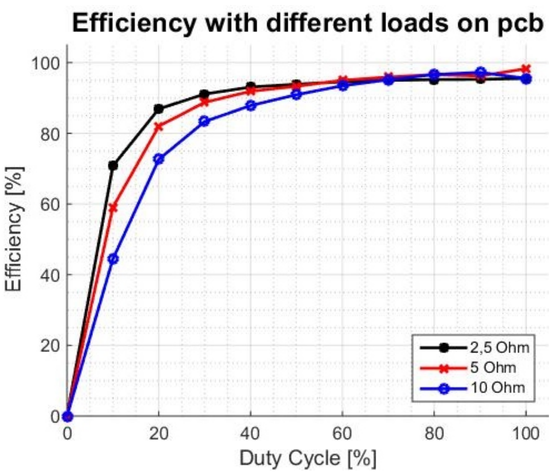

Fig. 6. Effeciency at different loads

B. *Ripple*

The output ripple was measured with a load of 2.5Ω at a 50% duty cycle, resulting in a peak-peak ripple of 140mV as seen in Fig. 7, which is equivalent to 56mA peak-peak current ripple. At max output the current ripple is:

$$\frac{56mA}{4.8A}\% = 1.16\% \tag{8}$$

This output ripple is well below our initial goal of a 10% ripple.

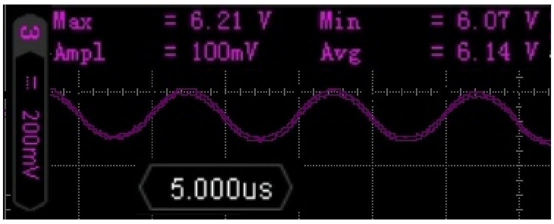

Fig. 7. Output ripple at 50% duty cycle with 2.5Ω

C. *Emulation*

To emulate the kayak the converter has to react much faster than a human can react (approx. 200ms)[4] for a smooth operation. Fig. 8 shows a rise time well under $60\mu s$ from duty cycle 30%-70%. This states that the converter is fast enough to meet the demand of seamless transition in emulation.

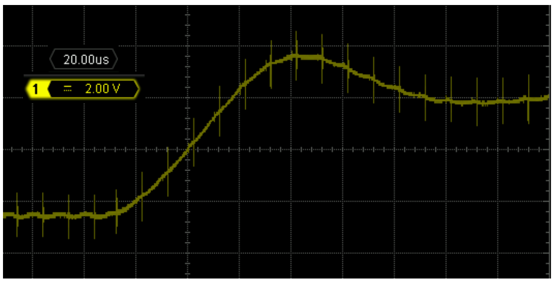

Fig. 8. Rise time output change

We also have to consider how fast the Arduino can adjust the control signal. This can be seen in Fig. 9, where the response time is 25.5ms which is fast considering the reaction time of a human as discussed previously. Note that the response time of the converter is added to the total response time, but it is so small that it is negligible. For faster emulation an Arduino Mega or an embedded controller would be the next step.

VIII. Conclusion

The purpose of this paper was to create an ergometer with resistance that is given electronically and controlled digitally. We have implemented the alternator and designed a control circuit for controlling the rotor current. We have

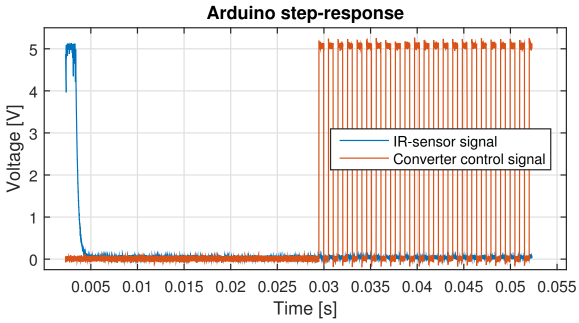

Fig. 9. Arduino control signal change time

then included an Arduino and sensors, and made a platform for implementation of high-end emulation of the kayaking ergometer.

The circuit was designed as a synchronous-rectified buck converter on a PCB. The specifications set for the circuit were all met. The duty cycle of the circuit is controlled by the Arduino, which can be adjusted to any desired system. By perfecting the digital regulator on the Arduino, an accurate emulation of the athlete-kayak-paddle system can be made.

The non-regulated design was presented at the 2015 kayaking world cup and received warmly (Fig. 10). Some rowers stated that it was superior to other ergometers, even in its then non-regulated state.

Acknowledgement

The authors would like to thank the staff of Skylab DTU, for helping with constructing the mechanical parts of the project. Special thanks to Dansprint ApS for supplying the kayaking ergometer.

Fig. 10. Professional athlete testing our ergometer at the 2015 Kayaking World Cup.

References

[1] M. Begon, O. Mourasse, and P. Lacouture, "A method of providing accurate velocity feedback of performance on an instrumented kayak ergometer," *Sports Engineering*, vol. 11, no. 2, pp. 57–65, 2009.

[2] N. Mohan, *Power electronics: a first course*, 1st ed. Wiley, 2012, ch. 3.

[3] R. Ivankovic, J. Cros, M. T. Kakhki, C. a. Martins, and P. Viarouge, *New Advances in Vehicular Technology and Automotive Engineering*, 1st ed. InTech, 2012, ch. 6.

[4] M. I. Posner, "Timing the Brain: Mental Chronometry as a Tool in Neuroscience," *PLoS Biology 3.2*, 2005.

[5] K. Lindberg-Poulsen, M. a. E. Andersen, A. Knott, and T. Andersen, "Energy harvesting from an exercise bike using a switch-mode converter controlled generator," *2010 IEEE International Conference on Sustainable Energy Technologies, ICSET 2010*, 2010.

[6] W. L. Soong and N. Ertugrul, "Inverterless high-power interior permanent-magnet automotive alternator," *IEEE Transactions on Industry Applications*, vol. 40, no. 4, pp. 1083–1091, 2004.

[7] R. Strzelecki, M. Jarnut, and G. Benysek, "Exercise bike powered electric generator for fitness club appliances," *2007 European Conference on Power Electronics and Applications, EPE*, 2007.

www.elektro.dtu.dk

Technical University of Denmark
Department of Electrical Engineering
Ørsteds Plads
Building 348
DK-2800 Kgs. Lyngby
Denmark
Tel: (+45) 45 25 38 00
Email: elektro@elektro.dtu.dk